TECHNISCHE UNIVERSITÄT MÜNCHEN

Ingenieurfakultät Bau Geo Umwelt

Numerical Methods for the Vibro-Acoustic Assessment of Timber Floor Constructions

Mathias Kohrmann

Vollständiger Abdruck der von der Ingenieurfakultät Bau Geo Umwelt der Technischen Universität München zur Erlangung des akademischen Grades eines

Doktor-Ingenieurs

genehmigten Dissertation.

Vorsitzender: Prof. Dr.-Ing. Stefan Winter

Prüfer der Dissertation:

1. Prof. Dr.-Ing. habil. Gerhard Müller
2. Prof. Carl Hopkins
3. Prof. Dr. Ulrich Schanda

Die Dissertation wurde am 20.09.2016 bei der Technischen Universität München eingereicht und durch die Ingenieurfakultät Bau Geo Umwelt am 16.01.2017 angenommen.

Abstract

This thesis focuses on the development of numerical models for predicting the vibro-acoustic behavior of timber floor constructions. It is a part of the recently finished research project, "VibWood", which aims at the development of design guidelines, that describe the acoustical and dynamic behavior of timber floors below 125 Hz, and for designing adaptive protection systems against vibrations.

Parametric Finite-Element (FE) models are developed for representative timber floor constructions including a floating floor and a suspended ceiling. The FE models are validated by accompanying measurements in a floor testing facility. The material parameters are calibrated by Model Updating, according to the measured and simulated eigenfrequencies. For the evaluation of the simulated floors with regard to their vibro-acoustic characteristics, an Integral Transform Method (ITM)-based acoustical evaluation model is developed to predict the floor's radiated sound power from measured or simulated structure-borne sound velocities. The data can be derived from either an Experimental Modal Analysis (EMA) or from a Harmonic Frequency Analysis. The advantages and disadvantages of the model, as compared with existing models, as well as the limitations of the model, due to its discrete nature are pronounced. For the evaluation of pedestrian-induced vibrations, a transient evaluation model is applied.

Focus lies on the investigation of the influence of the air inside the cavity - between the main load-bearing structure and suspended ceiling - on the sound transmission across the floor. The results of different numerical modeling approaches are compared with the measured data. A deeper insight into the physical phenomena is provided by a representation of the vibration pattern in the wavenumber domain.

Parametric studies are performed within an automated process for a large number of geometrical parameter combinations. A dimensional analysis concerning the first eigenfrequencies of the floors is performed. Further, the influence of individual parameters on the resulting radiated sound power is pointed out. A special focus lies on the geometrical parameters of the suspended ceiling. The effectiveness of Tuned-Mass-Dampers (TMDs) on the attenuation

of the radiated sound power is investigated. Coefficients are derived to enable a comparison of the simulated data to standardized single values for the evaluation of the impact sound insulation. The derived database is intended to be implemented into a Graphical User Interface (GUI) to support the practical engineer in the planning phase prior to construction.

Contents

List of Figures

List of Tables

List of Symbols

Superscripts and diacritics

Symbols	Description
$\tilde{\bullet}$	*Voigt* notation for matrices
$\tilde{\bullet}$	Dynamic variables in acoustical fluids
$\bullet^T$	Transposed tensor
$\bullet^{-1}$	Inverted tensor
$\bullet'$	Transformed coordinates
$\bullet^*$	Conjugate complex
$\hat{\bullet}$	*Fourier* coefficient
$\hat{\bullet}$	Amplitude
$\bar{\bullet}$	Averaged quantity
$\bar{\bullet}$	Approximated or related function or quantity
$\underline{\bullet}$	Complex quantity
$\bullet',\bullet''$	Per unit length, per unit area

Subscripts

Symbols	Description
$\parallel, \perp$	Parallel, perpetual to fiber direction
0	Ambient state index
0	Invariant Amplitude (plane wave)
1,2,3	Reference coordinates
α,β	Row and column index of the exponents of the fundamental dimensions
α,β	Spatial coordinates (discrete)
A	Air
alu	Aluminum
B	Bending (...)
C,D	Indicating a CTFT or a DTFT of a function
col	Column
d	(...) of the damper
e	External (...)

e	Element
eff	Effective (radiated)
$elasto$	Elastomer
$foot$	Footfall
gpb	Gypsum plaster board
$hang$	Hanger
i	Index of eigenvectors
i	Internal (. . .)
i,j	Index of eigenmodes
i,j	Index of measurement points
i,j,k,l	Indexes for reference axes
ins	Insulation
int	Integrated
L,T,R	Cylindrical coordinates
l	Literature parameter
m	Measured parameter
mu	Model updated parameter
opt	Optimized (. . .)
p	Sound pressure related
ped	Pedestrian
r,s	Spatial coordinates (discrete)
s	Structure-borne (. . .)/ (. . .) of the structure
scr	Screed
spr	Spruce
$subst$	Substituted (. . .)
sus	Suspension
tot	Total (. . .)
uc	U-channel
V	Volume element
v	Sound velocity related
x,y,z	*Cartesian* coordinates

Greek Letters

Symbols	Units	Description
α	–	Scale factor
α	°	Angle between sound velocity vector and enveloping surface vector
α,β	–	Mass and stiffness proportionality factor
α,β,γ	–	Discrete wavenumber and frequency sample indexes
α,β,γ	–	Dimensionless parameters

α,β,γ	°	Angles of rotation
γ	$-$	Engineering shear strain
ζ	$-$	Modal damping coefficient
$\boldsymbol{\varepsilon}$	$-$	Strain tensor
ε	$-$	Normal strain
θ	°	Angle of sound radiation
λ	m	Wave length
μ	$-$	Absorption coefficient
μ	$\frac{\text{kg}}{\text{m}^2}$	Mass per area
μ	$-$	Mass ratio between the structure and the damper
ν	$-$	*Poisson* ratio
Π	Nm	Elastic Potential
π	$-$	Dimensionless parameter
ρ	$\frac{\text{kg}}{\text{m}^3}$	Acoustically induced sound density perturbation
$\boldsymbol{\Sigma}$	$\frac{\text{N}}{\text{m}^2}$	2nd order *Cauchy* stress tensor
σ	$-$	Radiation efficiency
σ	$\frac{\text{N}}{\text{m}^2}$	Normal stress
τ	$-$	Shear stress
τ	s	Argument of a function in time
$\boldsymbol{\Phi}$	$-$	Eigenvector matrix
ϕ	rad	Phase constant
χ	m	Argument of a function in space
ω	$\frac{\text{rad}}{\text{s}}$	Circular frequency

Latin Letters

Symbols	Units	Description
A	arbitrary	Fundamental dimension for a Dimensional Analysis
A	arbitrary	Amplitude of a rectangular signal
a	$-$	Exponents of the fundamental dimensions
a,b	$-$	Substitution variables
a,d,x,y	m	Distances depending on the task
a_i,a_j	m^2	Approximated circle area of the piston at measurement points i and j
$\mathbf{B}$	$-$	Matrix of derivations
B	Nm^2	Bending stiffness
$\mathbf{C}$	$\frac{\text{N}}{\text{m}^2}$	4th order Stiffness tensor
$\mathbf{C}$	$\frac{\text{Ns}}{\text{m}}$	Damping matrix
C	$\frac{\text{N}}{\text{m}^2}$	Stiffness coefficient
C_I	dB	Spectrum adaption term

$C_{I,50-2500}$	dB	Spectrum adaption term (increased frequency range)
c	$\frac{\text{m}}{\text{s}}$	Wave speed
c	$\frac{\text{kg}}{\text{s}}$	Damping constant
d,t	m	Thicknesses (German and English notation)
d_ij	m	Distance between two measurement points i and j
$\mathbf{E}$	—	2$^{\text{nd}}$ order *Green-Lagrangian* strain tensor
E	$\frac{\text{N}}{\text{m}^2}$	*Young*'s modulus
e_{size}	m	Element size
$F(\omega),G(\omega)$	arbitrary	Continuous functions with variable circular frequency
$F(f)$	N	Force function with variable frequency
$F(t)$	N	Force function with variable time
f	$\frac{1}{\text{s}}$	Frequency
$f(t),g(t),x(t),y(t)$	arbitrary	Continuous functions with variable time
$f(Q_1,\ldots,Q_n)$	—	Equation of a mathematical model
$f(\pi_1,\ldots,\pi_{n-r})$	—	Replaced equation using dimensionless parameters
$f(\mathbf{x})$	—	Objective function
f_0	$\frac{1}{\text{s}}$	Fundamental frequency
f_c	$\frac{1}{\text{s}}$	Critical frequency
f_{Nq}	$\frac{1}{\text{s}}$	*Nyquist* frequency
f_n	—	Normalized frequency
f_s	$\frac{1}{\text{s}}$	Sampling rate
G	$\frac{\text{N}}{\text{m}^2}$	Shear modulus
$\mathbf{g}$	—	Metric tensor for a rotational transformation
g	—	Transformation coefficient
$H(f)$	arbitrary	Transfer function with variable frequency
$H_B(f)$	—	Transfer function (combined filter)
$H_{KB}(f)$	—	Transfer function (weighting filter)
$H_u(f)$	—	Transfer function (band limiting filter)
h	m	Height
$h(t)$	—	Rectangular window function
$\mathbf{I}$	$\frac{\text{W}}{\text{m}^2}$	Sound intensity vector
I	$\frac{\text{W}}{\text{m}^2}$	Sound intensity
I	m^4	Moment of inertia
I	Ns	Impulse
$\mathbf{K}$	$\frac{\text{N}}{\text{m}}$	Stiffness matrix
$\mathbf{K}$	—	Discrete kernel matrix
$K(k_x,k_y,f)$	—	Continuous kernel function
$K[\alpha,\beta,\gamma]$	—	Discrete kernel function
$KB(t)$	—	KB-signal
$KB_F(t)$	—	Weighted vibration severity
KB_{Fmax}	—	Maximum value of the weighted vibration severity

k	–	Unknown parameter for a Dimensional Analysis
k	–	Discrete time sample index
k	$\frac{\text{rad}}{\text{m}}$	Circular wave number
k	–	Number of considered eigenfrequencies
L	N	Modal force
L_p	dB	Sound pressure level
L_W	dB	Sound power level
L_i	dB	Impact sound pressure level
L_n	dB	Normalized impact sound pressure level
$L_{n,w}$	dB	Weighted normalized impact sound pressure level (laboratory measurements)
$L_{Sum,50-100}$	dB	Descriptor related to $L_{n,w}$
l	m	Length
$l(x,t)$	N	Force field
$\mathbf{M}$	kg	Mass matrix
M	–	Number of transformed domain samples
M^*	kg	Modal mass
m	kg	Mass
$\mathbf{N}(x,y,z)$	–	Matrix of form functions
N	–	Number of original domain samples
n	–	Number of variables
n_r	–	Refinement factor
n_{substep}	m	Number of substeps
P	W	Sound power
$\mathbf{p}$	W	Discrete sound power vector
$\mathbf{p_i}(x,y,z,t)$	N	*D'Alembert* force vector
$p,p(x,y,z,t)$	$\frac{\text{N}}{\text{m}^2}$	Acoustically induced sound pressure perturbation
Q	arbitrary	Variable for a Dimensional Analysis
$\mathbf{R}$	–	*Reuter* matrix
$R(f)$	$\frac{\text{m}}{\text{N}}$	Receptance over frequency
$R_{ff}(\chi,\tau)$	N	Auto-correlation function of the force field
$R_{L_i L_j}(\tau)$	N	Cross-correlation of modal forces
R^2	–	Coefficient of determination
r	–	Number of fundamental dimensions
r	–	Discrete frequency sample index
r,s	–	Discrete spatial sample indexes
$\mathbf{S}$	$\frac{\text{m}^2}{\text{N}}$	4$^{\text{th}}$ order Compliance tensor
$\mathbf{S}$	m^2	Enveloping surface area vector
S	m^2	Surface area
S	N^2	Force amplitude
S	$\frac{\text{m}^2}{\text{N}}$	Compliance coefficient

$S_1(f)$	–	Impulse train in the frequency domain
$S_2(f_n)$	–	Impulse train in the normalized frequency domain
s	$\frac{\text{N}}{\text{m}^3}$	Dynamic stiffness
$s_1(t)$	–	Continuous impulse train in the time domain
$s_2[k]$	–	Discrete impulse train in the time domain
s_i, s_j	m^2	Element area at measurement points i and j
$\mathbf{T}$	–	Coordinate transformation matrix
T	s	Duration of a signal
T	s	Reverberation time
T_1	s	Sampling interval in the time domain
t	s	Time
t	–	Floor type
$\mathbf{u}(t)$	m	Nodal displacement vector
$\mathbf{u}(x,y,z,t)$	m	Displacement field vector
$\hat{\mathbf{V}}$	$\frac{\text{m}}{\text{s}}$	Discrete structure-borne sound velocity matrix
V	m^3	Volume
$V(f)$	$\frac{\text{m}}{\text{Ns}}$	Mobility
$\mathbf{v}$	$\frac{\text{m}}{\text{s}}$	Acoustically induced airborne sound velocity perturbation
$v(x,y,t)$	$\frac{\text{m}}{\text{s}}$	Velocity
$v[\alpha,\beta,\gamma]$	$\frac{\text{m}}{\text{s}}$	Discrete *Fourier* transformed velocity
$\hat{v}(k_x,k_y,f)$	$\frac{\text{m}}{\text{s}}$	Continuous *Fourier* transformed velocity
v_i, v_j	$\frac{\text{m}}{\text{s}}$	Structure-borne velocity at measurement points i and j
W	J	Work
w	m	Width
$w(f)$	m	Displacement over frequency
$X(f), Y(f)$	arbitrary	Continuous functions with variable frequency
$X_0(f)$	arbitrary	*Fourier* transform of an infinite continuous signal with variable frequency
$X_1(f)$	arbitrary	*Fourier* transform of a truncated continuous signal with variable frequency
$X_2(f_n)$	arbitrary	Repeated continuous signal in the normalized frequency domain
$X_3[r]$	arbitrary	Repeated, discrete signal in the frequency domain
$X_{zp}[r]$	arbitrary	Zero-Padded, repeated, discrete signal in the frequency domain
$\mathbf{x}$	–	Vector of optimization variables
x,y,z	m	Locations in space
$x_0(t)$	arbitrary	Infinite continuous functions with variable time
$x_1(t)$	arbitrary	Truncated continuous signal with variable time
$x_2[k]$	arbitrary	Discrete signal in the time domain
$x_3[k]$	arbitrary	Repeated, discrete signal in the time domain

$x_{zp}[k]$	arbitrary	Zero-padded, repeated, discrete signal in the time domain
z_{ii}, z_{ij}	$\frac{\text{kg}}{\text{s}}$	Self, mutual radiation impedance
z_p	−	Zero-Padding factor

Mathematical Symbols

Symbols	Description
•	Placeholder
$|•|$	Absolute value
∞	Infinity
○——●	*Fourier* transform symbol
$*$	Convolution symbol
·	Multiplication symbol
•̈	Second derivative with respect to time
D•	Total derivative
$d•$	Differential
$\partial•$	Partial-derivative symbol
∇	Three-dimensional *Nabla* operator
∇^2	Three-dimensional *Laplace* operator
∇^4	Square of the two-dimensional *Laplace* operator
$\sum$	Sum
$\int$	Integral
$\Delta•$	Discrete value
$\delta•$	Virtual (. . .)
$\delta(•)$	*Dirac* delta function
π	Ratio of a circle's circumference to its diameter
$\det(•)$	Determinant
e	*Euler*'s number
$\mathcal{F}$	*Fourier* transform operator
$\Im$	Imaginary part
i	Imaginary number
J_1	First-order *Bessel*-function
$\Re$	Real part
S_1	*Struve*-function

Acronyms

APDL   Ansys Parametric Design Language

FWHM Full Width at Half Maximum

OMA   Operational Modal Analysis

EMA   Experimental Modal Analysis

CLT   Cross-Laminated Timber

LVL   Laminated Veneer Lumber

NLT   Nail-Laminated Timber

EWP   Engineering Wood Products

IJ   I-Joist

ERP   Effective Radiated Power

LS   Liquid Screed

FLF   Floating Floor

FFT   Fast *Fourier* Transform

DFT   Discrete *Fourier* Transform

CTFT   Continuous Time *Fourier* Transform

DTFT   Discrete Time *Fourier* Transform

LJ   Lumber Joist

HBG   Hollow Box Girder

ITM   Integral Transform Method

MAC   Modal Assurance Criterion

DS   Dry Screed

SC   Suspended Ceiling

CAD   Computer-Aided Design

FE	Finite-Element
FEM	Finite-Element-Method
DOF	Degree-of-Freedom
GUI	Graphical User Interface
OSB	Oriented Strand Board
RMS	Root Mean Square
SEA	Statistical Energy Analysis
FSI	Fluid-Structure-Interaction
DCM	Discrete Calculation Method
TMD	Tuned-Mass-Damper
SDOF	Single-Degree-of-Freedom
MDOF	Multiple-Degrees-of-Freedom
ROTR	Rain-on-the-Roof
IPO	Input-Process-Output

1 Introduction

1.1 Motivation

The market share of timber construction for multi-storied buildings for industrial as well as for residential use has been rapidly growing in recent years [Weimar and Jochem 2013]. This can, in part, be explained with regard to profitability. Wood is light in weight, reduces static requirements and enables a high degree of prefabrication, which, in turn, leads to less transportation and storage costs. Moreover, adding another floor to an already existing building is often only possible with timber construction. On the other hand, with regard to the necessity of developing sustainability in construction concepts, timber construction has its advantages, as wood is a renewable raw material.

Serviceability linked with vibrations is a key issue for light-weight structures, especially for timber floors. In particular, in the frequency range below 125 Hz, timber structures are prone to pedestrian-induced vibrations, impact sound, as well as re-radiated sound caused by induced vibrations. This leads to comfort problems that arise even when the vibrational and acoustical requirements of current standardizations are met.

During the last few decades, much research has been done on the human perception of floor vibrations. Several design guidelines have been proposed, starting from the limitation of deflections over subjective assessment-based methods, to dynamic response-based methods, as in the current European standardizations [Weckendorf et al 2015]. Most of these guidelines primarily focus on the limitation of the fundamental natural frequency achieved by simplified calculation models, which often lead to rather conservative predictions.

With regard to acoustical requirements, until now, there exists no practical applicable design model for the prediction of the vibro-acoustical behavior of timber floor constructions. The effect of system components, such as suspended ceilings, floating floors, and other noise and vibration abatement, is currently described by simplified design guidelines, that were

essentially developed for traditional heavy-weight constructions. This might be misleading due to differences in the mechanical impedances of the system's components.

The radiated sound power is often predicted by measuring vibration patterns and radiation efficiencies. This concept has been applied successfully to heavy construction; however, its precision is questionable for light-weight timber construction with more complex vibration fields and higher modal density.

Models that can predict vibro-acoustical behavior in a highly realistic way need to be developed prior to the construction [Negeira 2013]. As experimental testing is time-consuming and expensive, a promising approach applies numerical methods [Floden 2014]. Once precise parametric models, calibrated by representative measurements, are developed, extensive parametric studies can be extrapolated. Vibratory and acoustic performance, such as the fundamental natural frequency and the radiated sound power, can be predicted by validated numerical models and are used in existing, or for the development of new design guidelines.

1.2 State of the Art

The application of numerical models for the prediction of the vibro-acoustical behavior has become the subject of various research studies. The recently finished research project, *"Silent Spaces"* at the Lund University, Sweden, and the Aalborg University, Denmark, has focused partly on the development of FE models of timber volume element buildings for the use in the low frequency range of $20 - 200$ Hz. In this specific design, a full building level is prefabricated, including timber joist floors and self-supported ceilings. The modeling of the air inside the cavity between each building level is investigated for various configurations, including porous material. The effect of the transmission of structural vibration is examined [Floden 2014]. A multi-storied building with repeating geometry was investigated by Andersen et al [2012], where the influence of the air modeled inside each room was considered. Another contribution within the same project investigates the elastomer material, that is implemented between each of the levels [Negeira 2013].

The current research project, *"Vibroakustik im Planungsprozess für Holzbauten"* at the Technical University Munich (TUM), in cooperation with the University for Applied Science Rosenheim, follows a hybrid Finite-Element-Method (FEM)/Statistical Energy Analysis (SEA) approach, predicting the sound transmission across junctions of building components [Winter et al 2014] in an effort to close the so-called mid-frequency gap. A numerical model is developed of a T-junction, formed by a floor and a wall, both made of CLT. The dynamic

properties of the model are based mainly on the results from the "Vibwood" research project [Kohrmann et al 2014].

Current research at *Eidgenössische Materialprüfungs- und Forschungsanstalt* (EMPA) in Switzerland uses SEA approaches to model the airborne sound transmission across composite heavyweight-lightweight floors [Churchill et al 2011]. The floor is a hybrid construction, with slabs made of timber joists and a concrete topping. Further investigation focuses on a resilient suspended ceiling [Churchill and Hopkins 2013a]. Especially, the stiffness of the ceiling hangers is assessed, based on the measurement setup proposed by Brunskog and Hammer [2002]. Within the scope of this research, the material properties of CLT are determined by ultrasonic and laser scanning measurement techniques, and are compared to a Modal Analysis of a corresponding FE model [Churchill and Hopkins 2013b].

In 2009, the research project, *"Schwingungstechnische Optimierung von Holz und Holz-Beton-Verbunddecken"*, was completed at TUM. Parallel measurements and numerical simulations with updated FE models were performed for LJ, Nail-Laminated Timber (NLT), CLT, and composite concrete/timber floors. The serviceability, linked to the structural vibrations and its perception by humans inside buildings, was investigated. An alternative design method to the dynamic response-based method in DIN EN 1995-1-1:2010-12 is proposed [Winter et al 2010][Hamm et al 2010].

A simplified FE model of a CLT floor with floating floor was developed at the Technical University Graz. Models using $2D$-shell elements with idealized material properties as well as $3D$-volume elements were examined. Dry and liquid screed were modeled for light and heavy weight construction, with additional fillings. Experimental as well as numerical Modal Analyses were performed, and the resulting eigenfrequencies were compared. Time courses of vibrations caused by heel-drop excitation were examined [Bogensperger et al 2010].

Ljunggren [2006] investigated the dynamic properties of lightweight steel-framed constructions, including suspended ceilings. He performed modal testing to derive the modal parameters of the floor and developed a TMD made of visco-elastic material to control the resonant vibrations. Further, the human vibration perception was investigated for single and multi-frequency vibrations.

The material properties of CLT slabs were determined by a detailed measurement-based investigation by Gülzow [2008]. He updated the material properties of analytical models by means of modal parameters determined by EMAs. A non-destructive testing procedure was introduced. The fundamental mechanics of wood was summarized by Grimsel [1999]. Aicher and Dill-Langer [2000] described the rolling shear modulus of a board inside a CLT slab as

a smeared shear stiffness of the structural element, which depends on the cutting pattern rather than an intrinsic material parameter. A numerical study on the rolling shear modulus performed by Feichter [2013] showed the influence of the directions of the annular rings and the size of the board.

The optimal design parameters for TMD have been subject to research for decades. Den Hartog [1952] initially formulated equations for undamped Single-Degree-of-Freedom (SDOF) systems. Optimized parameters for Multiple-Degrees-of-Freedom (MDOF) systems and the use of multiple TMDs to attenuate the dynamic response of structures have appeared ever since Warburton and Ayorinde [1980], Sadek et al [1997], Rana [1996]. A more recent approach to optimize TMDs for damped systems was introduced by Bakre and Jangid [2007].

The determination of radiation efficiencies from sound intensity measurements is a standardized procedure [DIN EN ISO 9614-1:2009-11]. A method to derive radiation efficiency from structure-borne sound velocities in spatial domain was introduced by Hashimoto [2001], wherein he points out the advantage of possible measurements in a noisy environment. In an older, alternate approach, the velocity data are processed in the wave number domain and radiation efficiencies are calculated semi-analytically by means of averaged *Green*s functions [Williams and Maynard 1982].

1.3 Research Project "VibWood"

1.3.1 Goal of the research

This dissertation is part of the recently completed research project, "VibWood", which aims for the development of design guidelines, that describe the acoustical and dynamic behavior of timber floors and for designing adaptive protection systems against vibrations [Kohrmann et al 2014].

Within this project, comprehensive measurements are performed on characteristic timber floor systems. Parallel to that, corresponding hybrid FE and radiation models are developed, which are calibrated according to results measured. Based on those models, the physical experiments are supplemented with subsequent parametric simulations as regards the vibro-acoustical behavior of timber floor systems in the frequency range below 125 Hz. While the parameter combinations of the physical experiments are limited, the numerical simulations can cover a wide, practically relevant parameter space. In this section, the part of the research project, which is not covered by this dissertation, will be briefly described, since

it is mandatory for the understanding of input data of the numerical models. For a more detailed description, see [Kohrmann et al 2014].

For developing accurate FE models, it is inevitable to evaluate the material and dynamic properties of the modeled structures. Three different types of wooden floor constructions are tested in the floor testing facility at the University of Applied Science in Rosenheim. In addition, measures to improve the vibrational behavior with respect to vibrations and sound radiation are investigated, such as floating floors, suspended ceilings, and the application of TMDs [Hanke 2012]. Operational and Experimental Modal Analyses (OMAs and EMAs) are performed using shaker and modal hammer excitations. The radiated sound power is measured by an intensity probe, using discrete intensity measurement method. Simultaneously, the structure-borne velocity is measured by a grid of accelerometers, and the radiation efficiency is derived from both results.

1.3.2 Floor testing facility

The floor testing facility in Rosenheim stretches over two levels, with a source room in the upper level and a receiving room underneath. The floor separating both rooms consists of reinforced concrete with a floating floor. It has an aperture for test objects, measuring 5.52 m × 5.52 m. For the bearing of the test objects, L-shaped steel profiles are attached to the reinforced concrete. The receiving room has a volume of $V \approx 115.5$ m^3. For intensity measurements, it is equipped with sound absorbing polyester fiber blocks, CARUSO-ISO-BOND®, to reduce errors caused by reflexions. Data is acquired by a MÜLLER-BBM PAK MKII multi-channel measurement device.

1.3.3 Tested floor configurations

One of the main goals of the research project is to cover the main timber floor construction styles. Weckendorf et al [2015] give a classification of timber floor systems and identify essentially two main classes. One class combines composed parallel joist members with a semi-rigidly attached sub-floor. Subsystems can be identified by the chosen type of joists (e.g., sawn lumber, Engineering Wood Products (EWP), wooden I-Joists (IJs)). The second class covers massive timber constructions (e.g., NLT, Laminated Veneer Lumber (LVL), CLT). Not considered by this classification are floors that can be described as hollow box constructions. Within these floors, horizontal and vertical elements are rigidly attached and

(a) LJ floor

(b) CLT floor

(c) HBG floor
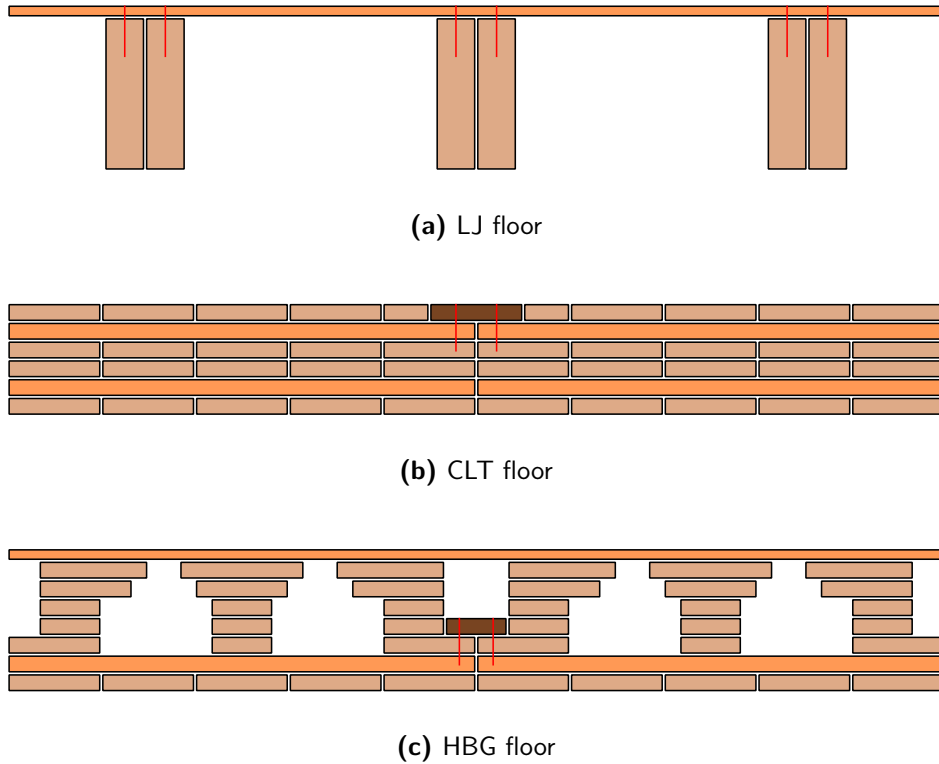
Figure 1.1: Schematic representation of cross-sections of tested floor styles normal to the main load-bearing direction

form a cavity inside the floor, which can be filled with functional material (e.g., additional loading, insulation, TMDs).

A schematic representation of floor styles, tested in this project, is given in Figure 1.1. An LJ floor using sawn lumber beams with screw-connected Oriented Strand Boards (OSBs) as sub-floor will represent the first class (see Fig. 1.1a.) For the second class, a CLT floor is chosen (see Fig. 1.1b). Finally, an Hollow Box Girder (HBG) floor completes the three considered floor systems (see Fig. 1.1c). The floors are tested in different states of construction. Besides the raw state, floating floors with cement and dry screeds, a suspended ceiling, or a combination of both is applied. To form reproducible support conditions in every configuration, stripes of elastomer material are arranged between the bearings and the main structural elements of each floor. Additionally, the main structural element's vertical displacement is restricted at the bearings to prevent lifting [Kohrmann et al 2014].

1.3.4 Measurements

1.3.4.1 Modal testing

The dynamic behavior of the test objects is derived from either an Operational Modal Analysis (OMA) or an EMA. Therefore, frequency response functions of all considered floor types and construction states are measured by shaker and modal hammer testing. The dynamic response of each layer of the construction is measured using a measurement grid of 12×12 accelerometers. This allows a comparison of the modal behavior of the main floor, the screed and the paneling of the suspended ceiling individually, as well as a change of their characteristics, when additional structures were applied.
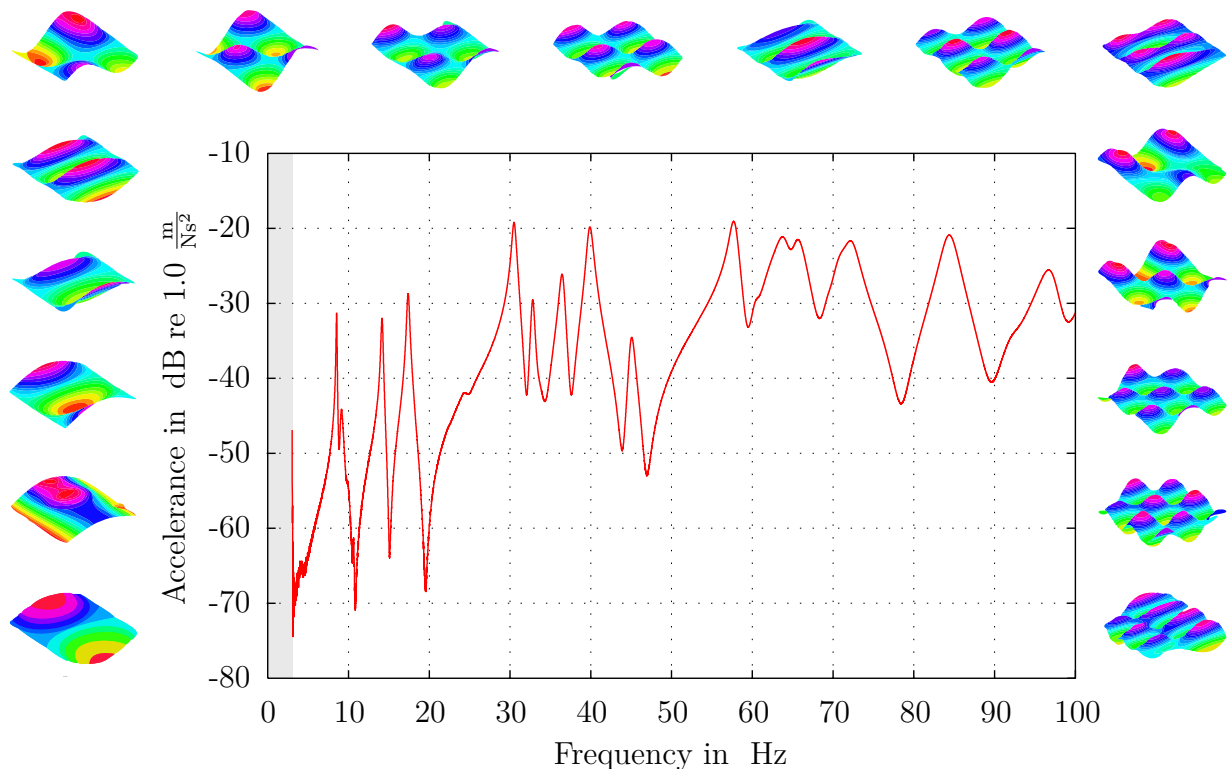
Figure 1.2: Example for measured frequency response functions and eigenmodes (The excitation signal is a logarithmic sine sweep with a duration of $256\,\mathrm{s}$ and a starting frequency of $3\,\mathrm{Hz}$)

As an example, a driving point acceleration of a raw five-layered CLT floor measuring $5.50\,\mathrm{m} \times 5.50\,\mathrm{m}$ composed of four coupled CLT slabs in the frequency range $0 - 100\,\mathrm{Hz}$ is shown in Figure 1.2. Since the resonance peaks are clearly separated in this frequency range, the modal shapes can be approximated out of an OMA at the peaks. The damping ratios are derived using the Full Width at Half Maximum (FWHM) criterion. The corresponding modal shapes are included into the figure for better visualization. The derived

modal parameters are compared to the results of an EMAs using the commercial software ME'SCOPEVES® from Vibrant Technology Inc. [Borch 2013]. Based on those modal parameters, the material properties of the developed FE models (see Section 3.2) are calibrated using Model Updating [Mottershead and Friswell 1993] [Friswell and Mottershead 1995].

1.3.4.2 Sound intensity testing

The sound radiation behavior of different floor constructions considered is determined by intensity measurements. Therefore, the test objects are excited by an electro-dynamic shaker, equivalent to the modal testing mentioned above. The location of the shaker is generally on top of the floor constructions, and measurements with direct excitations of the paneling of the suspended ceiling are also carried out [Winter 2012].

Figure 1.3: Simultaneous intensity and vibration measurement

The receiving room below the test objects, including the measurement set up, is shown in Figure 1.3. Discrete measurements using a pp-intensity probe are performed with variable measurement grid sizes from 0.5 m down to 0.125 m. To handle the large amount of measurement locations, the intensity probe is mounted to a manually moveable measurement apparatus. Parallel measurements of the dynamic response of the bottom structure of the floors are carried out. Therefore, an accelerometer is mounted to the ceiling or the main floor at the intersection of the intensity probe's axis with the surface of the test object. Figure 1.3 further shows the absorbing polyester fiber blocks at the walls to reduce lateral

reflections. The absorbers for the attenuation of vertical reflections are implemented into the shown boxes on the floor, with a depth of 0.80 m. The boxes are covered with steel grating to maintain accessibility. From the measured sound intensity, in combination with the structure-borne sound velocity derived from the measured acceleration, the radiated sound power as well as the radiation efficiency are determined. The results are used to calibrate the developed numerical models.

1.4 Outline

The goal of this thesis is to perform numerical studies complementing the measurement-based investigations of the research project "Vibwood". Parametric numerical models of the floor constructions considered are developed and optimized for use within parametric studies. Different excitation techniques are implemented for Harmonic Frequency and Transient Analyses. For the evaluation of the results, acoustical tools predicting the radiated sound power are designed based on ITMs. The models are calibrated by measured data with respect to modal parameters. A validation of the evaluation models is performed by laboratory testing. The results of parametric studies are evaluated with regard to the specific influence of each parameter of the system. A GUI is developed to support the engineer in the planing process.

Chapter Two presents the fundamental theory of selected topics that are focused on in this thesis. The knowledge of the orthotropic material behavior of wood is essential for the development of FE models. Special focus is given to coordinate transformation, since especially for CLT constructions, the orientation of the cutting pattern of the implemented boards influences the overall stiffness of the CLT slabs. In this context, the rolling shear modulus of wood is discussed. The procedure of a Dimensional Analysis is explained. The complex database achieved from a parametric study can be condensed to a number of nomograms using dimensionless parameters derived by the Dimensional Analysis.

A brief introduction into the *Fourier* Transform is given. The impact of the aliasing effect on finite sinusoidal signals is investigated. The theoretical basics of sound radiation of plates is examined. Near- and far-field conditions and the effect of finite plates in the wave number domain are derived. Modal parameters are essential for the calibration of numerical models with measurement data. The Modal Analysis to be performed, is described for undamped systems.

Chapter Three gives a detailed overview of the numerical models developed. The design of the entirely parametric FE-models is explained, covering the idealizations, that have been made, and the discretization process. The modular structure of the FE-models is described, which is necessary for a fully automated procedure during the intended parametric studies. In this context, the programmed interfaces between the individual used commercial software are introduced. Various excitation techniques covering single and Rain-on-the-Roof (ROTR) excitation are implemented for the use within Harmonic Frequency Analyses, as well as numerical step-by-step pedestrian loading for transient investigations. An acoustical evaluation model is developed for the prediction of the radiated sound power out of structure-borne sound velocities. This is necessary since the adjacent room below the floors is neglected in the numerical simulations, thus no sound pressure data is available.

The numerical models are respectively calibrated and validated in **Chapter Four**. A Model-Updating procedure is performed for the calibration of the material parameters of the numerical CLT models, based on a comparison of the modal parameters derived from OMAs and EMAs. For less complex structures, the stiffness parameters are achieved from measured first eigenfrequencies. A method is introduced to determine the idealized material parameters of complex composite plate structures by matching the curves of measured and simulated bending wave numbers over frequency. The developed acoustical prediction tool for plate-like structures is validated by laboratory measurements on an aluminum plate mounted into the aperture of a window-testing facility. Different approaches for the modeling of the air inside the cavity between floor and the suspended ceiling are investigated. A detailed investigation on the frequency range, to which the evaluation model can be applied is presented. A criterion is derived for the calculation of the maximal possible frequency range based on the bending stiffness of the plate and the sample interval.

In **Chapter Five**, the performed parametric studies are introduced, and the results are evaluated. Various parametric studies are carried out. A study investigates the influence of geometrical parameters on the resulting eigenfrequencies and the radiated sound power of CLT floors is evaluated with nomograms based on dimensionless parameters. An approach, that applies TMDs to only attenuate the amplification linked with those eigenmodes of a floor construction, that have a major impact on the sound radiation, is presented. Other parametric studies are performed, either giving an insight into the influence of specific parameters of suspended ceilings on the radiation behavior of the floor constructions or for establishing a database, that can be accessed by a graphical user interface. Coefficients are derived to evaluate the data regarding the expected impact sound insulation.

2 Fundamental Theory

2.1 Elastic Properties of Wood

The elastic properties of wood strongly depend on its anatomy which is governed by the direction of fibers and its annular rings. Three principal directions (L=longitudinal, T=tangential and R=radial) can be identified as sketched in Figure 2.1. For a detailed description of its macro and micro structure, see e.g. Grimsel [1999]. He also gives an explanation how the elastic properties can be identified by testing.
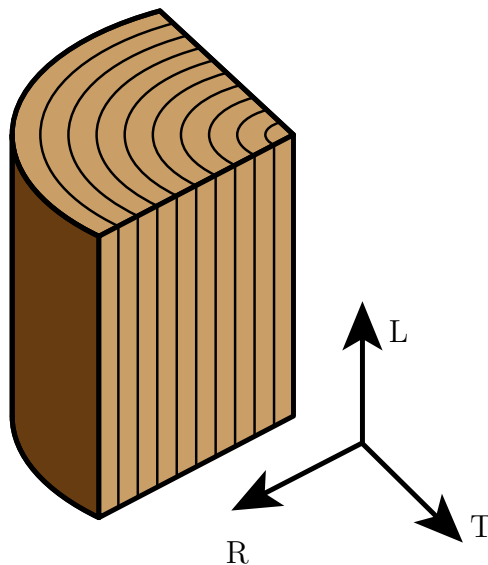
Figure 2.1: Anatomy of wood and coordinate system

On the macro level, the material's properties can be considered as smeared over the volume by assuming, that the impact of the inhomogeneous cellular structure is restricted to the micro level. In this case, wood can be described as an linear elastic, directional homogeneous and anisotropic solid with orthogonal isotropic (=orthotropic) properties [Ranz 2007]. It has symmetrical properties regarding the three principal directions (L,T,R) Lieblang [2000].

The following sections will give a short excursion on orthotropic material law and coordinate transformation. The influence of different sawing patterns will be discussed with a special focus on the rolling shear modulus.

2.1.1 Linear elastic anisotropic media

The deformation behavior of linear elastic anisotropic media due to applied loads can be expressed by *Hooke*'s law which, in general, is represented by the constitutive equation:

$$\mathbf{\Sigma} = \mathbf{C}\,\mathbf{E} \quad \text{resp.} \quad \mathbf{E} = \mathbf{S}\,\mathbf{\Sigma} \tag{2.1}$$

with

$$
\begin{aligned}
\mathbf{\Sigma} &\in \mathbb{R}^{3,3} &&:\ 2^{\text{nd}}\ \text{order } \textit{Cauchy}\ \text{stress tensor}\\
\mathbf{E} &\in \mathbb{R}^{3,3} &&:\ 2^{\text{nd}}\ \text{order } \textit{Green-Lagrangian}\ \text{strain tensor}\\
\mathbf{C} &\in \mathbb{R}^{3,3,3,3} &&:\ 4^{\text{th}}\ \text{order Stiffness tensor}\\
\mathbf{S} &\in \mathbb{R}^{3,3,3,3} &&:\ 4^{\text{th}}\ \text{order Compliance tensor,}
\end{aligned}
$$

which can also be written as

$$\sigma_{ij} = C_{ij}^{kl}\,\varepsilon_{kl} \quad \text{resp.} \quad \varepsilon_{kl} = S_{kl}^{ij}\,\sigma_{ij} \tag{2.2}$$

using *Einstein* notation with indexes $i,j,k,l = 1, 2, 3$ representing any *Cartesian* coordinates. Depending on the input and output variables, stiffness or compliance tensor has to be taken into account. The following section will focus on the stiffness tensor.

According to the principle of conservation of momentum, shear stress components σ_{ij} and σ_{ji} must be equal, which leads to a symmetric stress tensor. The strain tensors is symmetric due to the symmetry of the metric tensor. Thus, both are specified by six components and can be simplified to 1st order tensors $\tilde{\mathbf{\Sigma}}, \tilde{\mathbf{E}} \in \mathbb{R}^6$ using *Voigt* notation [Lieblang 2000].

$$\boldsymbol{\Sigma} = \begin{bmatrix} \sigma_{11} & \sigma_{12} & \sigma_{13} \\ & \sigma_{22} & \sigma_{23} \\ \text{sym} & & \sigma_{33} \end{bmatrix} \longrightarrow \tilde{\boldsymbol{\Sigma}} = \begin{bmatrix} \sigma_1 \\ \sigma_2 \\ \sigma_3 \\ \sigma_4 \\ \sigma_5 \\ \sigma_6 \end{bmatrix} = \begin{bmatrix} \sigma_{11} \\ \sigma_{22} \\ \sigma_{33} \\ \sigma_{23} \\ \sigma_{13} \\ \sigma_{12} \end{bmatrix} \tag{2.3}$$

The strain tensor in Equation (2.5) is chosen to represent the engineering shear strain which is twice the tensorial shear strain (e.g., $\gamma_{23} = 2\varepsilon_{23}$). Compared to the stress tensor, this factor 2 for engineering shear strain can be interpreted as a product of tensorial shear strain with the *Reuter* matrix [Reuter 1971]

$$\mathbf{R} = \begin{bmatrix} 1 & 0 & 0 & 0 & 0 & 0 \\ 0 & 1 & 0 & 0 & 0 & 0 \\ 0 & 0 & 1 & 0 & 0 & 0 \\ 0 & 0 & 0 & 2 & 0 & 0 \\ 0 & 0 & 0 & 0 & 2 & 0 \\ 0 & 0 & 0 & 0 & 0 & 2 \end{bmatrix} \tag{2.4}$$

$$\mathbf{E} = \begin{bmatrix} \varepsilon_{11} & \varepsilon_{12} & \varepsilon_{13} \\ & \varepsilon_{22} & \varepsilon_{23} \\ \text{sym} & & \varepsilon_{33} \end{bmatrix} \longrightarrow \tilde{\mathbf{E}} = \begin{bmatrix} \varepsilon_1 \\ \varepsilon_2 \\ \varepsilon_3 \\ \varepsilon_4 \\ \varepsilon_5 \\ \varepsilon_6 \end{bmatrix} = \mathbf{R} \begin{bmatrix} \varepsilon_{11} \\ \varepsilon_{22} \\ \varepsilon_{33} \\ \varepsilon_{23} \\ \varepsilon_{13} \\ \varepsilon_{12} \end{bmatrix} = \begin{bmatrix} \varepsilon_{11} \\ \varepsilon_{22} \\ \varepsilon_{33} \\ 2\varepsilon_{23} \\ 2\varepsilon_{13} \\ 2\varepsilon_{12} \end{bmatrix}. \tag{2.5}$$

In this way, the stored energy stays the same for both tensorical and *Voigt* notation [Chaves 2013]

$$\frac{1}{2}\sigma_{ij}\varepsilon_{ji} = \frac{1}{2}\tilde{\boldsymbol{\Sigma}}^{\mathbf{T}}\tilde{\mathbf{E}}. \tag{2.6}$$

Symmetric stress and strain tensors have an influence on the stiffness tensor's components

as well, leading to minor symmetry [Chaves 2013]:

$$C_{ij}^{kl} = C_{ji}^{kl} = C_{ij}^{lk} = C_{ji}^{lk}, \tag{2.7}$$

reducing the components of the stiffness tensor from 81 to 36 allowing the constitutive Equation (2.2) to be expressed in *Voigt* notation as follows:

$$
\begin{bmatrix} \sigma_{11} \\ \sigma_{22} \\ \sigma_{33} \\ \sigma_{23} \\ \sigma_{13} \\ \sigma_{12} \end{bmatrix} =
\begin{bmatrix}
C_{11}^{11} & C_{11}^{22} & C_{11}^{33} & C_{11}^{23} & C_{11}^{13} & C_{11}^{12} \\
C_{22}^{11} & C_{22}^{22} & C_{22}^{33} & C_{22}^{23} & C_{22}^{13} & C_{22}^{12} \\
C_{33}^{11} & C_{33}^{22} & C_{33}^{33} & C_{33}^{23} & C_{33}^{13} & C_{33}^{12} \\
C_{23}^{11} & C_{23}^{22} & C_{23}^{33} & C_{23}^{23} & C_{23}^{13} & C_{23}^{12} \\
C_{13}^{11} & C_{13}^{22} & C_{13}^{33} & C_{13}^{23} & C_{13}^{13} & C_{13}^{12} \\
C_{12}^{11} & C_{12}^{22} & C_{12}^{33} & C_{12}^{23} & C_{12}^{13} & C_{12}^{12}
\end{bmatrix}
\begin{bmatrix} \varepsilon_{11} \\ \varepsilon_{22} \\ \varepsilon_{33} \\ 2\varepsilon_{23} \\ 2\varepsilon_{13} \\ 2\varepsilon_{12} \end{bmatrix}
\tag{2.8}
$$

In case of existence of a two-fold derivable elastic potential for each volume element Π_{iV} (which can be assumed for wood in general Lieblang [2000], especially for acoustical problems, in which small deformations occur) stresses σ_{ij} can be derived as follows:

$$\sigma_{ij} = \frac{\partial \Pi_{iV}}{\partial \varepsilon_{ij}} \tag{2.9}$$

[Müller 2010a]. Applying *Schwarz'* theorem for the symmetry of second derivatives

$$\frac{\partial^2 \Pi_{iV}}{\partial \varepsilon_{ij} \partial \varepsilon_{kl}} = \frac{\partial^2 \Pi_{iV}}{\partial \varepsilon_{kl} \partial \varepsilon_{ij}}, \tag{2.10}$$

leads to:

$$\frac{\partial \sigma_{ij}}{\partial \varepsilon_{kl}} = C_{ij}^{kl} = \frac{\partial \sigma_{kl}}{\partial \varepsilon_{ij}} = C_{kl}^{ij}. \tag{2.11}$$

This results in major symmetry [Chaves 2013], and thus the independent components of the linear elasticity tensor for anisotropic materials are further reduced from 36 to 21. Again using *Voigt* notation the 4th order tensor, $\mathbf{C} \in \mathbb{R}^{3,3,3,3}$ can be reduced to a 2nd order tensor

$\tilde{\mathbf{C}} \in \mathbb{R}^{6,6}$ also called the stiffness matrix [Grimsel 1999].

$$\tilde{\mathbf{C}} = \begin{bmatrix} C_{11} & C_{12} & C_{13} & C_{14} & C_{15} & C_{16} \\ & C_{22} & C_{23} & C_{24} & C_{25} & C_{26} \\ & & C_{33} & C_{34} & C_{35} & C_{36} \\ & & & C_{44} & C_{45} & C_{46} \\ & \text{sym} & & & C_{55} & C_{56} \\ & & & & & C_{66} \end{bmatrix} \tag{2.12}$$

2.1.2 Property transformation

Anisotropic material properties change when the principal coordinate system is changed. After an arbitrary rotational transformation of principal axes $i',j',k',l' = x,y,z$ from the reference axes $i,j,k,l = 1,2,3$ the resulting stress and strain tensors can be expressed in *Einstein* notation as follows:

$$\sigma_{i'j'} = g_{i'}^i g_{j'}^j \sigma_{ij} \tag{2.13}$$

$$\varepsilon_{k'l'} = g_{k'}^k g_{l'}^l \varepsilon_{kl}. \tag{2.14}$$

Herein the stress and strain tensors are multiplied by metric tensors $g_{i'}^i$, $g_{j'}^j$, $g_{k'}^k$ and $g_{l'}^l \in \mathbb{R}^{3,3}$. Using (2.13) and (2.14), Equation (2.2) can be written in terms of the stress and strain tensor referred to the reference axes as

$$\sigma_{ij} = g_i^{i'} g_j^{j'} g_{k'}^k g_{l'}^l C_{ij}^{kl} \varepsilon_{kl} \tag{2.15}$$

leading to a new set of components of the stiffness tensor

$$C_{i'j'}^{k'l'} = g_i^{i'} g_j^{j'} g_{k'}^k g_{l'}^l C_{ij}^{kl}. \tag{2.16}$$

The metric tensors for a rotational transformation along the reference axes are [Allert 2014]:

$$\mathbf{g_1} = \begin{bmatrix} 1 & 0 & 0 \\ 0 & \cos(\alpha) & \sin(\alpha) \\ 0 & -\sin(\alpha) & \cos(\alpha) \end{bmatrix} \quad \mathbf{g_2} = \begin{bmatrix} \cos(\beta) & 0 & \sin(\beta) \\ 0 & 1 & 0 \\ -\sin(\beta) & & \cos(\beta) \end{bmatrix} \quad \mathbf{g_3} = \begin{bmatrix} \cos(\gamma) & \sin(\gamma) & 0 \\ -\sin(\gamma) & \cos(\gamma) & 0 \\ 0 & 0 & 1 \end{bmatrix}$$

$$\tag{2.17}$$

The angles of rotation are α, β and γ. As an example, a rotation along the first reference axis will be shown in matrix notation. Starting with the transformation of the stress tensor,

$$\tilde{\boldsymbol{\Sigma}}' = \mathbf{g_1}\ \tilde{\boldsymbol{\Sigma}}\ \mathbf{g_1^T}, \tag{2.18}$$

the transformed stress tensor must hold

$$\tilde{\boldsymbol{\Sigma}}' = \mathbf{T_1}\tilde{\boldsymbol{\Sigma}}. \tag{2.19}$$

Here, $\mathbf{T_1} \in \mathbb{R}^{6,6}$ represents the coordinate transformation matrix in *Voigt* notation. For a rotation along the first reference axis using the abbreviations $c = \cos\alpha$ and $s = \sin\alpha$, Equation (2.18) yields:

$$\begin{bmatrix} \sigma'_{11} & \sigma'_{12} & \sigma'_{13} \\ & \sigma'_{22} & \sigma'_{23} \\ \text{sym} & & \sigma'_{33} \end{bmatrix} = \begin{bmatrix} 1 & 0 & 0 \\ 0 & c & s \\ 0 & -s & c \end{bmatrix} \begin{bmatrix} \sigma_{11} & \sigma_{12} & \sigma_{13} \\ & \sigma_{22} & \sigma_{23} \\ \text{sym} & & \sigma_{33} \end{bmatrix} \begin{bmatrix} 1 & 0 & 0 \\ 0 & c & -s \\ 0 & s & c \end{bmatrix} \tag{2.20}$$

which solved in vector form

$$\begin{bmatrix} \sigma'_{11} \\ \sigma'_{22} \\ \sigma'_{33} \\ \sigma'_{23} \\ \sigma'_{13} \\ \sigma'_{12} \end{bmatrix} = \begin{bmatrix} \sigma_{11} \\ c^2\ \sigma_{22} + s^2\ \sigma_{33} + 2cs\ \sigma_{23} \\ s^2\ \sigma_{22} + c^2\ \sigma_{33} - 2cs\ \sigma_{23} \\ -cs\ \sigma_{22} + cs\ \sigma_{33} + (c^2 - s^2)\ \sigma_{23} \\ c\ \sigma_{12} - s\ \sigma_{13} \\ s\ \sigma_{12} + c\ \sigma_{13} \end{bmatrix} \tag{2.21}$$

leads to the coordinate transformation matrix [Mascia and Lahr 2006]

$$\mathbf{T_1} = \begin{bmatrix} 1 & 0 & 0 & 0 & 0 & 0 \\ 0 & c^2 & s^2 & 2cs & 0 & 0 \\ 0 & s^2 & c^2 & -2cs & 0 & 0 \\ 0 & -cs & cs & c^2 - s^2 & 0 & 0 \\ 0 & 0 & 0 & 0 & c & -s \\ 0 & 0 & 0 & 0 & s & c \end{bmatrix}. \tag{2.22}$$

For a general transformation,

$$\tilde{\boldsymbol{\Sigma}}' = \mathbf{g} \; \tilde{\boldsymbol{\Sigma}} \; \mathbf{g^T} \tag{2.23}$$

the transformation matrix yields the following:

$$\mathbf{T} = \begin{bmatrix} g_{11}^2 & g_{12}^2 & g_{13}^2 & 2g_{21}g_{31} & 2g_{11}g_{31} & 2g_{11}g_{21} \\ g_{21}^2 & g_{22}^2 & g_{23}^2 & 2g_{22}g_{32} & 2g_{12}g_{32} & 2g_{12}g_{22} \\ g_{31}^2 & g_{32}^2 & g_{33}^2 & 2g_{23}g_{33} & 2g_{13}g_{33} & 2g_{13}g_{23} \\ g_{13}g_{12} & g_{23}g_{22} & g_{33}g_{32} & g_{33}g_{22}+g_{32}g_{23} & g_{33}g_{12}+g_{13}g_{32} & g_{33}g_{32}+g_{33}g_{32} \\ g_{11}g_{13} & g_{21}g_{23} & g_{31}g_{33} & g_{33}g_{21}+g_{31}g_{23} & g_{11}g_{33}+g_{13}g_{31} & g_{33}g_{31}+g_{33}g_{31} \\ g_{12}g_{11} & g_{22}g_{21} & g_{32}g_{31} & g_{31}g_{22}+g_{32}g_{23} & g_{31}g_{12}+g_{11}g_{32} & g_{11}g_{22}+g_{21}g_{12} \end{bmatrix} . \tag{2.24}$$

The transformation of the engineering shear strain tensor (2.5) is performed in a slightly different manner:

$$\tilde{\mathbf{E}}' = \mathbf{RTR^{-1}}\tilde{\mathbf{E}} = \mathbf{T^{-T}}\tilde{\mathbf{E}} \tag{2.25}$$

with

$$\mathbf{RTR^{-1}} = \mathbf{T^{-T}}. \tag{2.26}$$

The property transformation can be derived in matrix notation from (2.1), (2.19) and (2.25)

$$\tilde{\boldsymbol{\Sigma}} = \mathbf{T^{-1}} \; \tilde{\boldsymbol{\Sigma}}' = \mathbf{T^{-1}} \; \tilde{\mathbf{C}} \; \tilde{\mathbf{E}}' = \mathbf{T^{-1}} \; \tilde{\mathbf{C}} \; \mathbf{T^{-T}} \; \tilde{\mathbf{E}} = \tilde{\mathbf{C}}' \; \tilde{\mathbf{E}} \tag{2.27}$$

where the transformed stiffness matrix is defined as

$$\tilde{\mathbf{C}}' = \mathbf{T^{-1}} \; \tilde{\mathbf{C}} \; \mathbf{T^{-T}}. \tag{2.28}$$

The transformation of the compliance matrix can be derived analogously, leading to

$$\tilde{\mathbf{S}}' = \mathbf{T^T} \; \tilde{\mathbf{S}} \; \mathbf{T}. \tag{2.29}$$

2.1.3 Orthotropy

In case of existence of three orthogonal planes along which the stiffness tensor has invariant components, the material is considered orthogonal isotropic or orthotropic. Thus, a mirror transformation along the normal axis to these planes must not change the tensor components. Rotating the first reference axis using $\mathbf{g_1}$ out of (2.17) by $\alpha = 180°$, the transformation matrix (2.24) becomes:

$$\mathbf{T_{1,180}} = \begin{bmatrix} 1 & 0 & 0 & 0 & 0 & 0 \\ 0 & 1 & 0 & 0 & 0 & 0 \\ 0 & 0 & 1 & 0 & 0 & 0 \\ 0 & 0 & 0 & 1 & 0 & 0 \\ 0 & 0 & 0 & 0 & -1 & 0 \\ 0 & 0 & 0 & 0 & 0 & -1 \end{bmatrix} \tag{2.30}$$

leading to a transformed stiffness matrix,

$$\mathbf{\tilde{C}'} = \mathbf{T_{1,180}^{-1}} \, \mathbf{\tilde{C}} \, \mathbf{T_{1,180}^{-T}} = \begin{bmatrix} C_{11} & C_{12} & C_{13} & C_{14} & -C_{15} & -C_{16} \\ & C_{22} & C_{23} & C_{24} & -C_{25} & -C_{26} \\ & & C_{33} & C_{34} & -C_{35} & -C_{36} \\ & & & C_{44} & -C_{45} & -C_{46} \\ & \text{sym} & & & C_{55} & C_{56} \\ & & & & & C_{66} \end{bmatrix}. \tag{2.31}$$

To fulfill the prerequisite that the components of the stiffness matrix must not change, it becomes clear by comparing Equation (2.31) with Equation (2.12), that the following components must be equal to zero:

$$C_{15} = C_{16} = C_{25} = C_{26} = C_{35} = C_{36} = C_{45} = C_{46} = 0. \tag{2.32}$$

This means that for materials with one symmetry plane, the independent non-zero components of the stiffness matrix are reduced to 13 (monoclinic symmetry) [Chaves 2013]

$$
\tilde{\mathbf{C}}_{monoclinic} = \begin{bmatrix} C_{11} & C_{12} & C_{13} & C_{14} & 0 & 0 \\ & C_{22} & C_{23} & C_{24} & 0 & 0 \\ & & C_{33} & C_{34} & 0 & 0 \\ & & & C_{44} & 0 & 0 \\ & \text{sym} & & & C_{55} & C_{56} \\ & & & & & C_{66} \end{bmatrix}.
\tag{2.33}
$$

Starting from monoclinic symmetry and assuming a second plane of symmetry (which implies there must also be a third one) and deriving in an analog way leads to the general form of *Hooke*'s law for orthotropic material with six independent non-zero components of the stiffness matrix as follows:

$$
\tilde{\mathbf{C}}_{orthotropic} = \begin{bmatrix} C_{11} & C_{12} & C_{13} & 0 & 0 & 0 \\ & C_{22} & C_{23} & 0 & 0 & 0 \\ & & C_{33} & 0 & 0 & 0 \\ & & & C_{44} & 0 & 0 \\ & \text{sym} & & & C_{55} & 0 \\ & & & & & C_{66} \end{bmatrix}.
\tag{2.34}
$$

It can be interpreted as a condition in which shear and normal strains do not interact. Further, shear strains are not coupled while normal strains are.

In order to express the constitutive Equation (2.2) with the engineering constants *Young*'s modulus E, *Poisson* ratio ν and shear modulus G, it is advantageous to use the compliance tensor which can be achieved by inverting the stiffness tensor.

$$
\begin{bmatrix} \varepsilon_x \\ \varepsilon_y \\ \varepsilon_z \\ \gamma_{yz} \\ \gamma_{xz} \\ \gamma_{xy} \end{bmatrix} = \begin{bmatrix} S_{11} & S_{12} & S_{13} & 0 & 0 & 0 \\ & S_{22} & S_{23} & 0 & 0 & 0 \\ & & S_{33} & 0 & 0 & 0 \\ & & & S_{44} & 0 & 0 \\ & \text{sym} & & & S_{55} & 0 \\ & & & & & S_{66} \end{bmatrix} \begin{bmatrix} \sigma_x \\ \sigma_y \\ \sigma_z \\ \tau_{yz} \\ \tau_{xz} \\ \tau_{xy} \end{bmatrix}
\tag{2.35}
$$

The relation between shear stresses τ_{ij} and shear strains γ_{ij} is given by the shear moduli

G_{ij}, leading to trivial terms for the components S_{44} - S_{66}. Since normal stresses and normal strains are coupled, the derivation of the components describing this relation is slightly more complicated. The components of the first row are as follows:

$$S_{11} = \frac{1}{E_x}, \quad S_{21} = -\frac{\nu_{xy}}{E_x}, \quad S_{31} = -\frac{\nu_{xz}}{E_x}. \tag{2.36}$$

The *Poisson* ratios are $\nu_{ij} = -\frac{\varepsilon_j}{\varepsilon_i}$.

Replacing the remaining components analogously, Equation (2.35) yields:

$$\begin{bmatrix} \varepsilon_x \\ \varepsilon_y \\ \varepsilon_z \\ \gamma_{yz} \\ \gamma_{xz} \\ \gamma_{xy} \end{bmatrix} = \begin{bmatrix} \frac{1}{E_x} & -\frac{\nu_{yx}}{E_y} & -\frac{\nu_{zx}}{E_z} & 0 & 0 & 0 \\ -\frac{\nu_{xy}}{E_x} & \frac{1}{E_y} & -\frac{\nu_{zy}}{E_z} & 0 & 0 & 0 \\ -\frac{\nu_{xz}}{E_x} & -\frac{\nu_{yz}}{E_y} & \frac{1}{E_z} & 0 & 0 & 0 \\ 0 & 0 & 0 & \frac{1}{G_{yz}} & 0 & 0 \\ 0 & 0 & 0 & 0 & \frac{1}{G_{xz}} & 0 \\ 0 & 0 & 0 & 0 & 0 & \frac{1}{G_{xy}} \end{bmatrix} \begin{bmatrix} \sigma_x \\ \sigma_y \\ \sigma_z \\ \tau_{yz} \\ \tau_{xz} \\ \tau_{xy} \end{bmatrix} \tag{2.37}$$

The stiffness tensor $\mathbf{C}$ can be derived by inverting $\mathbf{S}$.

From the symmetry of the compliance tensor the following relations can be derived:

$$\frac{\nu_{xy}}{E_x} = \frac{\nu_{yx}}{E_y}, \qquad \frac{\nu_{xz}}{E_x} = \frac{\nu_{zx}}{E_z}, \qquad \frac{\nu_{yz}}{E_y} = \frac{\nu_{zy}}{E_z}. \tag{2.38}$$

This shows that the *Poisson* ratios ν_{ij} and ν_{ji} are coupled by E_i and E_j, which leads to a minor and a major set of Poisson's ratios. To prevent errors during numerical simulations, attention has to be paid to the set of *Poisson* ratios that is in use. Thus, nine independent engineering material constants are necessary to describe an orthotropic material.

2.1.4 Sawing patterns

A major problem linked to numerical modeling of wood is caused by its anatomy. For wooden engineering products like CLT, the modeling of each component (individual boards) is not practical, since in most cases, the exact configuration is unknown. Simplified approaches are necessary. One possibility is to idealize the wooden components as plane material using *Cartesian* coordinates. This does not take into account, the circular characteristics of a log

and the dependency of the components material properties on the sawing patterns, used within a real construction.

For wooden engineering construction, logs are converted into timber by different types of sawing. Depending on its position inside the log, the pattern of annular rings changes. While timber joists are usually sawn from the higher quality log's center, the properties of timber boards, as used for CLT, depend mainly on the applied sawing pattern. Two examples for common sawing patterns are shown in Figure 2.2. Plain sawn boards have annular rings almost parallel to the face of the board, whereas rift sawn boards have almost perpendicular annular rings [Aicher and Dill-Langer 2000]. Also, patterns with different directionality or where the pith remains inside the piece are possible.
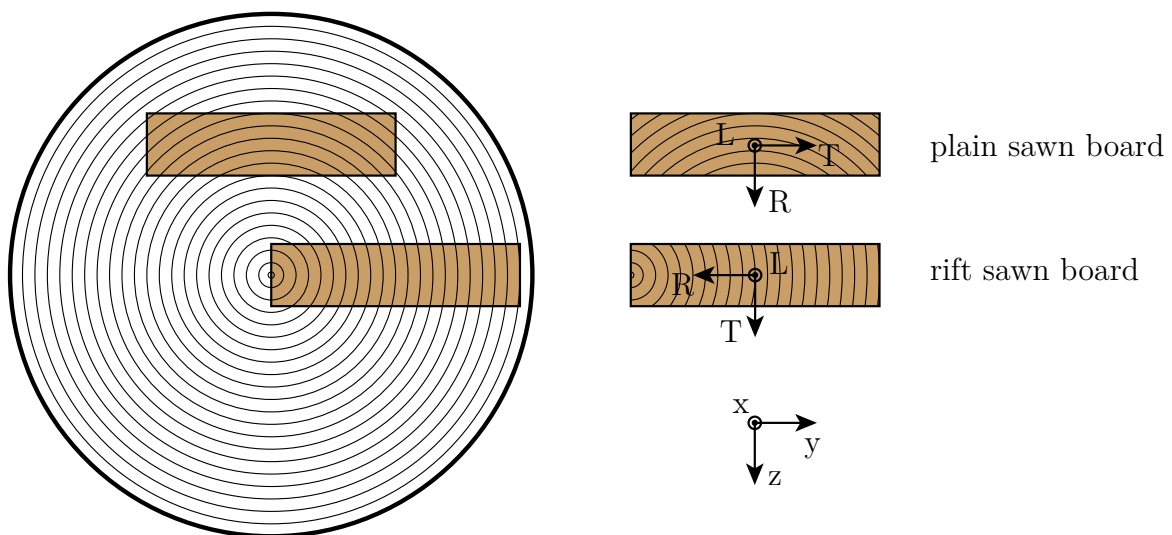
Figure 2.2: Sawing patterns

For the shown types of timber, the principal directions (L,T,R) of the material can be assigned to the principal directions of the structural element (x,y,z) [Gülzow 2008].

In timber engineering, different sawing patterns are used within a construction. Since it is usually not possible to predict the sawing pattern of every single board, a differentiation between anatomical tangential and radial direction is not practical. Therefore, it is common to combine both directions under the term 'perpendicular' to the fiber direction ($\perp$). The anatomical, longitudinal direction is described as 'parallel' to the fiber direction ($\parallel$) [Gülzow 2008]. Thus, the necessary independent material parameters of wood reduce from nine to

six. The error induced by this simplification is discussed in Section 2.1.5.

$$E_x = E_\parallel, \qquad E_y = E_z = E_\perp, \qquad \nu_{xy} = \nu_{xz} = \nu_{\parallel\perp}, \qquad \nu_{yz} = \nu_{\perp\perp}$$
$$G_{xy} = G_{xz} = G_{\parallel\perp}, \qquad G_{yz} = G_{\perp\perp} \tag{2.39}$$

$G_{\perp\perp}$ represents the rolling shear modulus. It is necessary to mention that even if it seems obvious from these assumptions, timber has no transverse isotropic behavior, since

$$G_{\perp\perp} \neq \frac{E_{\perp\perp}}{2(1 - \nu_{\perp\perp})}. \tag{2.40}$$

2.1.5 Rolling shear and perpendicular *Young*'s modulus

Rolling shear plays a minor role in timber joist constructions; its contribution to the effective stiffness of the construction can be neglected in general [Aicher and Dill-Langer 2000]. As against this, in case of CLT constructions, especially, layers perpendicular to the main span direction of the floor are subjected to rolling shear. Consequently, the magnitude of the rolling shear modulus has an impact on the effective bending stiffness of the floor [Aicher and Dill-Langer 2000].

According to Aicher and Dill-Langer [2000], rolling shear modulus is not an intrinsic material parameter. They describe the same on a macro scale, as dependent on meso-scale on-axis properties and on geometry and size of the timber. For different sawing patterns with varying locations of the pith leading to different curvatures of annular rings, FE simulations are performed to calculate the apparent rolling shear modulus. It is shown that for an angle of 45°, the apparent rolling shear modulus is up to four times higher compared to its nominal value. Blaß and Flaig [2012] test the rolling shear modulus of a large number of timber boards of varying cutting patterns. They formulate regression equations, showing a dependency on the width of the boards, the width of the annular rings, and the density. A dependency on the curvature of the annular rings, as proposed by Aicher and Dill-Langer [2000], is not verified by this study. This statement is questionable, since no proof is given in the research report.

FE simulations on a large scale are performed by Feichter [2013]. He compares the calculated effective rolling shear modulus to the nominal shear modulus given by a CLT fabricator. Two configurations with alternating board sizes are investigated. One, where the annual rings are assumed parallel with angles for $0° - 90°$ to the face of boards, as shown in Figure 2.3 and the other configuration is simulated, including the curvature of the annular rings, by using

material properties in cylindrical coordinates, where the distance of the origin (pith) to the middle of the board is varied. The study confirms the results from Aicher and Dill-Langer [2000]. The calculated effective rolling shear modulus shows a maximum at an angle of 45°, which is significantly higher than the nominal value. As another result, the bigger the aspect ratio of the board's dimensions, the higher the magnitude of the rolling shear modulus gets. The distance of the origin, obviously also, has an impact, since it changes the curvature of the annular rings. Feichter [2013] also shows, that relief grooves (see Fig. 2.5), which are common for boards used for CLT, are reducing the effective rolling shear modulus.
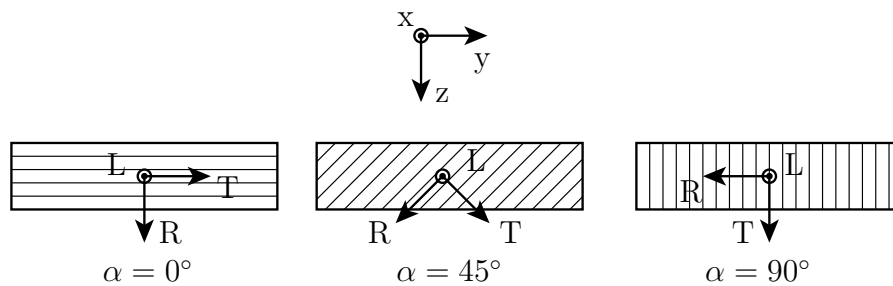
Figure 2.3: Idealized annular rings directions

Mascia and Lahr [2006] derive theoretical *Young*'s and shear moduli for a hard- and softwood Ipê and Pinus for an arbitrary oriented structural element, starting from initially determined parameters. *Euler*'s angles are used for the transformation. Three-dimensional diagrams show the transformation behavior of *Young*'s and shear elastic moduli. Perpendicular and rolling shear moduli's behavior can also be seen here for transformation of 90° along an axis perpendicular to the fiber direction. The following example will deal with this behavior in detail.
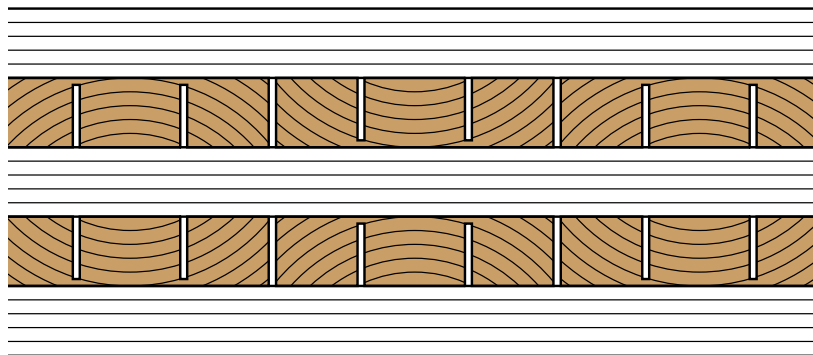
Figure 2.4: Cross-section of a five-layered CLT

A five-layered CLT construction is shown in Figure 2.4. A cross section with two perpendicular layers is depicted. Inside each layer plain sawn boards are arranged with relief grooves and small gapes in between.

For the development of a numerical model of a CLT floor, a full set of material parameters is needed. Since the rolling shear modulus is not an intrinsic material parameter [Aicher and Dill-Langer 2000], it has to be defined for each board individually, depending on its dimensions and sawing patterns.

standard board

board with relief grooves

idealized board
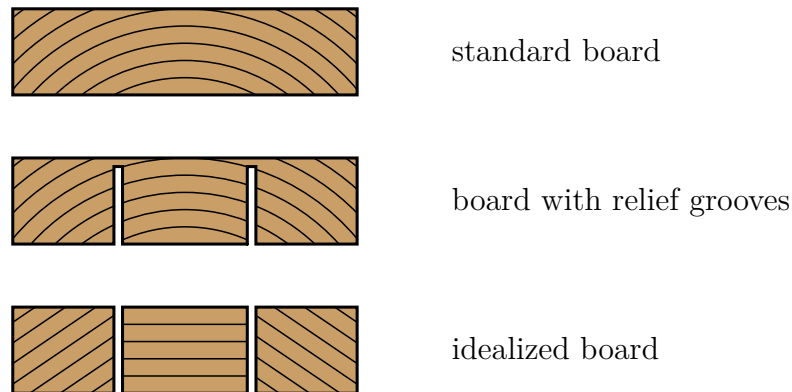
Figure 2.5: Idealization of plain boards with relief grooves

To cope with this, some simplifications will be introduced. In Figure 2.5, plain sawn boards are shown, with and without relief grooves. Since the grooves almost cut through the thickness of the board, and the remaining part usually ruptures at first loading, three separate boards can be assumed. These resulting smaller boards, on the one hand, have smaller aspect ratios, and on the other hand, the annular rings can be idealized, in most cases, to a good approximation, as parallel. The latter leading to one board with an angle of 0° and two boards with angles 30° − 45° to the face of the boards.

Neglecting the influence of the dimensions of the idealized boards, the apparent shear modulus can be calculated for each angle, using the coordinate transformation for lamina (2.29) along the longitudinal x-axis. A complete compliance matrix of spruce (see Eq. (2.41)) is presented by Grimsel [1999]. It is given for the principal directions of the material (L,T,R).

$$\tilde{\mathbf{S}}_{spruce} = \begin{bmatrix} 61.6 & -33 & -27 & 0 & 0 & 0 \\ & 2500 & -600 & 0 & 0 & 0 \\ & & 1430 & 0 & 0 & 0 \\ & & & 27000 & 0 & 0 \\ & \text{sym} & & & 1590 & 0 \\ & & & & & 1290 \end{bmatrix} 10^{-12} \quad \tfrac{\mathrm{m^2}}{\mathrm{N}} \tag{2.41}$$

The corresponding engineering material properties are summarized in Table 2.1.

Table 2.1: Material properties of spruce according to Grimsel [1999]

E_{L}	E_{T}	E_{R}	G_{TR}	G_{LR}	G_{LT}	
16200	400	699	37	628	775	$10^6 \quad \tfrac{\mathrm{N}}{\mathrm{m^2}}$
ν_{TR}	ν_{LR}	ν_{TL}	ν_{RT}	ν_{RL}	ν_{LT}	
0.419	0.0188	0.535	0.24	0.438	0.0132	$-$

They must be transformed into the principal directions of a structural element (e.g., board). The material property transformation for the compliance matrix is derived in Section 2.1.2 Equation (2.29). The transformation matrix given in Equation (2.22), is deployed for a rotational coordinate transformation along the fiber direction.

Solving the transformation for the resulting rolling shear modulus G_{yz} and applying the relations from Equation (2.37) yields the following:

$$\frac{1}{G_{\mathrm{yz}}} = S'_{44} = (4\ S_{22} + 4\ S_{33} - 8\ S_{23} - 4\ S_{44})\ s^2 c^2 + S_{44}\ (s^4 + c^4) \tag{2.42}$$

It becomes clear, that the rolling shear modulus is strongly connected to *Young*'s moduli in perpendicular direction. Obviously, a rotational transformation must have an effect on these parameters as well (and on the related *Poisson* ratios).

$$\frac{1}{E_{\mathrm{y}}} = S'_{22} = S_{22}\ c^4 + (2\ S_{23} + S_{44})\ s^2 c^2 + S_{33}\ s^4 \tag{2.43}$$

$$\frac{1}{E_{\mathrm{z}}} = S'_{33} = S_{22}\ s^4 + (2\ S_{23} + S_{44})\ s^2 c^2 + S_{33}\ c^4 \tag{2.44}$$

The graphs of the resulting rolling shear and the perpendicular *Young*'s moduli, calculated for a angle of rotation along the fiber axis from $0° - 90°$, are depicted in Figure 2.6.
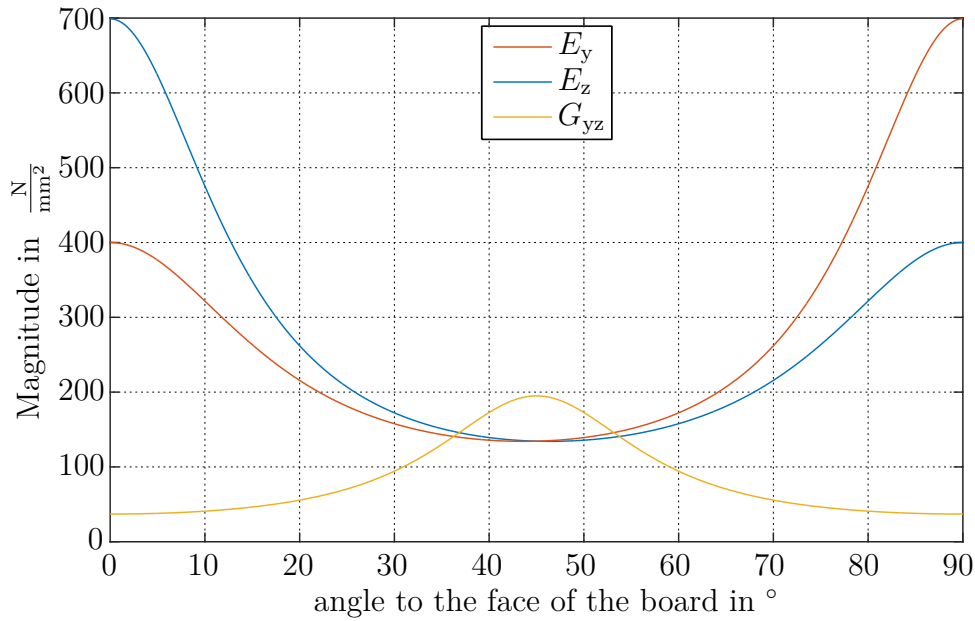
Figure 2.6: Coordinate transformation of material properties; y,z see Fig. 2.3

In this simplified example, as described by Aicher and Dill-Langer [2000] and Feichter [2013], it can be observed that the rolling shear modulus has a maximum at 45°, which is more than five times the nominal value. Furthermore, at this angle of rotation, both the perpendicular *Young*'s moduli become minimal and equal. The values are interchanged at 90°. This leads to the assumption that the rolling shear modulus is generally underestimated, when using the nominal value for CLT constructions, while the perpendicular *Young*'s moduli are overestimated. The assumption of a combined perpendicular modulus (see [Gülzow 2008]) is feasible for every angle.

When parametric studies of a large number of CLT floors are intended to be performed, it is clear, that a FE-model cannot be as detailed as to model each board individually regarding its local coordinate systems. Real structures, the necessary information can be taken from, are usually only available in case of few reference floors. Thus, the location of the gaps between the boards and the grooves inside the board cannot be accounted for as well. In Chapter 4, the global material properties for CLT floors, with smeared layers, are derived from an EMA on reference floors using a model-updating algorithm. The above described example is used to explain the results of the model-updating regarding their plausibility.

2.2 Dimensional Analysis

With the help of a dimensional analysis, complex physical problems can be reduced to their core context based on the concept of similarities. The method states that every physical quantity can be expressed as a product of basic physical dimensions, according to physical laws. Thus, for example, the physical quantity "force" can be derived form *Newton*'s second law of motion as a product of the dimensions mass and acceleration. It can also be expressed in scale units as $[\mathrm{F}] = \frac{\mathrm{kg \cdot m}}{\mathrm{s}^2}$. When physical phenomenons are described in practice, usually, dimensionless parameters are considered. Some examples are *Reynold*'s number, *Froud* number, *Mach* number and so on.

Different methods have been published for the derivation of the similitude. For mechanical problems, usually, *Buckingham*'s π-theorem is applied, which will be explained in the following. Introductions to other methods are given, for example, in Zierep [1982].

2.2.1 Buckingham π Theorem

The theorem states that if a system with n variables $Q_1, \ldots, Q_n$ is considered, in which r fundamental dimensions $A_1, \ldots, A_r$ are involved, $n - r$ dimensionless quantities π_i can be defined, which are products and quotients of the original variables and parameters [Buckingham 1914]. Each (scalar) model equation

$$f(Q_1, \ldots, Q_n) = 0, \tag{2.45}$$

between the physical quantities $Q_1, \ldots, Q_n$ of a mathematical model, can be replaced with a corresponding relation between the π_i:

$$f(\pi_1, \ldots, \pi_{n-r}) = 0. \tag{2.46}$$

This is especially useful for complex systems, that have not been researched so far, and thus no algebraic or differential equations are available. The derivation of this theorem is shown in the following.

The relevant physical quantities $Q_1, \ldots, Q_n$, that are involved in the problem have to be identified. The dimension of each of these quantities, indicated by [ ], can be expressed by a power product of the fundamental dimensions $A_1, \ldots, A_r$, according to *Bridgman*'s principle

of absolute significance of relative magnitude [Bridgman 1922]. For mechanical problems those are the triple: mass, length, and time.

$$[Q_1] = A_1^{a_{11}} \cdot A_2^{a_{21}} \cdot \ldots \cdot A_r^{a_{r1}}$$

$$\vdots \tag{2.47}$$

$$[Q_n] = A_1^{a_{1n}} \cdot A_2^{a_{2n}} \cdot \ldots \cdot A_r^{a_{rn}}$$

Herein the exponents of the fundamental dimensions are $a_{\alpha\beta}$ with $\alpha = 1,2,...,r$ and $\beta = 1,2,...,n$. The objective is to find independent power products of the derived physical quantities that form dimensionless parameters

$$\pi = Q_1^{k_1} \cdot Q_2^{k_2} \cdot \ldots \cdot Q_n^{k_n} \tag{2.48}$$

with unknown parameters for the exponents $k_1, k_2, \ldots, k_n$. Rewriting Equation (2.48) with Equation (2.47), and expressing the same in dimensions, yields the following:

$$[\pi] = A_1^0 \cdot \ldots \cdot A_2^0 = \left\{ A_1^{a_{11}} \cdot \ldots \cdot A_r^{a_{r1}} \right\}^{k_1} \cdot \ldots \cdot \left\{ A_1^{a_{1n}} \cdot \ldots \cdot A_r^{a_{rn}} \right\}^{k_n} \tag{2.49}$$

The exponents in Equation (2.49) can be written as a homogeneous linear system of equations, with r equations for the unknown parameters $k_1, k_2, \ldots, k_n$.

$$
\begin{array}{ccccccccc}
a_{11}k_1 & + & \ldots & + & a_{1\beta}k_\beta & + & \ldots & + & a_{1n}k_n & = 0 \\
a_{\alpha 1}k_1 & + & \ldots & + & a_{\alpha\beta}k_\beta & + & \ldots & + & a_{\alpha n}k_n & = 0 \\
a_{r1}k_1 & + & \ldots & + & a_{r\beta}k_\beta & + & \ldots & + & a_{rn}k_n & = 0
\end{array}
\tag{2.50}
$$

This system of equations transformed into matrix representation yields:

$$
\begin{array}{c|ccc}
 & Q_1 & Q_\beta & Q_n \\
\hline
A_1 & a_{11} & a_{1\beta} & a_{1n} \\
A_\alpha & a_{\alpha 1} & a_{\alpha\beta} & a_{\alpha n} \\
A_r & a_{r1} & a_{r\beta} & a_{rn}
\end{array}
\tag{2.51}
$$

Within this $r \times n$ dimensional matrix, the components in column β are related to the unit of the derived quantity Q_β. Thus, the problem of finding independent power products for a number of dimensionless parameters is substituted by a solution of a homogeneous linear system of equations with r equations and n unknown parameters. The constructed coefficient matrix is of rank r which leads to $n - r$ linearly independent solutions.

To solve this system of equations, the *Gauss*ian elimination algorithm is applied. This algorithm is repeated, until the matrix has a canonical form consisting of a $r \times r$ identity matrix to the left, and a remaining $(n - r) \times r$ matrix to the right:

$$
\begin{array}{c|ccc|ccc}
 & Q_1 & Q_\beta & Q_r & Q_{(r+1)} & Q_\beta & Q_{n-r} \\
\hline
A_1 & 1 & 0 & 0 & a_{1(r+1)} & a_{1\beta} & a_{1(n-r)} \\
A_\alpha & 0 & 1 & 0 & a_{i(r+1)} & a_{\alpha\beta} & a_{\alpha(n-r)} \\
A_r & 0 & 0 & 1 & a_{r(r+1)} & a_{r\beta} & a_{r(n-r)}
\end{array}
\tag{2.52}
$$

Thus, the quantities Q_β are linearly independent for $\beta \leq r$. For $\beta > r$, the dimension of Q_β can be expressed as a power product of the dimensions of $Q_1, \ldots, Q_r$, with the corresponding exponents in column β.

$$
[\mathrm{Q}_\beta] = [\mathrm{Q}_1]^{a_{1\beta}} \cdot [\mathrm{Q}_\beta]^{a_{i\beta}} \cdot \ldots \cdot [\mathrm{Q}_r]^{a_{r\beta}}
\tag{2.53}
$$

Finally, the systems dimensionless parameters $\pi_1, \ldots, \pi_i, \ldots, \pi_{n-r}$ yield the following [Sonon 2001]:

$$
\pi_i = \frac{Q_\beta}{Q_1^{a_{1i}} \cdot Q_\beta^{a_{\alpha i}} \cdot \ldots \cdot Q_r^{a_{ri}}} \quad \text{with} \quad [\pi_\mathrm{i}] = 1.
\tag{2.54}
$$

In an experiment, the independent quantities can be varied freely, while the remaining quantities are dependent on the former. This leads to some restrictions. The free quantities have to be chosen to be linear independent, and a matrix composed of them only must be of rank r itself. The dependent quantities contribute, each, only to a single dimensionless parameter, while the free quantities, in general, can effect all of them [Runtemund 2006]. Especially, when nomograms are intended to be created, an appropriate choice of the free quantities is necessary.

A dimensional analysis will be used to describe the aliasing effect of finite sinusoidal signals in Section 2.3.2.3 and the results of a parametric study in Chapter 5.

2.3 Fourier Transform of Time or Spatial Limited Signals

The Fourier Transform is a mathematical process that serves as a principal analysis tool for many scientific challenges [Brigham 1974]. It originally describes periodic but can also be applied to non-periodic phenomena. Thus, arbitrary functions can be represented as a

superposition of sine and cosine functions. Besides continuous problems in modern theory signal processing, a discrete version of the Fourier transform is used to analyze and process a sequence of measurements or data [Beerends et al 2003]. As a typical application, it relates the measured time signals to its frequency content. Therefore, a common notation is to distinguish between Continuous Time *Fourier* Transform (CTFT), Discrete Time *Fourier* Transform (DTFT) and Discrete *Fourier* Transform (DFT) [Mandal and Asif 2007]. In this chapter, the relationship between the three transform types is described for a time limited signal. The theory is analogously applicable to the two-dimensional spatial problem described in Section 2.4.

2.3.1 Continuous Time Fourier Transform (CTFT)

For time signals, the Fourier Transform relates a function $f(t)$ with variable time t to a function $F(\omega)$ with variable circular frequency ω. The Fourier integral and its inversion formula are defined as follows:

$$F(\omega) = \frac{1}{2\pi} \int\limits_{-\infty}^{\infty} f(t)e^{-i\omega t}d\omega \qquad\qquad \text{Fourier integral} \qquad\qquad (2.55)$$

$$f(t) = \int\limits_{-\infty}^{\infty} F(\omega)e^{i\omega t}dt \qquad\qquad \text{Inversion formula.} \qquad\qquad (2.56)$$

This holds true if the integral (2.55) exists for every value of ω. If $f(t)$ and $F(\omega)$ are related by Equations (2.55) and (2.56), the two functions are termed Fourier Transform Pair [Brigham 1974]. The relationship is indicted by the notation as follows:

$$f(t) \ \circ\!\!\!-\!\!\!-\!\!\!\bullet \ F(\omega) = \mathcal{F}\left[f(t)\right] \qquad\qquad\qquad (2.57)$$

with the operator of the Fourier transform $\mathcal{F}$. For more detailed descriptions and examples of Fourier Transform Pairs refer to Brigham [1974]. A different definition used in signal processing is based on the frequency f. Thus, the circular frequency ω is substituted by $f = \frac{\omega}{2\pi}$ and Equations (2.55) and (2.56) can be rewritten as follows:

$$X(f) = \int\limits_{-\infty}^{\infty} x(t)e^{-i2\pi ft}df \qquad\qquad\qquad (2.58)$$

$$x(t) = \int\limits_{-\infty}^{\infty} X(f)e^{i2\pi ft}dt. \qquad\qquad\qquad (2.59)$$

2.3.1.1 Properties of the CTFT

The properties of a CTFT can be found in literature (e.g. Brigham [1974]). However, two fundamental theorems are given for the multiplication of functions $f(t)$ and $g(t)$ (resp. $x(t)$ and y(t)) and their transformed, which are of particular importance for the following sections:

Convolution theorem

$$\mathcal{F}[f(t) \cdot g(t)] = \frac{1}{2\pi} \left(F(\omega) * G(\omega) \right) \tag{2.60}$$

$$\mathcal{F}[f(t) * g(t)] = F(\omega) \cdot G(\omega) \tag{2.61}$$

$$\mathcal{F}[x(t) \cdot y(t)] = X(f) * Y(f) \tag{2.62}$$

$$\mathcal{F}[x(t) * y(t)] = X(f) \cdot Y(f) \tag{2.63}$$

Herein the convolution of two continuous functions (e.g., $f(t)$ and $g(t)$) is defined as

$$f(t) * g(t) = \int_{-\infty}^{\infty} f(\tau)g(t-\tau)d\tau \tag{2.64}$$

$$= \int_{-\infty}^{\infty} f(t-\tau)g(\tau)d\tau \qquad \text{commutativity.} \tag{2.65}$$

An asterisk is used as convolution operator.

Generalized *Rayleigh-Parseval* theorem

$$\int_{-\infty}^{\infty} f(t) \cdot g^*(t)e^{-i\omega t}d\omega = \frac{1}{2\pi} \int_{-\infty}^{\infty} F(\omega) \cdot G^*(\omega)e^{i\omega t}dt \tag{2.66}$$

$$\int_{-\infty}^{\infty} x(t) \cdot y^*(t)e^{-i2\pi ft}df = \int_{-\infty}^{\infty} X(f) \cdot Y^*(f)e^{i2\pi ft}dt \tag{2.67}$$

2.3.1.2 Time-limited signals

The CTFT of a finite signal can be interpreted as an infinite signal $x_0(t)$ multiplied by a rectangular window function $h(t)$. This is illustrated in Figure 2.7 for a cosine function

with amplitude A and fundamental frequency f_0. The corresponding functions are listed in Table 2.2. The window function $h(t)$ has a duration of T centered at the origin with $T \cdot 2\pi f_0 = 5\pi$. Thus, a multiplication $x_0(t) \cdot h(t)$ leads to a finite signal of 2.5 periods. The CTFT of the continuous periodic function $x_0(t)$ leads to a non-periodic pair of $Dirac$ delta functions $X_0(t)$ of length $\frac{A}{2}$. Since the cosine function is real and symmetric, the corresponding transformed $X_0(f)$ is also real and symmetric. The same holds for the non-periodic rectangular window, that transforms into a continuous cardinal sine function $H(t)$ with peak value T. The distance between the zero-crossings, separating the characteristic so-called side-lobes, is $\frac{1}{T}$. According to Section 2.3.1.1, a multiplication in the original domain leads to a convolution in the transformed domain. Thus, the truncated signal $x_1(t) = x_0(t) \cdot h(t)$ is transformed into a pair of overlapping cardinal sines with individual peak values $\frac{TA}{2}$ (the superposed course has a slightly different peak value [Brigham 1974]). Superimposed in gray is the magnitude $|X_1(f)|$. It has to be mentioned, that when the infinite signal $x_0(t)$ is intended to be approximated by the finite signal $x_1(t)$, which is a common task in signal processing of discrete data, since the computation capacity is limited, an error is induced by the truncation that is referred to as leakage effect [Brigham 1974]. For investigations in the spatial domain, usually finite data are processed, due to the finite dimensions of the test object.
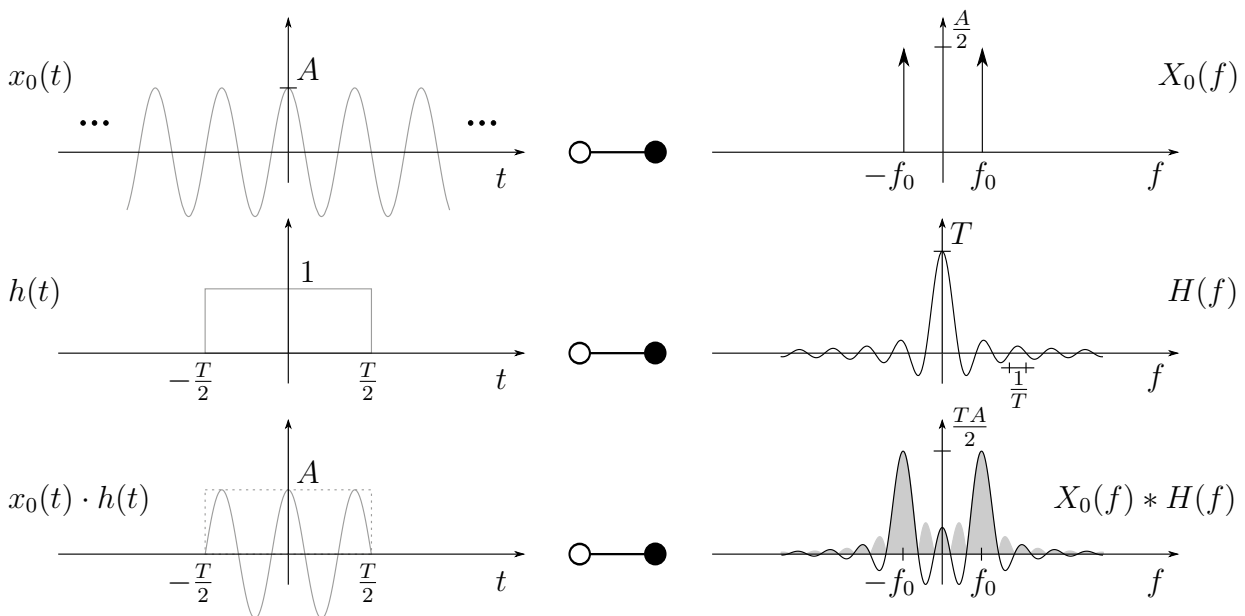
Figure 2.7: Continuous Time Fourier Transform of a finite sinusoidal signal

Table 2.2: Fourier transform pairs related to the time limitation of a cosine signal

Original domain	Transformed domain
$x_0(t) = A\cos(2\pi f_0 t)$	$X_0(f) = \dfrac{A}{2}\left[\delta(f - f_0) + \delta(f + f_0)\right]$
$h(t) = \begin{cases} 1 & |t| < \frac{T}{2} \\ \frac{1}{2} & |t| = \frac{T}{2} \\ 0 & |t| > \frac{T}{2} \end{cases}$	$H(f) = T\dfrac{\sin(\pi f T)}{\pi f T}$
$x_1(t) = x_0(t) \cdot h(t) = \begin{cases} A\cos(2\pi f_0 t) & |t| < \frac{T}{2} \\ 0 & |t| > \frac{T}{2} \end{cases}$	$\begin{aligned} X_1(f) &= X_0(f) * H(f) \\ &= \dfrac{A}{2}\left[H(f - f_0) + H(f + f_0)\right] \end{aligned}$

2.3.2 Discrete Fourier Transform (DFT)

Due to its continuous nature, the CTFT, briefly discussed above, is not suitable for digital computing. Thus, the DFT is introduced in this section, which can be computed on digital computers [Mandal and Asif 2007]. It should be mentioned, that the DFT in its original form is usually not applied due to the inefficient computation of large data, but replaced by the more efficient Fast *Fourier* Transform (FFT), which gives identical results and thus will not be discussed here. A DFT comprises three process steps as follows:

- Analog-to-digital conversion (time sampling)

- Time limiting

- Frequency sampling

The process is visualized in Figures 2.8 and 2.9 for a signal similar to the example in Section 2.3.1.2. The second process step is therefore negligible, since the signal is already time limited. The signal $x_1(t)$ is time-shifted by $+\frac{T}{2}$ to avoid notation problems, which leads to a complex $X_1(f)$ due to the odd sinusoidal function. The magnitude $|X_1(f)|$ stays identical.

2.3.2.1 Analog-to-digital conversion

A continuous time signal must be digitized to be stored into a digital computer. This so-called sampling is performed by multiplying the continuous signal $x_1(t)$ by an impulse train:
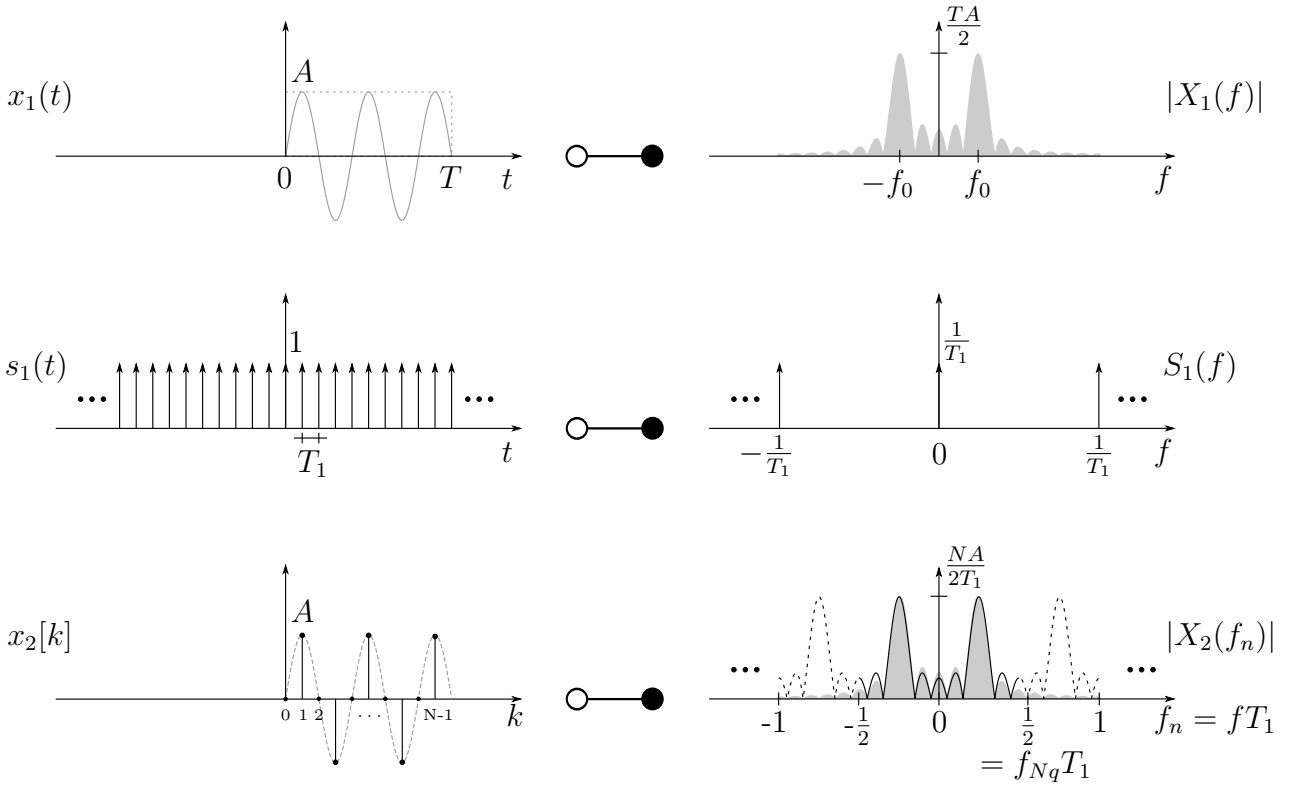
Figure 2.8: Analog-to-digital-conversion

$$s_1(t) = \sum_{m=-\infty}^{\infty} \delta(t - mT_1), \tag{2.68}$$

with the sampling interval T_1. Thus, a CTFT of the resulting sampled function

$$x_1(t) = x(t) \cdot s_1(t) = \sum_{m=-\infty}^{\infty} x(mT_1)\delta(t - mT_1) \tag{2.69}$$

is performed by a convolution of $X_1(f)$ with the transformed

$$S_1(f) = \frac{1}{T_1} \sum_{m=-\infty}^{\infty} \delta\left(\omega - \frac{m}{T_1}\right), \tag{2.70}$$

which yields:

$$X_1(f) = X(f) * S_1(f) = \frac{1}{T_1} \sum_{m=-\infty}^{\infty} X\left(f - \frac{m}{T_1}\right). \tag{2.71}$$

The discretized representation of the product of continuous signal and impulse train $x_2(t) = x_1(t)s_2(t)$ is achieved by converting the continuous impulses into discrete impulses:

$$x_2[k] = \sum_{m=-\infty}^{\infty} x_1(mT_1)\delta(t - mT_1). \tag{2.72}$$

When substituting $x_2[m] = x_1(mT_1)$ and introducing the normalized frequency $f_n = fT_1$, a DTFT of both sides leads to

$$X_2(f_n) = X_2(f)|_{f=f_n/T_1} = \sum_{m=-\infty}^{\infty} x_2[m]e^{-i2\pi m f_n}. \tag{2.73}$$

Since the signal is time-limited, the discretized signal consists of a finite number of samples $N = \frac{T}{T_1}$. Thus the discrete time signal can be rewritten as

$$x_2[k] = \sum_{k=0}^{N-1} x_1(kT_1)\delta(t - kT_1). \tag{2.74}$$

As shown in Figure 2.8, the sampling in the time domain causes periodic repetition of the original frequency spectrum with repetition interval $\frac{1}{T_1}$. Since $x_1(t)$ is time-limited $X_1(f)$ cannot be band-limited [Brigham 1974] and thus the repeating spectra wrap around at the *Nyquist* frequency $f_{Nq} = \frac{1}{2T_1}$ and overlap. For better visualization, the resulting DTFT spectrum $|X_2(f_n)|$ is superimposed by the CTFT spectrum $|X_1(f_n)|$. This so-called aliasing effect cannot be avoided for signals of finite length, but can be reduced by decreasing the sampling interval T_1 [Brigham 1974]. Thus, the CTFT can only be approximated by a DTFT or a DFT. A more detailed investigation is presented in Section 2.3.2.3.

2.3.2.2 Frequency sampling

The derived relations in Section 2.3.2.1 are insufficient for digital computing, since the DTFT of a digital signal is still a continuous function. In a further step, another sampling must be performed in the frequency domain to obtain the DFT. Therefore, $X(f_n)$ is multiplied by the impulse train

$$S_2(f_n) = \frac{1}{M} \sum_{m=-\infty}^{\infty} \delta\left(f_n - \frac{m}{M}\right) \tag{2.75}$$
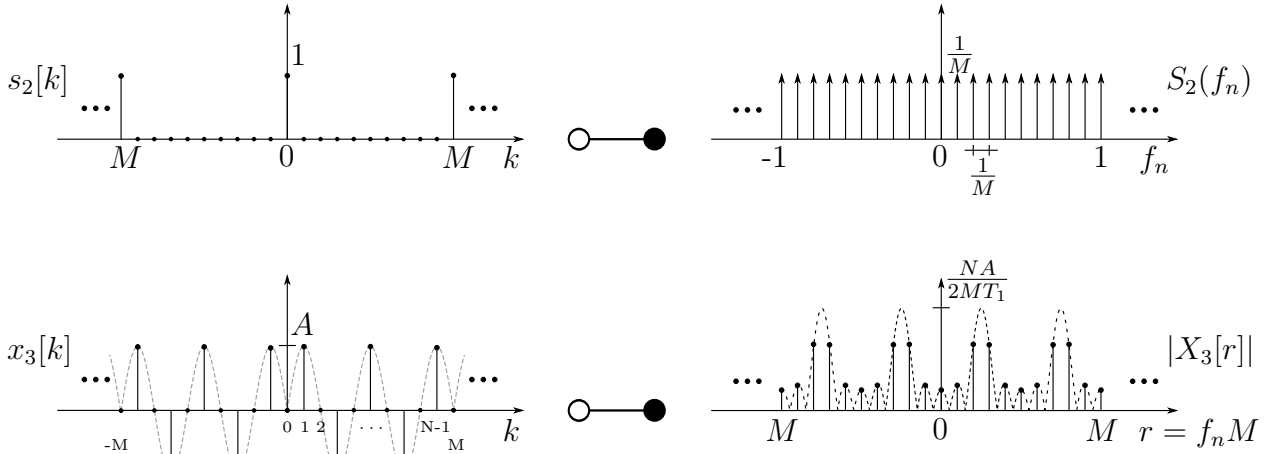
Figure 2.9: Frequency sampling

which is the DTFT of

$$s_2[k] = \sum_{m=-\infty}^{\infty} \delta\left(k - mM\right) \tag{2.76}$$

with the number of frequency samples within one period M and the sampling interval $\frac{1}{M}$. The number of frequency samples is typically set to be greater or equal to N. Figure 2.9 shows an example for $M = N$. Similar to Section 2.3.2.1 the sampling in the frequency domain $X_2(f_n)\cdot S_2(f_n)$ causes a repetition of the discrete signal in the time domain $x_3[k] = x_2[k]*s_2[k]$. A digitized version of the DTFT $X_3(f_n) = X_2(f_n)\cdot S_2(f_n)$ with $r = \frac{f_n}{M}$ yields the DFT analysis equation

$$X_3[r] = \sum_{k=0}^{N-1} x_3[k]e^{-i2\pi m\frac{r}{M}} \qquad \text{for} \qquad 0 \le r \le (M-1) \tag{2.77}$$

and the DFT synthesis equation becomes

$$x_3[k] = \frac{1}{M} \sum_{r=0}^{M-1} X_3[r]e^{i2\pi m\frac{r}{M}} \qquad \text{for} \qquad 0 \le k \le (N-1). \tag{2.78}$$

Different to the above definition, for computer platforms with matrix-based programming languages (e.g., MATLAB®) the index starts at 1 instead of 0. By comparing the CTFT spectrum in Figure 2.7 to the DFT spectrum in Figure 2.9, the following approximation can be extracted,

$$X_1(f) \approx \frac{MT_1}{N}X_3[r] \tag{2.79}$$

keeping in mind errors induced by the aliasing and leakage effect. Further, when implementing this equation into a software, special attention has to be payed for the algorithm programmed by the author. In case of the FFT command, implemented in MATLAB$^{\circledR}$, the term $\frac{M}{N}$ in Equation 2.79 must be omitted, when approximating the CTFT.

The dotted line superimposed to $x_3[k]$ does not reassemble the continuous function $x_0(t + T/2)$, since T was not chosen to be a multiple of its period $\frac{1}{f_0}$. Thus, the frequency spectrum results in a poor approximation of the CTFT of $x_0(t+T/2)$ caused by the leakage effect. The discretized spectrum $X_3[r]$ with $r = f_n M$ shows multiple peaks instead of only repeating pairs at the fundamental frequency $\pm f_0$, which is also referred to as the picket fence effect [Mandal and Asif 2007]. When the actual time-limited signal should be approximated, leakage does not cause any error as mentioned above. Nevertheless, the spectrum $X_3[r]$ is still a poor approximation of the CTFT caused by the insufficient duration T which leads to large frequency sample intervals. To improve the resolution of the frequency axis in the DFT domain, an approach for aperiodic sequences is to append the discrete time signal of length N with additional zero-valued samples.

$$x_{zp}[k] = \begin{cases} x[k] & 0 \leq k \leq (N-1) \\ 0 & N \leq k \leq (M-1) \end{cases} \tag{2.80}$$

This process is called zero-padding [Mandal and Asif 2007]. The resulting sequence has a length of M and the frequency resolution is improved by a factor of $z_p = MN$. The improvement is illustrated for a zero-padding factor of $z_p = 2$ in Figure 2.10.
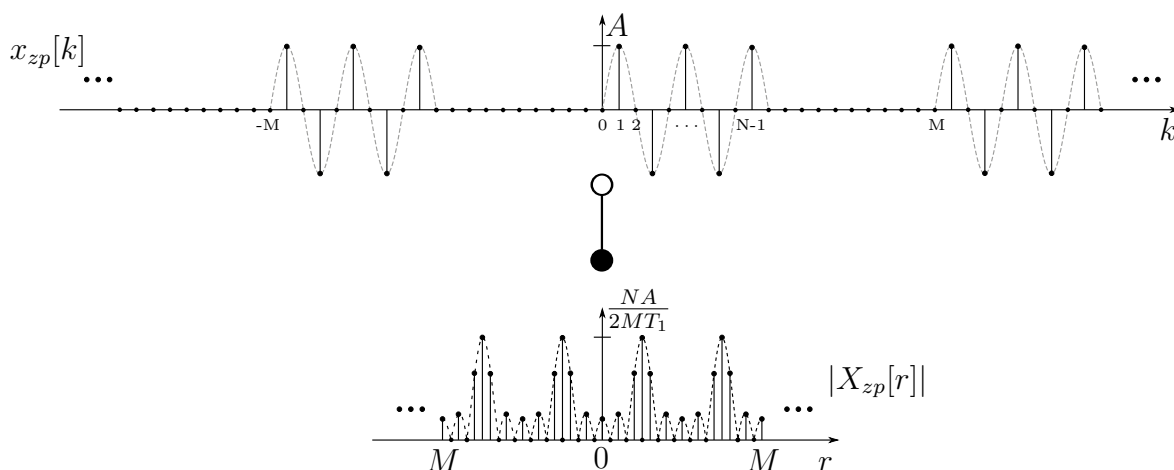
Figure 2.10: Zero Padding

2.3.2.3 On the aliasing effect of time/spatial limited sinusoidal functions

As described above, truncated signals are linked to the aliasing effect. It can be reduced but not totally avoided by increasing the sampling rate $f_s = \frac{1}{T_1}$. Since an arbitrary signal can be represented by a sum of sine and cosine functions, the impact of the aliasing effect on a sinusoidal function will be investigated in detail in the following.

For the investigation, a Dimensional Analysis (see Section 2.2) is performed for sinusoidal functions

$$y(t) = A\sin(2\pi f_0 t) \tag{2.81}$$

with $t = k \cdot T_1$, $0 \le k \le (N-1)$ and $N = \frac{T}{T_1}$, that oscillate with a frequency f_0.
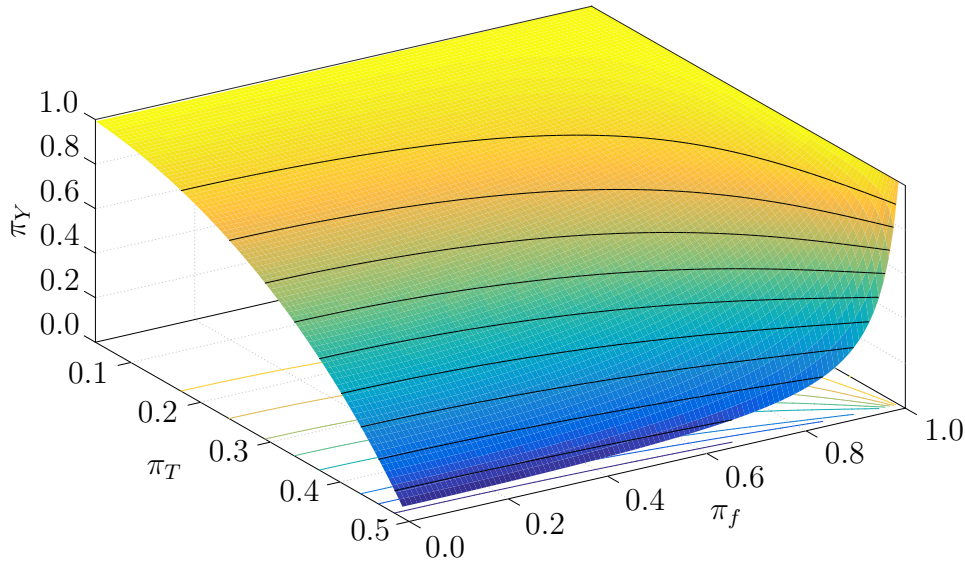
Figure 2.11: Dimensional Analysis of the impact of the aliasing effect on finite sinusoidal signals below the fundamental frequency

Within a parametric study, the duration of the signal was varied in steps of half a period $T = \frac{nT_0}{2}$ with $n = 1,2,...$ to ensure zero values at $k = 0$ and $k = N$. The range of interest of the sampling interval is $0 < T_1 < \frac{T_0}{2}$, which results in sampling rates smaller than the *Nyquist* frequency $f_{Nq} = 2f_0$. The resulting erroneous DTFT $Y_D(f_n)$ scaled by T_1 is subsequently compared to the correct CTFT $Y_C(f)$. The frequency range of interest is below the frequency of oscillation $0 \le f \le f_0$. For a Dimensional Analysis, three dimensionless parameters can

be derived:

$$\text{Normalized sampling interval:} \qquad \pi_T = \frac{T_1}{T_0} \qquad\qquad 0.05 \leq \pi_T \leq 0.45 \qquad (2.82)$$

$$\text{Normalized frequency:} \qquad \pi_f = \frac{f}{f_0} = \frac{f_n}{T_1 f_0} \qquad\qquad 0 \leq \pi_f \leq 1.0 \qquad (2.83)$$

$$\text{Aliasing factor:} \qquad \pi_Y = \frac{T_1 \cdot Y_D(\pi_f)}{Y_C(\pi_f)}. \qquad\qquad\qquad\qquad (2.84)$$

with sampling interval T_1 and normalized frequency $f_n = f T_1$. The resulting three-dimensional course is shown in Figure 2.11. For better visualization, the surface is complemented by contour lines. The course is perfectly continuous, which was not obvious due to the singularities at the zero-crossings of the appearing side lobes. As expected, the aliasing diminishes for $\pi_T = 0$ ($T_1 \longrightarrow 0$). For $\pi_T = 0.5$ the *Nyquist* criterion is breached, resulting in an aliasing factor $\pi_Y = 0$ ($y[k] = 0$). At $\pi_f = 1$ the aliasing factor is unity for all sampling intervals. The aliasing effect has an exponential increasing impact towards $\pi_f = 0$ with a steeper decline for higher values of π_T. For example, at $\pi_T = 0.25$ the aliasing effect decreases the resulting spectrum at $\pi_T = 0$ by $\approx 20\%$ and at $\pi_T = 0.75$ by $\approx 10\%$. As mentioned before, a similar investigation can be done for cosine-shaped signals, where the aliasing effect results in DTFT spectra above the correct CTFT result. The derived relations have to be considered, when processing finite data as in the numerical, acoustical evaluation model for the prediction of the radiated sound power of plate-like structures presented in Section 3.7.1 based on theoretical aspects in Section 2.4. Detailed investigations of the limitations of the developed model, that are related to the aliasing effect, are discussed in Section 4.6.

2.4 Sound Radiation of Finite Plates

The standardized characterization of the vibro-acoustical behavior of floor constructions is performed by measurement of the sound pressure level in the receiving room caused by a standardized excitation [DIN EN ISO 717-2:2013-06]. Since the focus of this contribution lies only on the numerical modeling of floor constructions and neglects the adjacent receiving room, an alternative examination process is mandatory. A more specific quantity is the radiated sound power. Since a floor construction usually has a plane radiating surface, it can be approximated as a finite plane radiator inside an infinite rigid baffle. The following sections will give an introduction of the theoretical aspects of the radiation of finite plates, based on the work of Pierce [2007], Lerch et al [2009] and Cremer et al [2005].

2.4.1 Sound waves in fluids

2.4.1.1 Wave equation for linear acoustics

Hydrodynamic problems can be described in general by non-linear *Euler*'s equations for ideal compressible fluids. Here, the dissipation process linked to thermal conductivity and viscosity is neglected [Pierce 2007]. Thus, *Newton*'s second law reduces to the first *Euler* equation

$$\tilde{\rho}\frac{\mathrm{D}\tilde{\mathbf{v}}}{\mathrm{D}t} + \nabla\tilde{p} - \mathbf{g}\tilde{\rho} = 0, \tag{2.85}$$

with the medium's position- and time-dependent dynamic variables mass density $\tilde{\rho}$, particle velocity $\tilde{\mathbf{v}}$ and absolute pressure $\tilde{p}$ (arguments (x,y,z,t) are neglected). The Further, $\mathbf{g}$ represents the vector acceleration due to gravity. $\nabla = \left(\frac{\partial}{\partial x}, \frac{\partial}{\partial y}, \frac{\partial}{\partial z}\right)$ marks the three-dimensional *Nabla* operator for Cartesian coordinates x, y and z. The material derivative is indicated by D. The second *Euler* equation describes the conservation of mass

$$\frac{\mathrm{D}\tilde{\rho}}{\mathrm{D}t} + \nabla \cdot (\tilde{\rho}\tilde{\mathbf{v}}) = 0. \tag{2.86}$$

The relation between pressure $\tilde{p}$ and density $\tilde{\rho}$ can be described by an adiabatic process

$$\frac{\mathrm{D}\tilde{p}}{\mathrm{D}t} = c^2\frac{\mathrm{D}\tilde{\rho}}{\mathrm{D}t}, \tag{2.87}$$

with thermodynamic coefficient c representing the sound speed Pierce [2007].

The dynamic variables for sound in fluids can be separated into quantities describing the ambient state (p_0, ρ_0 and $\mathbf{v}_0$) and acoustically induced perturbations (sound pressure p, sound density ρ and airborne sound velocity $\mathbf{v}$) [Lerch et al 2009].

$$\begin{aligned} \tilde{p} &= p_0 + p \\ \tilde{\rho} &= \rho_0 + \rho \\ \tilde{\mathbf{v}} &= \mathbf{v}_0 + \mathbf{v} \end{aligned}$$

For linear acoustical problems, the perturbations are considered to be small. The gravity is neglected and the ambient velocity is assumed to be zero, leading to a constant ambient

pressure. Thus, the convective accelerations can be neglected

$$\frac{\mathrm{D}\tilde{\mathbf{v}}}{\mathrm{D}t} \to \frac{\partial \mathbf{v}}{\partial t} \tag{2.88}$$

and the non-linear Equations (2.85) and (2.86) combined with (2.87) can be linearized [Pierce 2007]:

$$\rho_0 \frac{\partial \mathbf{v}}{\partial t} + \nabla p = 0 \tag{2.89}$$

$$\frac{1}{c^2}\frac{\partial p}{\partial t} + \rho_0 \nabla \cdot \mathbf{v} = 0 \tag{2.90}$$

These two partial differential equations can be combined by taking the time derivative of (2.90) and re-express the time derivative of the fluid velocity in terms of pressure by using (2.89). Assuming the ambient density is independent of position leads to the wave equation for linear acoustics (here: for sound pressure)

$$\nabla^2 p - \frac{1}{c^2}\frac{\partial^2 p}{\partial t^2} = 0, \tag{2.91}$$

where $\nabla^2 = \frac{\partial^2}{\partial x^2} + \frac{\partial^2}{\partial y^2} + \frac{\partial^2}{\partial z^2}$ marks the three-dimensional *Laplace* operator for Cartesian coordinates x, y and z [Lerch et al 2009].

2.4.1.2 Plane waves in fluids

For the one-dimensional case, the wave Equation (2.91) can be solved by the *D'Alembert* solution

$$p(x,t) = f(x - ct) + g(x + ct), \tag{2.92}$$

with arbitrary two fold derivable position- and time-dependent functions f and g describing traveling waves in positive and negative x-directions at a velocity c [Lerch et al 2009]. Acoustic disturbances can, in general, be described by purely sinusoidal oscillations with constant frequency about a mean value [Pierce 2007]. E.g., the acoustic pressure of an harmonic plane wave traveling in a positive x-direction can be expressed equivalently by one of the following

equations (subscripts A indicate the medium air):

$$
\begin{aligned}
p(x,t) &= \left|\hat{\underline{p}}_0\right| \cos\left[k_A\left(-x + ct\right) + \phi_0\right] = \left|\hat{\underline{p}}_0\right| \cos\left[-k_x x + \omega t + \phi_0\right] & (2.93) \\
&= \frac{1}{2}\left|\hat{\underline{p}}_0\right| \left[e^{i(-k_x x + \omega t + \phi_0)} + e^{-i(-k_x x + \omega t + \phi_0)}\right] & (2.94) \\
&= \Re\left\{\hat{\underline{p}}_0 \; e^{-ik_x x} e^{i\omega t}\right\}. & (2.95)
\end{aligned}
$$

The circular wavenumber of air is

$$
k_A = \frac{2\pi}{\lambda_A}, \tag{2.96}
$$

with the wavelength λ_A, which in the one-dimensional case is equal to the wavenumber component in x-direction k_x. The circular frequency ω is identified as follows:

$$
\omega = k_A c_A. \tag{2.97}
$$

The phase constant ϕ_0 describes the wave at $x = 0$ and $t = 0$. Equation (2.94) is the complex representation of (2.93). Hence, the argument combination $x - ct$ is exchanged by $-x + ct$ to achieve the $e^{i\omega t}$ time dependance, which is common in vibrations literature [Pierce 2007]. In Equation (2.95) the phase constant ϕ_0 is included into the complex number

$$
\hat{\underline{p}}_0 = \left|\hat{\underline{p}}_0\right| e^{i\phi_0}. \tag{2.98}
$$

The subscript 0 indicates the invariant character in case of a plane wave, underlining indicates complex quantities. This solution can be extended for the three-dimensional case

$$
p(x,y,z,t) = \Re\left\{\hat{\underline{p}}_0 \; e^{-ik_x x} e^{-ik_y y} e^{-ik_z z} e^{i\omega t}\right\} = \Re\left\{\underline{p}(x,y,z) \; e^{i\omega t}\right\}, \tag{2.99}
$$

with wavenumber components k_x, k_y and k_z into the spatial directions x, y and z and the complex amplitude of acoustic pressure

$$
\underline{p}(x,y,z) = \hat{\underline{p}}_0 \; e^{-ik_x x} e^{-ik_y y} e^{-ik_z z}, \tag{2.100}
$$

that in general varies with position. For the wave equation (2.91) is a homogeneous, linear, partial differential equation with time-independent coefficients, a separation of the variables

for space and time is performed, and the field variable $p(x,y,z,t)$ can be replaced by the complex amplitude $\underline{p}(x,y,z)$ [Pierce 2007]. Subsequently, all time derivatives can be substituted by

$$\frac{\partial}{\partial t} \rightarrow i\omega. \tag{2.101}$$

Thus, the wave equation (2.91) reduces with (2.97) to the *Helmholtz* equation for the complex pressure amplitude

$$\left(\nabla^2 + k^2\right) \underline{p}(x,y,z) = 0. \tag{2.102}$$

For a single set of wavenumber components at a fixed circular frequency ω, inserting Equation (2.100) into (2.102) yields:

$$\left((-ik_x)^2 + (-ik_y)^2 + (-ik_z)^2 + k_A^2\right) \underline{p}(x,y,z) = 0 \tag{2.103}$$

This is fulfilled for any harmonic plane when

$$k_x^2 + k_y^2 + k_z^2 = k_A^2. \tag{2.104}$$

Equation (2.100) does not represent a full solution of the wave equation for harmonic problems, but can serve as a fundamental solution. General acoustic problems can therefore be solved as a superposition of plane waves or by integration using the *Fourier* integral for a fixed frequency ω Pierce [2007]:

$$\underline{p}(x,y,z) = \frac{1}{(2\pi)^3} \int\limits_{-\infty}^{\infty} \int\limits_{-\infty}^{\infty} \int\limits_{-\infty}^{\infty} \hat{\underline{p}}(k_x,k_y,k_z) \; e^{-ik_x x} e^{-ik_y y} e^{-ik_z z} dk_x dk_y dk_z. \tag{2.105}$$

This solution represents one frequency component of a multi-frequency disturbance. An inverse *Fourier* transformation yields the sound pressure amplitudes in the wave number domain

$$\hat{\underline{p}}(k_x,k_y,k_z) = \int\limits_{-\infty}^{\infty} \int\limits_{-\infty}^{\infty} \int\limits_{-\infty}^{\infty} \underline{p}(x,y,z) \; e^{ik_x x} e^{ik_y y} e^{ik_z z} dx dy dz. \tag{2.106}$$

2.4.2 Bending waves in plates

2.4.2.1 Bending wave equation

Similar to acoustic waves, again, considering purely sinusoidal oscillations with constant frequency, the bending waves in plates in the $x-y$-plane can be described for the complex out of plane structure-borne sound velocity $\underline{v}_s$ (subscript s indicates structure-borne quantities) by the two-dimensional bending wave equation [Cremer et al 2005]:

$$\left(\nabla^4 + k_B^4\right)\underline{v}_s(x,y) = 0, \tag{2.107}$$

with the two-dimensional bending wave number k_B. It is defined for isotropic plates as

$$k_B^4 = \omega^2\frac{m''}{B'} = \left(\frac{2\pi}{\lambda_B}\right)^4, \tag{2.108}$$

with mass per unit area m'', bending stiffness per unit length B' and bending wavelength λ_B. Different to Equation (2.85) $\nabla^4 = \left(\frac{\partial^2}{\partial x^2} + \frac{\partial^2}{\partial y^2}\right)^2$ marks the square of the two-dimensional *Laplace* operator for Cartesian coordinates x, y.

2.4.2.2 Plane bending waves

Analogous to section 2.4.1.2, the simplest solution for Equation (2.107) is a plane bending wave, represented by its complex velocity amplitude

$$\underline{v}_s(x,y) = \hat{\underline{v}}_{s0}\ e^{-ik_x x}e^{-ik_y y}, \tag{2.109}$$

with complex number $\hat{\underline{v}}_{s0}$ [Cremer et al 2005]. Any harmonic plane bending wave solves the bending wave equation for

$$(k_x^2 + k_y^2)^2 = k_B^4. \tag{2.110}$$

A full solution for one frequency component is given by the *Fourier* integral in spatial

$$\underline{v}_s(x,y) = \frac{1}{(2\pi)^2}\int\limits_{-\infty}^{\infty}\int\limits_{-\infty}^{\infty}\hat{\underline{v}}_s(k_x,k_y)\ e^{-ik_x x}e^{-ik_y y}dk_x dk_y \tag{2.111}$$

and wave number domain

$$\hat{\underline{v}}_s(k_x,k_y) = \int\limits_{-\infty}^{\infty} \int\limits_{-\infty}^{\infty} \underline{v}_s(x,y)\ e^{ik_x x}e^{ik_y y}dxdy. \tag{2.112}$$

2.4.3 Sound radiation of infinite plates

The derivation of the radiation of infinite plates will be shown for a one-dimensional plane wave traveling in positive $x-$direction ($k_y = 0$, $k_x = k_B$). Thus, the out-of-plane velocity $\underline{v}_s(x)$ is given by

$$\underline{v}_s(x) = \hat{v}_{s0}\ e^{-ik_B x}. \tag{2.113}$$

As a boundary condition, the component of the airborne sound velocity at $z = 0$ perpendicular to the plate must equal the structure-borne sound velocity on the plate

$$\underline{v}_z(x,z=0) = \underline{v}_s(x). \tag{2.114}$$

Using Equation (2.90), the airborne sound velocity at the surface of the plate $\underline{v}_z(x,z=0)$ can be expressed in terms of the sound pressure

$$\underline{v}_z(x,z=0) = -\frac{1}{i\omega\rho_A}\frac{\partial \underline{p}(x,z)}{\partial z}\bigg|_{z=0} = \frac{k_z\,\hat{p}_0}{\omega\rho_A}\ e^{-ik_B x}. \tag{2.115}$$

Inserted into Equation (2.114) yields

$$\hat{p}_0 = \rho_A c_A \frac{k_A}{k_z}\hat{v}_{s0}. \tag{2.116}$$

For the sound pressure in front of the plate, the following approach is made [Cremer et al 2005]:

$$\underline{p}(x,z) = \hat{p}_0\ e^{-ik_B x}e^{-ik_z z}. \tag{2.117}$$

This approach must solve the *Helmholtz* equation (2.102), which is fulfilled according to Equation (2.104) for

$$k_z^2 = k_A^2 - k_B^2. \tag{2.118}$$

Thus, the sound pressure in the half space in front of the plate can be derived by inserting Equations (2.118) and (2.116) into (2.117)

$$\underline{p}(x,z) = \rho_A c_A \frac{k_A}{\sqrt{k_A^2 - k_B^2}} \ \hat{v}_{s0} \ e^{-ik_B x} e^{-i\sqrt{k_A^2 - k_B^2}z}. \tag{2.119}$$

The radiation characteristics depend on the wavenumber of air k_A and the bending wavenumber of the plate. For infinite systems three cases can be distinguished:

- For $k_B < k_A$ the exponent of $e^{-ik_z z}$ in Equation (2.119) is real, which means that pressure and velocity are in phase. A far field is generated, i.e. an obliquely propagating plane wave is radiated (see Fig. 2.12). The angle of radiation into direction $\bar{x}$ is caused by the coupling of the wavelengths of plate vibration and airborne sound. The smaller the bending wavelength, the closer it gets to the wavelength of the air and the amount of radiation increases. At the same time the angle of radiation ϑ is tending to 90°. It is defined as: $\sin \vartheta = \frac{\lambda_A}{\lambda_B}$.
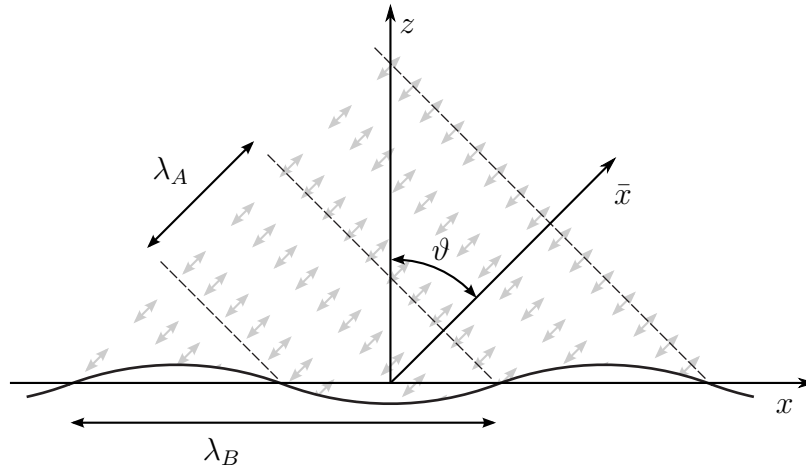
Figure 2.12: Far field (similar to Cremer et al [2005])

- For the singular case $k_B = k_A$, the wavenumbers and wavelengths of plate and air are the same for every specific frequency. The angle of radiation ϑ is 90°. k_z is tending to zero, which leads according to Equation (2.119) to a theoretically infinite amount of sound radiation. In practice, damping effects lead to a finite value. This is also called a grazing radiation.

- For $k_B > k_A$ the sound pressure to sound velocity relation (see Eq. (2.119)) is imaginary. This means that there is no time averaged radiated sound power. The sound

field fades exponentially with the distance to the plate (near field). In this region the in-plane components of the sound velocity are 90° out of phase to the components in z-direction. The air particles move along elliptic paths (see Fig. 2.13). Air particles in front of a vibrating radiator evade from a wave peak to a nearby trough and thus the air is not compressed. This effect is also called acoustical short circuit [Cremer et al 2005].
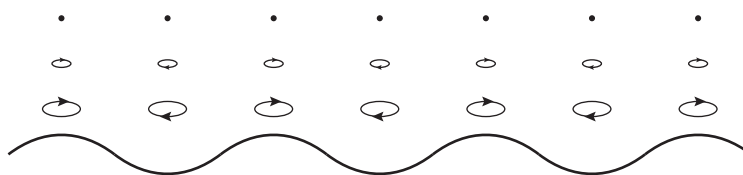
Figure 2.13: Near field [Cremer et al 2005]

The bending wavenumber k_B is often characterized by the bending wave speed $c_B = \frac{\omega}{k_B}$. For a free propagation on a plate, it depends on the frequency. The coincidence or critical frequency f_c describes the specific frequency, where the propagation speed on the plate equals the speed of sound in the air, respectively when $k_A = k_B$. It describes the transition from far to near field.

The radiation of a plate with arbitrary structure-borne velocity pattern $\underline{v}_s(x,y)$ can be described by expanding Equation (2.119) for a two-dimensional case as a superposition of plane wave solutions for every value of k_x and k_y. For one frequency component, the sound pressure can be derived by the *Fourier* integral

$$\underline{p}(x,y,z) = \frac{\rho_A c_A}{(2\pi)^2} \int\limits_{-\infty}^{\infty} \int\limits_{-\infty}^{\infty} \frac{k_A}{\sqrt{k_A^2 - k_x^2 - k_y^2}} \, \hat{\underline{v}}_s(k_x,k_y) \, e^{-ik_x x} e^{-ik_y y} e^{-i\sqrt{k_A^2 - k_x^2 - k_y^2}z} dk_x dk_y. \quad (2.120)$$

2.4.4 Finite plates

Expressions (2.112) and (2.120) can also be used to describe arbitrary plane radiators inside a rigid baffle, for which the structure-borne velocity outside the radiating finite surface is set to $v_s(x,y,t) = 0$ [Cremer et al 2005].

The effect of time limitation of harmonic signals on the frequency spectrum in the *Fourier* transformed domain has already been derived in Section 2.3.1.2. The observations can equivalently be applied to problems in the spatial domain. Caused by the limited dimensions, side lobes appear due to a convolution with a cardinal sine function. A one-dimensional example of an finite plate vibrating below the coincidence frequency is shown in Figure 2.14 for the wavenumber domain (compare Figure 2.7). The side lobes affect the radiation characteristics. They lead to a far field radiation ($k_B < k_A$) even in case of vibration below the coincidence frequency.
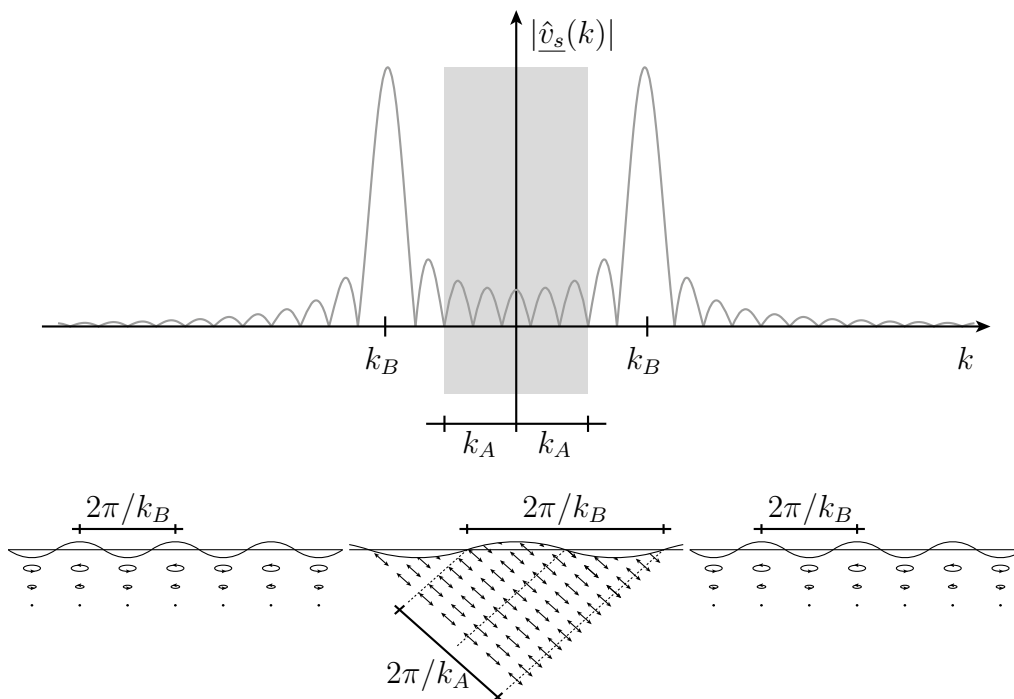
Figure 2.14: Radiation conditions in spatial and wave number domain

Equivalent observations can be made for the two-dimensional case. A numerical example of an isotropic square plate vibrating in its (5,5) eigenmode is depicted in Figure 2.15 for spatial and wavenumber domain. In this case, the distance of the peaks represents the bending wave number k_B. It can be shown, that the peaks of every vibration pattern of the plate lie on a ideal circle with center at the origin and a radius k_B (white empty circle). The radiation conditions ($k_B < k_A$) are marked with an solid white circle of radius k_A. This behavior is described by means of a measurement example in Section 4.1.

spatial domain

wave number domain
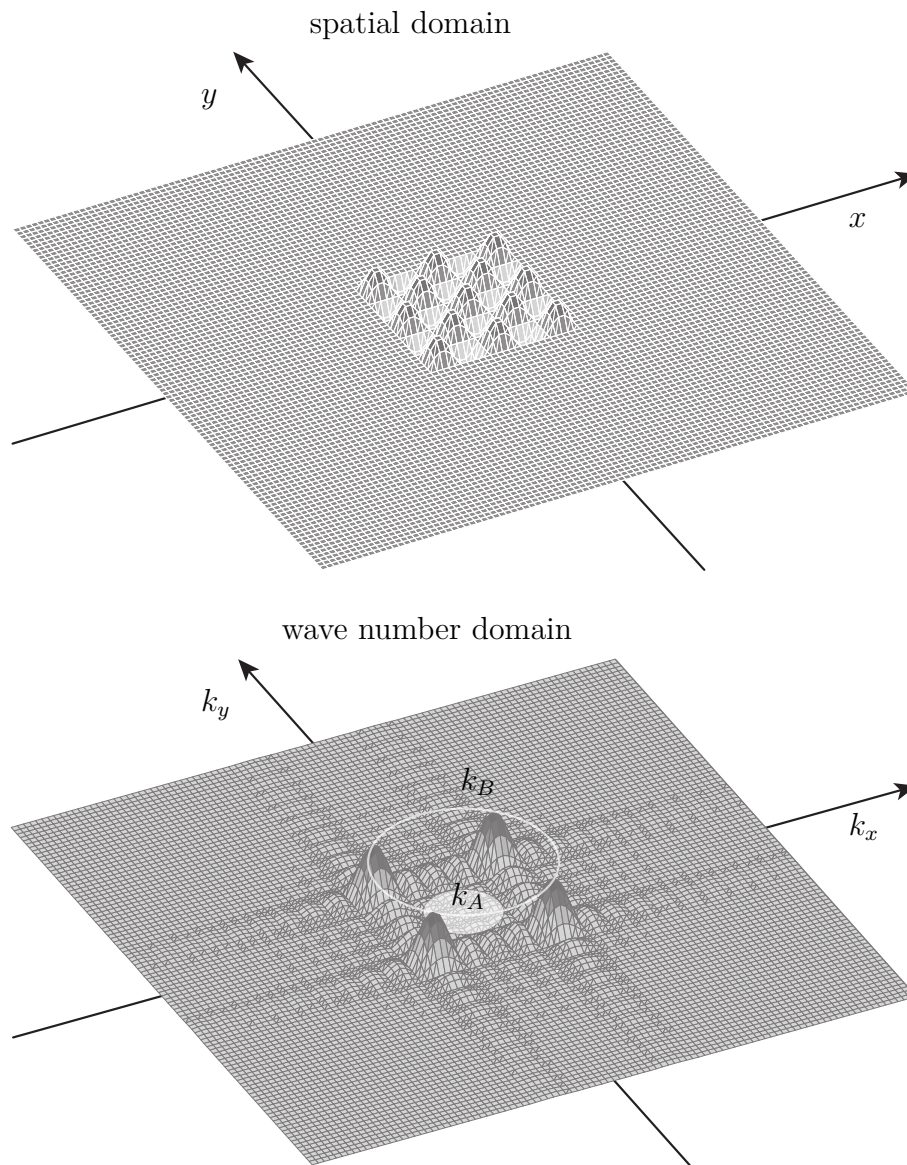
Figure 2.15: Example illustrating the radiation conditions below the coincidence frequency

2.4.5 Sound power, sound intensity and radiation efficiency

The product of the sound velocity vector and the sound pressure scalar results in the sound intensity vector $\mathbf{I} = p\,\mathbf{v}$. It represents the sound power per unit area, and thus the sound energy flow within a volume. It is also called acoustic intensity. and can be used to indicate the energy flow's direction and to locate the sound source [Brüel & Kjaer 1993] [Müller 2010b]. The sound power emitted from a source can be derived via an integration over the

sound intensity of an enveloping surface.

$$P = \int\limits_{(\mathbf{S})} p \, \mathbf{v} \, d\mathbf{S} = \int\limits_{(\mathbf{S})} \mathbf{I} \, d\mathbf{S} \tag{2.121}$$

The length of the surface vector $\mathbf{S}$ corresponds to the total area and is directing perpendicular to the surface. In case of a sound velocity parallel to the surface according to the scalar product $\mathbf{v} \cdot d\mathbf{S} = |\mathbf{v}| \cdot |d\mathbf{S}| \cdot \cos\alpha$ no sound power is transmitted (α: angle between sound velocity vector $\mathbf{v}$ and surface vector $\mathbf{S}$). Neglecting damping effects in the propagation the resulting sound power is independent from the form of the enveloping surface and its distance from the source.

2.4.5.1 Sound intensity of plates for purely harmonic oscillations

When steady sound fields are considered, the sound intensity perpendicular to a vibrating plate can be averaged over a time T. The time averaged characteristics are indicated by a bar. In case of purely harmonic oscillations, it can be derived for one frequency component by substituting the field variables for the sound pressure at the surface $p = p(x,y,z = 0,t) = p_s(x,y,t)$ and the structure-borne sound velocity $v_s = v_s(x,y,t)$ by their complex amplitudes $\underline{p} = \underline{p}(x,y,z = 0) = \underline{p}_s(x,y)$ and $\underline{v}_s = \underline{v}_s(x,y)$ and corresponding phase information ϕ_p and ϕ_v according to Equation (2.95). This substitution yields (arguments are neglected in the following equations):

$$\begin{aligned}
\bar{I} &= \frac{1}{T} \int\limits_0^T p_s \, v_s \, dt \\
&= \frac{1}{T} \int\limits_0^T \Re\left\{\underline{p}_s \, e^{i\omega t}\right\} \Re\left\{\underline{v}_s \, e^{i\omega t}\right\} \, dt \\
&= \frac{1}{T} \int\limits_0^T \Re\left\{\left|\underline{p}_s\right| e^{i\omega t} e^{i\phi_p}\right\} \Re\left\{\left|\underline{v}_s\right| e^{i\omega t} e^{i\phi_v}\right\} \, dt \\
&= \frac{1}{T} \int\limits_0^T \left|\underline{p}_s\right| \left|\underline{v}_s\right| \cos\left(\omega t + \phi_p\right) \cos\left(\omega t + \phi_v\right) \, dt \\
&= \frac{1}{T} \int\limits_0^T \left|\underline{p}_s\right| \left|\underline{v}_s\right| \frac{1}{2} \left[\cos\left(2\omega t + \phi_p + \phi_v\right) + \cos\left(\phi_p - \phi_v\right)\right] \, dt.
\end{aligned} \tag{2.122}$$

This equation consists of a term multiplied by $\cos\left(2\omega t + \phi_p + \phi_v\right)$, that averages out to zero, and a time-independent term. Thus, Equation (2.122) can be further simplified, leading to

$$
\begin{aligned}
\bar{I} &= \frac{1}{2}\left|\underline{p_s}\right|\left|\underline{v_s}\right|\cos\left(\phi_p - \phi_s\right) \\
&= \frac{1}{2}\Re\left\{\left|\underline{p_s}\right|e^{i\phi_p}\right\}\Re\left\{\left|\underline{v_s}\right|e^{-i\phi_s}\right\} \\
&= \frac{1}{2}\Re\left\{\underline{p_s}\;\underline{v_s}^*\right\}.
\end{aligned}
\tag{2.123}
$$

2.4.5.2 Radiated sound power of finite plates

For a finite plate inside an infinite rigid baffle, the sound power can be calculated by an integration of Equation (2.123) over the infinite $x-y$ plane. Thus, the sound power radiated by a plate for one frequency component in case of purely harmonic oscillations yields:

$$
\bar{P} = \frac{1}{2}\Re\left\{\int\limits_{-\infty}^{+\infty}\int\limits_{-\infty}^{+\infty}\underline{p_s}(x,y)\;\underline{v_s}(x,y)^*\;dxdy\right\}.
\tag{2.124}
$$

Applying the generalized *Rayleigh-Parseval* theorem for Harmonic Analysis (see Eq. (2.3.1.1))

$$
\int\limits_{-\infty}^{+\infty}\int\limits_{-\infty}^{+\infty}\underline{p_s}(x,y)\;\underline{v_s}(x,y)^*\;dxdy = \frac{1}{(2\pi)^2}\int\limits_{-\infty}^{+\infty}\int\limits_{-\infty}^{+\infty}\hat{\underline{p}}_s(k_x,k_y)\;\hat{\underline{v}}_s(k_x,k_y)^*\;dk_xdk_y,
\tag{2.125}
$$

Equation (2.124) can be rewritten in terms of the wavenumber spectra

$$
\bar{P} = \frac{1}{8\pi^2}\Re\left\{\int\limits_{-\infty}^{+\infty}\int\limits_{-\infty}^{+\infty}\hat{\underline{p}}_s(k_x,k_y)\;\hat{\underline{v}}_s(k_x,k_y)^*\;dk_xdk_y\right\}.
\tag{2.126}
$$

The spectral components of the sound pressure at the plate's surface $\hat{\underline{p}}_s(k_x,k_y)$ can be extracted from Equation (2.120) for $z = 0$:

$$
\hat{\underline{p}}_s(k_x,k_y) = \rho_A c_A \frac{k_A}{\sqrt{k_A^2 - k_x^2 - k_y^2}}\;\hat{\underline{v}}_s(k_x,k_y)
\tag{2.127}
$$

Inserting Equation (2.127) into Equation (2.126) yields:

$$
\bar{P} = \frac{\rho_A c_A}{8\pi^2}\Re\left\{\int\limits_{-\infty}^{+\infty}\int\limits_{-\infty}^{+\infty}\frac{k_A}{\sqrt{k_A^2 - k_x^2 - k_y^2}}\;\left|\hat{\underline{v}}_s(k_x,k_y)\right|^2\;dk_xdk_y\right\}.
\tag{2.128}
$$

Thus, the radiated sound power can be described by the spectral components of the structure-borne sound velocity and a wave number dependent kernel $K = \frac{k_A}{\sqrt{k_A^2 - k_x^2 - k_y^2}}$. The underline indicator for complex quantities, the bar for time averaged quantities and the subscript s for structure-borne will be omitted in the following, when misunderstanding can be excluded.

2.4.5.3 Radiation efficiency

According to Cremer et al [2005] the radiation efficiency σ describes the radiated sound power of a given structure in relation to the sound power of a large in phase vibrating plane surface (piston) of the same size and mean vibrational velocity.

$$\sigma = \frac{P}{\rho_A c_A S |\overline{v^2}|} \tag{2.129}$$

P denotes the radiated sound power of a structure with a surface area S, which is described in Section 2.4.5. $\rho_A \cdot c_A$ equals the air's impedance and $|v^2|$ represents the spatial averaged effective square velocity of the radiating surface. The denominator

$$P_{eff} = \rho_A c_A S |\overline{v^2}| \tag{2.130}$$

is also referred to as Effective Radiated Power (ERP).

Applying the *Rayleigh-Parseval* theorem (see Eq. (2.66)) for the two-dimensional case

$$P_{eff} = \frac{1}{2} \rho_A c_A \int\limits_{-\infty}^{+\infty} \int\limits_{-\infty}^{+\infty} |v(x,y)|^2 \mathrm{d}x \mathrm{d}y = \frac{1}{2} \frac{\rho_A c_A}{4\pi^2} \int\limits_{-\infty}^{+\infty} \int\limits_{-\infty}^{+\infty} |\hat{v}(k_x,k_y)|^2 \mathrm{d}k_x \mathrm{d}k_y \tag{2.131}$$

the radiation efficiency can be computed via integration in the wave number domain

$$\sigma = \frac{\Re \left\{ \int\limits_{-\infty}^{+\infty} \int\limits_{-\infty}^{+\infty} \frac{k_A}{\sqrt{k_A^2 - k_x^2 - k_x^2}} |\hat{v}(k_x, k_y)|^2 \mathrm{d}k_x \mathrm{d}k_y \right\}}{\int\limits_{-\infty}^{+\infty} \int\limits_{-\infty}^{+\infty} |\hat{v}(k_x, k_y)|^2 \mathrm{d}k_x \mathrm{d}k_y}. \tag{2.132}$$

2.5 Modal Analysis

For the calibration of the numerical models in Section 4.2, eigenmodes of the testing structure as well as the numerical model shall be compared. Eigenmodes of an FE-model can

be computed using modal analysis. This section deals with the theoretical basics of an undamped Modal Analysis [Stelzmann et al 2008] [Müller 2011].

The FE method reduces a continuous system's infinite number of Degrees-of-Freedom (DOFs) to a finite number of DOFs of the element nodes of the FE model. This will be explained in detail for an 8-node 3D volume element in the following. For this kind of element, every node has three translational DOFs, i.e., $3 \cdot 8 = 24$ DOFs in total, that can be combined in a vector $\mathbf{u_e}(t)$. The displacements of the node's DOFs are linked to the displacement field of the element via form functions. Those form functions describe the deformation of the element for occurring nodal displacements. They have to be chosen in order to approximate the continuous system as good as possible (indicated by a bar). The matrix $\mathbf{N}(x,y,z)$ contains all form functions. Thus, the displacement field of the element can be expressed as [Stelzmann et al 2008]:

$$\overline{\mathbf{u}}(x,y,z,t) = \mathbf{N}(x,y,z)\mathbf{u_e}(t) \tag{2.133}$$

Derivations along the local coordinates of the displacement field lead to the strain field of the element. Derivations of the form functions $\mathbf{N}$ are indicated by matrix $\mathbf{B}$. Thus, the strains can be obtained by:

$$\boldsymbol{\varepsilon} = \mathbf{B} \cdot \mathbf{u_e} \tag{2.134}$$

Generally, the same form functions are used for displacements and accelerations. Thus, the *D'Alembert* force results in [Müller 2011]:

$$\mathbf{p_i}(x,y,z,t) = -\rho\mathbf{N}(x,y,z)\mathbf{u_e}^{\bullet\bullet}(t) \tag{2.135}$$

with density ρ. The finite element's equation of motion will be derived using the virtual work principal [Müller 2011]. The internal virtual work is:

$$\delta W_i = -\int\limits_{V_e} \delta\boldsymbol{\varepsilon} \cdot \boldsymbol{\sigma}\,\mathrm{d}v = -\int\limits_{V_e} \delta\mathbf{u_e}^T\mathbf{B}^T\underbrace{\mathbf{D}\mathbf{B}\mathbf{u_e}}_{\boldsymbol{\sigma}}\,\mathrm{d}v \tag{2.136}$$

where $\mathbf{D}$ is the material matrix and V_e is the volume of the element.

For the external virtual work, the *D'Alembert* force is taken into account. Due to the goal to find the eigenfrequencies and mode shapes of the system, no other external forces are

applied.

$$\delta W_e = \int\limits_{V_e} \underbrace{\delta\overline{\mathbf{u}}}_{\delta\mathbf{u_e}^T\mathbf{N}^T}\ \mathbf{p_i}\,\mathrm{d}v \tag{2.137}$$

The total work results in:

$$\delta W = \delta W_i + \delta W_e = \delta\mathbf{u_e}^T\left\{-\underbrace{\int\limits_{V_e}\mathbf{B}^T\mathbf{D}\mathbf{B}\,\mathrm{d}v}_{\mathbf{K_e}}\ \mathbf{u_e} - \underbrace{\int\limits_{V_e}\varrho\mathbf{N}^T\mathbf{N}\,\mathrm{d}v}_{\mathbf{M_e}}\ \mathbf{u_e}^{\bullet\bullet}\right\} = 0 \tag{2.138}$$

Equation (2.138) can only be equal to zero, when the expression in curly brackets is equal to zero. This leads to the homogeneous differential equation of motion:

$$\mathbf{M_e}\,\mathbf{u_e}^{\bullet\bullet} + \mathbf{K_e}\,\mathbf{u_e} = 0. \tag{2.139}$$

where $\mathbf{K_e}$ is the stiffness matrix and $\mathbf{M_e}$ is the mass matrix of the element.

To obtain the equations of motion for the total system, all DOFs of the system are combined in the displacement vector $\mathbf{u}$. The stiffness and mass matrices of the element are assembled into the corresponding matrices of the total system according to the DOFs in the vector $\mathbf{u}$.

$$\mathbf{M}\,\mathbf{u}^{\bullet\bullet} + \mathbf{K}\,\mathbf{u} = 0 \tag{2.140}$$

The product approach

$$\mathbf{u} = \mathbf{\Phi} \cdot e^{i\omega t} \tag{2.141}$$

for an unknown displacement vector separates the spatial and the time domain. After inserting Equation (2.141) into the differential equation of motion leads to the following homogeneous system of equations. It describes a matrix eigenvalue problem.

$$\left(\mathbf{K} - \omega^2\mathbf{M}\right)\mathbf{\Phi} = 0 \tag{2.142}$$

A non-trivial solution exists only if

$$\det\left(\mathbf{K} - \omega^2\mathbf{M}\right) = 0. \tag{2.143}$$

Equation (2.143) shows a characteristic polynomial of nth order for ω^2 (n = number of DOFs). The zeros of this polynomial (eigenvalues) represent the squared circular eigenfrequencies ω_i. Thus, the eigenfrequencies f_i are

$$f_i = \frac{1}{T_i} = \frac{\omega_i}{2\pi} \tag{2.144}$$

The eigenvectors $\boldsymbol{\Phi}_i$ can be obtained by insertion of the corresponding eigenvalues ω_i^2 into Equation (2.142). They represent the systems eigenmodes or eigenforms. Equation (2.142) describes a set of linear dependent equations, i.e. to obtain the eigenvectors $\boldsymbol{\Phi}_i$ a value for one coordinate must be predefined. Thus, every scaled vector $\alpha \cdot \boldsymbol{\Phi}_i$ is an eigenvector of the differential equation of motion of the system (2.140) [Müller 2011]. It is common to scale the eigenvectors normalized to the mass matrix [Stelzmann et al 2008]:

$$\boldsymbol{\Phi}_i^T \mathbf{M} \boldsymbol{\Phi}_i = 1 \qquad \text{and} \qquad \boldsymbol{\Phi}_i^T \mathbf{K} \boldsymbol{\Phi}_i = \omega_i^2 \tag{2.145}$$

3 Numerical Model Development

The measurement-based investigations of floor constructions performed within the research project "VibWood" are complemented by numerical simulations. Therefore, FE-models are created and calibrated according to the experimental results. Furthermore, adapted numerical evaluation models to describe the vibro-acoustical characteristics are developed. The numerical modeling aims on the performing of parametric studies, which implies the necessity of an intractability between the different models, as well as a completely parametric representation of the models. For the FE simulations, CADFEM's commercial FE software ANSYS® Classic is used. It holds the requirements concerning parametrization and automation due to its program intern design language (Ansys Parametric Design Language (APDL)). For the implementation of the evaluation models, THE MATHWORKS's computer algebra software MATLAB® is used.

3.1 Description of the FE-Analyses

For numerical simulations, the FEM is used. An example of a full FE model is shown in Figure 3.1. A detailed description of the method can be found in the literature for example
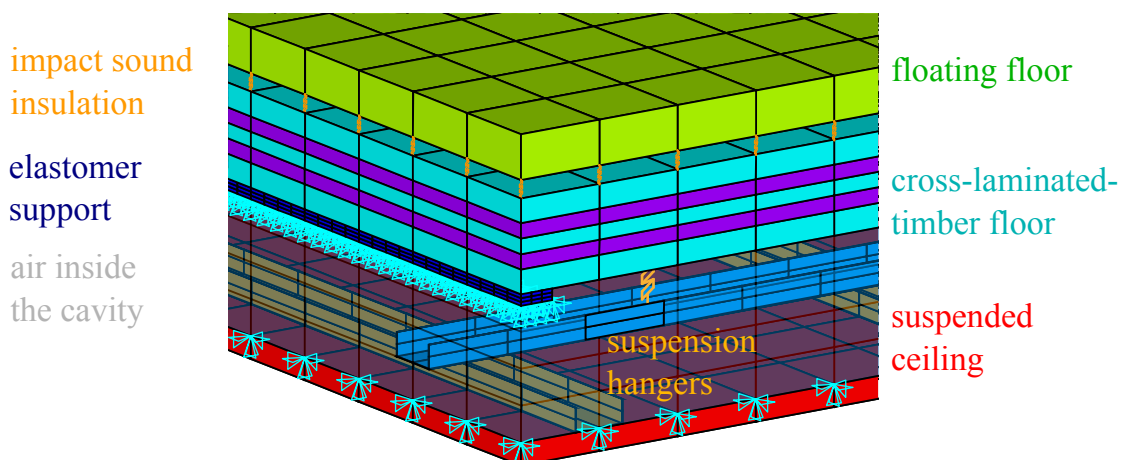

Figure 3.1: Detail of a developed FE model

in Bathe [2002], Müller and Groth [2007] and Stelzmann et al [2008]. In general, such a simulation is performed in three process steps: pre-processing, solution and post-processing. Each of them consists of several sub-steps. Due to the fact that the structural models have to be simulated in a number of construction states, loaded with different kinds of load and evaluated with several analysis types, a modular approach for the programming is pursued, that at the same time allows parametrization and automation.

3.1.1 Simulation process

Figure 3.2 gives a sketch of the Input-Process-Output (IPO) structure of the dynamic analyses. The individual process steps are described as follows:
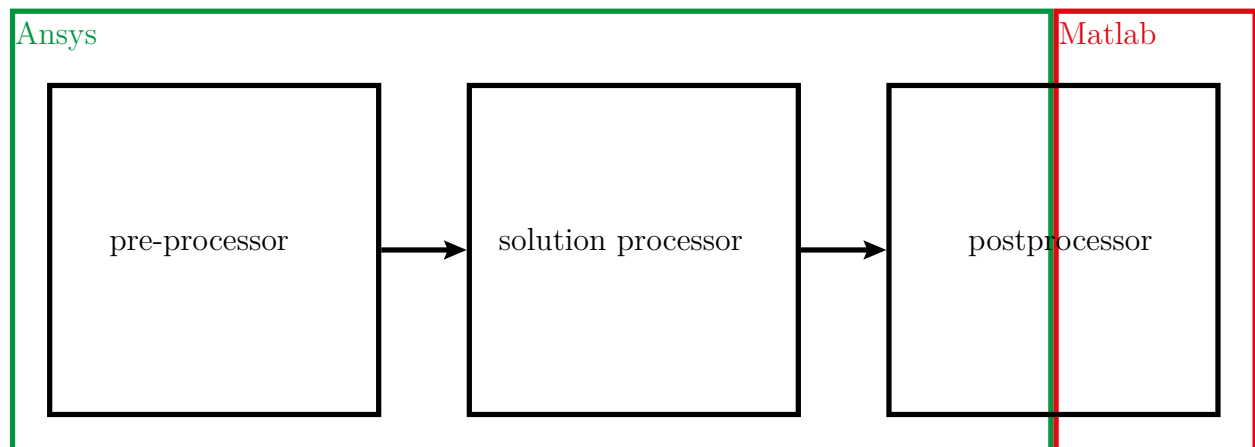

Figure 3.2: IPO model for FE-simulations

3.1.1.1 Pre-processor

In the first step, the following sub-steps are performed:

- System geometry development

- Element type and material property application

- FE-mesh generation

- Boundary conditions application

To achieve full parametrization, an import of the system geometry from an external Computer-Aided Design (CAD) software is not feasible. The system geometries are modeled in APDL as well. A brief description of the applied element types is given in Appendix A.

3.1.1.2 Solution processor

This process step contains the following:

- Load application

- Choice of analysis type and analysis options

    ○ Modal Analysis

    ○ Harmonic Frequency Analysis

    ○ Transient Analysis

- Definition of the parameters of the analysis (depending on the analysis type)

- Solution of the systems of equation

In this thesis, different types of dynamic analyses will be performed. Eigenfrequencies and eigenmodes, that are used for the characterization of the models, are obtained by Modal Analyses. For the description of the vibrational behavior of the numerical models, Harmonic Frequency Analyses are performed. By means of those analyses, frequency response functions at all relevant position, in a predefined frequency range, for a specific loading are obtained. To reduce the computational effort for this type of analysis, a modal superposition is carried out. In case this is not possible, e.g. if elements with unsymmetrical matrices are used (Section 3.2.6), a full solution of the system's matrices has to be performed. For the simulation of a walking pedestrian, transient loading is applied to the structural model. Its time dependent load function is adapted to measured data (Section 3.4.3). For this, transient analyses are carried out, based on *Newmark*-Beta time step integration.

3.1.1.3 Post-processor

In the last process step, the results of the calculations are evaluated. With Ansys® Classic's implemented tools, it is possible to evaluate single analyses graphically, to print results into tables or to export data for further investigations (Section 3.6). A calculation of the radiated sound power is not implemented. To cope with that issue, a semi-analytical evaluation model is implemented in Matlab®, based on the frequency response functions of the velocities of the structural models (Section 3.7.1). For automation, a Fortran-based interface is implemented into the APDL-code of the simulation, that exports the velocity data to Matlab®.
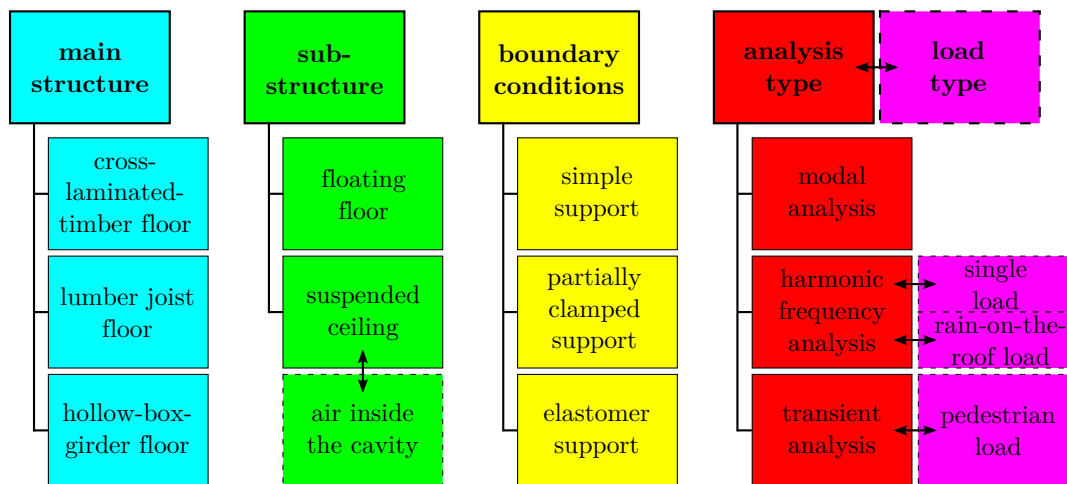
Figure 3.3: Modular concept

3.1.2 Modular design

A classical approach, when developing an FE simulation using APDL would be, to program a single input file, containing all relevant process steps. Since an automated parametric study of varying structures, with different load configurations is intended, a modular approach is established. The structural model is divided into modules for main structure, substructures and boundary conditions. Further modules for the dynamic analyses and applied loadings are developed. The modular concept is depicted in Figure 3.3.

Thus, the different construction states and the intended analyses can be realized by combining the appropriate modules. The simulation process is sketched in Figure 3.4. It is controlled by a main input file. The modules for the structural model contain every process step for the pre-processor. Analysis modules are more complex. For example, a Harmonic Frequency Analysis, using modal superposition, needs a preliminary Modal Analysis. Depending on the analysis type, varying load configurations are applied, controlled by the analysis module (no load needs to be applied in case of a Modal Analysis). When averaging of different loads is intended (e.g. for ROTR excitation), a loop inside the module is needed containing load application, solution process and post-processing of the results (via an implemented interface).

The intended parametric survey is controlled by a MATLAB® code. The interactivity between the two softwares is established by sub-modules, that contain the parameters of each appropriate main module and their specific values. These sub-modules are accessible by the MATLAB® code.
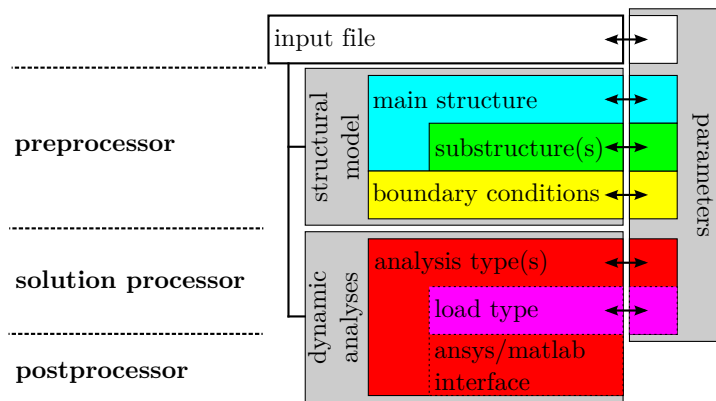
Figure 3.4: Modular simulation process

As an advantage of this modular approach, a change of the code of one module affects all simulations, which increases the robustness, especially in the development phase. Also, the comparability of different simulated construction states is enhanced. An extension of the considered structural elements for further research is easily possible by implementing additional modules. These advantages come with increased requirements concerning the compatibility of the different modules. The separated parameter definition in sub-modules increases the robustness of the parametric studies.

3.1.3 Parametric representation

To ensure the highest possible flexibility of FE-models, a full parametric representation has been applied. Special subscripts are used in the following sections to describe the parameters (e.g. (spr) indicates a parameter for the material spruce) and whether the values of the parameters are measured (m), resulting from a model-updating (mu) or have been taken from literature (l). The number of significant digits of each parameter is varying, depending on the source. Measured and model-updated parameters are given in a more detailed manner. Three types of parameters can be identified as follows.

3.1.3.1 Geometric parameters

These parameters refer to the testing structure, as the data gained experimentally is supposed to be compared to the results of the simulation. They can be subdivided into modular parameters (e.g. joist width) that only have an impact on the specific module geometry and inter-modular parameters (e.g. length), which control the geometry of the total FE-model.

3.1.3.2 Material parameters

The number of material parameters depends on the individual material model and FE-type. For homogeneous components, the parameter values for the used material can be found in standards or in case of a substitute model can be derived from them. Another possibility is, to use values determined by preliminary experiments (Section 4.2).

3.1.3.3 Analysis parameters

These parameters define the discretization of the model. They have an influence on the accuracy and the computational effort of the simulation. In general, the more detailed the analysis parameters, the more accurate the models will be. At the same time the computational effort increases. They are as follows:

- Element size

- Number of modes to be calculated within a Modal Analysis

- Frequency range and frequency step size within an Harmonic Frequency Analysis

- Duration and time step size within a Transient Analysis

3.2 Structural Models

The FE-models of the structure are generated in the pre-processor. They consist of combined modules of the three investigated ceiling constructions as follows:

- Cross-Laminated Timber (CLT)

- Lumber Joist (LJ)

- Hollow Box Girder (HBG)

Additional components include the following:

- Floating Floor (FLF)

- Suspended Ceiling (SC)

and the modules for the boundary conditions. Figure 3.5 shows a sketch of the pre-processor.
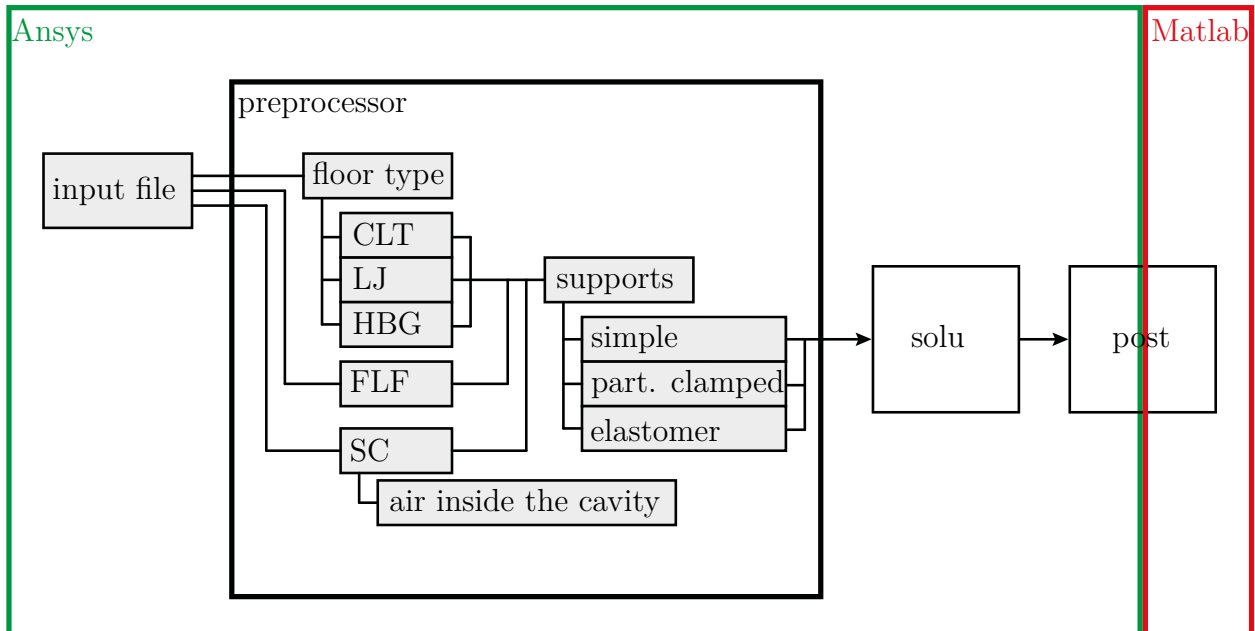

Figure 3.5: Modular structure of the pre-processor

The following section gives a description of the individual modules.

3.2.1 General predefinitions

In this section parameters and assumptions, that have an impact on all structural models will be introduced.

3.2.1.1 Idealization

The static system of the floor constructions considered can be idealized by line-supported plane plates of a rectangular geometry. Depending on the support conditions, the plates are modeled as one-way slabs with two-sided bearing or as two-way slabs with all-sides bearing. Every ceiling construction has a main load-bearing direction, characterized by a homogeneous longitudinal stiffness contribution. Perpendicular to the load-bearing direction, the stiffness is much lower and distributed inhomogeneous (e.g. caused by the joists of an LJ floor). The global coordinate system is chosen, so that the global x-axis points into main load-bearing direction and the global y-axis points into perpendicular load-bearing direction.

3.2.1.2 Discretization

The in-plane element size is, according to the convergence study in Section 4.2.1, set to $e_{size} = 0.1$ m. A good accuracy of the results is shown for this element size. In none of the models, the lower limit of the aspect ratio $1 : 10$ recommended in Müller and Groth [2007] is exceeded.

3.2.1.3 Parameters

In addition to the element size e_{size} the inter-modular parameters consist of the dimensions length l and width w . They are defined in the input file. For the modeling of the testing structures, the dimensions of the floors are predefined by the size of the testing lab in Rosenheim (see Tab. 3.1).

Table 3.1: Inter-modular parameter

Parameter	Variables	Amount	Unit
Length	l	5.50	m
Total width	w	5.50	m
Element size	e_{size}	0.10	m

3.2.2 Cross-laminated timber CLT floor

The CLT floors are formed by a number of slabs that are line-coupled longitudinally. The individual slabs have an multi-layer design consisting of cross laminated end-joint spruce boards. Only in vertical direction these boards are laminated, whereas they are but-joined in horizontal direction (see Fig. 3.6). The investigated CLT floors are fabricated by *Züblin Merk*. Their portfolio comprises different types of CLT of varying thickness. Their number of layers vary from three to nine. Spruce boards with thicknesses of 0.017 m, 0.027 m and 0.033 m are used. The individual slabs are coupled by embedded and LVL boards (see Fig. 3.7).

Figure 3.6: CLT cross-section

Figure 3.7: LVL board

3.2.2.1 Idealization

For the modeling of this structure, each layer of boards is modeled individually. The gaps and relief grooves in between and inside the broads are neglected as well as the individual annular rings (according to Section 2.1.5). All boards of the same layer will be smeared into a single volume, which introduces some major uncertainties. Between the layers, a rigid coupling is applied, the flexibility of the glue is neglected as well. For the coupling of the individual slabs, the laminated veneer lumber boards are substituted by elastic springs (see Figs. 3.9 and 3.10). Uncertainties due to the idealization will be compensated by an adaptation of the material parameters.

3.2.2.2 Discretization

The volumes are modeled by 3D-volume elements. The cubic form of the volumes allows it to generate a structured mesh with hexagonal elements [Müller and Groth 2007]. A number of different 3D volume elements are implemented in Ansys®. They can be distinguished by the number of nodes per element and by the polynomial degree of the used form functions. An evaluation showed that the 8-node SOLID185-element produces adequate results. Furthermore, a convergence study is performed, as shown in Section 4.2.1, which approves, that a single element per layer in vertical direction gives results of sufficient accuracy. Because of the varying width of the individual slabs, the element size in horizontal direction is modified in order to obtain a homogeneous distribution. The value predefined in Section 3.2.1 is taken as an upper limit. To ensure a later combination, the mesh geometry of substructure (e.g., FLF) has to be adapted in the same way. Because the volumes of the layers share the same boundary area rigid coupling of the layers is automatically generated by coincident nodes at the interface. A detail of the FE-Model is depicted in Figure 3.8.
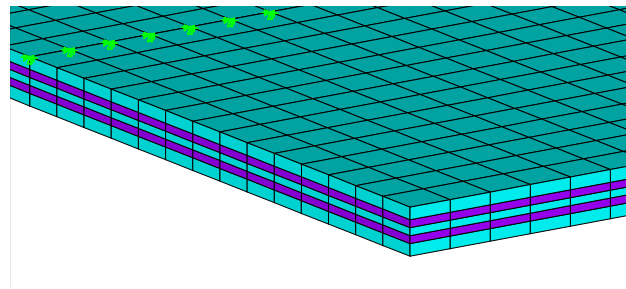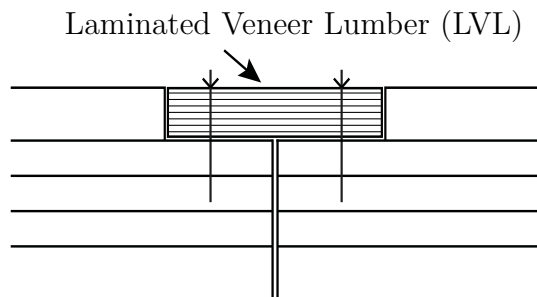
Figure 3.8: Detail of the CLT floor; FE-model

Figure 3.9: Sketch of the LVL board coupling
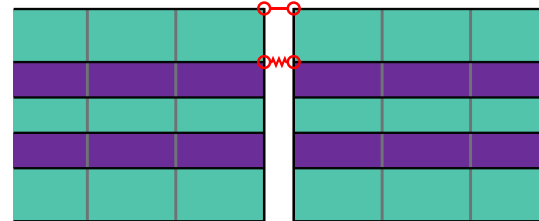

Figure 3.10: Detail of the coupling; FE-model

For the modeling of the connection between two neighboring slabs, the top layer of each slab is coupled. The volume elements lack rotational DOFs. Hence, a simple solution by using one-dimensional torsional spring elements is not possible. Only the translational DOFs can be coupled. Thus, the nodes at the interface are coupled in two ways. For the top nodes per slab all DOFs are coupled whereas for the coupling of the lower nodes of the top layer 1D-spring elements in global y-direction are applied. Thus, a connection is established with an rotational stiffness depending on the stiffness of the spring element. The COMBIN14-element in ANSYS® matches these requirements.

3.2.2.3 Parameters

The layer design can be defined by the parameter CLT-type t_{CLT}. It represents the total thickness of a specific slab which is in case of the fabricator *Züblin Merk* unique for every CLT-type. The number of layers and their individual thicknesses can be taken from the fabricator's data sheet [Metsä Wood Merk GmbH 2012]. In a first step, based on this data, a single slab is generated. Its width corresponds to the total width of the floor w

divided by the number of slabs that are used n. Later, this slab is copied n-times in y-direction to generate the whole floor. For the five- and six-layered CLT-types Leno105 and Leno162 experimental measurements have been carried out [Kohrmann et al 2014]. To compare measured with simulated data, FE-models of both types are created. The cross-sectional dimensions are listed in Table 3.2.

Table 3.2: Cross-sectional dimensions of CLT-types 105 and 162

| | CLT-type | | | |
| | 105 | | 162 | |
layer	thickness in m	orientation	thickness in m	orientation
1	$2.70 \cdot 10^{-2}$	$\parallel$	$2.70 \cdot 10^{-2}$	$\parallel$
2	$1.70 \cdot 10^{-2}$	$\perp$	$2.70 \cdot 10^{-2}$	$\perp$
3	$2.70 \cdot 10^{-2}$	$\parallel$	$2.70 \cdot 10^{-2}$	$\parallel$
4	$1.70 \cdot 10^{-2}$	$\perp$	$2.70 \cdot 10^{-2}$	$\parallel$
5	$2.70 \cdot 10^{-2}$	$\parallel$	$2.70 \cdot 10^{-2}$	$\perp$
6	—	—	$2.70 \cdot 10^{-2}$	$\parallel$

Table 3.3: Parameters of the CLT-Modul

Parameter	Variable	Value	Unit
Number of slabs	n	4	—
CLT-type	t_{CLT}	105 / 162	—
Density	$\rho_{\mathrm{spr,m}}$	$0.47 \cdot 10^2$	$\frac{\mathrm{kg}}{\mathrm{m}^3}$
Elasticity modulus in x-direction	$E_{\parallel,\mathrm{spr,mu}}$	$1.01 \cdot 10^{10}$	$\frac{\mathrm{N}}{\mathrm{m}^2}$
Elasticity modulus in y-direction	$E_{\perp,\mathrm{spr,mu}}$	$1.37 \cdot 10^8$	$\frac{\mathrm{N}}{\mathrm{m}^2}$
Elasticity modulus in z-direction	$E_{\perp,\mathrm{spr,mu}}$	$1.37 \cdot 10^8$	$\frac{\mathrm{N}}{\mathrm{m}^2}$
Shear modulus in xy-direction	$G_{\parallel\perp,\mathrm{spr,mu}}$	$4.59 \cdot 10^8$	$\frac{\mathrm{N}}{\mathrm{m}^2}$
Shear modulus in yz-direction	$G_{\perp\perp,\mathrm{spr,mu}}$	$7.40 \cdot 10^7$	$\frac{\mathrm{N}}{\mathrm{m}^2}$
Shear modulus in xz-direction	$G_{\parallel\perp,\mathrm{spr,mu}}$	$4.59 \cdot 10^8$	$\frac{\mathrm{N}}{\mathrm{m}^2}$
Poisson ratio in xy-direction	$\nu_{\parallel\perp,\mathrm{spr,mu}}$	$5.00 \cdot 10^{-2}$	—
Poisson ratio in yz-direction	$\nu_{\perp\perp,\mathrm{spr,l}}$	$3.00 \cdot 10^{-1}$	—
Poisson ratio in xz-direction	$\nu_{\parallel\perp,\mathrm{spr,mu}}$	$5.00 \cdot 10^{-2}$	—
Spring stiffness of the linear coupling	$k_{y,\mathrm{lin}}$	$1.00 \cdot 10^1$	$\frac{\mathrm{N}}{\mathrm{m}}$

The CLT floors are made of spruce. As presented in Section 2.1, wood can be described by an orthotropic material model. Due to idealization, the material parameters cannot be taken from the literature, but are derived from experimental data by model-updating, which is described in Section 4.2.2. The density of the used spruce for the CLT floor is obtained

by weighing the individual slabs and averaging the results. Table 3.3 lists the parameters of the CLT-module and their values used for the modeling.

3.2.3 Lumber joist LJ floor

The LJ floor consists of parallel arranged spruce joists designed either as single or double joists (see Fig. 3.11 left). The cross-sectional area of a single joist is given as $0.06 \, \text{m} \times 0.24 \, \text{m}$. Crossbars are installed at the bearings between the ends of the joists to secure their position. The paneling is made of OSBs with a thickness of 19 mm. The individual OSBs measure 2.5 m x 1.25 m. A staggered arrangement is applied with main load bearing direction perpendicular to the direction of the joists (see Fig. 3.11 right). Paneling and joists are connected by screws.

Figure 3.11: Real structure LJ floor

3.2.3.1 Idealization

Single as well as double joists are modeled as a single orthotropic volume with smeared material properties (according to Section 2.1.4). The ends of the joists are fixed in y-direction to secure their position as in the real construction. For the paneling the OSBs are modeled as a single orthotropic plate without gaps. This plate is connected to the volumes of the joists with a rigid contact at the interfaces.

3.2.3.2 Discretization

The joists are modeled with 3D-volume elements and a hexagonal mesh. The 20-node SOLID186-element was chosen. Compared to other types of elements, the SOLID186-
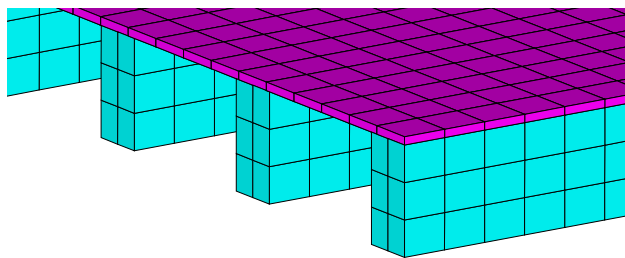
Figure 3.12: FE model of the LJ floor

element showed the best representation of the reality, due to its higher order form functions. An additional advantage is the enhanced connect-ability, due to the additional middle nodes (the hangers' 1D COMBIN14-elements can only be defined between two nodes).

For modeling of the OSBs, four-node SHELL181-elements are used. A grid of evenly distributed rectangular elements is created which is a requirement for the acoustic evaluation model described in Section 3.7.1. However, the positions of the joists don't match this grid and the element of the joists have a higher order. Thus, the connection between the volume elements of joists and the shell elements of the OSB is established by a surface-surface-contact. Therefore, contact pairs are modeled at the interface consisting of eight-node CONTA174-elements for the face of the volume elements and four-node TARGE170-elements for the face of shell elements. A rigid contact is chosen without the possibility of separation. Figure 3.12 shows a detail of the FE model of an LJ floor.

3.2.3.3 Parameters

Geometrical and material parameters of this model are listed in Tables 3.4, 3.5 and 3.6. Two types of LJ floor can be modeled depending on whether they are made of single or double joists. Parameter t_{TBC} defines which type is used, i.e., it determines the width of the joist volume. The testing structure is of type $t_{\text{LJ}} = 2$. It was found that the number of joists in a model, although it is an integer value, is less relevant for a parametric study than the distance between the individual joists d_{joist}. However, the latter is not well suited for parametric studies, because, in most cases, no common values for different total widths

Table 3.4: Geometrical parameters of the LJ floor

Parameter	Variable	Value	Unit
LJ-type	t_{LJ}	2	–
Distance between joists	d_{joist}	$5.00 \cdot 10^{-1}$	m

of the floors w can be found. To solve this problem the number of joists is determined indirectly by d_{joist}. Therefore, w_{tot}, subtracted by the width of one joist's volume, is divided by d_{joist} rounded up and increased by 1. That means that d_{joist} is only an approximation for the resulting distance.

Table 3.5: Material parameters of spruce (LJ floor)

Parameter	Variable	Value	Unit
Density of the joists	$\rho_{\text{spr,l}}$	$5.00 \cdot 10^2$	$\frac{\text{kg}}{\text{m}^3}$
Elasticity modulus in x-direction	$E_{\parallel,\text{spr,l}}$	$1.00 \cdot 10^{10}$	$\frac{\text{N}}{\text{m}^2}$
Elasticity modulus in y-direction	$E_{\perp,\text{spr,l}}$	$4.50 \cdot 10^8$	$\frac{\text{N}}{\text{m}^2}$
Elasticity modulus in z-direction	$E_{\perp,\text{spr,l}}$	$4.50 \cdot 10^8$	$\frac{\text{N}}{\text{m}^2}$
Shear modulus in xy-direction	$G_{\parallel\perp,\text{spr,l}}$	$6.50 \cdot 10^8$	$\frac{\text{N}}{\text{m}^2}$
Shear modulus in xz-direction	$G_{\perp\perp,\text{spr,l}}$	$4.00 \cdot 10^7$	$\frac{\text{N}}{\text{m}^2}$
Shear modulus in yz-direction	$G_{\parallel\perp,\text{spr,l}}$	$6.50 \cdot 10^8$	$\frac{\text{N}}{\text{m}^2}$
Poisson ratio in xy-direction	$\nu_{\parallel\perp,\text{spr,l}}$	$1.40 \cdot 10^{-2}$	—
Poisson ratio in yz-direction	$\nu_{\perp\perp,\text{spr,l}}$	$2.70 \cdot 10^{-1}$	—
Poisson ratio in xz-direction	$\nu_{\parallel\perp,\text{spr,l}}$	$1.40 \cdot 10^{-2}$	—

The LJs are made of spruce, the same wood as used for the boards of the CLT floor. The material parameters for the spruce joists have been taken from the literature [Neuhaus 2009]. As shown in Section 4.2.3.1, they have been validated by measurements. The density was slightly increased. The average values of the measured eigenfrequencies of every used joist have a good correlation to the simulation results of a single joist.

Table 3.6: Material parameters of the OSBs

Parameter	Variable	Value	Unit
Density of the boards	$\rho_{\text{OSB,m}}$	$6.23 \cdot 10^2$	$\frac{\text{kg}}{\text{m}^3}$
Elasticity modulus in x-direction	$E_{x,\text{OSB,m}}$	$6.10 \cdot 10^9$	$\frac{\text{N}}{\text{m}^2}$
Elasticity modulus in y-direction	$E_{y,\text{OSB,m}}$	$2.06 \cdot 10^9$	$\frac{\text{N}}{\text{m}^2}$
Elasticity modulus in z-direction	$E_{z,\text{OSB,l}}$	$2.50 \cdot 10^8$	$\frac{\text{N}}{\text{m}^2}$
Shear modulus in xy-direction	$G_{xy,\text{OSB,l}}$	$1.09 \cdot 10^9$	$\frac{\text{N}}{\text{m}^2}$
Shear modulus in xz-direction	$G_{yz,\text{OSB,l}}$	$6.00 \cdot 10^7$	$\frac{\text{N}}{\text{m}^2}$
Shear modulus in yz-direction	$G_{xz,\text{OSB,l}}$	$1.09 \cdot 10^9$	$\frac{\text{N}}{\text{m}^2}$
Poisson ratio in xy-direction	$\nu_{xy,\text{OSB,l}}$	$2.70 \cdot 10^{-1}$	—
Poisson ratio in yz-direction	$\nu_{yz,\text{OSB,l}}$	$2.50 \cdot 10^{-1}$	—
Poisson ratio in xz-direction	$\nu_{xz,\text{OSB,l}}$	$2.50 \cdot 10^{-1}$	—

The parameter values for OSBs are determined in various ways. Density is obtained by

weighing, and the elasticity moduli in main and perpendicular load-bearing directions have been derived from EMA. Final results have been obtained by averaging over the results of the individual boards. The remaining parameter values that couldn't be measured are taken from the literature [Meistring 2005].

3.2.4 Hollow box girder HBG floor

The investigated HBG floor is - as the CLT floor - designed by single slabs made of spruce that are connected longitudinally. The slabs for different types of HBG floors have a varying cross-sectional design, whereas its width of 0.625 m stays the same for all designs. Every slab is made of several glued laminated timber joists, that are glued on-top of a two layered cross laminated timber plate. The number of layers of the joists vary depending on the chosen HBG-type. For the coupling of neighboring slabs, spruce boards are installed on top of the butt joint between two slabs and fixated with screws on both sides.

3.2.4.1 Idealization

Idealized, the HBG floor can be seen as a combination of CLT floor for the bottom plate with ribs similar to an LJ floor glued on top of it. The cross-section of the ribs is idealized rectangular neglecting the varying widths of the board layers. They are modeled in the same way as the lumber joists in Section 3.2.3 as an homogeneous volume neglecting the different layers and glue joints. The connection between ribs and bottom plate is modeled as an rigid contact at the interface. Coupling between the individual slabs is done in the same way as for the CLT floor in Section 3.2.2. The spruce boards are substituted by elastic springs.
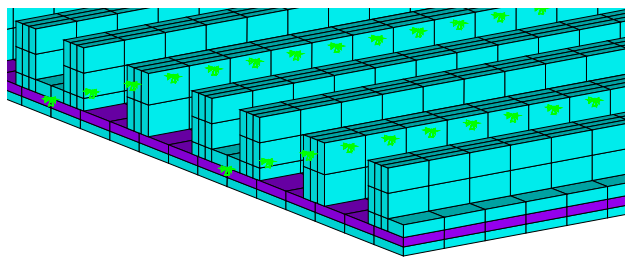

Figure 3.13: FE model of the HBG floor

3.2.4.2 Discretization

The volumes of the ribs and both CLT layers are modeled with 3D volume elements SOLID185 (see Fig. 3.13). The connection between the two structural elements is done by a surface to surface contact, in the same way, as the connection between LJ and OSB in Section 3.2.3. Coupling of two neighboring slabs is performed analogously to the coupling of the CLT floor slabs in Section 3.2.2.

3.2.4.3 Parameters

The different designs of HBG floor can be set by the parameter t_{HBG} with n_s for the number of slabs. The material parameters of spruce are chosen to be the same as in Table 3.5. For the stiffness of the coupling spring, the value of $k_{y,\mathrm{lin}}$ out of Table 3.3 is taken, assuming similar behavior as for CLT floor coupling.

3.2.5 Floating floor FLF

For some of the construction states, an FLF module is added to the main floors. Cement-based Liquid Screed (LS) and Dry Screed (DS) are tested each on top of a layer of impact sound insulation (see Fig. 3.14).

Figure 3.14: FLF (DS) in the testing lab

3.2.5.1 Idealization

The screed layer is modeled as an isotropic plate with different material parameters for each type of screed. The footfall noise insulation layer is simplified by longitudinal spring in out of plan direction coupling the plate of the screed with the main floor.

3.2.5.2 Discretization

The screed plate is discretized by shell elements (SHELL181). The element grid is adapted for every construction to exactly fit the element grid of the main floor beneath. Thus, the impact sound insulation can be modeled by COMBIN14 spring elements that are installed respectively between nodes from the main floor and the screed plate that lie vertically on top of each other. Figure 3.15 shows an example of an FE model with FLF.
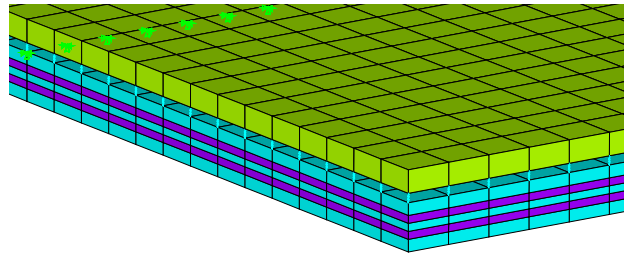
Figure 3.15: FE model of the FLF

3.2.5.3 Parameters

In this section, only the cement-based screed is described. The material parameters are given by the product information sheets of the fabricator KNAUF [Knauf 2014]. For the impact sound insulation, the dynamic stiffness is given in $[s_{\mathrm{ins}}] = \frac{\mathrm{N}}{\mathrm{m}^3}$ and have to be transformed into the spring stiffness $[k_{\mathrm{ins}}] = \frac{\mathrm{N}}{\mathrm{m}}$. Therefore, it has to be divided by the spring's fictional reference area which corresponds to the size of a single shell element $e_{\mathrm{size}} \times e_{\mathrm{size}}$.

Tables 3.7 and 3.8 list the geometric parameters of the FLF-module and the values used for the material parameters of the model.

Parameter	Variable	Value	Unit
Thickness of the screed	d_{scr}	0.05	m
Thickness of the impact sound insulation	d_{ins}	0.02	m

Table 3.8: Material parameters of screed and impact sound insulation

Parameter	Variable	Value	Unit
Density of the screed	$\rho_{\mathrm{scr,l}}$	$2.00 \cdot 10^3$	$\frac{\mathrm{kg}}{\mathrm{m}^3}$
Elasticity modulus of the screed	$E_{x,\mathrm{scr,l}}$	$2.50 \cdot 10^{10}$	$\frac{\mathrm{N}}{\mathrm{m}^2}$
Poisson of the screed	$\nu_{\mathrm{scr,l}}$	$2.00 \cdot 10^{-1}$	—
Dynamic stiffness of impact sound insulation	$s_{\mathrm{ins,l}}$	$2.00 \cdot 10^7$	$\frac{\mathrm{N}}{\mathrm{m}^3}$

3.2.6 Suspended ceiling

A second module to add is the SC. It is designed by two layers of gypsum fiber boards consisting of individual rectangular boards each with a size of 2.50 m x 1.25 m x 0.0125 m. Theses are screwed together crosswise and mounted on a grid of steel U-channels 60/27/06 (see Figure 3.16). This grid-work itself is suspended from the main floor by uni-body molded rubber and steel resilient hangers.

Figure 3.16: Parts of the grid-work of the SC in the testing lab

3.2.6.1 Idealization

The resilient hangers are simplified as single spring-damper-elements that are arranged between main floor and suspension grid. As a side effect compared to a more detailed model in this case different types of suspension systems can be modeled by simply changing the element parameters. The U-channels are idealized as a grid of 1D beams in x- and y-direction.

The two layers of gypsum fiber boards are designed as a single isotropic plate neglecting the individual boards and layers. The resulting overestimation of the bending stiffness is compensated by adapted material parameters (see Section 4.4.1). The individual beams of the suspension grid are connected by direct coupling of the translations at the intersections and allow free rotation. The air cushion between the structures is treated as a cubic volume with interfaces to the upper surface of the plate of gypsum plaster boards and the lowest full scale surface of the main floor. This means that in case of the LJ floor, the volumes of the lumber joists pierce the air volume and overlaying it. Section 4.5 shows that the influence of this simplification on the accuracy of the simulation can be neglected.
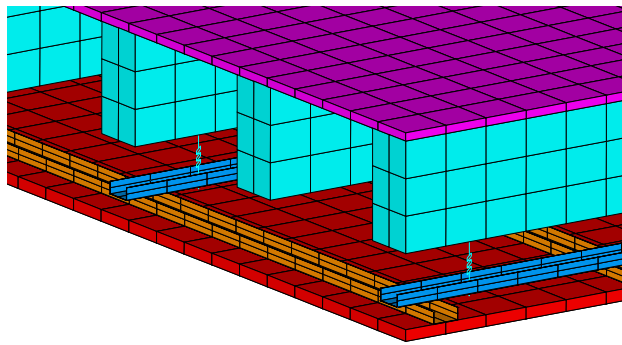
Figure 3.17: FE model of the SC underneath an LJ floor

3.2.6.2 Discretization

Figure 3.17 shows an example of an FE model with SC. The spring-damper-elements of the sound isolation hangers are modeled with COMBIN14-elements and the U-channels with 1D BEAM188-elements. The cross-section of the U-channels is considered as additional parameters for the element. The plates are modeled as shell elements of type SHELL181and the volume of the air cushion is discretized by hexahedral acoustical fluid elements FLUID30. The connection between the fluid and structural elements is established by coupling the translational DOFs. This is possible because of the coincident nodes caused by the same grid as the neighboring structures. Additionally, the sound pressure DOF of the fluid elements is coupled by a Fluid-Structure-Interaction (FSI) boundary condition applied at the surfaces on the interface. In a horizontal direction at the surfaces of the fluid volume, an impedance boundary condition is applied to consider absorbing effects. The cell size of the suspension grid and its nodal discretization must be chosen to match the nodes of the grid of the gypsum plaster boards as well as the nodal grid of the main floor. Thus, the beams of the grid-work and the COMBIN14-elements of resilient hangers have node pairs for the

coupling that lie on top of each other in vertical direction. In the special case of the LJ floor, the distance between the joists doesn't match the grid. Here, the beams of the suspension grid in x-direction are modeled matching the lumber joists, because the nodes are no longer coincident for the interconnection of the sub-structural beams in x- and y-direction, and the coupled translation needs to be interpolated between the two closest nodes.

For testing purposes, the SC can be simulated with or without the air cushion, because implementation of FLUID30-elements leads to a major increase in computational effort, which is discussed in detail in Section 3.5.1).

3.2.6.3 Parameters

The cross-sectional dimensions of the U-channels and the total thickness of the gypsum plaster boards are given in Table 3.9. These are fix dimensions and they are not subject to the later parametric studies.

Table 3.9: Dimensions of the SC components

Parameter	Variable	Value	Unit
Thickness of the gypsum plaster boards	t_{gpb}	$2.50 \cdot 10^{-2}$	m
Wall thickness of the U-channels	t_{uc}	$6.00 \cdot 10^{-3}$	m
Leg width of the U-channels	$w_{1,\mathrm{uc}}$	$2.70 \cdot 10^{-3}$	m
Web depth of the U-channels	$w_{2,\mathrm{uc}}$	$6.00 \cdot 10^{-3}$	m

The suspension grid is defined by the geometrical parameters in Table 3.10. As an example, the values of the dimensions are listed for the tested SC combined with a CLT floor.

Table 3.10: Geometrical parameters of the SC

Parameter	Variable	Value	Unit
Longitudinal edge distance of the U-channels	$a_{\mathrm{y,edge}}$	$2.35 \cdot 10^{-1}$	m
Longitudinal distance between U-channels	a_{y}	$1.00 \cdot 10^{0}$	m
Perpendicular edge distance of the U-channels	$a_{\mathrm{x,edge}}$	$1.00 \cdot 10^{-1}$	m
Perpendicular distance between U-channels	a_{x}	$5.00 \cdot 10^{-1}$	m
Edge distance of the hangers	$a_{\mathrm{x,hang,edge}}$	$3.35 \cdot 10^{-1}$	m
Distance between hangers	$a_{\mathrm{x,hang}}$	$9.50 \cdot 10^{-1}$	m
Length of the hangers	l_{hang}	$1.35 \cdot 10^{-1}$	m

The density of the gypsum plaster boards is derived from the total weight of the construction that has been measured in Tröbs [2013]. The idealized elasticity modulus of the boards is approximated in Section 4.4.1 by comparing the frequency depended, measured and simulated bending wavelengths [Winter 2012]. The stiffness and damping parameters of the resilient hangers, simplified as spring-damper elements, are derived from EMAs, as shown in Section 4.4.2. The level of absorption of the structure that surrounds the air cushion is defined by the parameter $\mu_{\mathrm{wall,i}}$. It can range from 0.0 to 1.0 which represents either full reflexion or full absorption. For the testing lab in Rosenheim, $\mu_{\mathrm{wall,i}} = 0.03$ is evaluated iteratively as shown in Section 3.7.1. The rest of the parameters are chosen according to the literature.

The material parameters for the SC-module are listed in Table 3.11.

Table 3.11: Material parameters of the SC

Parameter	Variable	Value	Unit
Density of gypsum plaster boards	$\rho_{\mathrm{gpb,m}}$	$8.56 \cdot 10^2$	$\frac{\mathrm{kg}}{\mathrm{m}^3}$
Elasticity modulus of gypsum plaster boards	$E_{\mathrm{x,gpb,m}}$	$1.02 \cdot 10^9$	$\frac{\mathrm{N}}{\mathrm{m}^2}$
Poisson ratio of gypsum plaster boards	$\nu_{\mathrm{gpb,l}}$	$2.00 \cdot 10^{-1}$	–
Density of steel	$\rho_{\mathrm{st,l}}$	$7.85 \cdot 10^3$	$\frac{\mathrm{kg}}{\mathrm{m}^3}$
Elasticity modulus of steel	$E_{\mathrm{x,st,l}}$	$2.10 \cdot 10^{11}$	$\frac{\mathrm{N}}{\mathrm{m}^2}$
Poisson ratio of steel	$\nu_{\mathrm{st,l}}$	$3.00 \cdot 10^{-1}$	–
Spring stiffness of the suspension	$k_{\mathrm{sus,m}}$	$1.65 \cdot 10^5$	$\frac{\mathrm{N}}{\mathrm{m}}$
Damping constant of the suspension	$c_{\mathrm{sus,m}}$	$7.80 \cdot 10^1$	$\frac{\mathrm{Ns}}{\mathrm{m}}$
Density of air	$\rho_{\mathrm{air,l}}$	$1.20 \cdot 10^0$	$\frac{\mathrm{kg}}{\mathrm{m}^3}$
Speed of sound in air	$c_{\mathrm{air,l}}$	$3.44 \cdot 10^2$	$\frac{\mathrm{m}}{\mathrm{s}}$
Absorption coefficient	$\mu_{\mathrm{wall,i}}$	$3.00 \cdot 10^{-2}$	–

3.2.7 Support conditions

One of the following support modules is added for any considered floor system and construction state that have been modeled by a combination of the modules described before. The support modules can display different static situations of varying complexity. One model displays a simple line support another one includes clamping effects. In the third and the most detailed model, an additional layer of elastomer material is added to the structure.

3.2.7.1 Simple line support

For this support condition, the translational DOFs of the nodes at the lower edge of the main floor construction are fixed. Depending on the static system, either two or all sides of the floor can be *Navier*-supported. To prevent compulsion in case of two-sided support, the DOFs in the x-direction stays free on one side (see Fig. 3.18).
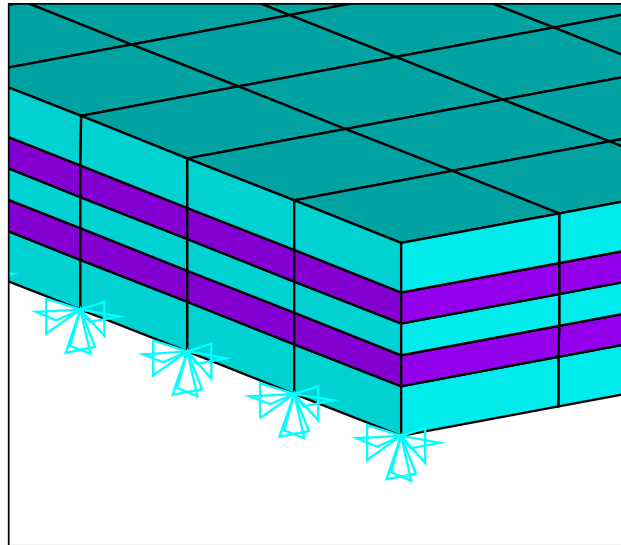

Figure 3.18: FE model of a simple support

3.2.7.2 Partially clamped support

Partial clamping is modeled with additional torsional spring elements (see Fig. 3.19). The nodes or the volume elements used for the modeling of the floors lack rotational Degree-of-Freedoms (DOFs) as a counterpart for the spring elements. Therefore, a numerical workaround has to be found. Starting from the module for a simple support described above additional nodes are created overlaying the existing nodes at the support (only cyan arrows). These nodes are discretized as mass elements (MASS21) of zero mass, that include torsional DOFs. Later, the translations of every node on a line, vertically above the support, are coupled to the mass element's rotations by constrained equations (magenta arrows and lines). As a result, all these nodes have the same rotation, which leads to a restrained warping of the, now plane, cross-sectional area in z-direction. In a further step, a second row of mass element nodes with fixed DOFs is created, slightly shifted in x-direction, outside the structure (orange and cyan arrows). Finally, torsional spring elements are modeled between the two rows of mass element nodes. With a change of the torsional stiffness of the spring elements $k_{\phi,\text{support}}$ the degree of clamping can be adapted. However, the restrained

warping of the cross-sectional areas is a disadvantage of this model. With decreasing degree of clamping the induced numerical error increases. The same holds in case of short characteristic wavelength of the system. Moreover, in case of the CLT floor, the advantage of a modeling of uneven cross-sectional areas over the thickness of the slab, related to a shell model, gets lost at the edges. Instead of using this module with $k_{\phi,\text{support}} = 0$, the module for a simple support should be preferred.
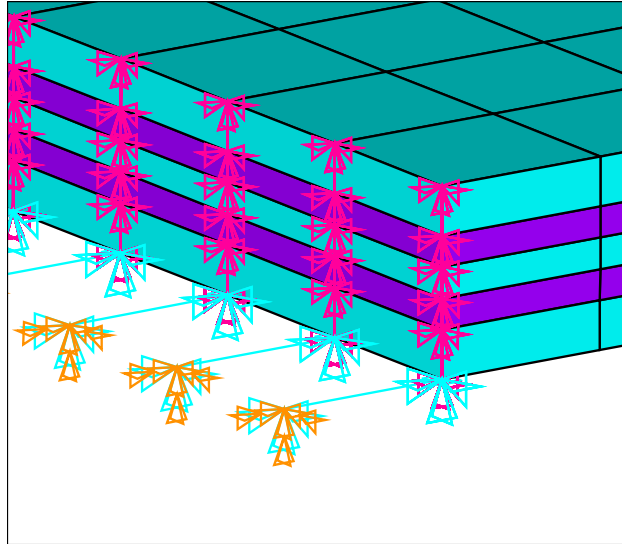
Figure 3.19: FE model of a partially clamped support

3.2.7.3 Elastomer support

For the experimental investigation, a more complex construction for the bearing of the test objects was chosen (see Figs. 3.20 and 3.21). Its design is aimed on the development of defined, reproducible and equal support conditions for every tested floor configuration. Therefore, the main load-bearing structural elements are applied upon stripes of elastomer material. To prevent a lifting of the test object, steel U-profiles are attached on top. They are fixed to the test stand via threaded rods and pre-stressed screws. Between the steel profiles and the wooden structure, the same elastomer stripes are arranged.
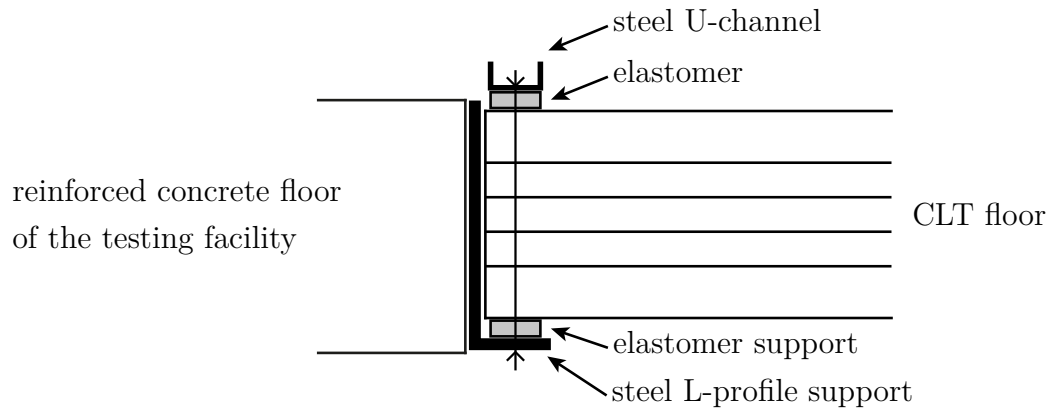
Figure 3.20: Sketch of the elastomer support

The lower elastomer stripes are idealized as a single volume and discretized by SOLID185-elements. Due to the small cross section, a resolution of 3×3 elements is chosen, which leads to edge lengths in x-direction much smaller than those of the modeled floor constructions. For the attachment of the elastomer elements to the main floor, constrained equations between the nodes at the interface are implemented, to form a rigid contact by interpolating the nodal displacement. A modeling of the steel profiles is neglected, since a lifting of the structure is already excluded.
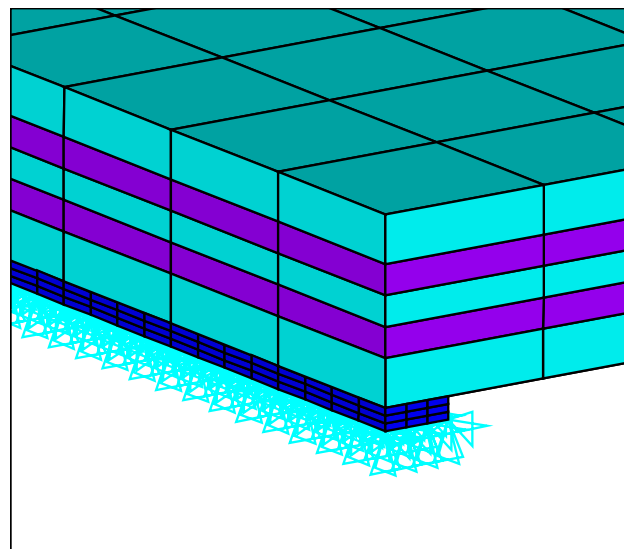
Figure 3.21: FE model of an elastomer support

The elastomer material SYLOMER manufactured by GETZNER WERKSTOFFE GMBH is used here. The dimensions of the applied cross sections measured 0.0125 m × 0.04 m. Negeira [2013] investigated its material properties, and described it as a highly non-linear material.

If the exact dimensions and load situation are known, the material properties can be approximated by the data sheets, as well as a calculation tool distributed by the manufacturer. Negeira [2013] and Müller and Buchschmid [2011] derived the material properties by testing. As described in Section 4.2.2, a model-updating algorithm is used to calibrate the material properties of the CLT model and the elastomer support. *Young*'s modulus of the elastomer is first approximated by the data sheet and the result is used as initial values for the model-updating. As a simplification, isotropic material law is applied. The resulting elasticity modulus is listed in Table 3.12.

Table 3.12: Parameters of the elastomer support

Parameter	Variable	Wert	Einheit
Height	h_{elasto}	$1.25 \cdot 10^{-2}$	m
Width	w_{elasto}	$4.00 \cdot 10^{-2}$	m
Density	$\rho_{\text{elasto,l}}$	$2.00 \cdot 10^2$	$\frac{\text{kg}}{\text{m}^3}$
Young's modulus	$E_{\text{x,elasto,m}}$	$1.13 \cdot 10^7$	$\frac{\text{N}}{\text{m}^2}$
Poisson ratio	$\nu_{\text{elasto,l}}$	$1.00 \cdot 10^{-1}$	–

3.3 Damping Model

Damping, proportional to the mass and stiffness contribution inside the model, is assumed. Hence, *Rayleigh* damping is considered for the Harmonic Frequency Analyses. Thus, the damping matrix $\mathbf{C}$ can be calculated from mass and stiffness matrix $\mathbf{M}$ and $\mathbf{K}$ using the proportionality factors α and β.

$$\mathbf{C} = \alpha \, \mathbf{M} + \beta \, \mathbf{K} \tag{3.1}$$

The derivation of these values from damping coefficients out of EMA measurements is shown in Section 4.3. α_{R} and β_{R} for CLT and LJ floors are listed in Table 3.13. For HBG and CLT floors, the same damping coefficients are considered.

Table 3.13: Damping parameters

Parameter	Variable	Value	Unit
Mass proportionality factor	α_{CLT}	$1.21 \cdot 10^0$	–
Stiffness proportionality factor	β_{CLT}	$4.71 \cdot 10^{-5}$	–
Mass proportionality factor	α_{LJ}	$1.69 \cdot 10^0$	–
Stiffness proportionality factor	β_{LJ}	$8.00 \cdot 10^{-5}$	–

3.4 Load Models

3.4.1 Single load

The test objects for experimental evaluations are excited by an electrodynamic shaker in a discrete point on top of the structure. To match the results of the measurements, a single load is applied to the FE models. The driving point, in case of the numerical simulations, has to coincide with a node at the upper surface of the model. Thus, a slightly different configuration is chosen, since the element grid does not match the experimental location in every simulation. The error induced is assumed to be negligible for the considered frequency range and the occurring wavelengths. For the comparison of measured and simulated results, this type of loading is well suited. A force with a value of 1.0 N is applied. Thus, the resulting response spectra can be compared directly to the measured transfer functions (see Section 5.3). Some restrictions have to be introduced. Since the model has several eigenmodes in the investigated frequency range, the system's response varies depending on the chosen location of the applied load. Thus, some modes are excited over-proportionately, while others may be not excited at all. The vibro-acoustical behavior of the floor systems can therefore not be described for the general case using this type of loading.

3.4.2 Rain-on-the-roof load

To solve the problem described above, a stochastic approach is investigated. To obtain a evenly excitation over the whole floor surface, a stochastic area load, uncorrelated in space and time, is applied [Nilsson and Liu 2013]. Single loads with varying phases are applied to every node of the upper floor surface. The individual phase shifts are evenly distributed, while the absolute value stays equal. Real and imaginary parts of the individual load vectors are generated by random numbers using a uniform distribution. The absolute values are chosen to give an equal total area load for every simulation. An FE model with applied stochastic loading is shown in Figure 3.22. The individual arrows describe the real part of the single loads.

This type of excitation is commonly referred to as Rain-on-the-Roof (ROTR) excitation [Lafont et al 2013]. It follows the modal approach of the SEA, where the external force distribution is assumed to be statistically independent [Lyon and DeJong 1995]. Thus, all
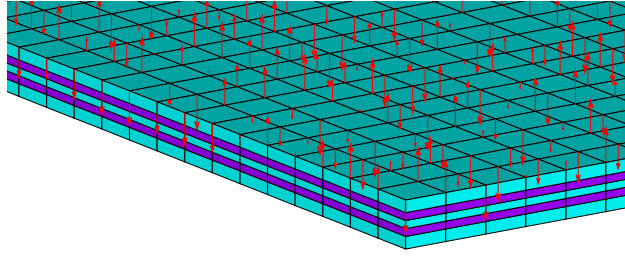
Figure 3.22: Stochastic area load (ROTR excitation)

modes of a structure are excited with the same level [Lafont et al 2013]. The auto-correlation function of the force field $f(x,t)$ of a ROTR excitation with a constant amplitude S_0 is

$$R_{ff}(\chi,\tau) = \langle f(\chi,t)f(x+\chi,t+\tau)\rangle = \delta(\chi)\delta(\tau)S_0. \tag{3.2}$$

The modal force of mode i with the corresponding eigenvector $\mathbf{\Phi}_i$ is

$$L_i = \int f(x,t)\mathbf{\Phi}_i dx. \tag{3.3}$$

Since the eigenmodes are orthonormal, the cross-correlation with the modal force of mode j yields the following:

$$R_{L_i L_j}(\tau) = \langle L_i(t)L_j(t+\tau)\rangle = S_0\delta(\tau)\delta_{ij}. \tag{3.4}$$

Thus, the modal forces are uncorrelated white noises with the same power spectral density S_0 [Lafont et al 2013]. An infinite number of uncorrelated excitation points would be necessary for a strict ROTR field. As explained above, in case of numerical investigations a large number of excitation points is usually placed randomly on the structure.

The random character of this type of excitation requires an iteration process for the simulations using varying random load conditions. Averaging over multiple simulations increases the accuracy of the results. This type of loading avoids uneven excitation of modes, and thus increases the significance of the results. The computational effort is multiple times higher, than when a single load is applied.

3.4.3 Pedestrian load

A parametric description of the loading by a simulated pedestrian requires a time domain analysis approach. For each footfall a load/time function is applied to the model (compare Fig. 3.23). Those functions are derived parametrically according to Butz [2006] and Müller

and Buchschmid [2011] and are adapted to the considered FE model. Therefore, several person specific parameters (mass, distance between the footfalls, etc.) as well as the walking path of the pedestrian have to be accounted for.
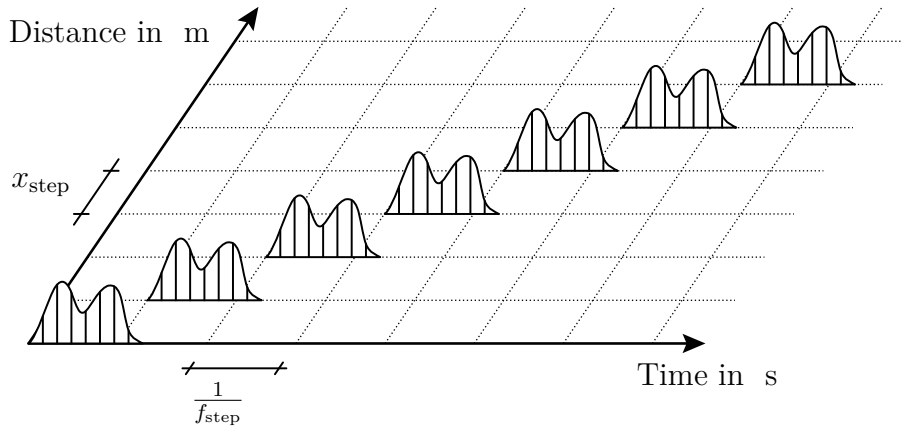
Figure 3.23: Sketch of the step-by-step-load approach [Reuter 2011]

Initially, the load/time function of a single footfall has to be determined. According to Butz [2006] both its shape and duration depends on the footfall frequency f_{step}. The discretization of the load function has to be according to the chosen time step size of the analysis Δt. Its amplitude is governed by the weight of the simulated pedestrian $m_{ped} \cdot 9.81 \, \frac{m}{s^2}$. Subsequently the walking path has to be chosen. A reasonable choice is a path along the main span of the floor with a distance to the edge of $y_{foot,edge}$. With the length of the floor and the distance between each footfall x_{foot} as well as the initial distance $x_{foot,start}$ the total number of footfalls and their location on the floor can be determined. As a simplification the load of each footfall is concentrated in a single point and all footfalls are located along a straight line. With a temporal offset defined by the reciprocal value of the footfall frequency the load/time function is applied to the previously defined locations as a load vector.

3.5 Dynamic Analyses

The following dynamic analyses are performed for the structural models depending on the objective:

- Modal Analysis

- Harmonic Frequency Analysis

- Transient Analysis

Individual modules for each analysis type are developed, that partly build on one another. In Figure 3.24, a scheme of the modules in the solution processor is depicted. Depending on the analysis type, the structural models are applied by different types of loads. The individual analyses will be described as follows.
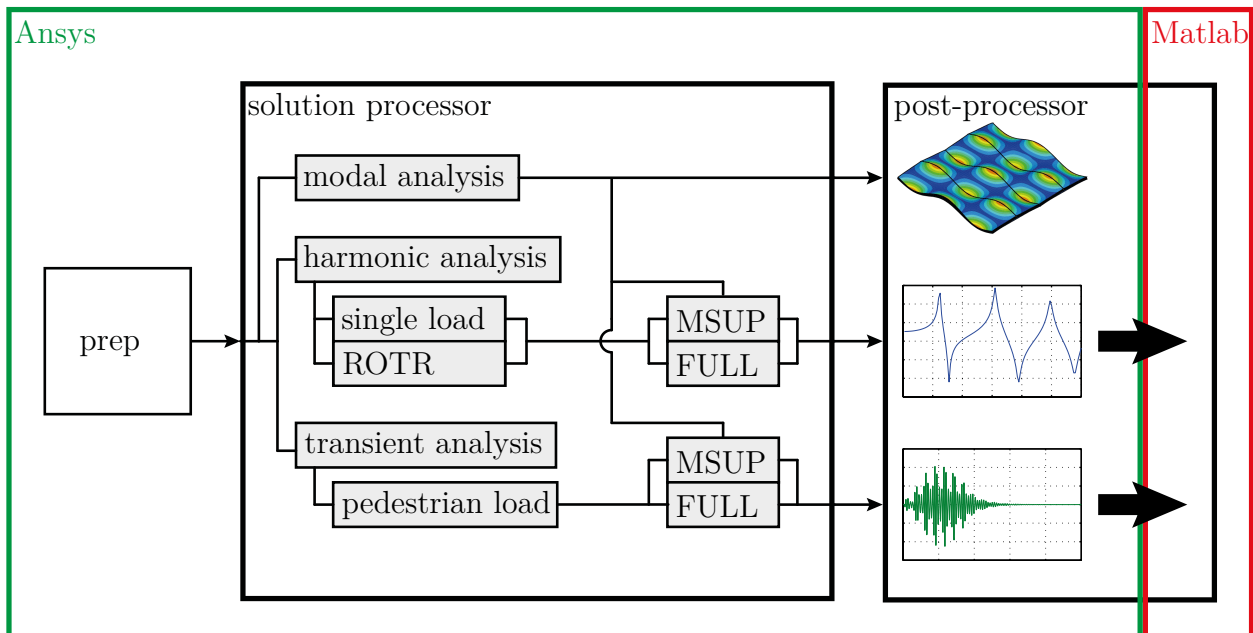
Figure 3.24: Modular design of solution and post-processor (ANSYS®)

3.5.1 Modal Analysis

In Section 2.5, the fundamental theory of a undamped Modal Analysis for FE models is described. Due to the small damping of the investigated wooden structures (see Section 4.3), damped Modal Analyses are not considered. The variation between damped and undamped eigenfrequencies is assumed to be negligible.

3.5.1.1 Applied Modal Analysis methods

Two Modal Analysis methods implemented in ANSYS® are considered. In general the *Block-Lanzcos* method is applied. For models including acoustical fluid elements, a different method, capable of the solving unsymmetrical matrices, must be referred to.

The *Block-Lanzcos* method is a common procedure to derive eigenvalues especially capable of large matrix problems. For most numerical models, it is an efficient method for the extraction of a large number of eigenmodes. Typically, it is applied for complex models, composed of a mixture of different element types. On top of that, rigid body modes can be processed [Stelzmann et al 2008].

The unsymmetrical method is used in general for acoustical problems including FSI, but also for other applications with unsymmetrical mass and stiffness matrices. Complex eigenvalues are derived. The real part represents the eigenfrequency, whereas the imaginary part gives information about the stability [Stelzmann et al 2008].

3.5.2 Harmonic Frequency Analysis

The Harmonic Frequency Analysis represents the numerical equivalent to the experimental OMA. In a predefined frequency range, the dynamic response of the FE models, caused by a specific load situation, is derived. The overall goal is to evaluate the radiated sound power of the simulated models, caused by an excitation from above and radiated into the space below the structure. Thus, the top structure (e.g screed) must be excited and the bottom structure (e.g. paneling of the ceiling) gives the systems response. Therefore, the location of the load as well as the nodes for the evaluation are adapted to the considered state of construction. For the prediction model of the effective and the radiated sound power described in Section 3.7.1, the mean square structure-borne sound velocity for all nodes of the radiating surface is calculated in the wave number domain in every simulated frequency step. The frequency range and discretization for all models is set by the parameters $f_{\min}$, $f_{\max}$, and Δf. In Table 3.14 those values are given, chosen to match the experimental data.

Table 3.14: Parameters for the Harmonic Frequency Analysis

Parameter	Variable	Value	Unit
Minimum frequency	$f_{\min}$	0	Hz
Maximum frequency	$f_{\max}$	130/200	Hz
Frequency step size	Δf	1.0	Hz

3.5.2.1 Analysis methods

For the Harmonic Frequency Analysis, several methods with varying computational effort are implemented in Ansys®. Two possible solution methods will be presented which can be adapted depending on the simulated model's complexity.

Modal superposition   When modal superposition is chosen, a preliminary Modal Analysis has to be performed. For the derivation of the dynamic response, the results for the individual modes are superposed. The number of considered eigenmodes is recommended to be chosen to cover a minimum of 1.5 times the considered frequency range [Stelzmann et al 2008]. However, it has to be checked, whether stiffness controlled modes are irrelevant for the radiation [Müller 2002]. This method provides an enhanced speed of computation but cannot be applied to every simulation configuration. Among other restrictions symmetrical matrices of the system must be present. Construction states with suspended ceiling and implemented acoustical fluid elements cannot be solved using this method due to the resulting unsymmetrical matrices.

Full solution   In case, modal superposition cannot be applied, the standard method of Ansys® for the solution of a Harmonic Frequency Analysis is considered. Here, the complete matrices must be solved which, compared to a solution using modal superposition, leads, especially for large models, to a significant increase of the computational effort.

3.5.3 Transient Dynamic Analysis

For the evaluation of the numerical models regarding pedestrian-induced vibrations, an excitation by a simulated walking person described in Section 3.4.3 is applied. Such a transient load requires an analysis in the time domain, a transient dynamic analysis. For the time-step-iteration, the *Newmark*-Beta method is considered using a constant acceleration approach [Stelzmann et al 2008]. Analysis method and damping is specified according to the harmonic analysis (see Section 3.5.2).

3.5.3.1 Discretization in the time domain

The time domain is defined by the time step size Δt and the overall number of time steps n_{substep} resulting in a total duration of the analysis of $T_{\mathrm{tot}} = \Delta t \cdot n_{\mathrm{substep}}$. The time step size

has to be chosen sufficiently small to prevent numerical errors. The number of time steps is defined by the duration the pedestrian load needs to pass the floor including the time until the floor's forced oscillation attenuates. Both values have an impact on an eventual evaluation in the frequency domain as well.

3.5.3.2 Evaluation of an example

Figure 3.25 shows an example of the displacement/time curve of the floor caused by a pedestrian load. The load propagates along the main span with a footfall frequency of 2.0 Hz. The displacement of a node in the center of the floor is considered. A model of a CLT floor without additional constructions was simulated. Table 3.15 lists the parameters applied for the analysis. Clearly, the seven footfalls are recognizable from the shape of the curve, as well as the forced oscillation of the floor. The total duration was 10.0 s.
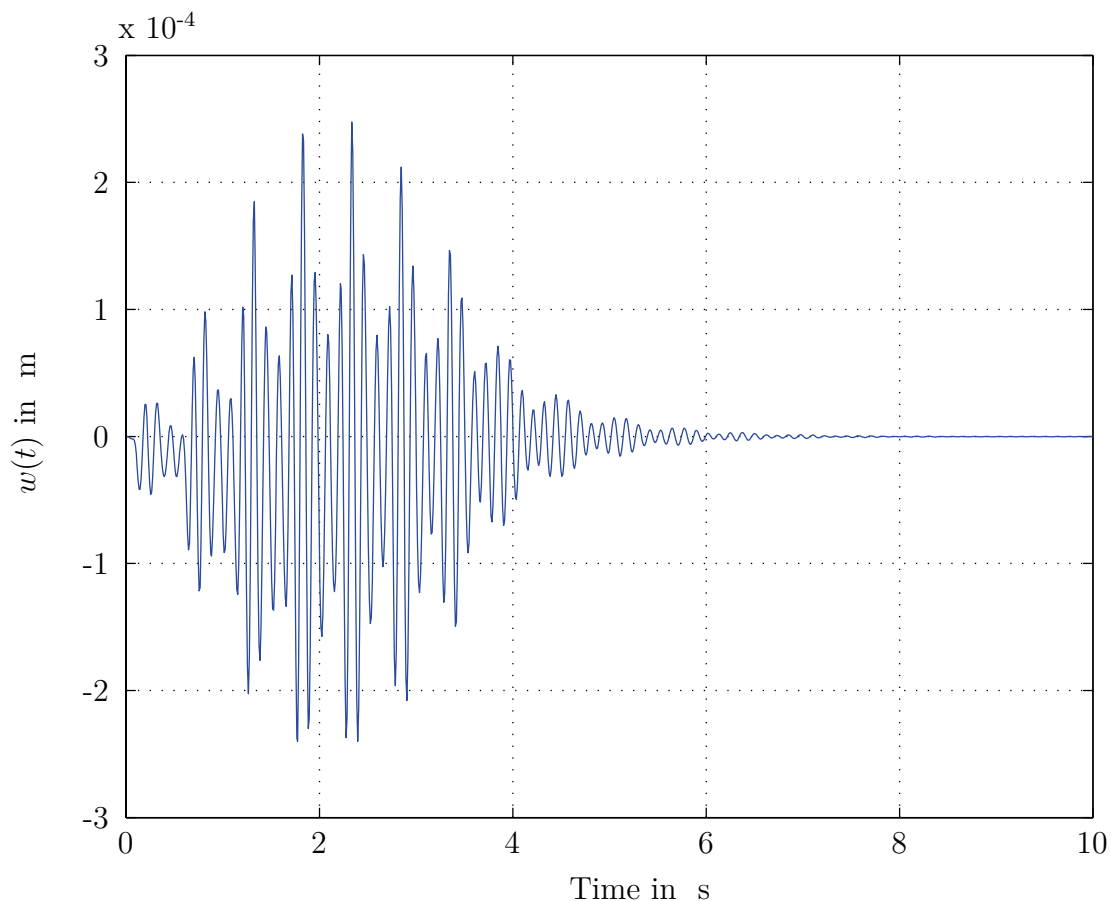
Figure 3.25: Example of the vibrations caused by a pedestrian walking with 2.0 Hz footfall frequency

<div align="center">

Table 3.15: Parameters for a Transient Analysis with a pedestrian load

Parameter	Variable	Value	Unit
Step distance	x_{foot}	$7.50 \cdot 10^{-1}$	m
Starting distance of the first footfall	$x_{\text{foot,start}}$	$3.75 \cdot 10^{-1}$	m
Edge distance of the load path	$y_{\text{foot,edge}}$	$6.88 \cdot 10^{-1}$	m
Footfall frequency	f_{foot}	$2.00 \cdot 10^{0}$	Hz
Mass of the pedestrian	m_{ped}	$7.5 \cdot 10^{1}$	kg
Time step size	Δt	$1.00 \cdot 10^{-2}$	s
Number of time steps	n_{substep}	$1.00 \cdot 10^{3}$	–

</div>

3.6 Post-Processing of the Simulated Data

Simulation results can be evaluated in $\text{Ansys}^{\circledR}$ using the graphical user interface. For the acoustical prediction model, described in Section 3.7.1, an interface between $\text{Ansys}^{\circledR}$ and $\text{Matlab}^{\circledR}$ is needed.

3.6.1 $\text{Ansys}^{\circledR}$-post-processor

The frequency response functions of individual nodes of the model can be displayed within the $\text{Ansys}^{\circledR}$-post-processor. An example of such a frequency response function due to a single load at the driving point is shown in Figure 3.26. Since the force value of the single load for every frequency step was $\hat{F}(f) = 1.0\,\text{N}$ the shown spectrum represents the receptance $R(f) = \frac{\hat{w}(f)}{\hat{F}(f)}$.

The graphical user interface is used for preliminary examinations only. Further investigations are performed using the computer algebra software $\text{Matlab}^{\circledR}$.

3.6.2 $\text{Ansys}^{\circledR}$-to-$\text{Matlab}^{\circledR}$-interface

To ensure an automatic procedure for the acoustical evaluation within a parametric study, as well as for the iteration of the stochastic simulations mentioned in Section 3.4.2, an interface between $\text{Ansys}^{\circledR}$ and $\text{Matlab}^{\circledR}$ is implemented. For every frequency step, the dynamic response of the models is exported. Therefore, the real and imaginary part of the structure borne sound velocity, for every node of the radiating surface, is extracted. The dynamic data,
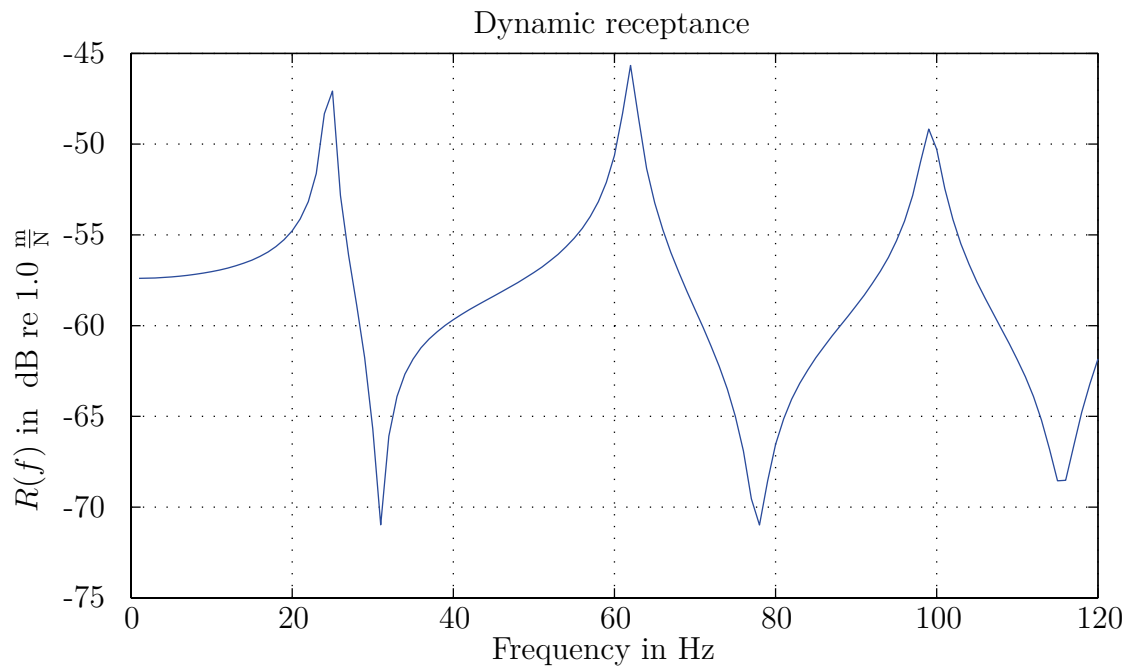
Figure 3.26: Driving point receptance

as well as the specific coordinates of every node, is subsequently transferred to MATLAB® in vector form. These vectors are transformed into three-dimensional matrices according to the specific coordinates that describe the velocity pattern per frequency step.

3.7 Evaluation Models

For the acoustical evaluation of the simulated data, a numerical model for the prediction of the radiated sound power of the modeled structures is developed, based on the semi-analytical procedure, derived in Section 2.4. Pedestrian induced vibrations can be evaluated according to VDI 2038 Blatt 2: 2013-01. Figure 3.27 shows the complete flow chart of the numerical investigations including the evaluation models.
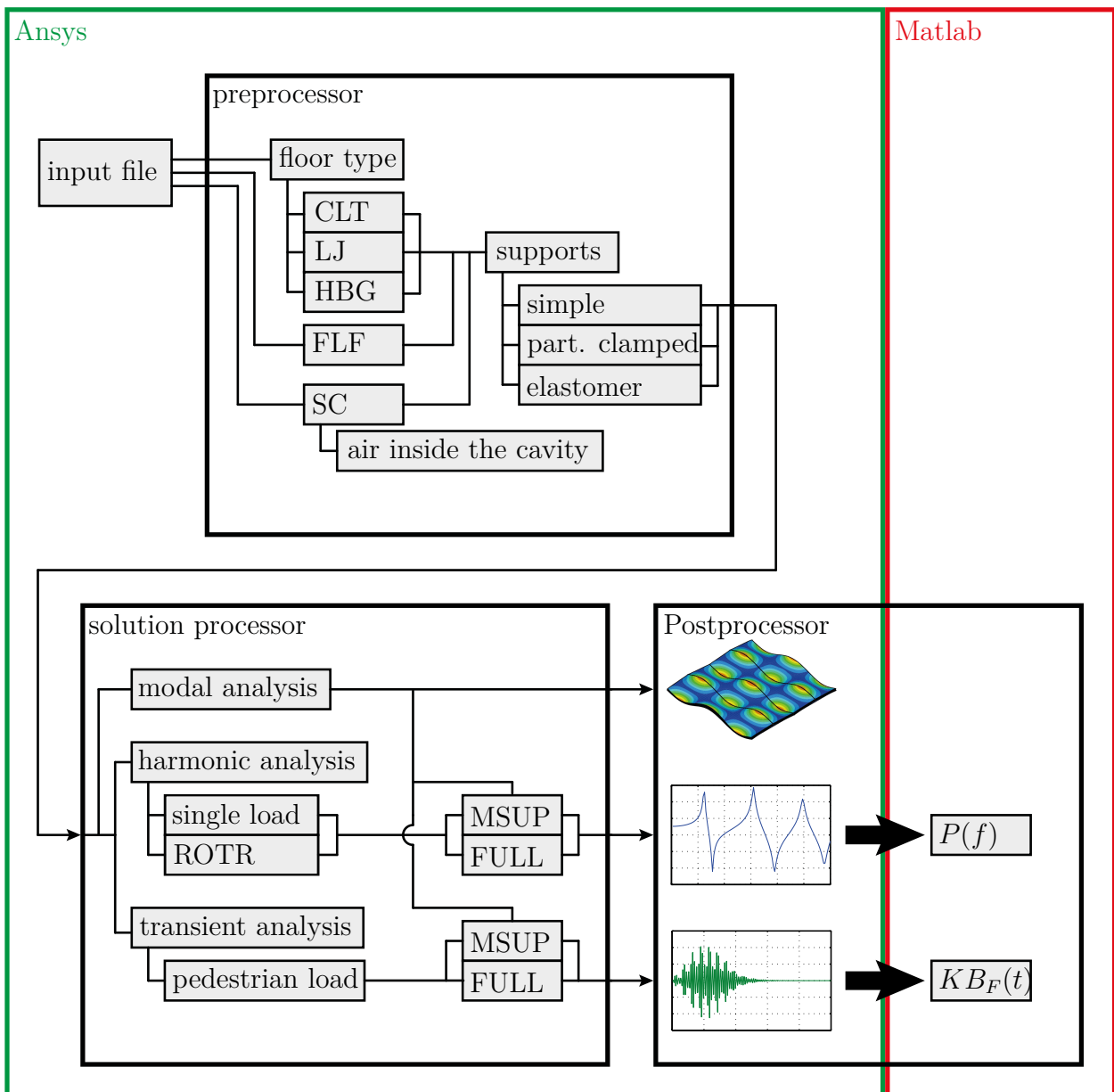
Figure 3.27: Flow chart of the numerical investigations

3.7.1 Numerical model for the prediction of the radiated sound power

The radiated sound power can be calculated semi-analytically using ITM as described in Section 2.4. Equation (2.128) was derived for one frequency component assuming pure harmonic oscillations. It can be extended to the calculation of the frequency depended radiated sound power $P(f)$ from the velocity pattern of a plane radiator in the wave number

domain.

$$P(f) = \frac{1}{2} \frac{\rho_A c_A}{4\pi^2} \Re \left[\int\limits_{-\infty}^{\infty} \int\limits_{-\infty}^{\infty} \frac{k_A(f)}{\sqrt{k_A(f)^2 - k_x^2 - k_y^2}} |\hat{v}(k_x, k_y, f)|^2 dk_x dk_y \right] \tag{3.5}$$

$\hat{v}(k_x, k_y, f)$:   Velocity pattern in the wave number domain

ρ_A :   Density of air

c_A :   Speed of sound

$k_A(f) = \frac{2\pi f}{c_A}$:   Wave number of air

k_x, k_y :   Wave number domain coordinates

Compared to the ERP of a piston (Eq. (2.131))

$$P_{\text{eff}}(f) = \frac{1}{2} \frac{\rho_A c_A}{4\pi^2} \int\limits_{-\infty}^{\infty} \int\limits_{-\infty}^{\infty} |\hat{v}(k_x, k_y, f)|^2 dk_x dk_y \tag{3.6}$$

the two Equations (3.5) and (3.6) differ by a kernel named K in the following

$$K(k_x, k_y, f) = \Re \left[\frac{k_A(f)}{\sqrt{[k_A(f)]^2 - k_x^2 - k_y^2}} \right] . \tag{3.7}$$

since only the real part contributes to the radiated sound power and the values of the remaining terms of Equation 3.5 are real, it is obvious, that this term is of special importance for the radiation. The term K can be transformed into cylindrical coordinates using $\frac{k_x}{k_A(f)} = r \cdot cos(\phi)$ and $\frac{k_y}{k_A(f)} = r \cdot sin(\phi)$.

$$K(r, \phi, f) = [k_A(f)]^2 \Re \left[\frac{1}{\sqrt{1 - r^2}} \right] \tag{3.8}$$

which implies:
$$\begin{aligned} K(r, \phi, f) &\to \infty \quad \text{for} \quad r \to 1 \\ K(r, \phi, f) &= 0 \quad\;\; \text{for} \quad r > 1 \; . \end{aligned}$$
The integral of this function over the total wave number domain converges and yields:

$$\int\limits_{-\infty}^{\infty} \int\limits_{-\infty}^{\infty} \Re \left[\frac{k_A(f)}{\sqrt{[k_A(f)]^2 - k_x^2 - k_y^2}} \right] dk_x dk_y = [k_A(f)]^2 \cdot \int\limits_{0}^{\infty} \int\limits_{0}^{2\pi} \Re \left[\frac{r}{\sqrt{1 - r^2}} \right] d\phi dr \tag{3.9}$$

$$= 2\pi [k_A(f)]^2 \tag{3.10}$$

K can be described figuratively as a circle shaped bowl with a value of unity in the origin and asymptotic top edges tending to infinity (a numerical representation is depicted in

Figure 3.29). Beyond this circle with a radius corresponding to the wave number of air the integrand has imaginary value and is therefore set to zero. Thus, an integration of Equation 3.7 accordingly 3.5 yields finite values despite of the singularity at $r = 1$. While an analytical solution can be achieved easily a numerical solution is prone to errors that will be discussed in the following.

For numerical evaluation, the frequency dependent analytical equation for the radiated sound power must be transformed in to a numerical expression. Thus, evaluating Equation (3.5) for every considered discrete frequency step $f[\gamma] = \gamma \Delta f$ with $\gamma \in 1,2,\dots N_\gamma$ and

$$N_\gamma = \frac{f_{\max} - f_{\min}}{\Delta f}. \tag{3.11}$$

$P(f)$ transforms into a vector $\mathbf{p}$, while $K(k_x, k_y, f)$ and $\hat{v}(k_x, k_y, f)$ become three-dimensional $M_\alpha \times M_\beta \times n_f$-matrices $\mathbf{K}$ and $\hat{\mathbf{V}}$.

$$\mathbf{p} = \begin{bmatrix} P[1] \\ \vdots \\ P[\gamma] \\ \vdots \\ P[N_\gamma] \end{bmatrix}, \quad \mathbf{K}_\gamma = \begin{bmatrix} K[1,1,\gamma] & \dots & K[1,\beta,\gamma] & \dots & K[1,M_\beta,\gamma] \\ \vdots & \ddots & \vdots & \ddots & \vdots \\ K[\alpha,1,\gamma] & \dots & K[\alpha,\beta,\gamma] & \dots & K[\alpha,M_\beta,\gamma] \\ \vdots & \ddots & \vdots & \ddots & \vdots \\ K[M_\alpha,1,\gamma] & \dots & K[M_\alpha,\beta,\gamma] & \dots & K[M_\alpha,M_\beta,\gamma] \end{bmatrix},$$

$$\hat{\mathbf{V}}_\gamma = \begin{bmatrix} \hat{v}[1,1,\gamma] & \dots & \hat{v}[1,\beta,\gamma] & \dots & \hat{v}[1,M_\beta,\gamma] \\ \vdots & \ddots & \vdots & \ddots & \vdots \\ \hat{v}[\alpha,1,\gamma] & \dots & \hat{v}[\alpha,\beta,\gamma] & \dots & \hat{v}[\alpha,M_\beta,\gamma] \\ \vdots & \ddots & \vdots & \ddots & \vdots \\ \hat{v}[M_\alpha,1,\gamma] & \dots & \hat{v}[M_\alpha,\beta,\gamma] & \dots & \hat{v}[M_\alpha,M_\beta,\gamma] \end{bmatrix}$$

$$\tag{3.12}$$

The dimensions correspond to the discretization in the wave number domain $k_x[\alpha] = \alpha \Delta k_x$ and $k_y[\beta] = \beta \Delta k_y$ with $\alpha \in 1,2,\dots M_\alpha$ and $\beta \in 1,2,\dots M_\beta$. $\mathbf{K}_\gamma$ and $\hat{V}_\gamma$ are the two-dimensional matrices for one frequency step γ. According to Section 2.3, the individual spectral amplitudes $\hat{v}[\alpha,\beta,\gamma]$, can be derived out of the structure-borne sound velocity pattern in the spatial domain $v[r,s,\gamma]$ for a discrete frequency step γ. It can be provided either by an EMA or by a Harmonic Frequency Analysis, in case of a numerical investigation. Applying the DFT or FFT analysis equation (2.77) for two-dimensional problems with indexes starting

at unity yields

$$\hat{v}[\alpha,\beta,\gamma] = \sum_{r=1}^{N_r} \sum_{s=1}^{N_s} v[r,s,\gamma] e^{-i2\pi\left((\alpha-1)\frac{(r-1)}{M_\alpha} + (\beta-1)\frac{(s-1)}{M_\beta}\right)} \quad \text{for} \quad \begin{cases} 1 \leq \alpha \leq M_\alpha \\ 1 \leq \beta \leq M_\beta \end{cases} \tag{3.13}$$

Square brackets indicate the discrete nature of this equation. The number of samples in the spatial domain (N_r, N_s) depend on the measurement set-up or on the discretization of the FE model (see Section 3.2.1). For a rectangular plate $(l \times w)$ with a regular sampling interval $(\Delta x, \Delta y)$ they yield:

$$N_r = \frac{l}{\Delta x} \quad , \quad N_s = \frac{w}{\Delta y}. \tag{3.14}$$

The number of samples (M_α, M_β) and the sampling interval $(\Delta k_x, \Delta k_y)$ in the wavenumber domain depend on the considered amount of zero-padding. When an FFT is applied, it is often mandatory. With the zero padding factor z_p, introduced in Section 2.3.2.2, they can be expressed depending on the dimensions of the plate as follows:

$$M_\alpha = z_p \frac{l}{\Delta x} \quad , \quad M_\beta = z_p \frac{w}{\Delta y} \tag{3.15}$$

$$\Delta k_x = \frac{2\pi}{z_p l} \quad , \quad \Delta k_y = \frac{2\pi}{z_p w} \tag{3.16}$$

In case of an implementation into MATLAB®, the CTFT can be approximated out of Equation (3.13) by applying Equation (2.79) for the two-dimensional case

$$\hat{v}(k_x, k_y, \gamma) \approx \Delta x \Delta y \cdot \hat{v}[\alpha,\beta,\gamma]. \tag{3.17}$$

Thus, the individual terms in **p** can be expressed numerically as follows:

$$P[\gamma] = \frac{1}{2} \frac{\rho_A c_A}{4\pi^2} \Re \left[\sum_{\alpha=1}^{M_\alpha} \sum_{\beta=1}^{M_\beta} K[\alpha\beta\gamma] \cdot |\hat{v}[\alpha\beta\gamma]|^2 \Delta x^2 \Delta y^2 \right] \Delta k_x \Delta k_y \tag{3.18}$$

The corresponding components of the matrix **K** are:

$$K[\alpha\beta\gamma] = \frac{k_A[\gamma]^2}{\sqrt{k_A[\gamma]^2 - k_x[\alpha]^2 - k_y[\beta]^2}} \tag{3.19}$$

with the wave number of air

$$k_A[\gamma] = \frac{2\pi f[\gamma]}{c_A}. \tag{3.20}$$

An example of the velocity pattern in spatial and wave number domain is given in Figure 3.28. It shows simulated results for a simply supported steel plate ($l = 1.0$ m, $w = 1.0$ m, $t = 0.001$ m $\Delta x = 0.05$ m, $\Delta y = 0.05$ m) excited by a single load in the quarter point. The structure-borne sound velocity pattern (imaginary part) is depicted for a frequency step close to its third eigenfrequency ($\gamma = 100$, $\Delta f = 1$ Hz). The zero-wave number components are shifted to the center of the spectrum. This representation will be used for all subsequent wave number spectra. Clearly, the side lobes, caused by the physical leakage effect, are observable (see Section 2.3.1.2). Only minor aliasing is expected (see Fig. 2.11), since the normalized sampling interval for this eigenmode is $\pi_T = \frac{T_1}{T_0} = \frac{\Delta x}{l} = 0.05$. The resolution of the wave number spectrum is increased by a zero-padding factor of $z_p = 50$.
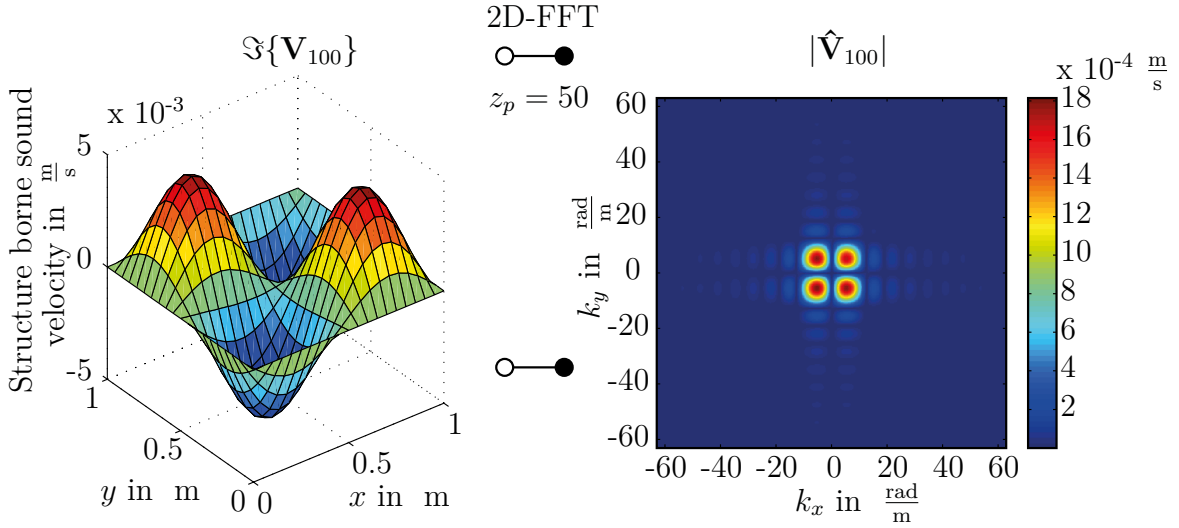
Figure 3.28: Velocity pattern in the spatial and the wave number domain

Figures 3.29 and 3.30 show three- and two-dimensional details of $\mathbf{K}_{100}$ (at 100 Hz) for a zero-padding factor of $z_p = 40$.

Discontinuities appear at a circle with a radius of the wave number of air k_A. Outside this circle, where

$$k_x[\alpha]^2 + k_y[\beta]^2 > k_A[\gamma]^2, \tag{3.21}$$

the components of $\mathbf{K}$ are zero. Since the wave number of air increases with increasing frequency, the total number of non-zero components increases, when a new set of wave number combinations meet the upper requirement. Caused by the shape of the term $\mathbf{K}$ these additional values are very large compared to the components already present in the
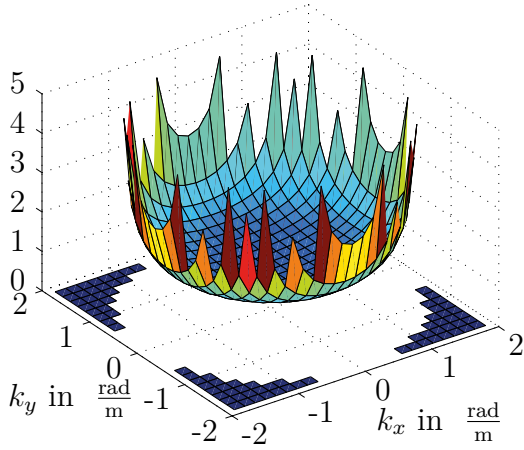
Figure 3.29: $\mathbf{K}_{100}$ in 3D for $zp = 40$ at 100 Hz
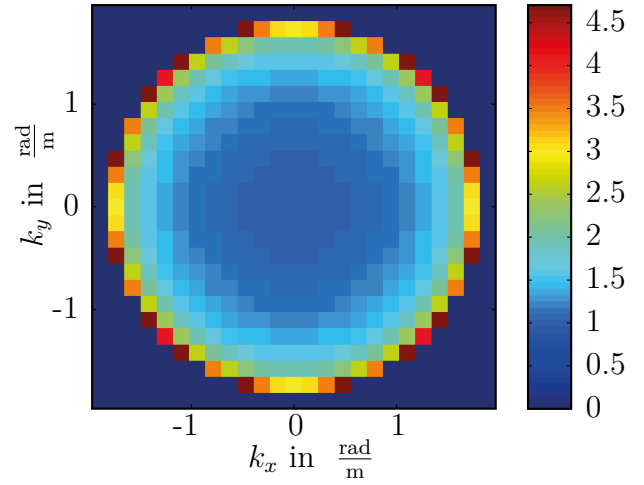
Figure 3.30: $\mathbf{K}_{100}$ in 2D for $zp = 40$ at 100 Hz

previous frequency step. The same behavior appears analogously for the product of the matrices $\mathbf{K} \cdot \hat{\mathbf{V}} \cdot \hat{\mathbf{V}}^*$ for the calculation of the radiated sound power expressed by vector $\mathbf{p}$ (see Eq. (3.12)). The corresponding components in the velocity spectrum $\left|\hat{\mathbf{V}}_{100}\right|$ are given in Figure 3.31. It shows a detail of the spectrum, where components not contributing to the radiated sound power are set to zero.
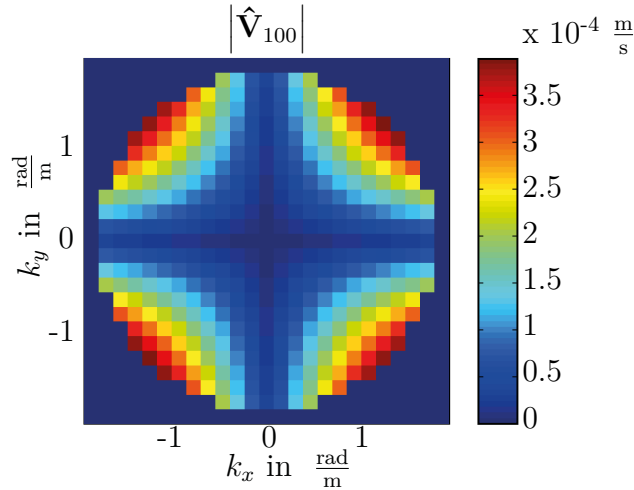
Figure 3.31: Detail of the wave number spectrum contributing to the radiated sound power

The discontinuities in $\mathbf{K}$ also lead to discontinuities in the graph of the radiated sound power $P[\gamma]$. The radiated sound power level of the plate in the example mentioned before, with a zero-padding factor of $z_p = 10$, is shown in Figure 3.32 in the frequency range $0 - 120$ Hz. The discontinuities are marked by vertical dashed lines. Between each line the number of non-zero components of $\mathbf{K}$ stays equal, resulting in a continuous curve. The corresponding details of the matrices are depicted underneath the curve with a superimposed

white circle representing the wave number of air at the frequency step after the discontinuity. Another problematic fact is, that the eigenfrequencies of the plate at approximately 25 Hz, 63 Hz and 100 Hz can hardly be distinguished from the discontinuities. As described before,
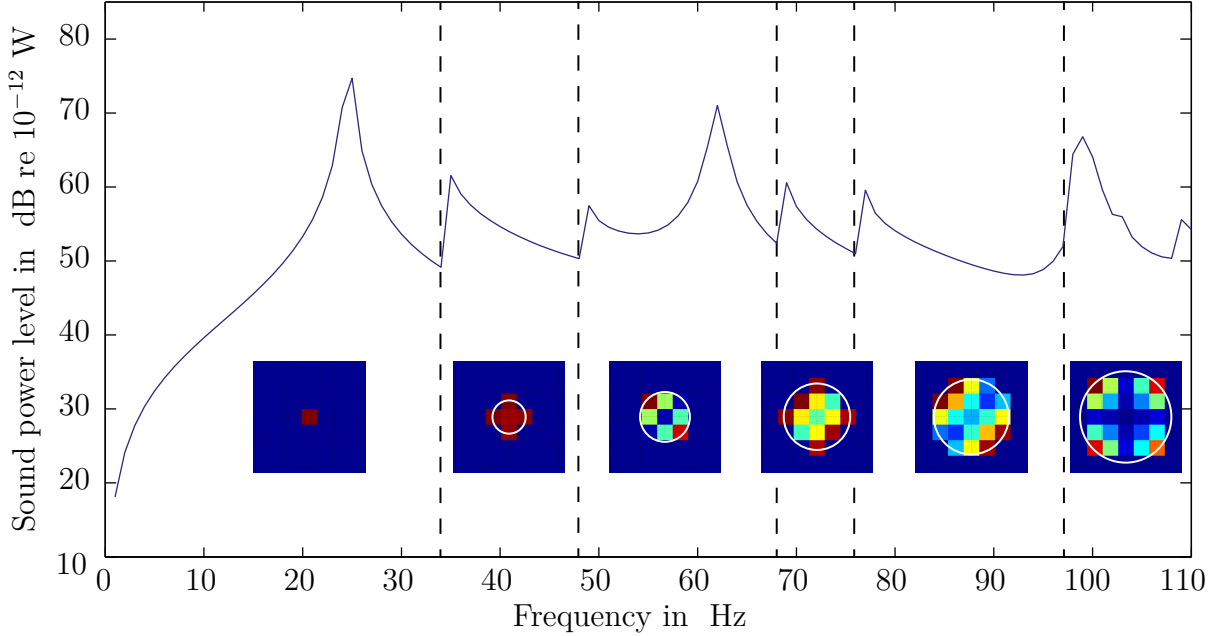
Figure 3.32: Discontinuities in the curve of the sound power level caused by biased data

this problem arises because of the discretization of the analytical but discontinuous term $K(k_x, k_y, f)$ (see Eq. (3.8)). Measures to tackle this problem are discussed in the following section.

3.7.2 Further considerations on the prediction model

3.7.2.1 Influence of the zero-padding factor

A simple approach to cope with the discontinuities, that appeared in Section 3.7.1, is to increase the zero-padding factor z_p. This results in a significant increase in computational costs. Figure 3.33 shows an increase of the number of artifacts for a zero-padding factor of $z_p = 40$ while at the same time, the values of the individual discontinuities are decreased. To gain an approximately continuous curve an even higher zero-padding factor is needed. For reasons of comparison, the result of the same data, processed without zero-padding, is shown in Figure 3.34. It becomes clear, that a minimum zero-padding is necessary. In this case of a simple supported plate, the original domain corresponds for the third eigenmode at ≈ 100 Hz

exactly to a multiple of the period (wavelength) in both directions. Thus, the special case of the DFT, where the limited signal gives the exact results of an infinite signal, occurs [Brigham 1974]. This leads to only discrete impulses in the transformed domain corresponding to the bending wavenumber of the plate at this frequency. Since the wavenumber of the air is still below the wave number of the bending wave at this frequency, Equation (3.18) yields a radiated sound power of zero. The same holds for one spatial direction in case of the second eigenfrequency at ≈ 63 Hz, leading to a continuous curve, since the remaining spatial direction of this mode is, as the first eigenmode, shaped like a half-sine. In both figures the curves for the ERP calculated according to Equation (3.6) is superimposed as a visual reference.
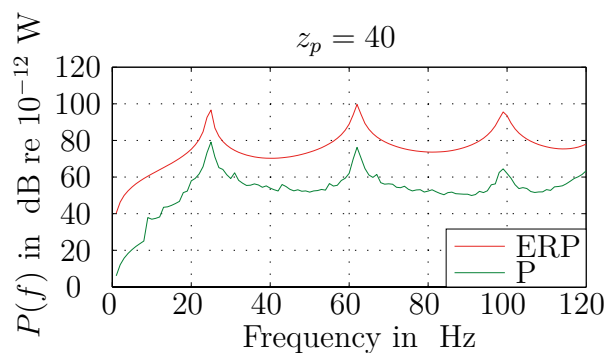
Figure 3.33: Zero-padding factor $z_p = 40$
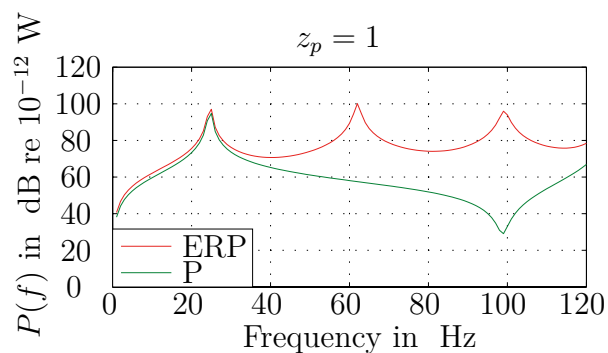
Figure 3.34: Zero-padding factor $z_p = 1$

3.7.2.2 Reducing discontinuities by discrete integration of the term K

By adapting the zero-padding factor, numerical problems, resulting from the poor resolution of the spectrum of the velocity pattern $\hat{\mathbf{V}}$, can be handled. However, the number of components depends on the discretization of the measured or simulated results. As described in Section 3.7.1, the term $K(k_x, k_y, f)$ can be integrated analytically. A consecutive approach can take advantage of that. Therefore, the individual components of the spectra $\hat{\mathbf{V}}$ can be multiplied by the integral of $K(k_x, k_y, f)$ over the sample spacing of every component measuring $\Delta k_x \cdot \Delta k_y$. This can be done either analytically or by numerical averaging.

Analytical approach

Williams and Maynard [1982] introduced a method to prevent the bias error described above. Their approach for the prediction of the radiated sound power and radiation efficiency focuses on the numerical evaluation of the *Rayleigh* integral interpreting sound pressure as a

convolution of the structure-borne sound velocity pattern by the *Green* function. This very similar approach also deals with bias errors due to the numerical discretization of the *Green* function in the wave number domain, which reassembles the described kernel $K(k_x, k_y, f)$. The problem is solved by replacing of the discrete *Fourier* transformed *Green* function by an averaged *Green* function in the wave number domain, integrated over a square box defined by the sampling space centered on a lattice point.

The presented approach follows closely the method described above. The lattice point of every spectral component in the wave number domain is defined by $k_x[\alpha]$ and $k_y[\beta]$. Keeping this location as the center, analytical double integrating over the rectangular area $\Delta k_x \cdot \Delta k_y$ yields the integrated matrix components:

$$K_{\text{int}}[\alpha,\beta,\gamma] = \int\limits_{\Delta k_x\left(\alpha-\frac{1}{2}\right)}^{\Delta k_x\left(\alpha+\frac{1}{2}\right)} \int\limits_{\Delta k_y\left(\beta-\frac{1}{2}\right)}^{\Delta k_y\left(\beta+\frac{1}{2}\right)} K(k_x,k_y,\gamma)\mathrm{d}k_x\mathrm{d}k_y \tag{3.22}$$

This integral has to be calculated for every lattice point (α,β) in every frequency step γ. Thus, the numerical Equation (3.18) can be rewritten semi-analytically as:

$$P[\gamma] = \frac{1}{2}\frac{\rho_{\mathrm{A}}c_{\mathrm{A}}}{4\pi^2}\left[\sum_{\alpha=1}^{M_\alpha}\sum_{\beta=1}^{M_\beta} K_{\text{int}}[\alpha\beta\gamma] \cdot \left|\hat{v}[\alpha,\beta,\gamma]^2\right| \cdot \Delta x^2 \Delta y^2\right]. \tag{3.23}$$

The spectral velocity pattern is assumed to be slowly varying and can be taken outside the integrals without any large errors [Williams and Maynard 1982]. This approach completely resolves the problem of discontinuities, but comes with a significant increase in computational effort, caused by the multiple use of the analytical integration. The main advantage compared to the method described by Williams and Maynard [1982] is its applicability combined with the zero-padding mentioned above. It is also not prone to aliasing caused by repeating sources described by Williams and Maynard [1982] limiting their method to large structures in case of low frequencies.

Numerical approach

To enhance the results and at the same time to limit the computational effort a numerical approach is suggested. Therefore, a numerical integration is performed over the rectangular area $\Delta k_x \cdot \Delta k_y$ replacing every $k[\alpha,\beta,\gamma]$ by spatial averaged

$$\bar{k}[\alpha,\beta,\gamma] = \frac{1}{n_r^2}\sum_{\alpha_r=1}^{n_r}\sum_{\beta_r=1}^{n_r} \frac{k_A[\gamma]^2}{\sqrt{k_A[\gamma]^2 - \left(\Delta k_x\bar{\alpha}\right)^2 - \left(\Delta k_y\bar{\beta}\right)^2}} \tag{3.24}$$

with

$$\bar{\alpha} = \left(\alpha - \frac{1}{2} + \frac{1}{n_r} \left(\alpha_r - \frac{1}{2} \right) \right) \quad , \quad \bar{\beta} = \left(\beta - \frac{1}{2} + \frac{1}{n_r} \left(\beta_r - \frac{1}{2} \right) \right) \tag{3.25}$$

Thus, the resolution in the wave number domain before the averaging is refined within the rectangular area $\Delta x \cdot \Delta y$ by a factor n_r.

Different to the analytical integration, this procedure is again prone to numerical errors, since $\bar{k}[\alpha,\beta,\gamma]$ reaches very high to infinite values in case

$$(\Delta k_x \bar{\alpha})^2 - \left(\Delta k_y \bar{\beta} \right)^2 \cong k_A[\gamma]^2.$$

This becomes more likely the higher the refinement factor is chosen. such results must be excluded from averaging.
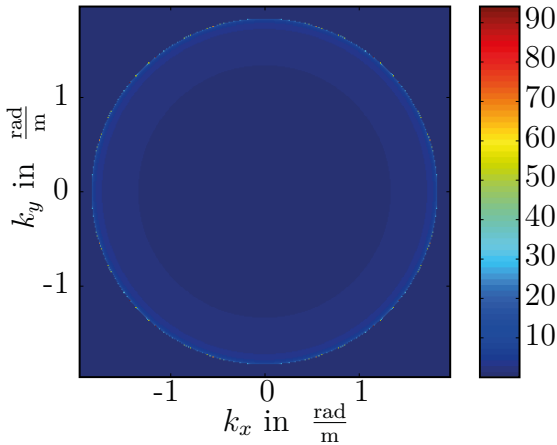
Figure 3.35: Matrix $\mathbf{K}_{100}$ with $z_p = 40$ and $n_r = 15$
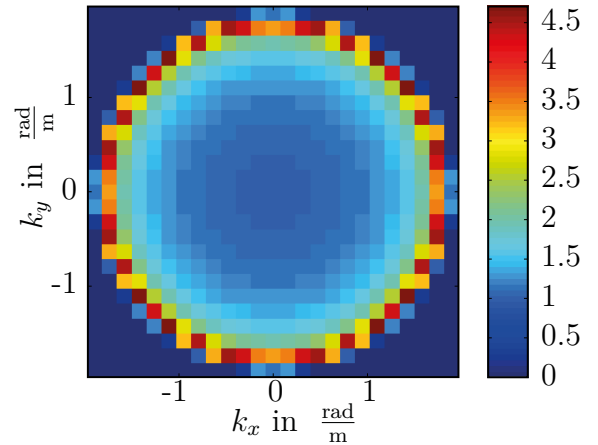
Figure 3.36: Matrix $\bar{\mathbf{K}}_{100}$ after averaging

Figuratively, the $M_\alpha \times M_\beta$-matrix $\mathbf{K}_\gamma$ is replaced by an $(n_r \cdot M_\alpha) \times (n_r \cdot M_\beta)$-matrix. Figure 3.35 shows this matrix for $z_p = 40$ and $n_r = 15$. For a multiplication with $\hat{\mathbf{V}}$, its dimensions is decreased again. Compared to $\mathbf{K}$ (see Fig. 3.30), the spatial averaged matrix $\bar{\mathbf{K}}$ (see Fig. 3.36) has a much smoother shape both in the individual spectrum and by comparing the spectra of neighboring frequency steps. The latter is caused by a slow increase of the averaged value of additional non-zero components with increasing wave number of air k_A.

3.7.2.3 Computational effort and resulting radiated sound power level

A comparison of the computational effort resulting from an increased zero-padding factor compared to a numerical integration of $K(k_x, k_y, f)$ with different refinement factors n_r is shown in Figure 3.37. The calculations of the radiated sound power are performed on the same machine based on the same data with varying values for z_p and n_r. A quadratic increase is observable for both variables, while the amount is significantly bigger with increasing z_p. This diagram, however, lacks the information about the quality of the results.
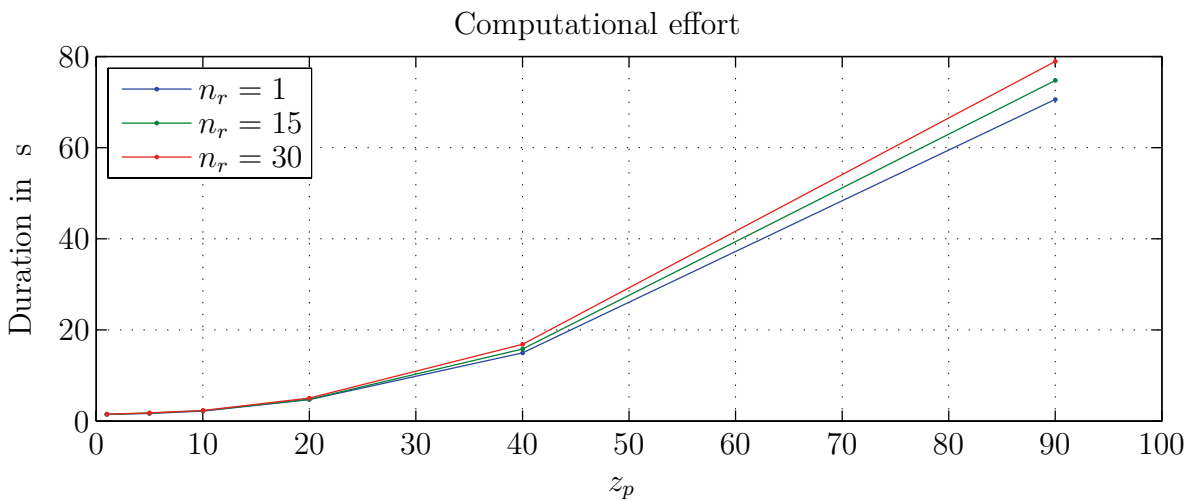
Figure 3.37: Computational effort comparing varying z_p and n_r

A good quality with a reasonable computational effort is found for values $z_p = 20$ and $n_r = 30$. The computation time for this example is 2.8 s, whereas, when analytical integration is considered (Section 3.7.2.2), the duration is 28.8 s. The resulting sound power levels, with the ERP as a reference, are given in Figure 3.38. Thus, the analytical integrals cause a 10 times higher computational effort while the results are of comparable quality. The adaptation of the described procedure for measured data is validated in Section 4.1.

3.7.2.4 Radiation efficiency compared to the Discrete Calculation Method

The method will finally be compared to the Discrete Calculation Method (DCM) proposed by Hashimoto [2001]. It is developed for a similar objective, to calculate the sound radiation efficiency in the low frequency range from vibrational data, without the requirement of measurements of the sound field. According to the number of measurement points, plane vibrators of arbitrary shape are divided virtually into small elements, that are treated as
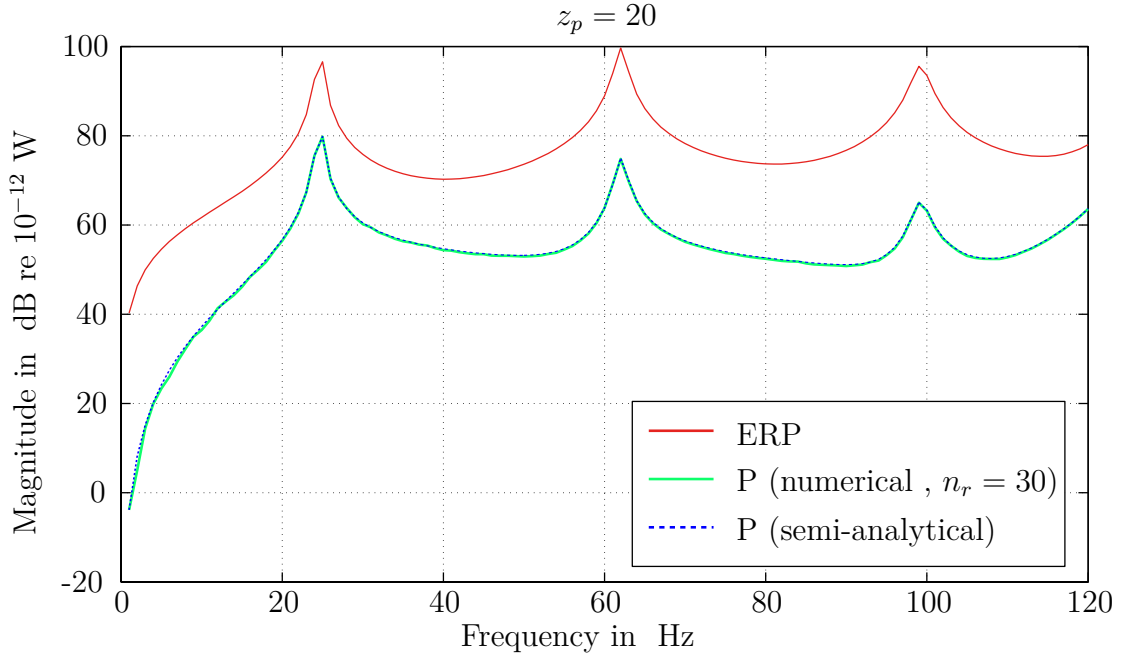
Figure 3.38: Sound power level example for $z_p = 20$ with $n_r = 30$ and analytical approach

circular pistons. It is a hybrid method that processes measurements of vibrations in the spatial domain v with self radiation impedance z_{ii} of each element v_i and mutual radiation impedance z_{ij} between every single element v_i and v_j. Thus, the sound power of each measured point is described by

$$W_i = \Re(z_{ii})|v_i|^2 + \sum_j \Re(z_{ij}v_iv_j^*) \tag{3.26}$$

with the self radiation impedance

$$z_{ii} = \rho_A c_A s_i \left[1 - \frac{J_1(2ka_i)}{k_A a_i} + i\frac{S_1(2k_A a_i)}{k_A a_i} \right] \tag{3.27}$$

and the mutual radiation impedance

$$z_{ij} = \frac{\rho_A c_A k_A^2 s_i s_j}{2\pi} \left[2\frac{J_1(k_A a_i)}{k_A a_i} \right] \left[2\frac{J_1(k_A a_j)}{k_A a_j} \right] \left(\frac{\sin(k_A d_{ij})}{k_A d_{ij}} + i\frac{\cos(k_A d_{ij})}{k_A d_{ij}} \right), \tag{3.28}$$

with

J_1	First-order *Bessel* function
S_1	*Struve* function
s_i, s_j	Element area
$a_i = \sqrt{\frac{s_i}{\pi}}, a_= \sqrt{\frac{s_j}{\pi}}$	Approximated circle area of the piston
k_A	Wave number of air
ρ_A	Density of air
c_A	Speed of sound
d_{ij}	Distance between two measurement points

The radiation efficiency can then be calculated by dividing the sum of all sound power components by the ERP

$$\sigma = \sum_i \frac{W_i}{\rho_\mathrm{A} c_\mathrm{A} S |v^2|}. \tag{3.29}$$

For a comparison, the sound radiation efficiency of the example plate, presented above, is calculated analogously by the DCM, using spatial data, and by the presented ITM-based method with analytically integrated term K. The resulting radiation efficiencies in the frequency range $0 - 120$ Hz are shown in Figure 3.39.
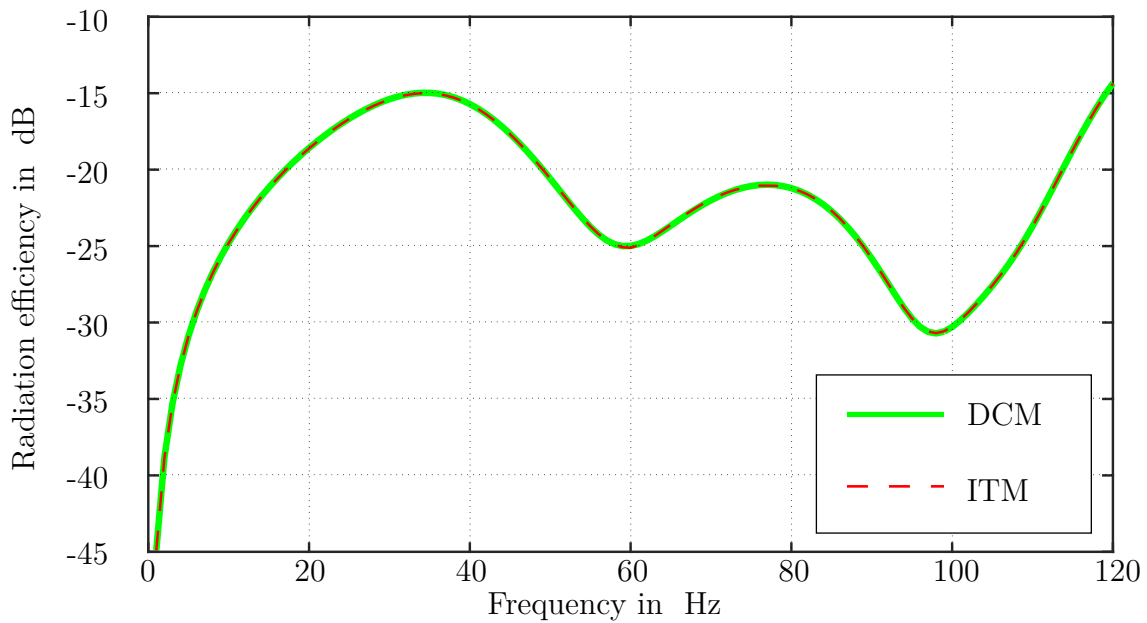
Figure 3.39: Radiation efficiency, calculated by the DCM compared to the ITM-based method

Both methods produce equivalent results. It can be seen that both curves almost perfectly match. The maximum deviation in this case is 0.13 dB at 60 Hz. The computational effort

for the DCM is equal to the ITM-based method using numerical averaging. A disadvantage of the DCM is its difficult adaptation to problems with a large number of measurement points. Especially, when it is supposed to be implemented into an automated process, the distance and relation between each virtual element has to be calculated anew every time the data grid is changed. Therefore, the ITM-based method is preferred for parametric studies described in Chapter 5. Further, the representation in the wave number domain has proven to give a deeper insight into appearing physical effects, as will be shown in Chapter 4.

3.7.3 Evaluation of pedestrian induced vibrations

In Section 3.5.3, a transient numerical model for the simulation of pedestrian-induced vibrations is introduced. The German standard DIN 4150-2:1999-06 describes a procedure to evaluate vibrations, that effect on humans in buildings based on measurements. A numerical model is developed to adapt this procedure to process the results of numerical simulations.

For the evaluation, the measured raw velocity data in the time domain $v(t)$ are band limited according to DIN 45669-1:2010-09 and a weighting filter is impinged. The resulting weighted velocity $v_{\mathrm{B}}(t)$ is subsequently normalized to $1.0\ \frac{\mathrm{mm}}{\mathrm{s}}$. Thus, the dimensionless so called KB-signal $KB(t)$ is obtained. The weighting function of the KB-signal consists of a frequency band limitation and a weighting filter independently applied to the raw signal. For the frequency band limitation the raw signal is multiplied by the complex transfer function

$$H_{\mathrm{u}}(f) = \frac{1}{\left[1 - i\sqrt{2}\,\frac{0.8f_{\mathrm{u}}}{f} - \left(\frac{0.8f_{\mathrm{u}}}{f}\right)^2\right] \cdot \left[1 + i\sqrt{2}\,\frac{0.8f}{f_{\mathrm{o}}} - \left(\frac{0.8f}{f_{\mathrm{o}}}\right)^2\right]}. \tag{3.30}$$

This function is composed of a bipolar high-pass and a bipolar low-pass filter, where a frequency range from $f_{\mathrm{u}} = 1.0$ Hz to $f_{\mathrm{o}} = 80$ Hz is considered in general.

The frequency weighting is carried out according to DIN 4150-2:1999-06 by a high-pass filter with $f_0 = 5.6$ Hz. The appropriate transfer function yields:

$$|H_{\mathrm{KB}}(f)| = \frac{1}{\sqrt{1 + \left(\frac{f_0}{f}\right)^2}} \tag{3.31}$$

$$H_{\mathrm{KB}}(f) = \frac{1}{1 - i\frac{f_0}{f}} \tag{3.32}$$

A combination of band limiting and weighting functions results in the complex transfer function

$$H_{\mathrm{B}}(f) = H_{\mathrm{KB}}(f) \cdot H_{\mathrm{u}}(f). \tag{3.33}$$

Figure 3.40 shows the individual transfer functions of the filters in logarithmic scale. The combined filter $H_{\mathrm{B}}(f)$ is applied to the simulated velocity signals.

The weighted vibration severity $KB_F(t)$ is derived by calculating the moving average of resulting KB-signals expressed in general by the following equation

$$KB_\tau(t) = \sqrt{\frac{1}{\tau} \int\limits_{\xi}^{t} e^{-\frac{1-\tau}{\tau}} KB^2(\xi) \mathrm{d}\xi} \tag{3.34}$$

In this case, the time constant τ is chosen to be 0.125 s which is indicated by the index F for fast. Taking the maximum value of the resulting curve KB_{Fmax} the signal can be evaluated according to VDI 2038 Blatt 2: 2013-01.
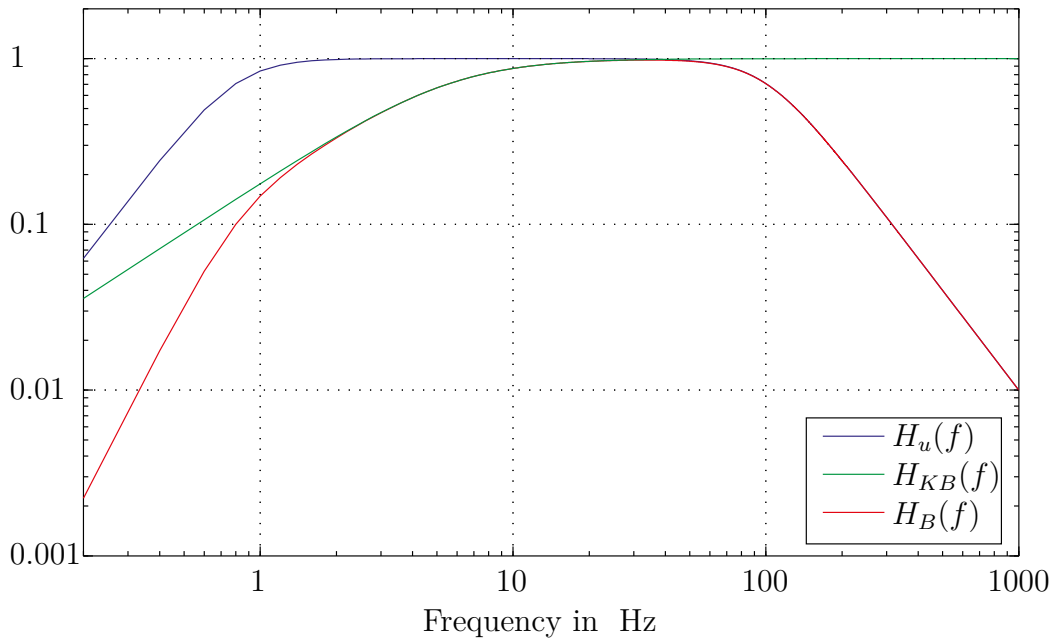
Figure 3.40: Transfer functions of the band limitation and the weighting filters

The final example in Figure 3.41 shows the KB-signal with its appropriate weighted vibration severity $KB_F(t)$ for a simulated pedestrian load. The FE-model, the load is applied to, is a CLT floor of type Leno 105 (5.5 m × 5.5 m) composed of four coupled slabs and supported
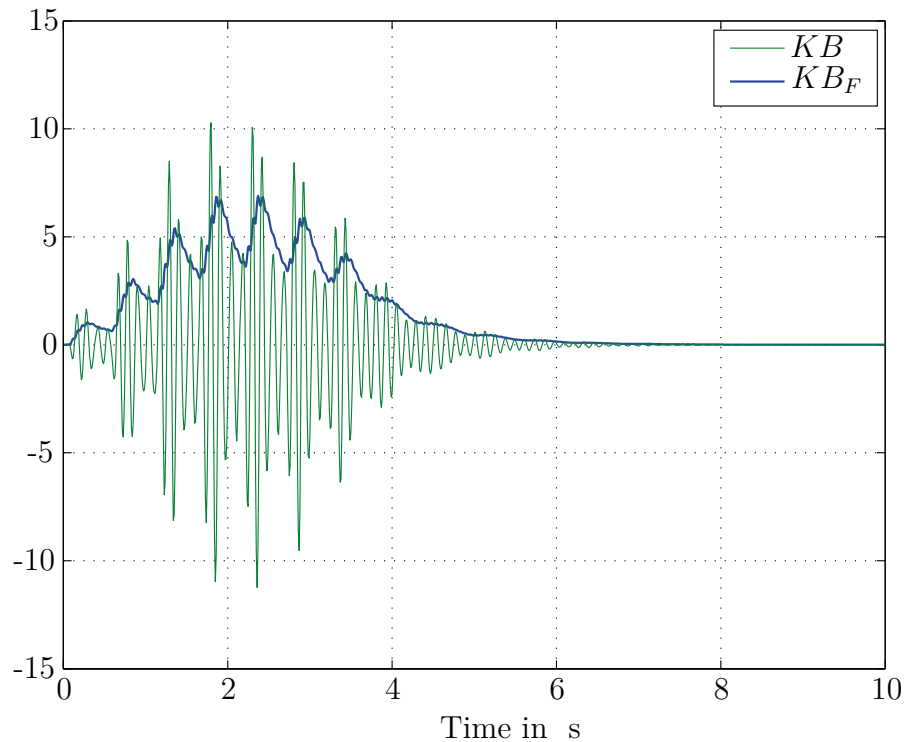
Figure 3.41: KB- and KB_F-signal of a pedestrian with a footfall frequency of 2 Hz

on two sides. The mass of the pedestrian load is 75 kg. It propagates along the main load bearing direction on a straight line in the middle of the first slab. Seven footfalls are needed. For this configuration the limit values proposed by VDI 2038 Blatt 2: 2013-01 are not met (see Tab. 3.16). Thus the investigated floor does not meet the requirements concerning pedestrian-induced vibrations. The bending stiffness of the floor is insufficient and has to be increased by choosing a CLT type with a bigger thickness. Additional measures, like adding TMDs, have to be considered.

Table 3.16: Comfort levels for floors in residential and industrial buildings [VDI 2038 Blatt 2: 2013-01]

Level of comfort	KB_{Fmax}-value
High comfort	$KB_{\mathrm{Fmax}} < 0.2$
Medium comfort	$0.2 \leq KB_{\mathrm{Fmax}} \leq 1.0$
Low comfort/discomfort	$1.0 \leq KB_{\mathrm{Fmax}} \leq 2.5$

4 Validation and Calibration of the Numerical Models

The developed numerical models are presented in Chapter 3. Before starting parametric studies, extensive investigations of the individual components are performed, to prevent errors and to achieve the best possible accuracy of the models, compared to the real structures. The FE models are examined by convergence and case studies. Unknown material properties are derived from experimental measured data. The developed acoustical model to predict the radiated sound power is validated by measured data from tests in the laboratory.

4.1 Validation of the Prediction Model for Sound Radiation

A numerical procedure to predict the radiated sound power of plate shaped structures from structure-borne sound velocities is presented in Section 3.7.1. It is shown that this model is applicable to simulated data and gives accurate results when the presented settings to prevent numerical errors are considered. This section shows, that the procedure is likewise applicable to measured data. Concurrently, this will prove the validation of the procedure.

4.1.1 Measurement set up

The data used in this section are taken from measurements, that are carried out at MÜLLER-BBM's window testing facility [Sremcevic Witzig 2012][Angerer 2011]. The measurement set up provides perfect conditions for a validation. For the testing, a aluminum plate of thickness 2 mm is arranged airtight inside a reverberant wall. The aperture measures $1.50 \text{ m} \times 1.30 \text{ m}$. The wall divides the laboratory into one source and one receiving room. In both source and receiving room, the walls opposite to the aluminum plate are covered with sound absorbing material (see Fig. 4.1), so that almost free field conditions are achieved. The plate is exited
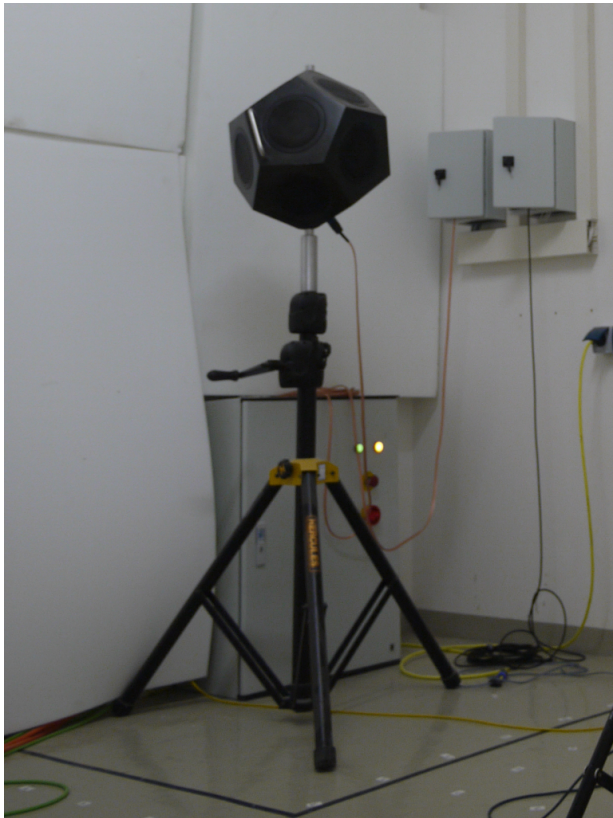
Figure 4.1: Dodecahedra loudspeaker [Angerer 2011]

Figure 4.2: Measurement robot [Angerer 2011] [Sremcevic Witzig 2012]

by a dodecahedra loudspeaker in the source room (see Fig. 4.1). Pink noise is used for the excitation to produce a signal of equal subjective loudness over frequency range.

The vibrational response of the plate, from which the radiated sound power is derived, is measured via a measurement robot (see Fig. 4.2). A grid of $n_\mathrm{x} \times n_\mathrm{y} = 25 \times 21$ measurement points, evenly distributed with a distance of $\Delta x = \Delta y = 0.059$ m, is scanned one by one. In every point, simultaneous measurements of the sound velocity of the plate as well as the sound intensity in a distance of 0.1 m orthogonal to the plate are carried out. Here, a pp-intensity probe with a coaxial arranged laser *Doppler* vibrometer is used. The arrangement of the measurement devices, attached to the robot's arm, is shown in Figure 4.3 and is sketched in Figure 4.4.

Figure 4.3: Aluminum plate with the intensity probe and the vibrometer [Angerer 2011] [Sremcevic Witzig 2012]
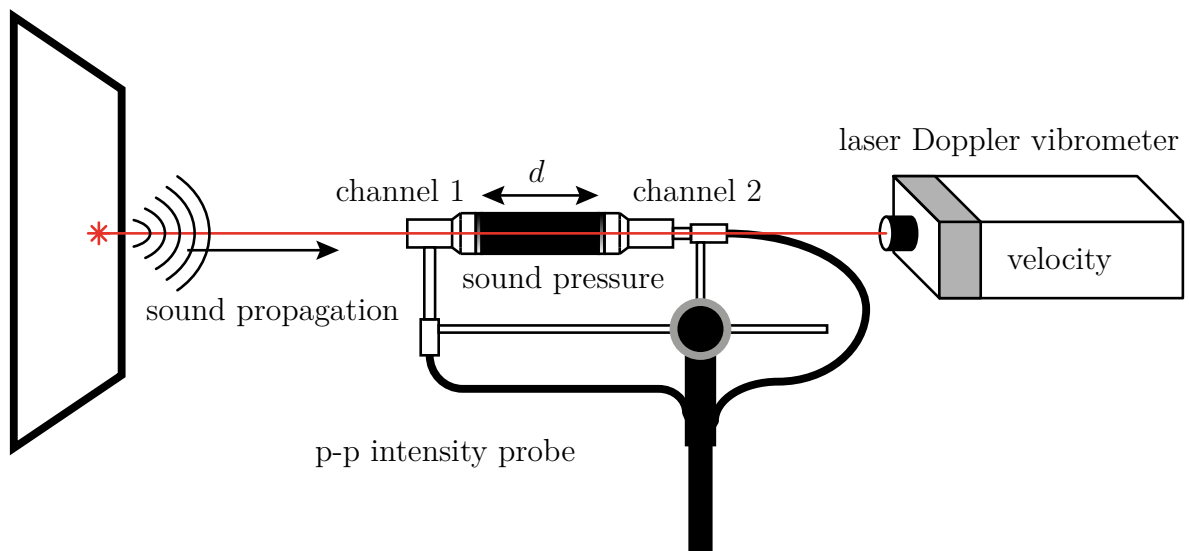
Figure 4.4: Sketch of the measurement set up [Angerer 2011] [Sremcevic Witzig 2012]

4.1.2 Comparison of measurement results

The radiated sound power of the aluminum plate is evaluated in two different ways. On the one hand, it is achieved from the structure-borne sound velocity on the plate's surface, that is measured by the laser *Doppler* vibrometer, using the prediction model, presented in Section 3.7.1. On the other hand the radiated sound power is calculated by Equation (4.1) for the discrete measurement technique [Jacobsen et al 1998]. Thus, the sound pressures measured by the intensity probe's two microphones $p_1(f)$ and $p_2(f)$ are taken into account .

$$p[\gamma] = -\frac{\Delta x \Delta y}{4\pi f_\gamma \rho_A d} \cdot \Im \left[\sum_{\alpha=1}^{N_x} \sum_{\beta=1}^{N_y} p_1[\alpha,\beta,\gamma] \cdot p_2^*[\alpha,\beta,\gamma] \right] \tag{4.1}$$

with

$d = 0.05$ m	Length of the spacer/ Distance between the microphones
$\rho_A = 1.21\ \frac{\text{kg}}{\text{m}^3}$	Air density
$N_x = 25,\ N_y = 21$	Number of measurement points (samples)
$f[\gamma]$	Discrete frequency
$p_1[\alpha,\beta,\gamma],\ p_2[\alpha,\beta,\gamma]$	Discrete sound pressure
α,β,γ	Spatial and frequency steps

The sample rate is 24600 Hz with a frequency step-width of $\Delta f = 2.0$ Hz.

The diagram in Figure 4.5 shows a comparison of both methods in the frequency range $0 - 400$ Hz. In addition to the radiated sound power levels out of the structure-borne velocity (vibrometer) and the sound intensity (pp-probe) a third graph is depicted, showing the ERP of a plane radiator (see Eq. (3.6)). The distance in between can be interpreted by the radiation efficiency level. The graphs match well above a frequency of ≈ 65 Hz. No reliable measurement results could be achieved in the frequency range below (highlighted in gray). This is caused by the measurement set-up. In that frequency range, the power level of the excitation signal is very low, free field conditions are questionable, since the absorption coefficient of the absorbing material at the receiving room, as well as its depth are insufficient. On top of that, the accuracy of the intensity probe decreases dramatically in this frequency range [Bangert 2000]. Contrary to that, the velocity measurements deliver results of even accuracy over the whole observed frequency range. As a result, the prediction model based on structure-borne velocity has proven to be equivalent to the common sound intensity based procedure for plate shaped structures. Only for very low frequencies the two

methods aren't comparable, while the surface velocity based method, here, is expected to deliver more accurate results.
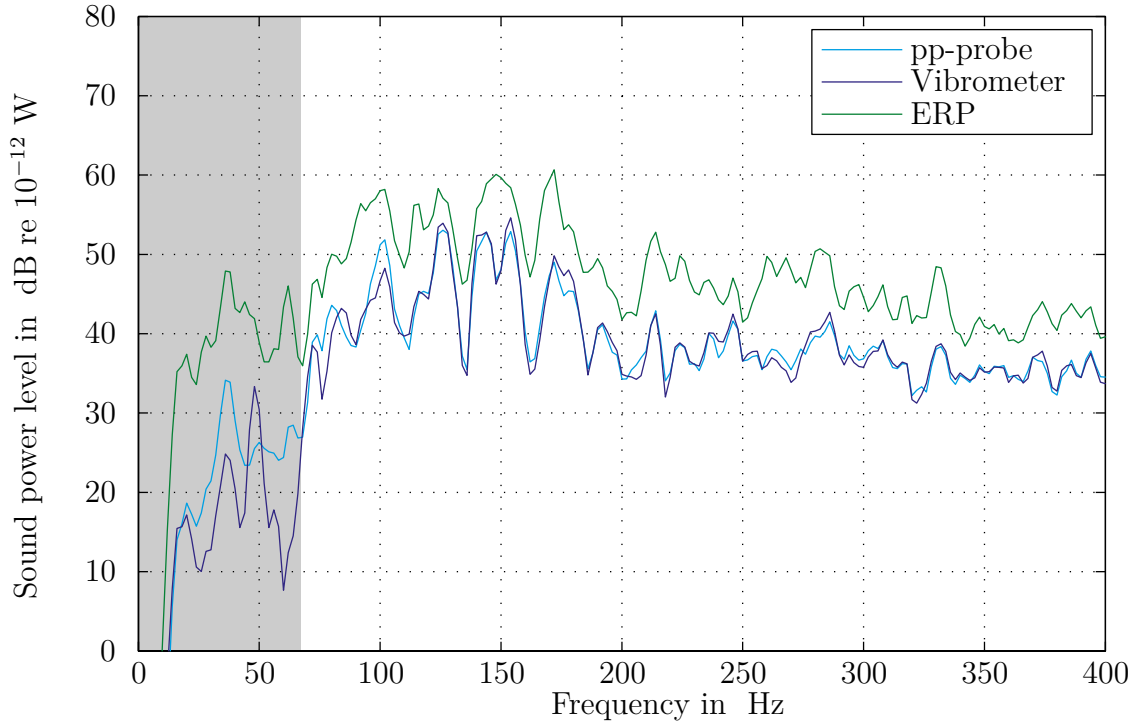
Figure 4.5: Comparison of sound power from intensity and velocity measurements. Additionally the (ERP) is depicted.

4.1.3 Evaluation in the wavenumber domain

A further possibility to evaluate the measured data is an investigation of the structure-borne sound velocity pattern of the surface of the plate in the wavenumber domain. Figure 4.6 shows an image plot of the spectral components for a single frequency step $\gamma = 267$ at 534 Hz. Clearly, two regions of high amplitudes are recognizable. Resonant vibrations appear at wavenumber combinations yielding for the bending wavenumber of the isotropic aluminum plate at this frequency

$$k_B = \sqrt{k_x^2 + k_y^2}.$$

Their main peaks lie on an ideal empty circle with the center at the origin and a radius k_B. The bending wavenumber can be calculated according to Equation (2.108) for every
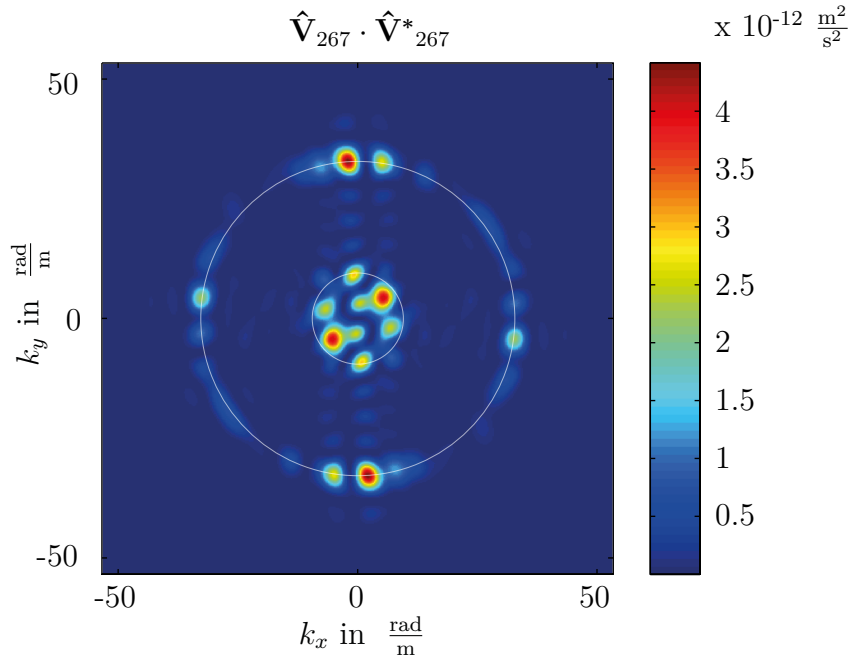
Figure 4.6: Example of an auto-power spectrum of the plate's velocity pattern in the wave number domain at 534 Hz

frequency step γ:

$$k_B[\gamma] = \sqrt{\sqrt{\frac{\rho_{\text{alu}} \cdot d}{E_{\text{alu}} \cdot \frac{d^3}{12}}} \cdot \sqrt{2\pi \cdot \Delta f \cdot \gamma}} \tag{4.2}$$

$$k_B[267] = 33.8 \ \tfrac{\text{rad}}{\text{m}} \tag{4.3}$$

with the dimensions and material properties of the plate

$d = 0.002$ m   thickness

$E_{\text{alu}} = 70000 \cdot 10^6 \ \tfrac{\text{N}}{\text{m}^2}$ *Young*'s modulus

$\rho_{\text{alu}} = 2700 \ \tfrac{\text{kg}}{\text{m}^3}$ density

$\Delta f = 2.0$ Hz   frequency step width.

The second (inner) region corresponds to the forced vibrations, leading to a solid circle with high amplitudes. The spectral components (wave numbers) inside this circle are those, excited by the airborne sound, caused by the loudspeaker. The wave number of air at this

frequency step yields

$$k_A[\gamma] = \frac{2\pi \cdot \Delta f \cdot \gamma}{c_A} \tag{4.4}$$

$$k_A[267] = 9.8 \, \tfrac{\text{rad}}{\text{m}}. \tag{4.5}$$

The sound field is considered to be diffuse due to the high modal density. Thus, the angle of the incident sound is arbitrarily oriented. This causes the excitation of vibration patterns with wavelengths $\lambda_x^2 + \lambda_y^2 \geq \lambda_A^2$. In the wave number spectrum, this is recognizable as well, since not only the wave number combinations on the circle with radius k_A, but all the region inside the circle $(k_x^2 + k_y^2 \leq k_A^2)$ is filled with high amplitudes .

The phenomenon of coincidence frequency can be explained quite descriptively using this representation. While the bending wave numbers of a plate k_B increase according to Equation (4.3) with the square root of the frequency, the wave number of air k_A grows linearly (see Eq. (4.5)). Subsequently, beyond the coincidence frequency, the spectral components on the radius k_B lie inside the circle with radius k_A, where all wave numbers are excited by the incident airborne sound.

4.2 Calibration of the Models of the Main Load-bearing Structures

The underlying structural models are introduced in Section 3.2. For the modeling of model components, a number of assumptions are made, that will be focus on in this section.

4.2.1 Convergence study on discretization

An important parameter during the developing process of a numerical model is the level of discretization respectively e.g. the edge length of volume or shell elements e_{size}. This parameter has a crucial impact on the models accuracy. With a higher level of discretization, the accuracy is increased, but the computational effort increases simultaneously. Since the developed structural models are linked parametrically, the edge length of each element was implemented as a global parameter. A convergence study is performed to find a value for e_{size} leading to best possible accuracy-to-effort relation. Therefore, the most complex structural model, the CLT floor, was tested [Greim 2012]. In this model, besides the edge length,

the number of elements per layer is of interest. The models eigenvalues serve as objective function.

Figure 4.7 shows the results of the convergence study of a five-layered CLT floor in the frequency range up to 125 Hz. The dimensions of the floor were 5.50 m × 5.50 m. On the right side of the diagram the individual level of discretization is depicted. The following configurations were investigated while paying attention to a maximum length ratio ($> 1 : 10$) with thinnest possible layer of 17.0 mm.

- Edge length: 0.1 m, Elements per layer:1

- Edge length: 0.05 m, Elements per layer:1

- Edge length: 0.05 m, Elements per layer:2

- Edge length: 0.05 m, Elements per layer:3

- Edge length: 0.25 m, Elements per layer:3

It becomes clear, that, although the number of DOF is increasing, the values of the monitored eigenfrequencies show no significant change. Hence the model's accuracy is sufficient for the initial level of discretization for most eigenfrequencies. A minor deviation is observable with increasing frequency. The mean deviation of the eigenvalues comparing the minimal and maximal configuration yields 1.2 %. Therefore, to minimize the computational effort, a global edge length of $e_{\text{size}} = 0.1$ m is chosen for all models. In case of CLT floors the study additionally proved that one element per layer is acceptable.
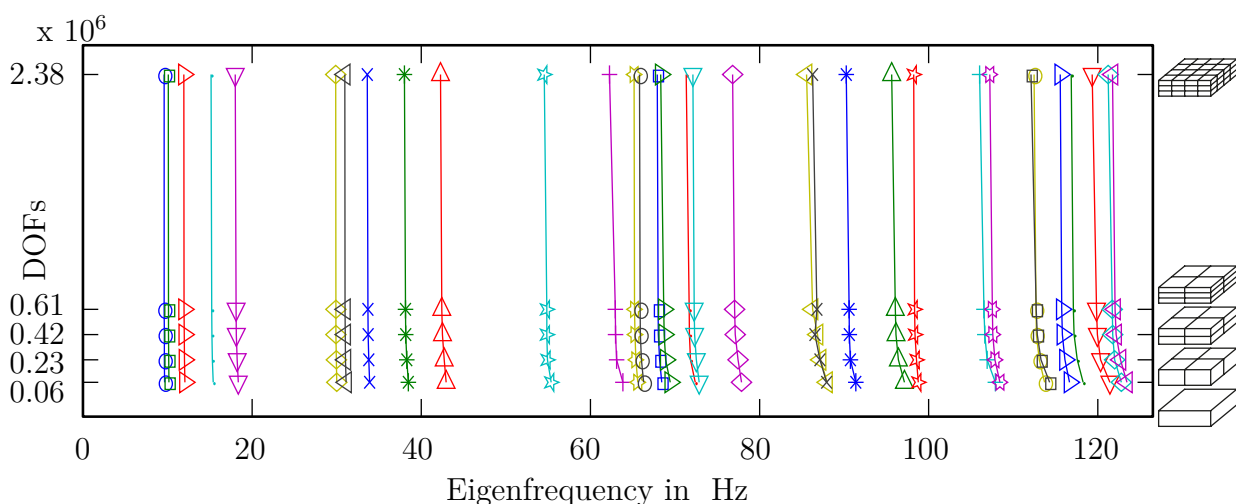
Figure 4.7: Convergence study on the element's edge length [Greim 2012]

4.2.2 Calibration of CLT's material parameters using Model-Updating

The prediction of the material properties of CLT has been subject to numerous studies in recent years. In most cases, large scale static laboratory testing to achieve the overall bending stiffness is performed and compared to the numerical model's result (e.g. [Blaß and Flaig 2012], [Feichter 2013]). The needed material properties are taken from literature or are derived from EMAs. Another approach is the calculation of the effective modulus of elasticity from measured quasi-longitudinal wavespeeds Churchill and Hopkins [2013b] Mahn and Hopkins [2013]. With the resulting parameters, the structure's eigenfrequencies are calculated and compared to frequencies from EMA results. [Churchill and Hopkins 2013b] compared measured to simulated eigenfrequencies using FE-software ABAQUS®. Also, an optimization algorithm of the elasticity parameters to match the measured eigenfrequencies was applied. However, the CLT was modeled by one layer of shell elements so the procedure aimed at the identification of optimized global elasticity parameters for the structural element rather than in material properties. A similar approach is shown in this section for the identification of idealized material properties for each layer.

In Section 3.2.2, several idealizations for the CLT model are introduced. The individual boards of one layer are modeled as a single volume neglecting the annular rings, the gapes between the boards and the relief groves. The connection between the layers is assumed to be rigid. Additionally, as derived in Section 2.1, the rolling shear, perpendicular *Young*'s modulus and consecutively the *Poisson* ratios cannot be predicted since the orientation of the annular rings of the individual boards is arbitrary. To deal with that issue, idealized material properties are used that are optimized compared to measured data [Greim 2012]. As an objective function $f(\mathbf{x})$ the Root Mean Square (RMS) value of the deviation of simulated and measured eigenfrequencies in the observed frequency range $0 - 150$ Hz is used.

$$f(\mathbf{x}) = \sqrt{\frac{1}{k} \sum_{i=1}^{k} \left(\frac{f_{s,i}(\mathbf{x}) - f_{m,i}}{f_{m,i}} \right)^2}, \quad k = \text{number of considered eigenfrequencies} \qquad (4.6)$$

Opposite to the measured eigenfrequencies $f_{m,i}$ the simulated eigenfrequencies $f_{s,i}$ depend on the vector of optimization variables $\mathbf{x}$. The optimization consists in two steps. First a grid search (zero order method) is performed to find a global minimum of the objective function. The achieved results serve as initial parameters for the second step, an optimization algorithm using the steepest decent method (first order).

4.2.2.1 Grid search - zero order optimization

In this step, a single CLT element on elastomer supports was tested. The initial parameter grid given in Table 4.1 is chosen. Those initial parameters representing the material properties of spruce are taken from [Gülzow 2008] and [Lieblang 2000]. A change of parameter $\nu_{\perp\perp,\mathrm{spr}}$ has negligible influence on the result and is therefore set fix to 0.3 [Hopkins 2007].

An accurate analytical determination of *Young*'s modulus of the elastomer supports is difficult. As described by Negeira [2013] the applied material Sylomer manufactured by Getzner Werkstoffe GmbH has material properties that behave non-linearly with frequency, shape factor and boundary conditions. To deal with that issue its *Young*'s modulus is introduced as an additional optimization parameter. As initial value the manufacturer's data is considered [Getzner 2016].

Table 4.1: Parameter grid for a single CLT element

	Min. value	Increment	Max. value	Unit
$E_{\parallel,\mathrm{spr}} = E_{x,\mathrm{spr}}$	$9700 \cdot 10^6$	$300 \cdot 10^6$	$11200 \cdot 10^6$	$\frac{\mathrm{N}}{\mathrm{m}^2}$
$E_{\perp,\mathrm{spr}} = E_{y,\mathrm{spr}} = E_{z,\mathrm{spr}}$	$400 \cdot 10^6$	$100 \cdot 10^6$	$800 \cdot 10^6$	$\frac{\mathrm{N}}{\mathrm{m}^2}$
$G_{\parallel\perp,\mathrm{spr}} = G_{xy,\mathrm{spr}} = G_{xz,\mathrm{spr}}$	$400 \cdot 10^6$	$50 \cdot 10^6$	$600 \cdot 10^6$	$\frac{\mathrm{N}}{\mathrm{m}^2}$
$G_{\perp\perp,\mathrm{spr}} = G_{yz,\mathrm{spr}}$	$40 \cdot 10^6$	$10 \cdot 10^6$	$80 \cdot 10^6$	$\frac{\mathrm{N}}{\mathrm{m}^2}$
$\nu_{\parallel\perp,\mathrm{spr}} = \nu_{xy,\mathrm{spr}} = \nu_{xz,\mathrm{spr}}$	0.02	0.01	0.07	$-$
E_{elasto}	$7 \cdot 10^6$	$1.5 \cdot 10^6$	$13 \cdot 10^6$	$\frac{\mathrm{N}}{\mathrm{m}^2}$

A minimum and maximum value as well as increment is chosen for each parameter defining the range of the grid search. The chosen grid results in approximately 15000 tested parameter combinations with the corresponding objective function depicted in Figure 4.8. Clearly regions of constant parameters are observable. For a better visualization, the corresponding parameters are depicted in Figure 4.8 along with a gray window marking the constant region. One can see that for parameter combination 14475 a minimum of 2.01 % is reached.

The corresponding parameter combination is shown in Table 4.2. It has to be noticed that in most cases the chosen extrema were found and the trend of the graph in Figure 4.8 doesn't ultimately prove a global minimum. Hence, it is clear that the found results can only serve as initial values for a more detailed optimization.

Table 4.2: Grid search results for a single CLT element

$E_{\parallel,\mathrm{spr}}\ \frac{\mathrm{N}}{\mathrm{m}^2}$	$E_{\perp,\mathrm{spr}}\ \frac{\mathrm{N}}{\mathrm{m}^2}$	$G_{\parallel\perp,\mathrm{spr}}\ \frac{\mathrm{N}}{\mathrm{m}^2}$	$G_{\perp\perp,\mathrm{spr}}\ \frac{\mathrm{N}}{\mathrm{m}^2}$	$\nu_{\parallel\perp,\mathrm{spr}}\ -$	$E_{x,\mathrm{elasto}}\ \frac{\mathrm{N}}{\mathrm{m}^2}$
11200	400	550	80	0.07	13
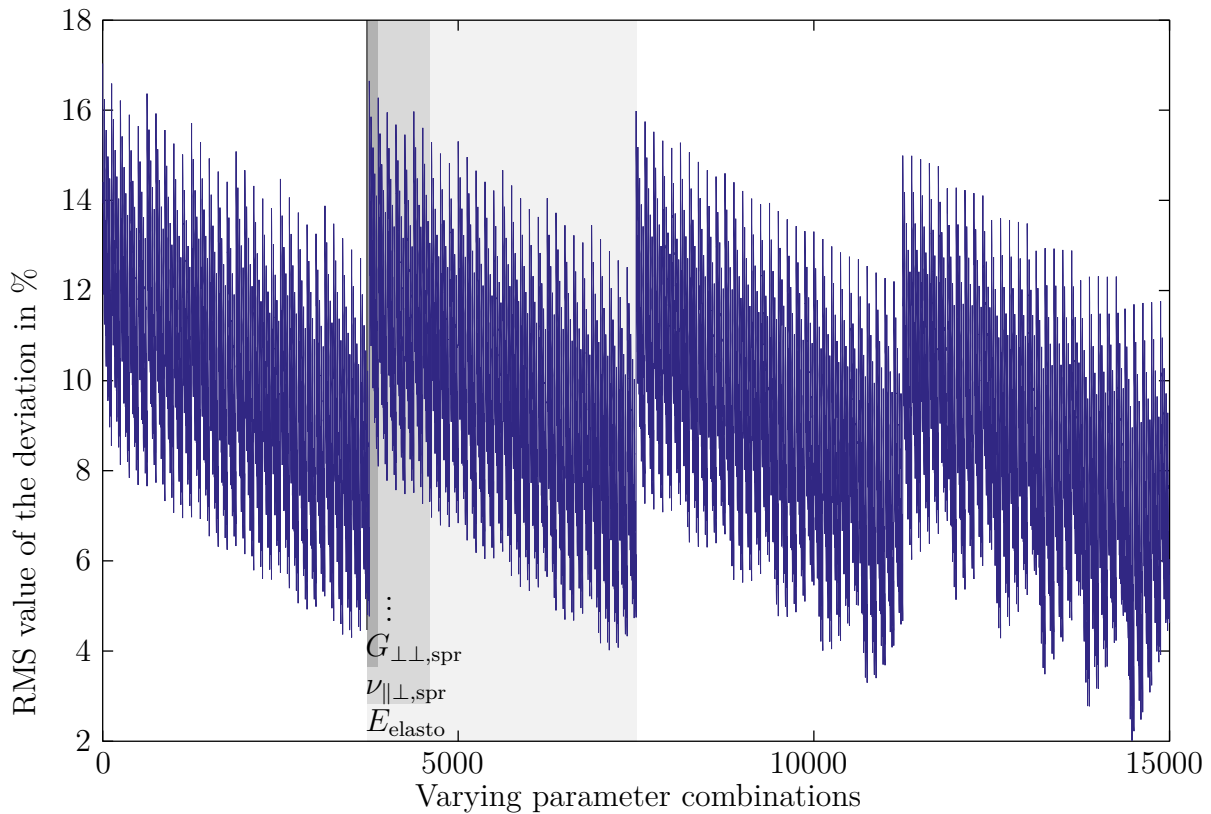
Figure 4.8: Results of the grid search [Greim 2012]

4.2.2.2 Steepest descent - first order optimization

Starting from the material parameters achieved in the last section by a grid search, a second optimization phase is performed using the gradient based steepest descent method. Different to the grid search which only based on a single CLT element in this step different models of floors consisting of $1-4$ interconnected elements are simulated and updated parallel. Therefore, the coupling between the individual elements has to be taken into account. Thus, the spring stiffness of the coupling $k_{y,\text{lin}}$ is introduced as an additional optimization parameter. Its initial value of $10.0 \ \frac{\text{N}}{\text{m}}$ is approximated by preliminary calculations from the stiffness properties of the connecting KERTO LVL boards [Greim 2012].

A scheme of the optimization process is sketched in Figure 4.9. The entire process is started and controlled in MATLAB®. First, the initial values for the material properties are implemented into the sub modules of the structural models. Next, the simulation in ANSYS® is started in batch mode reading from the input file that includes modules of CLT floor, elastomer support and Modal Analysis. The resulting eigenvalues and eigenvectors are read out of the output file. Before introducing the eigenvalues into the objective function, care has to be taken for a matching of simulated and measured eigenmodes. Depending on the cho-
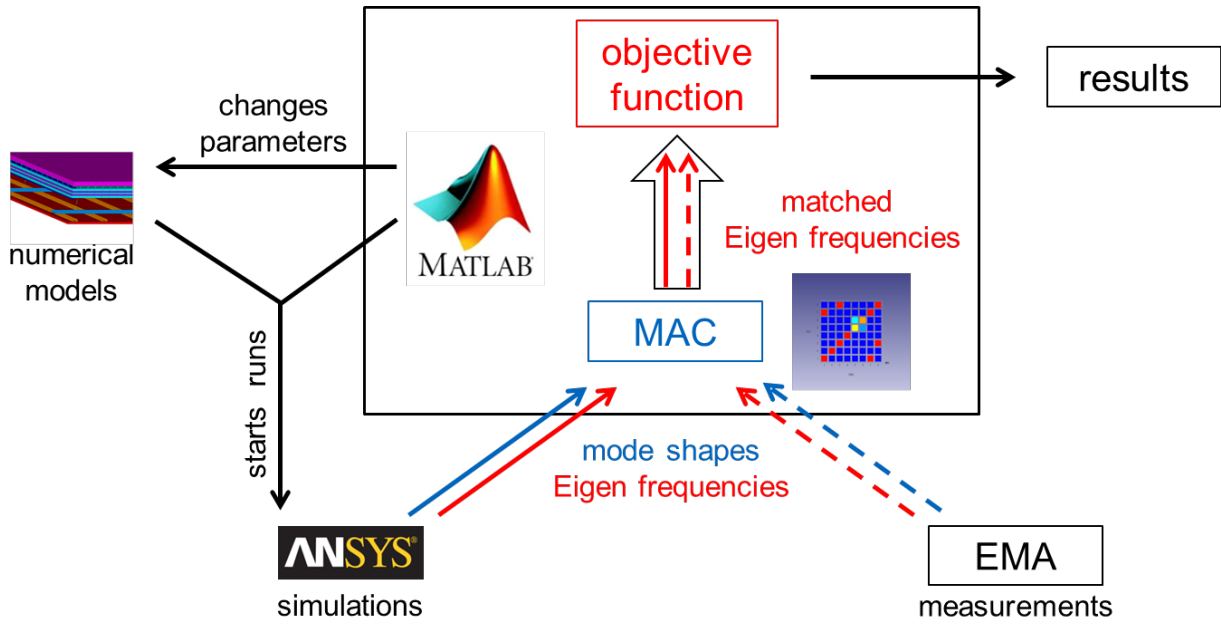
Figure 4.9: Optimization process

sen parameter, the order of eigenmodes can change. Therefore, the individual eigenvectors (m: measured, s: simulated, j,k: ascending number of the eigenmode) are compared by the Modal Assurance Criterion (MAC) which is defined as [Friswell and Mottershead 1995]:

$$\mathbf{MAC}_{jk} = \frac{\left|\mathbf{\Phi}_{mj}^T \mathbf{\Phi}_{sk}\right|^2}{(\mathbf{\Phi}_{sk}^T \mathbf{\Phi}_{sk})(\mathbf{\Phi}_{mj}^T \mathbf{\Phi}_{mj})} \tag{4.7}$$

Results from the MAC function range from $0 - 1$, where a value near unity indicates, that two observed eigenmodes can be assumed to coincide [Allemang 2003]. Only those are considered for the objective function, which can also include a preliminary reordering. After that, the value of the objective function is calculated and the optimization parameters are recalculated using a steepest descent algorithm, described by Greim [2012]. Finally a new simulation based on these parameters is started and the procedure is repeated, until an interruption criterion is achieved.

The results of the model-updating and the initial values are listed in Table 4.3. The objective function's RMS value was improved from the initial value of 7.32 % to 5.01 %. Multiple floor models are optimized in parallel, which leads to a difference between the initial value and the result of the grid search in Section 4.2.2.1. The newly found idealized material parameters lie within expected range. The idealization of the individual boards neglecting the gaps in between and relief grooves inside the boards lead to a low value of $E_\perp$. As described in

Table 4.3: Final parameters of optimization

Parameter		Initial value	Result
$E_{\parallel}$	$\frac{\text{MN}}{\text{m}^2}$	11200	10981
$E_{\perp}$	$\frac{\text{MN}}{\text{m}^2}$	400	137
$G_{\parallel\perp}$	$\frac{\text{MN}}{\text{m}^2}$	550	459
$G_{\perp\perp}$	$\frac{\text{MN}}{\text{m}^2}$	80	74.2
$E_{x,Syl}$	$\frac{\text{MN}}{\text{m}^2}$	13	11.3
$k_{y,lin}$	$\frac{\text{MN}}{\text{m}}$	10	10.1
$\nu_{\parallel\perp}$	—	0.07	0.052
RMS value for initial values			7.32 %
RMS value after Model-Updating			5.01 %

Section 2.1.5, the angle of annular rings suggests a reduction of $E_{\perp}$. The higher value of $G_{\perp\perp}$ compared to the nominal value can be explained analogously. Thus, a complete set of validated material properties is achieved for the considered CLT floors.

4.2.3 Investigations on material properties of LJ floors

In Section 3.2.3, LJs as well as OSBs are modeled as orthotropic materials. Even if in both cases theoretical material properties can be found in manufacturer's data sheets and standards a scatter is assumed within the assembled components. Therefore, in this section, the material properties are subject to investigations. Eigenfrequency measurements carried out for each of the individual components and compared to numerical or analytical estimated eigenfrequencies. In case of greater deviations the material parameters will be adapted.

4.2.3.1 Lumber joists

As discussed in Chapter 2.1, besides its density, nine independent elasticity constants are needed to completely describe orthotropic material. These constants can be derived from laboratory testing. Caused by the anatomy of wood, this results in a cylindrical coordinates representation that is longitudinal, tangential and radial to the fibers and annular rings (L,R,T). The elasticity constants for spruce have been derived by numerous distributions (e.g. [Lieblang 2000], [Kretschmann 2010], [Neuhaus 2009], [Grimsel 1999] etc.). For numerical simulations, the material properties have to be converted into component properties using *Cartesian* coordinates. Since the sawing pattern is arbitrary, elasticity constants can be summarized into parallel and perpendicular to the fibers $E_{\parallel}$, $E_{\perp}$, $G_{\parallel\perp}$, $G_{\perp\perp}$, $\nu_{\parallel\perp}$ and $\nu_{\perp\perp}$
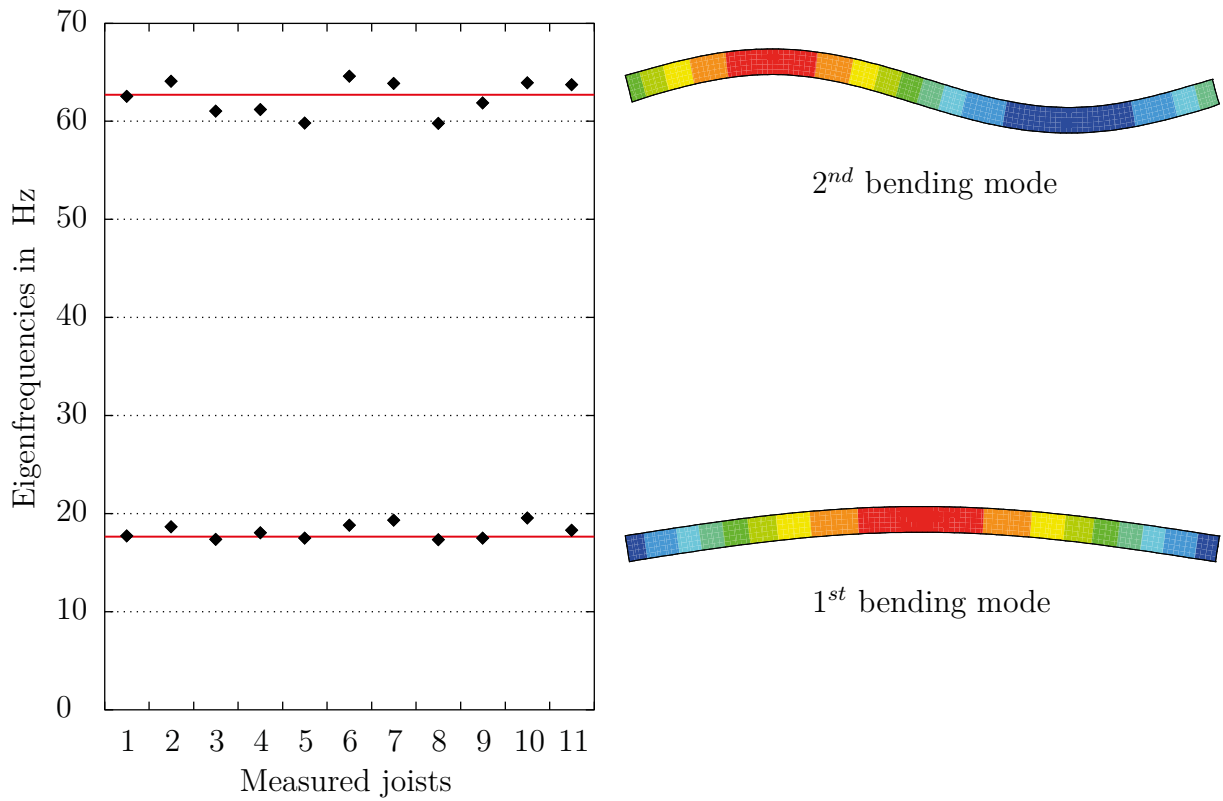
Figure 4.10: First two eigenfrequencies of joists - measurement and numerical results

reducing them to six independent components. Different from CLT, in LJs, $E_\perp$ and $G_{\perp\perp}$ have negligible impact on the simulation results, since only torsional and bending deformations along the fiber direction appear. Consequently, the material properties of wooden joists can be approximated according to Neuhaus [2009] and Gülzow [2008] as follows:

$$E_{\mathrm{x}} = E_\parallel = E_{\mathrm{L}}$$
$$E_{\mathrm{y}} = E_{\mathrm{z}} = E_\perp = E_{\mathrm{T}}$$
$$G_{\mathrm{xy}} = G_{\mathrm{xz}} = G_{\parallel\perp} = G_{\mathrm{LT}}$$
$$G_{\mathrm{yz}} = G_{\perp\perp} = G_{\mathrm{RT}}$$
$$\frac{\nu_{\mathrm{xy}}}{E_{\mathrm{x}}} = \frac{\nu_{\mathrm{xz}}}{E_{\mathrm{x}}} = \frac{\nu_{\mathrm{yx}}}{E_{\mathrm{y}}} = \frac{\nu_{\mathrm{zx}}}{E_{\mathrm{z}}} = \frac{\nu_{\parallel\perp}}{E_\parallel} = \frac{\nu_{\perp\parallel}}{E_\perp} = \frac{\nu_{\mathrm{LR}} + \nu_{\mathrm{LT}}}{2E_{\mathrm{L}}}$$
$$\implies \nu_{\mathrm{xy}} = \nu_{\mathrm{xz}} = \frac{\nu_{\mathrm{LR}} + \nu_{\mathrm{LT}}}{2}$$
$$\frac{\nu_{\mathrm{yz}}}{E_{\mathrm{y}}} = \frac{\nu_{\mathrm{zy}}}{E_{\mathrm{z}}} = \frac{\nu_{\perp\perp}}{E_\perp} = \frac{\nu_{\mathrm{TR}}}{E_{\mathrm{T}}}$$
$$\implies \nu_{\mathrm{yz}} = \nu_{\mathrm{TR}}$$

To verify the material parameters, eigenfrequency measurements for the eleven individual lumber joists are carried out. Models with material properties from literature result in higher eigenfrequencies compared to the measured data. This is solved by an increase of the density. Iteratively, the parameters listed in Table 3.5 are found. The altered results for the first two eigenfrequencies are subsequently compared to corresponding eigenvalues from an FE simulation. Figure 4.10 shows both results, measured eigenfrequencies are indicated by black diamonds, the simulated results by red horizontal lines. The diagram shows the scatter of the measured results. The first eigenfrequency varies from $18 - 20$ Hz the second from $60 - 65$ Hz. The simulated data correlate with the mean values of the measurements when the density is increased by $\approx 10\%$.

4.2.3.2 OSB material properties

In case of the applied OSBs, the manufacturer gives only an incomplete set of material properties. The data sheet for the product called AGEPAN OSB/4 PUR fabricated by GLUNZ lists the values summarized in Table 4.4 [Glunz 2016]:

Table 4.4: Material parameters for AGEPAN OSB/4 PUR from data sheet

Parameter	Value	Unit
ρ	> 600	$\frac{\text{kg}}{\text{m}^3}$
E_0	$6780 \cdot 10^6$	$\frac{\text{N}}{\text{m}^2}$
E_{90}	$2680 \cdot 10^6$	$\frac{\text{N}}{\text{m}^2}$
G_v	$1090 \cdot 10^6$	$\frac{\text{N}}{\text{m}^2}$
G_r	$60 \cdot 10^6$	$\frac{\text{N}}{\text{m}^2}$

These are the values required by standard the DIN 12369-1:2001-04, which implies, that no testing was done by GLUNZ to achieve accurate data. Therefore, the applied eight OSBs, each with dimensions of 1.25 m × 2.50 m × 0.018 m, will be investigated to achieve the most important parameters ρ_{OSB}, $E_{\text{x,OSB}}$ and $E_{\text{y,OSB}}$. In a first step, the individual board's density is figured out by weighting and a mean density is derived from all samples. Bending stiffnesses in $x-$ and $y-$direction are deduced from EMA measurements. Each board is uni-axial simple line supported in the main (x) and secondary (y) load bearing direction and excited in the center of the board by a modal hammer. An accelerometer gives the systems response. Out of the resulting frequency response function, the first natural eigen-frequencies are extracted. The corresponding *Young*'s moduli can in turn be approximated

by rearranging of the equation for eigenfrequencies of beams in bending [Müller 2011]:

$$f_n = \frac{\pi \cdot n^2}{2 \cdot l^2} \cdot \sqrt{\frac{E \cdot I_{\mathbf{z}}}{\mu}} \tag{4.8}$$

Figure 4.11 shows a diagram of the resulting density and *Young*'s moduli in the main load bearing direction for the individual boards. All achieved results are summarized in Table 4.5 including the measured eigenfrequencies. Clearly a major scatter between the values of the individual boards is visible in Figure 4.11.
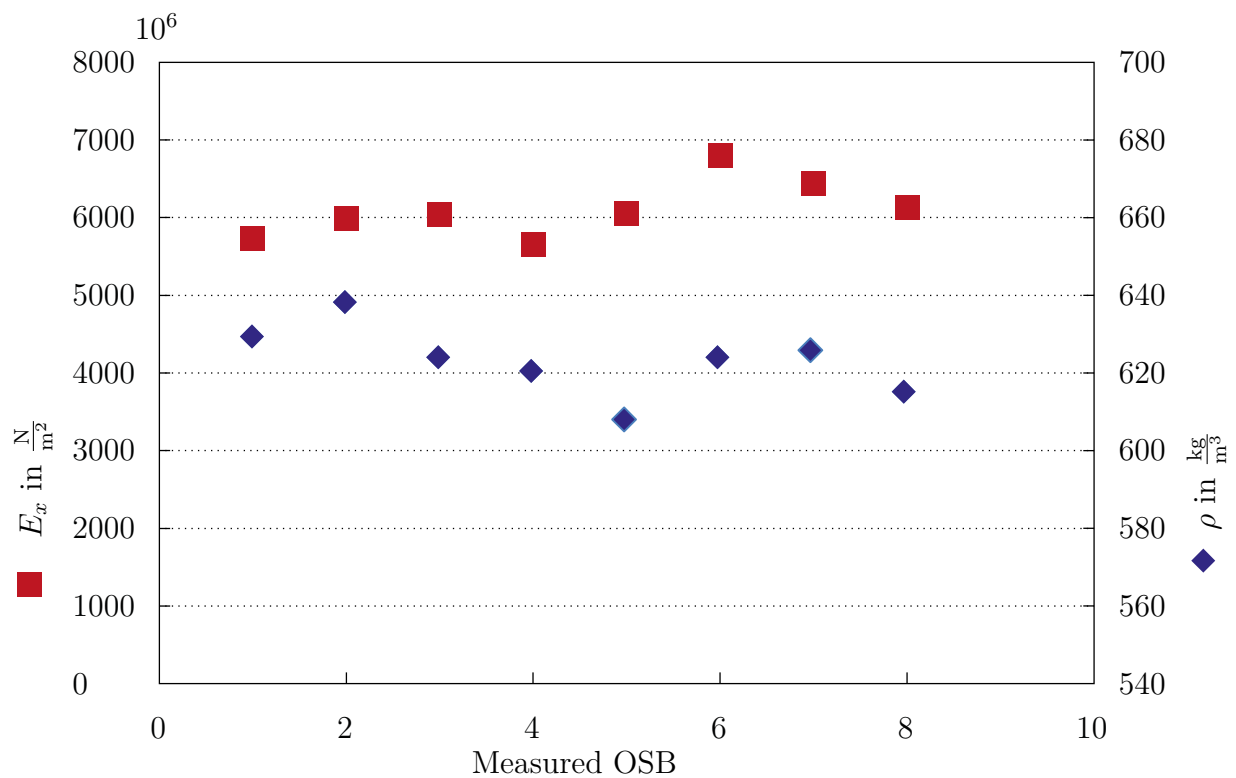
Figure 4.11: Measured and derived parameters per OSB sample

Table 4.5: Measurement results for implemented OSBs

Sample	m kg	ρ $\frac{\text{kg}}{\text{m}^3}$	$f_{1\text{x}}$ Hz	E_{x} $\frac{\text{N}}{\text{m}^2}$	$f_{1\text{y}}$ Hz	E_{y} $\frac{\text{N}}{\text{m}^2}$
1	35.4	629.3	3.9	$5728 \cdot 10^6$	9.6	$2108 \cdot 10^6$
2	35.9	638.2	4.0	$5988 \cdot 10^6$	9.4	$2058 \cdot 10^6$
3	35.1	624.0	4.1	$6031 \cdot 10^6$	9.1	$1877 \cdot 10^6$
4	34.9	620.4	3.9	$5647 \cdot 10^6$	9.4	$2026 \cdot 10^6$
5	34.2	608.0	4.1	$6051 \cdot 10^6$	9.7	$2092 \cdot 10^6$
6	35.1	624.0	4.3	$6797 \cdot 10^6$	9.6	$2116 \cdot 10^6$
7	35.2	625.8	4.2	$6442 \cdot 10^6$	9.7	$2153 \cdot 10^6$
8	34.6	615.1	4.1	$6122 \cdot 10^6$	9.4	$2009 \cdot 10^6$
mean value	35.1	623.1	4.1	$6097 \cdot 10^6$	9.5	$2055 \cdot 10^6$

However, the density and the stiffness seem to be correlated. This results in a much smaller scatter of the measured eigenfrequencies, which, in turn, indicates that the modeling of each board individually is not necessary. The calculated mean values are therefore considered for the simulations. While the density matches the manufacturer's data, the elasticity moduli are much lower than given in Table 4.4. The missing parameter for an orthotropic model are set according to Meistring [2005].

4.3 Damping Coefficients derived from Measurements

Damping effects are included into the FE models by proportional damping, by introducing the *Rayleigh* damping factors α and β. Thus, the problem can be diagonalized by splitting the damping matrix $\mathbf{C}$ into one part proportional to the mass matrix $\mathbf{M}$ and a second part proportional to the stiffness matrix $\mathbf{K}$ [Petersen 1996].

$$\mathbf{C} = \alpha\,\mathbf{M} + \beta\,\mathbf{K}. \tag{4.9}$$

The damping factors for CLT and LJ floors are derived from EMA measurements using the commercial software ME'scopeVES® from Vibrant Technology Inc. [Borch 2013].

The resulting modal damping coefficients ζ_i per measured eigenfrequency $f_i = \frac{\omega_i}{2\pi}$ for both floor constructions are depicted in Figure 4.12. They are related to the *Rayleigh* damping
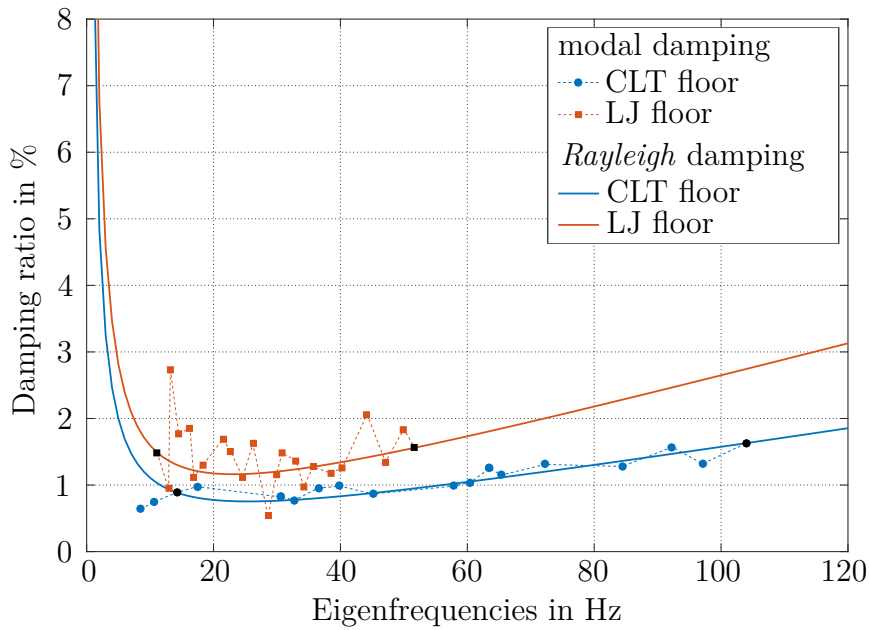
Figure 4.12: Measured modal damping coefficients ζ_i for an LJ and an CLT floor compared to the resulting *Rayleigh* damping

factors by the following equation:

$$\alpha + \beta \omega_i^2 = 2\zeta_i \omega_i \tag{4.10}$$

When the modal damping for two eigenfrequencies (e.g. for $i = 1$ and $i = 2$) is known, Equation (4.10) can be solved, using the substitutions

$$\omega_2 = a\omega_1 \quad (a > 1) \qquad\qquad \zeta_2 = b\zeta_1 \tag{4.11}$$

to derive the *Rayleigh* damping factors

$$\alpha = \frac{a - b}{a^2 - 1} a \cdot 2\omega_1 \zeta_1 \qquad\qquad \beta = \frac{ab - 1}{a^2 - 1} a \cdot 2\frac{\omega_1}{\zeta_1}. \tag{4.12}$$

The modal damping coefficients for the LJ floor are scattered, while for the CLT floor, almost a linear behavior is observable. Additionally, in case of the LJ floor, only eigenfrequencies up to ≈ 50 Hz are identified. Thus, the resulting values for α and β depend on the choice of the two specific reference eigenfrequencies and the assigned modal damping coefficient (black markers). In case of the CLT floor, a good correlation is achieved, while for the LJ floor, a less accurate but still feasible approximation is found. The resulting values of α and β for both floor constructions are listed in Table 3.13 in Section 3.3.

4.4 Calibration of the Suspended Ceiling Model

Similar to the main structures, simplified assumptions have been met for the model of the SC. The real model of the paneling consists of two layers of individual plaster boards that are arranged crosswise and screwed together, whereas the numerical model is simplified as a single homogeneous plate. The hangers are modeled as simple one-dimensional linear spring-damper elements. Idealized material parameters have to be achieved to compensate the introduced uncertainties.

The applied gypsum plaster boards of type GKB A are manufactured by KNAUF. The individual boards measure $1.25\,\text{m} \times 2.50\,\text{m} \times 0.0125\,\text{m}$. Density and *Young*'s moduli according to the manufacturer's data sheet [Knauf 2013] are listed in Table 4.6 with *Poisson* ratio set to $\nu_{\text{gypsum}} = 0.2$ [Wiechert 2005].

Table 4.6: Material parameters according to the manufacturer (data sheet GKB A)

Parameter	Value	Unit
ρ	≥ 680	$\frac{\text{kg}}{\text{m}^3}$
E_0	$\geq 2800 \cdot 10^6$	$\frac{\text{N}}{\text{m}^2}$
E_{90}	$\geq 2200 \cdot 10^6$	$\frac{\text{N}}{\text{m}^2}$

Those values lack the accuracy for a detailed FE model, and thus are be calibrated by measurements. The density can be achieved by weighing of the individual plates. Tröbs [2013] measures a density of $\rho_{\text{gypsum}} = 856\,\frac{\text{kg}}{\text{m}^3}$. The paneling's elasticity modulus is derived from investigations in the wave number domain.

4.4.1 Elasticity properties of the paneling derived in the wave number domain

Here, it is assumed that the cross-wise arrangement of the two layers of the paneling leads to an equal bending stiffness in both directions. The idealized plate is therefore assumed to have isotropic properties with a equal mean *Young*'s modulus in both load bearing directions. The numerical model simplifies the paneling into a single plate, which can be interpreted, as a rigid shear contact between the two board layers. This leads to overestimation of the bending stiffness, when the manufacturers elasticity data are considered. Thus, the bending stiffness has to be idealized to match the real construction. Its value can range from an

upper limit, representing a solid plaster board of twice the thickness $(2 \cdot d)$, to its lower limit, when two parallel boards without shear contact are assumed.

$$EI_{\mathrm{max}} = E \cdot \frac{(2 \cdot d)^3}{12 \cdot (1 - \nu^2)}$$

$$EI_{\mathrm{min}} = 2 \cdot E \cdot \frac{d^3}{12 \cdot (1 - \nu^2)}$$

$$\frac{EI_{\mathrm{max}}}{EI_{\mathrm{min}}} = 4$$

Within the numerical model, the thickness of the plate is set to $2 \cdot d$. Thus, idealizing the bending stiffness is performed by an adaptation on the elasticity modulus. Analogously to the bending stiffness the following range must be considered:

$$\frac{E_{90}}{4} \leq E_{\mathrm{x,gpb}} \leq E_0 \tag{4.13}$$

As shown in Section 4.1.3, the bending wave number of a plate at a specific frequency can be figured out by investigating the location of the peaks in the wave number domain. For higher frequencies the bending wave numbers reassemble those of an infinite plate as in Equation (4.3). Thus, the idealized elasticity modulus of the paneling can be approximated by fitting the curve described by Equation (4.3) to the measured bending wave number over frequency.
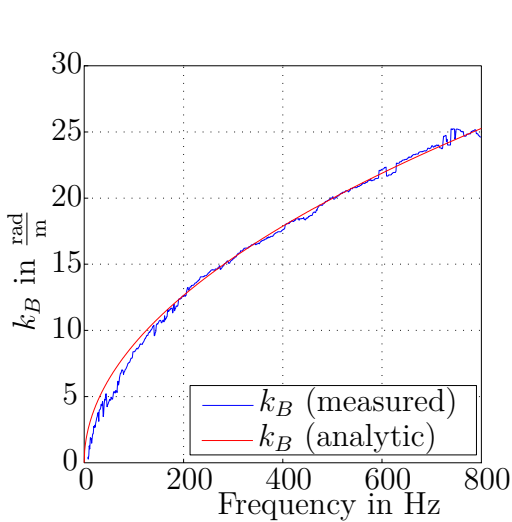
Figure 4.13: Bending wave number curve for the applied SC; measured vs. analytical solution for infinite plates
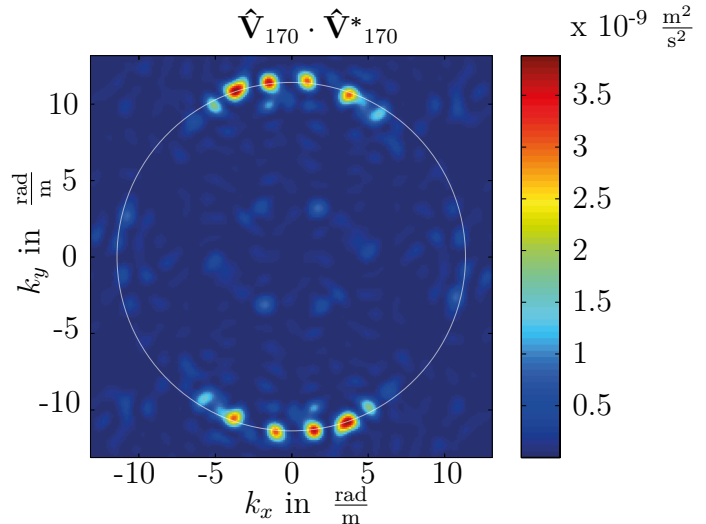
Figure 4.14: Velocity pattern of a directly excited SC in the wave number domain at 170 Hz with superimposed k_B-circle

The graph of the measured bending wave numbers in the frequency range from $0 - 800$ Hz for a paneling suspended from a CLT floor is shown in Figure 4.13 (blue). The function of the bending wave number of an infinite plate with an iteratively adapted *Young*'s modulus of $E_{\mathrm{x,gpb}} = 1020 \cdot 10^6 \; \frac{\mathrm{N}}{\mathrm{m}^2}$ is superimposed in red. The curves show a very good match. *Young*'s modulus lies within the estimated range (see Eq. (4.13)). Figure 4.14 shows the velocity pattern in the wave number domain at 170 Hz. The results are derived form the same SC applied to a different main floor (LJ floor). Direct shaker excitation was performed. The bending wave number of the paneling at this frequency calculated with Equation (4.3) for the elasticity modulus derived above yields $k_{\mathrm{B}} = 11.5 \; \frac{\mathrm{rad}}{\mathrm{m}}$. To compare the bending wave numbers the calculated result is inserted into the measured spectrum by an superimposed circle with radius k_{B}. The peaks of the shown spectrum perfectly match the circle, which verifies the resulting material properties are independent of the main floor the ceiling is suspended from.

4.4.2 Determination of stiffness data for suspended ceiling hangers

The resilient hangers are idealized as linear spring-damper-elements in Section 3.2.6. A possible determination of the stiffness data is presented in Brunskog and Hammer [2002]. An apparatus for the measurements is described, where the resilient hangers are mounted in between a two-fold rigid body setup exited by a shaker. Churchill and Hopkins [2013a] investigate a rubber isolator type of resilient hanger using the apparatus described by Brunskog and Hammer [2002] and compare it to results from a SEA model. The application of a one-dimensional wave continuum for this hanger type is not verified.

Since the numerical investigations in this thesis focus on a frequency range up to 150 Hz, the stiffness and damping properties of the hangers can be assumed to be constant in the considered frequency range. Maznikova [2012] derives the stiffness data for several resilient hanger systems using EMA. A measurement setup is chosen where the hangers are mounted to a concrete floor of very high bending stiffness that can be assumed as rigid in the evaluated frequency range. One of the load configurations is equal to the in-situ situation. From the measured first natural frequency the stiffness and damping data are derived. For the applied sound isolation hangers, shown in Figure 4.15, the data given in Table 4.7 are taken from Maznikova [2012].

Table 4.7: Spring stiffness and damping constant of the simulated sound insulation hanger

Parameters	Value	EUnit
$k_{\text{hang,m}}$	$0.165 \cdot 10^6$	$\frac{\text{N}}{\text{m}}$
$c_{\text{hang,m}}$	$0.78 \cdot 10^2$	$\frac{\text{Ns}}{\text{m}}$

Figure 4.15: Sound insulation hanger

4.5 Aspects Regarding the Modeling of Air Inside a Cavity

The air cushion between main floor and the suspended ceiling paneling can be modeled using different approaches that vary as regards the level of idealization and consequently, the computational effort is affected. Two approaches are investigated in this section. In the first approach, the cushion is assumed as individual columns of air, without interaction in horizontal direction, idealized as one-dimensional vertical springs (COMBIN14) or rods (BEAM181) (see Fig. 4.16). Alternatively, the air inside the cavity is modeled as a volume using acoustical fluid elements (FLUID30) (see Fig. 4.17). The latter approach is associated with a significant increase in computational effort. The interaction between fluid and structure causes unsymmetrical matrices. Therefore, higher order solution methods are necessary,

as described in Section 3.5. Additionally, the number of DOFs is significantly higher than in the first approach.
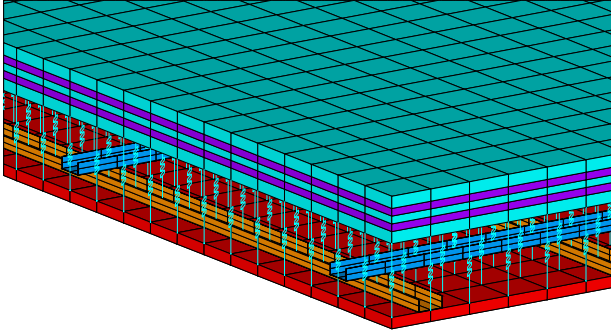
Figure 4.16: Air, modeled as spring elements
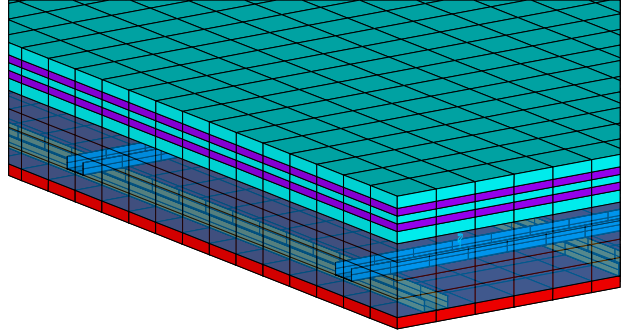
Figure 4.17: Air, modeled as fluid elements

4.5.1 Validation of reference data

The different approaches will be evaluated by comparing to reference data from measurements. Therefore, a set of measurement results must be first validated. As described in Section 4.1, the radiated sound power from intensity measurements is compared to the results derived from structure-borne sound velocities on the surface of the suspended ceiling, using the prediction model, which was presented in Section 3.7.1. Different to the validation in Section 4.1, in this case acceleration data from transducers are used and converted into velocity data. The excitation is done by a electrodynamic shaker unit. Figure 4.18 shows a comparison of the resulting graphs of the sound power level. For comparable results to the simulated data, the force spectrum induced by the shaker is normalized to 1.0 N. The graphs match very good from ≈ 30 Hz on. The deviations below this frequency (marked in gray) is caused by the excitation signal. A logarithmic sinus sweep was used that induced very little energy within this range.

However, since the spatial resolution of the measurement positions ($\Delta x = 0.25$ m) is chosen very coarse, the good match, at first glance, comes unexpected. Taking the bending stiffness of the paneling into account, which is derived in Section 4.4.1, the *Shannon*-Criterion is fulfilled up to 198 Hz (see Section 4.6). Thus, severe aliasing effects are expected starting well below 200 Hz, because of the finite nature of the signal (see Section 2.3.2.3). This behavior is investigated in detail in Section 4.6. Nevertheless, for the following investigations, the results from the acceleration data is used as reference result.
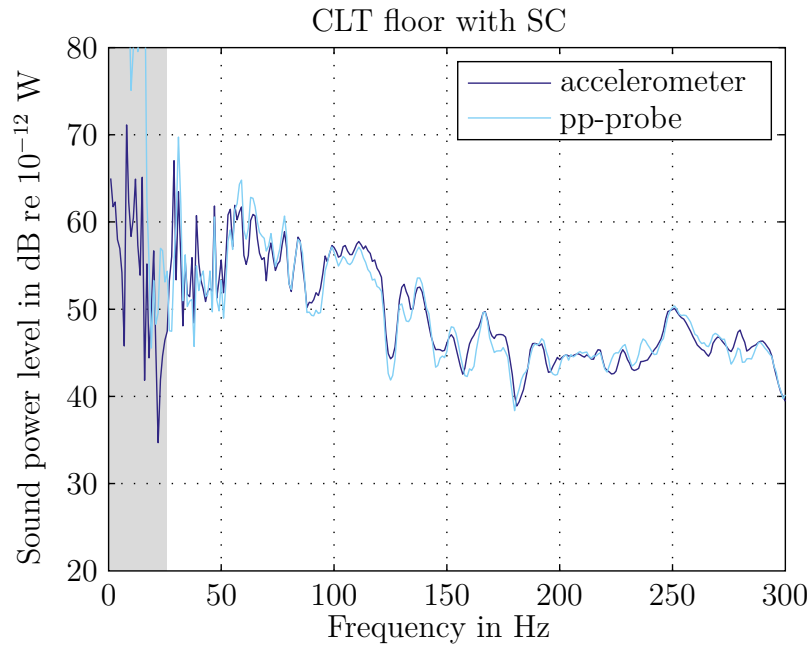
Figure 4.18: Comparing sound power levels derived from intensity and acceleration data

4.5.2 Case study on modeling

In the first approach, air is substituted by spring elements. Since those elements neglect the air's mass, a slightly adapted model, that discretizes the assumed air columns as unidirectional mass-loaded beam elements is considered parallel. Two-node spring or beam elements are applied in between all vertically opposite nodes of the upper and lower bordering structure's elements. Its lengths comply with the distance $h_{\text{air}} = l_{\text{hang}} + w_{1,\text{profil}}$. The cross section of a single considered air column corresponds to the area of a single shell element of the paneling $A_{\text{col,air}} = e_{\text{size,x}} \cdot e_{\text{size,y}}$. Thus, equivalent stiffness parameters for spring and beam elements can be derived from the characteristic values of air. They yield the following:

$$EA_{\text{subst,A}} = \rho_{\text{A}} \cdot c_{\text{A}}^2 \cdot A_{\text{col,A}}$$
$$k_{\text{subst,A}} = \frac{EA_{\text{subst,A}}}{h_{\text{A}}}$$

For the model, using acoustical fluid elements initially, only FSI between air and modeled structure is included. The remaining boundaries (concrete walls in case of the testing facility) are considered reverberant. Thus, potential damping of air moving horizontally is neglected. The resulting radiated sound power from the simulation of different models is shown in Figure 4.19. The ceiling was suspended from a CLT floor as in the reference measurements and excited from above in the same place. Both models substituting the air by spring or
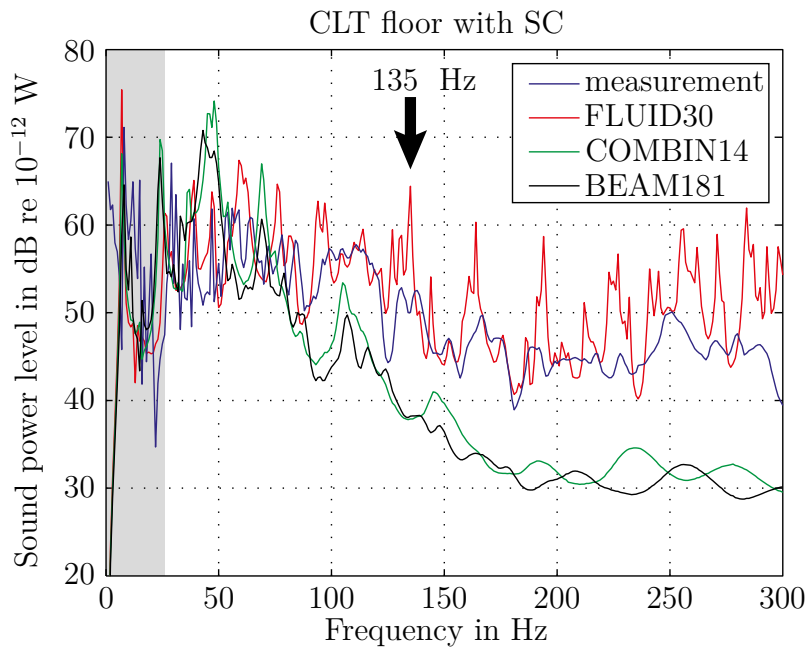
Figure 4.19: Comparing result of different modeling approaches

beam elements show a poor match compared to the reference. In the frequency range up to 80 Hz, the graphs follow the reference and overestimate it in some peaks, but in higher frequencies, the curves level is up to 20 dB below. Opposite to that, the data simulated with acoustical fluid elements predominately match the reference curve while sharp resonant peaks are observable. The other models lack those peaks, leading to the assumption that those resonances are of special importance for the accurate prediction of the radiated sound power. Therefore, in the following section, the vibration pattern at one of the resonance peaks at 135 Hz is investigated.

4.5.3 Investigation in the wave number domain

Modeling the air inside the cavity using fluid elements showed results that agreed well with the measured reference data. This approach is therefore investigated in more detail in the wave number domain. In the previous section, an examination in the wave number domain already proved to deliver convincing results and a deeper insight into physical effects. Figure 4.20 shows the velocity pattern of the ceiling's lower surface at a frequency of 135 Hz in the wave number domain. The pattern can be compared to the measurement data with direct excitation of the paneling shown in Figure 4.14. Again, a circle of peaks indicating the plates bending wave number is visible (outer circle). Different from the former investigation, additionally high amplitudes appear in Figure 4.20. These peaks also lie on a circle with

radius corresponding to the wavenumber of air at this frequency.

$$k_A(135 \text{ Hz}) = 2\pi \cdot \frac{135 \text{ Hz}}{340 \text{ } \frac{\text{m}}{\text{s}}} = 2.49 \text{ } \frac{\text{rad}}{\text{m}}$$
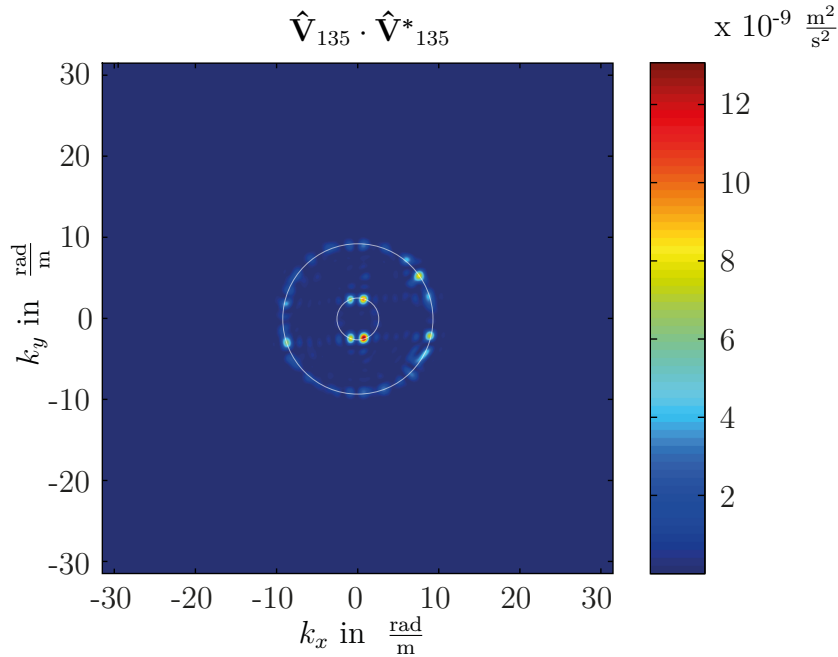
Figure 4.20: Wave number spectrum at the resonance peak at 135 Hz with superimposed k_B and k_A-circles

Those vibrational components with longer wavelengths cannot be observed in the spatial domain of the velocity pattern at the surface of the ceiling in Figure 4.21 (left). They are masked by the plate's resonant vibrations with shorter wavelengths. A horizontal cross section of the pressure distribution inside the cavity (see Fig. 4.21 right) indicates the nature of the resonance peak at 135 Hz in the sound power spectrum. At this frequency, a cavity mode is excited.

Thus, the mechanism of sound transmission through the suspended ceiling construction can be explained as follows: The vibrating main floor - in this case, a CLT floor - causes vibrations of the air cushion. According to Equation (3.5), sound power is transmitted for each frequency step mainly within the range of the wave number of the air. Thus, cavity modes are excited in particular. They can be approximated for a rectangular cavity by the

following equation described by *Lord Rayleigh*

$$f_{n_x,n_y,n_z} = \frac{c_A}{2}\sqrt{\left(\frac{n_x}{l_x}\right)^2 + \left(\frac{n_y}{l_y}\right)^2 + \left(\frac{n_z}{l_z}\right)^2} \tag{4.14}$$

where l_x, l_y and l_z represent the dimensions of the cavity. The mode depicted in Figure 4.21 (right) has indexes $n_x = 1$, $n_y = 4$ and $n_z = 0$. The corresponding eigenfrequency according to Equation (4.14) yields $f_{1,4,0} = 127.4$ Hz.
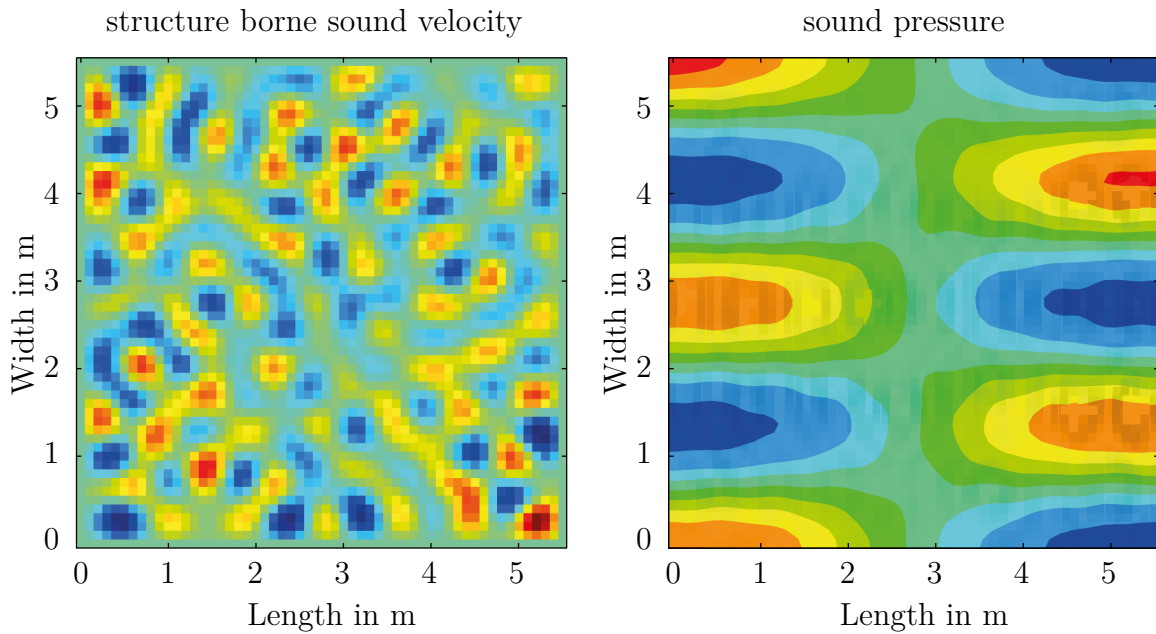
Figure 4.21: Spatial domain at the resonance peak at 135 Hz

The air inside the cavity vibrates in many modes. Thus, the models with substituted air columns are not capable of describing the reality. Even when mass loaded beam elements are considered only the pure vertical modes are included whereas the lateral modes are neglected. As shown in Figure 4.19 many of those modes are present in the observed frequency range up to 300 Hz, which can be approximated by Equation (4.14). The dimensions of the construction have an important influence.

The system consisting of air cavity and hangers excite the paneling of the suspended ceiling, causing forced and resonant vibrations. Resonant vibrations occur according to the bending wavenumber at this frequency. Superimposed but masked at the surface, the paneling is also forced to vibrate with the vibrational components, produced by the cavity modes. Although masked in the spatial domain (see Fig. 4.21 left), those components contribute to a large extend to the radiated sound power. The corresponding wave numbers lie exactly on a

circle with radius k_A where, as described in Section 3.7.1, the wave-number dependent term $K(k_x, k_y, f)$ in Equation 3.7 tends to infinity. Thus, those wave number components have a large impact on the resulting radiated sound power.

Consequently, in a frequency range with a high density of cavity modes, the sound power radiated from the SC is decisively dependent on the air inside the cavity. In the presented example, this is the case in a frequency range higher than ≈ 100 Hz. As a further consideration the impact of a change of the stiffness parameters of the hangers as well as their length or contribution on the improvement of the vibro-acoustical behavior of the suspended ceiling is questionable. Further research is recommended, especially since no additional absorbing material was applied into the cavity in this example [Floden 2014]. The absorbing material is expected to weaken the effect of the cavity modes.
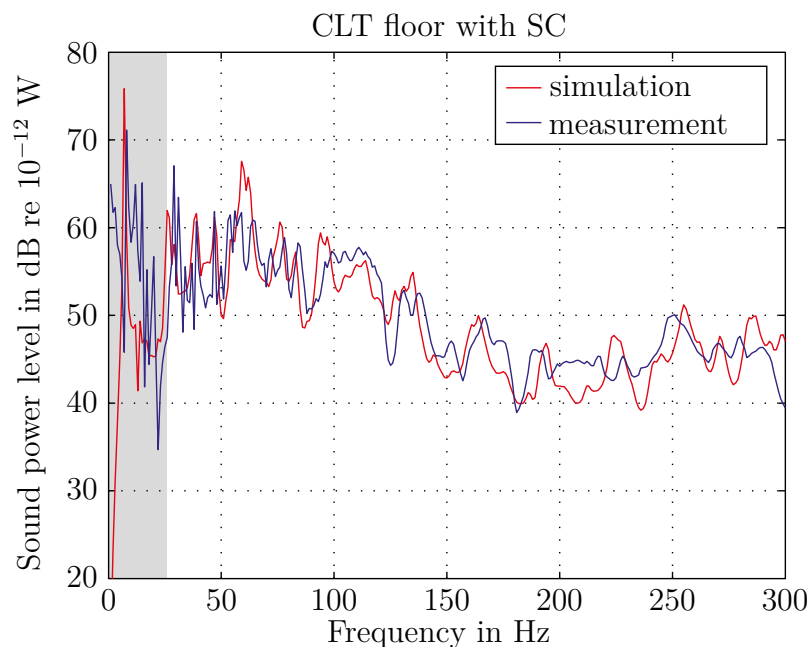
Figure 4.22: Comparing measurement and simulation results for a CLT floor with SC

4.5.4 Calibrating the boundary impedance and comparing the results

In Section 4.5.2, the boundaries of acoustical fluid elements that are not bordering structural elements are modeled reverberant. The used simulation software $\text{ANSYS}^{\circledR}$ features absorption at those boundaries via impedance boundary conditions. A coefficient μ_{wall}, describing the absorption of the walls of the testing facility, can range from zero to unity indicating
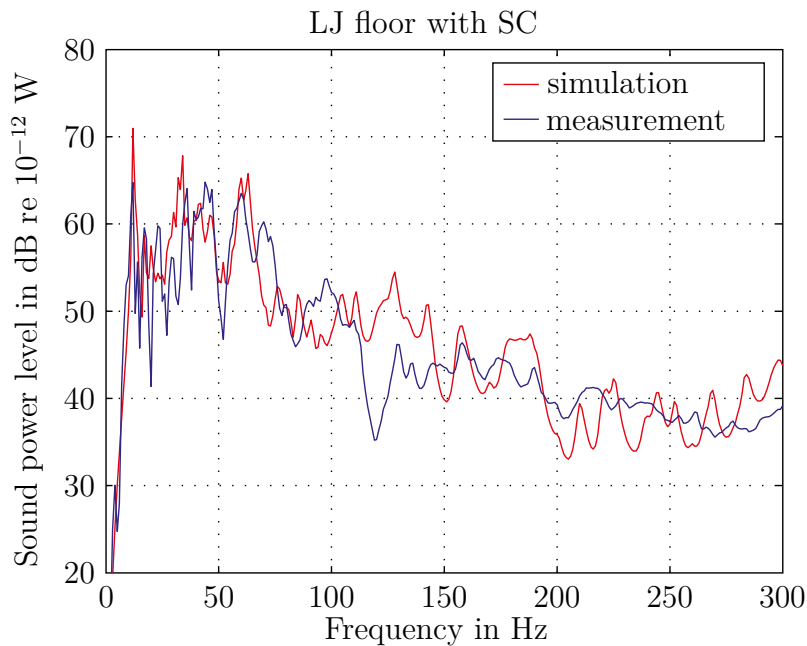
Figure 4.23: Comparing measurement and simulation results for a lumber joist floor with SC

reverberant to fully absorbing boundaries. As already mentioned in Section 3.2.6, this factor was iteratively determined to $\mu_{\text{wall}} = 0.03$.

Figure 4.22 shows the simulated and measured radiated sound power level for a CLT floor with suspended ceiling. The latter is normalized to an excitation of 1.0 N to match the simulated data. It can be observed that the inclusion of absorption via impedance boundary conditions significantly reduces the resonance peaks of the cavity modes. This results in a very good correlation of simulated and measured data, with deviations ≤ 5 dB in the narrow-band spectrum. The model can be considered verified for this example. To verify its modular applicability to varying floor systems, the same model is applied to a lumber joist floor without changing the configuration. The result shown in Figure 4.23 correlates less, but still good, with the measured data. Especially around 120 Hz deviations up to 10 dB are observable.

4.6 Limitations for the Prediction of Sound Power in the Wave Number Domain

A model for the prediction of the radiated sound power out of the structure-borne sound velocity in the wave number domain was presented in Section 3.7. The data, that can be

processed by this model are restricted to some limitations. One of them is obviously, that the sound power can only be predicted within the frequency ranges, where vibrational energy was induced into the test object by e.g. a shaker or loud speaker. As another restriction, minimum distances between the measurement points have to be maintained. This is due to the discrete nature of the model. Analogously to measurements in the time domain, in this case, spatial aliasing must be minimized. A common measure to overcome this problem is to chose a sampling interval well below the *Nyquist* frequency [Brigham 1974]. However, as shown in Section 4.5.1, for the calculation of the radiated sound power out of structure-borne sound velocity measurements, adequate results are achieved even above the critical frequency in case of a floor with an SC.
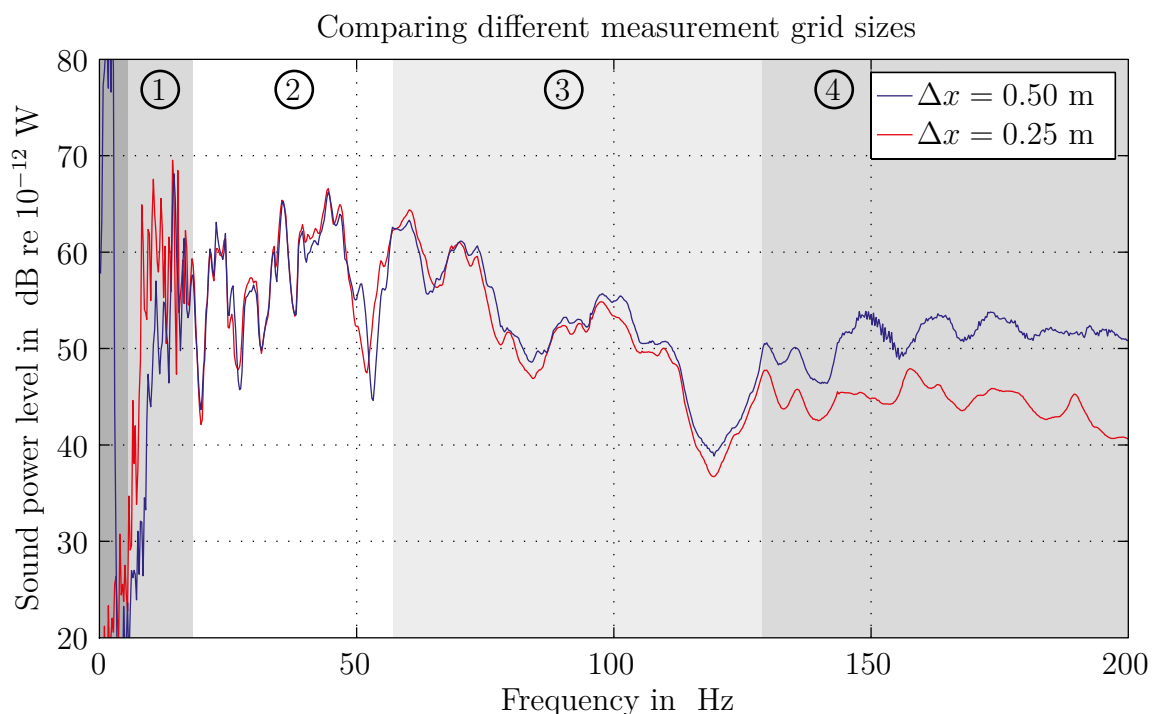
Figure 4.24: Comparison of the influence of different measurement grids

To explain this behavior, two measurements on the same test object with different measurement grids and excitation signals are compared. Figure 4.24 shows the radiated sound power of a ceiling paneling, suspended from a lumber joist floor. The construction is excited by a shaker with a logarithmic sine sweep. The blue curve describes measurements with a grid of $\Delta x = 0.5$ m (12×12 Accelerometers) and an excitation range $4 - 200$ Hz, the red one a measurement with a grid of $\Delta x = 0.25$ m (23×23 Accelerometers) and an excitation range $16 - 200$ Hz. When the *Shannon*-Criterion is applied, the resolutions lead to measurable
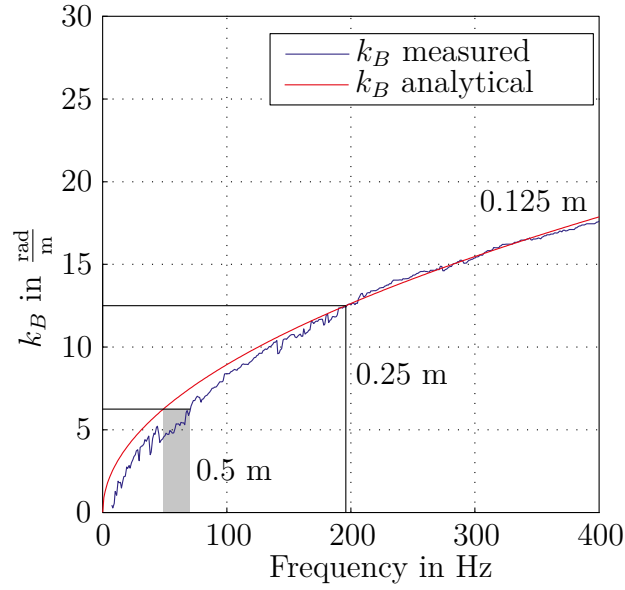
Figure 4.25: Shannon Criterion in the wave number domain

wave number ranges up to 6.28 $\frac{\text{rad}}{\text{m}}$ resp. 12.57 $\frac{\text{rad}}{\text{m}}$.

$$k_{\text{x,max,0.5}} = k_{\text{y,max,0.5}} = \frac{2\pi}{2 \cdot 0.5 \text{ m}} = 6.28 \ \ \frac{\text{rad}}{\text{m}}$$

$$k_{\text{x,max,0.25}} = k_{\text{y,max,0.25}} = \frac{2\pi}{2 \cdot 0.25 \text{ m}} = 12.57 \ \ \frac{\text{rad}}{\text{m}}$$

Those limits are marked in Figure 4.25. The diagram represents a detail of the data already introduced in Section 4.4, that had been measured with a higher resolution of $\Delta x = 0.125$ m. By raising the perpendicular from the intersection between the limit lines for the wave number and the curves in the diagram, the maximum valid frequency can be read out. For a grid of 0.25 m a frequency range up to ≈ 200 Hz, for a grid of 0.25 m a frequency range up to ≈ 60 Hz is valid when the *Shannon*-Criterion is applied. According to the investigations in Section 2.3.2.3, in case of finite signals, aliasing effects must be considered. However, the resulting sound power of the measurements using a $\Delta x = 0.5$ m measurement grid matched very good to data from an intensity measurement (see Section 4.5.1).

Analytically, these limits can be derived from the Criterion

$$k_{\text{x,max}} \geq k_{\text{B}}, \tag{4.15}$$

which can be solved for the *Nyquist* frequency

$$2\pi \cdot f_{Nq} = \frac{k_{\text{x,max}}^2}{a} \tag{4.16}$$

with the substitution

$$a = \frac{k_{\text{B}}^2}{2\pi f} = \sqrt{\frac{12\rho}{E \cdot d^2}}. \tag{4.17}$$

Applying the matching parameters of the example (see Section 4.4) yields:

$$f_{Nq,0.5} = 49.5 \text{ Hz} \qquad \text{and} \qquad f_{Nq,0.25} = 198.0 \text{ Hz}.$$

In case of a grid of $\Delta x = 0.5$ m, the assumption of an infinite isotropic plate does not hold properly in the observed frequency range. This leads to deviations of the curves, and thus the frequency limits vary (marked in gray).

Four frequency sectors can be identified by an investigation of the structure-borne sound velocity spectra in the wave number domain. They are indicated in Figure 4.24 by different shades of gray. The specific characteristics of each sector are listed in Table 4.8. It shows the approximated frequency range and whether it was excited during the specific measurement. Also, it indicates when the *Shannon*-Criterion is met and if the measurements give equivalent results (within a considerable limit of deviation).

Table 4.8: Characteristics of the sectors in Figure 4.24

Sector	Frequency range	Excitation	Criterion met	Curves match
1	$4 - 16$ Hz	only $\Delta x = 0.5$ m	both	yes
2	$16 - 60$ Hz	both	both	yes
3	$60 - 130$ Hz	both	only $\Delta x = 0.25$ m	yes
4	$130 - 200$ Hz	both	only $\Delta x = 0.25$ m	no

Examples of a specific frequency step for each sector are given from Figures 4.26 to 4.29. Below 4 Hz no energy is induced for both measurements.

Sector 1: $(4 \text{ Hz} - 16 \text{ Hz})$
In this sector, only in case of the measurement with $\Delta x = 0.5$ m the test object was excited by the shaker. Figure 4.26 depicts the wave number spectra of both measurements close to an eigenfrequency of the panelings at 10 Hz. In the spectrum of $\Delta x = 0.5$ m (right) the

two characteristic peaks of the eigenmode are clearly visible. For $\Delta x = 0.25$ m those peaks can also be identified, but the vibration pattern is superimposed by artifacts caused by the phase error due to the missing force signal.
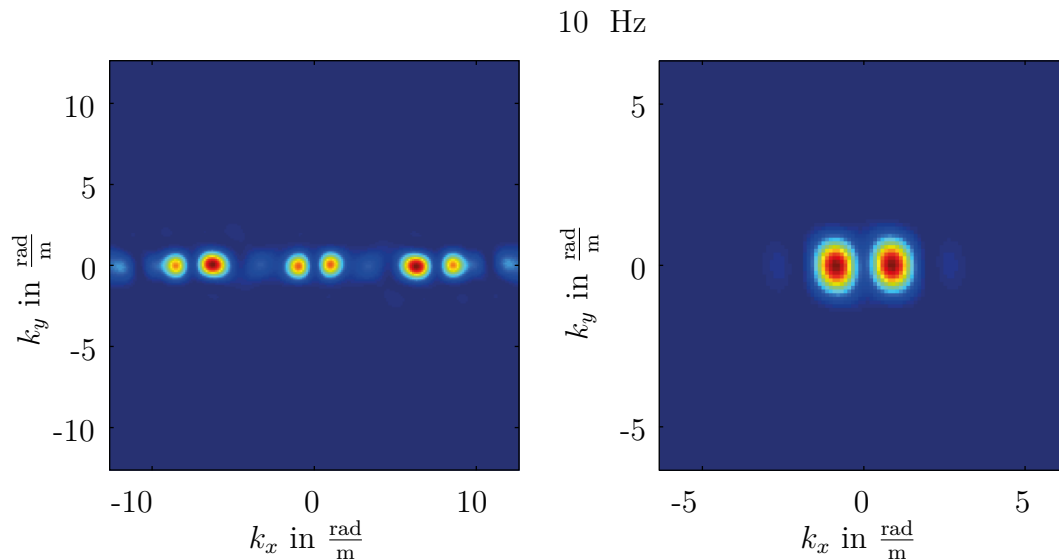
Figure 4.26: Sector 1: Wave number spectra at 10 Hz for a sampling interval of $\Delta x = 0.25$ m (left) and $\Delta x = 0.5$ m (right)

Sector 2:   (16 Hz$-\approx 60$ Hz)

In this sector, for both $\Delta x = 0.5$ m and $\Delta x = 0.25$ m the *Shannon*-Criterion is met. Figure 4.27 shows the wave number spectra at 20 Hz. Clearly, the typical circle shaped arrangement of the peaks lies within the limits of the spectra for both cases. Aliasing effects appear, but are considered small in case of $\Delta x = 0.25$ m and within an acceptable range for $\Delta x = 0.25$ m. thus, the resulting patterns match very well. This also leads to a good match for the calculated sound power level in this sector.

Sector 3:   (≈ 60 Hz$-\approx 130$ Hz)

Although the *Shannon*-criterion is violated in this sector, in case of $\Delta x = 0.5$ m, the curves of the sound power still match quite good. A comparison of the wave number spectra in Figure 4.28 at the lower limit of the frequency band at 59 Hz shows, that the bending wave number of the paneling for a $\Delta x = 0.5$ m grid (right) opposite to the $\Delta x = 0.25$ m grid (left) has already reached the limits of the wave number spectrum. Thus, in case of $\Delta x = 0.5$ m, a major error, caused by aliasing is induced, while for $\Delta x = 0.25$ m aliasing is considered within an acceptable range. However, the sound power level show a good accordance.
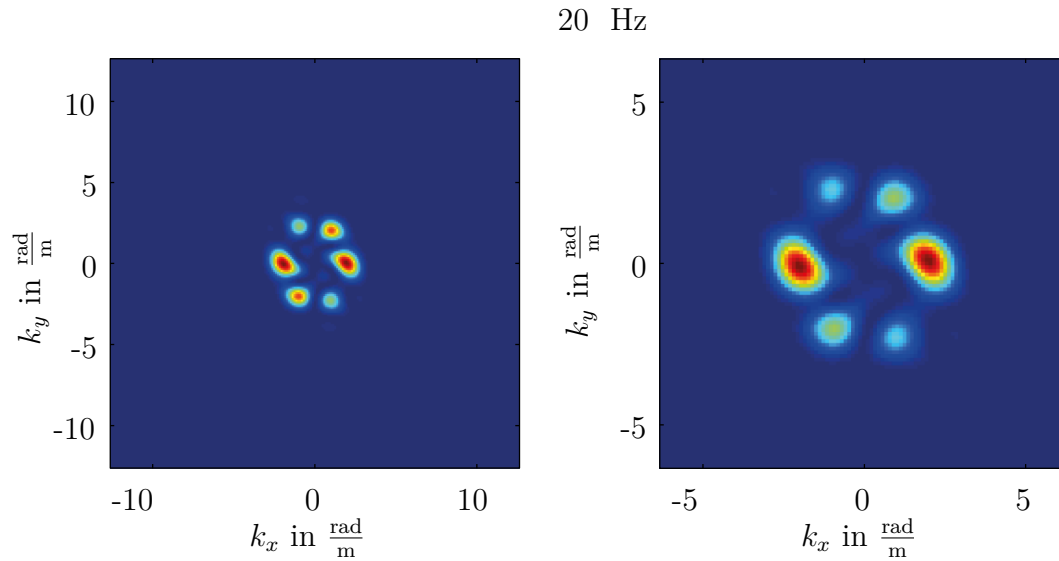
Figure 4.27: Sector 2: Wave number spectra at 20 Hz for a sampling interval of $\Delta x = 0.25$ m (left) and $\Delta x = 0.5$ m (right)

This can be explained by the fact that only those wave number components contribute to the radiated sound power that lie within a circle with radius corresponding to the wave number of air (see Eq. (3.5)). Since the transmission in case of a suspended ceiling is governed by the air inside the cavity (see Section 4.5.3), additional peaks, representing forced vibrations appear on a circle according to the wave number of air. They are less affected by the aliasing effect due to the longer wavelengths. The sound power is mainly emitted by the forced vibrations. Thus, the resonant vibrations, that are heavily distorted by aliasing in case of $\Delta x = 0.5$ m only lead to small differences between the two measurements.

Different appearance of both spectra are due to the different scaling factor of the coloring. The peaks, in this case, form an ellipse. This indicates a slightly different bending stiffness of the paneling for each spatial direction at this frequency. This is caused by the different number of steel U-channels attached for each spatial direction. For higher frequencies, this effect is negligible.

Sector 4   (from ≈ 130 Hz)

In this sector, the curves drift clearly apart. As an example, in Figure 4.29, the wave number spectra of the structure-borne sound velocity at 141 Hz are depicted. In case of $\Delta x = 0.25$ m the circle imposed by its bending wave number does not reach the limits of the spectrum. However, major aliasing of the resonant vibrations is assumed. If the limits of $\Delta x = 0.5$ m are superimposed (white square), it becomes clear that in the latter case, the limits are exceeded
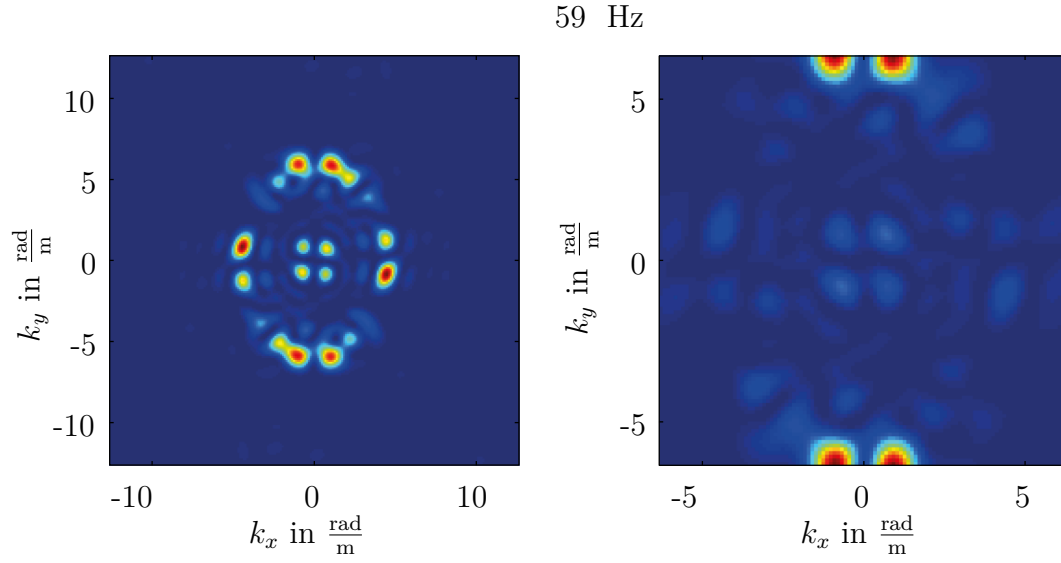
59 Hz

Figure 4.28: Sector 3: Wave number spectra at 59 Hz for a sampling interval of $\Delta x = 0.25$ m (left) and $\Delta x = 0.5$ m (right)

by far. The wave number of air yields $2.5 \ \frac{\text{rad}}{\text{m}}$ at this frequency, indicated by the peaks inside the square. Caused by the aliasing-effect not only the side lobes, as in the former figures, but also the main peaks of the spectral amplitudes outside the square wrap around [Maynard et al 1985] (more precisely: are repeated) into the range of the spectrum to the right and superimpose a wide section of the wave number spectrum. In particular, at this frequency, the wrapped around bending wave number components of the paneling, superimpose wave number components inside a circle with a radius corresponding to the wave number of air. As explained before, this region contributes to the radiated sound power into the far-field. By overlapping with the originally near-field components the results are heavily distorted. Therefore, the measurements with a grid of 0.5 m are not valid in sector 4.

For the extended frequency band beyond the limits, according to the *Shannon*-Criterion, the following additional criterion is suggested for plate-shaped structures, where a cavity is a part of the sound transmission or in cases where the plate is excited by a airborne sound as follows:

$$2 \cdot k_{\text{max}} \geq k_{\text{B}} + k_{\text{A}} \tag{4.18}$$

Inserting Equations (4.3), (4.5) and (4.17) and solving for the critical frequency, Equation (4.18) yields:

$$2\pi \cdot f_{max} = \frac{c_{\text{A}}}{2} \left(a \cdot c_{\text{A}} - \sqrt{(a \cdot c_{\text{A}})^2 + 8(a \cdot c_{\text{A}})k_{max}} + 4k_{max} \right). \tag{4.19}$$
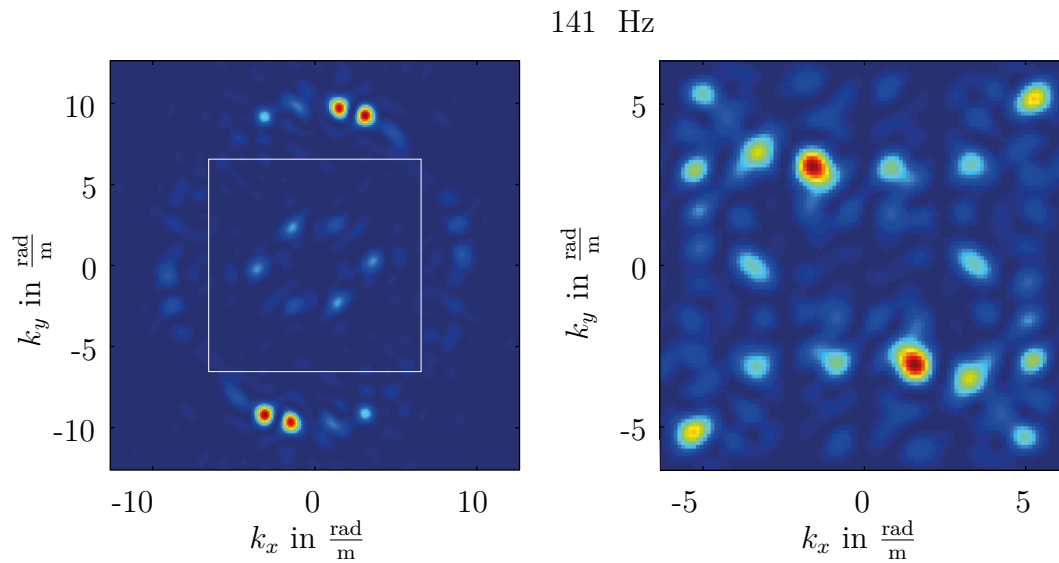
141 Hz

Figure 4.29: Sector 4: Wave number spectra at 141 Hz for a sampling interval of $\Delta x = 0.25$ m (left) and $\Delta x = 0.5$ m (right)

For orthotropic plates with anisotropic stiffness properties, the weaker direction is decisive. For a measurement grid of 0.5 m resp. 0.25 m the maximum valid frequency range yields:

$$f_{max,0.5} = 130.2 \text{ Hz}$$
$$f_{max,0.25} = 399.1 \text{ Hz}.$$

Obviously, the limit is, other than the *Shannon*-Criterion for plates, not increasing parabolic with a decrease of the sampling interval. It has to be added that when this criterion is applied, a limited amount of aliasing is introduced. Nevertheless, the results from the reference measurement in Section 4.5.1 can be explained, and thus be considered validated.

5 Numerical Simulations and Evaluation of the Results

In this chapter, the performed parametric studies are described. Thus, the general approach for the implementation of the study, as well as the chosen variable parameters and their parameter range are discussed. Two kinds of parametric studies are implemented directing on different aspects. First, the influence of individual parameters on the radiated sound power of the structures considered is investigated. Thus, preliminary information about the predicted vibro-acoustical behavior of the floors is obtained. Based on the results of a second study, a catalog for relevant parameter combinations is created. The results of the simulation, in the form of transfer functions, are further implemented as a database into a graphical user interface, that enables the user to predict and compare the vibro-acoustical behavior of different floor configurations for varying excitation sources.

5.1 Parametric Studies

The developed numerical models used for the parametric studies are described in Chapter 3. As already mentioned in the chapter, the models are fully parametrized and optimized for an automated simulation process. For the implementation of the parametric study, an interface between the used commercial FE simulation software ANSYS® and commercial numerical computing software MATLAB® is programmed. The individual simulations and their configurations as well as the evaluation of the results are controlled by MATLAB®.

5.1.1 Programming in MATLAB®

The process of the parametric studies can be divided into three steps.

5.1.1.1 Process step 1

Before the start of each simulation run, the relevant parameters are identified and their specific parameter range is set. Depending on the scope of the study, some parameters are varied, while others stay constant. The parameter range is determined based on its practical relevance, as well as the computational effort. Particularly, for models with construction states requiring a full solution for the Harmonic Frequency Analysis, the computational effort is significantly higher. The range of parameters for those models must therefore be reduced.

The computational effort strongly depends on the size of the models, and thus on the applied number of DOFs. The following durations per simulation were measured depending on the method for the analysis:

- Modal superposition: $\approx 1 - 10$ minutes

- Full solution: ca. $\approx 1 - 6$ hours

5.1.1.2 Process step 2

Section 3.1.2 describes the modular structure of the FE models, where each main module has an associated sub-module containing the parameter information. Such a structure is advantageous for the parametric study, since for every simulation run, only those sub-modules have to be adapted, controlled by the interface inside Matlab®. This results in a robust process. After the transfer of the set of parameters, the simulations in Ansys® are started inside Matlab®. With the help of the output data interface described in Section 3.6, the simulation results are stored to be transferred back into Matlab®. After each simulation run, the structure-borne sound velocity data as well as the associated geometry data are stored to an output data file containing the specific parameter configuration information.

5.1.1.3 Process step 3

Subsequent to the simulations in Ansys®, the output data files are read into Matlab®, where they are evaluated using the ITM base model for the prediction of the radiated sound power (see Section 3.7.1). The results of this evaluation are then archived for each floor type and construction state for further investigations.
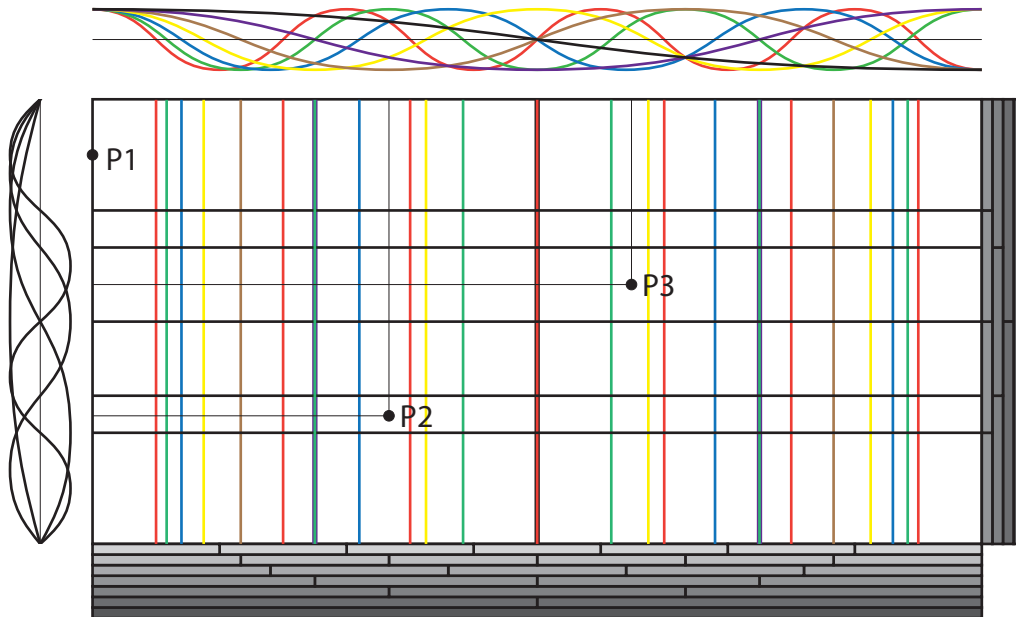
Figure 5.1: Locations of single load excitation

5.1.2 Choice of parameters

As described in Section 3.1.3, the parameters are organized into three groups. For the parametric studies, predominately geometry and model parameters are varied, since material parameters are already calibrated by measurements or chosen according to literature. The only exception is the boundary impedance inside the air cavity of the suspended ceiling. This parameter is adapted iteratively, and will therefore, be further investigated concerning its influence on the results of the simulations. The vibro-acoustical behavior of the investigated floor constructions can be predicted most reliable by an application of a stochastic rain-on-the-roof loading, as described in Section 3.4.2. Since this procedure would cause an out of question amount of computational effort for the parametric studies a different approach applying single loads is chosen. For each parameter combination, three simulation runs with different locations for the point excitation are performed. Those locations are chosen to avoid zero-crossings of eigenmodes of the structures. Figure 5.1 shows these locations (P1, P2 and P3) on a fictional area superimposed by lines where zero-crossings are assumed. They have to be adapted depending on the dimensions of the simulated structures. Thus, by comparing the results of the individual load locations and averaging, a similar accuracy is assumed. An additional advantage of this approach is the possibility to derive transfer function for each

load locations which can be multiplied by the excitation signal of e.g. a standard tapping machine, and thus compared to measurement results (see Sections 5.3 and 5.4).

The relevant parameters are listed in the following. Depending on the individual main floor construction, different specific parameters must be evaluated. For performed parametric studies, only the CLT and lumber joist floors are concerned. A single type of floating floor is applied (see Section 3.2.5), causing it to be not well adjusted for some floor dimensions.

- Specific parameters of the CLT floor:

    ◦ Floor type: 28 different types can be modeled

    ◦ Number of slabs

- Specific parameters of the lumber joist floor:

    ◦ Floor type: single or double joists

    ◦ Distance between the joists

- General parameters:

    ◦ Construction state

    ◦ Load position

    ◦ Length

    ◦ Total width: controlled by the aspect ratio $\alpha = \frac{l}{w_{\text{tot}}}$

    ◦ Length of the hangers

    ◦ Suspension grid

    ◦ Distance between main floor and paneling

    ◦ Boundary impedance inside the air cavity

5.1.3 Performed studies

The number of parameter combinations increases exponentially with every additional vary-ing parameter. Since the computational capacity is limited, a preliminary selection has to be done. To cover a wider range of evaluated parameters, three different parameter studies are performed. One, simulating parameter combinations for a later use as database for the graphical user interface (PS-GUI) the others dealing with the influence of specific parame-ters, not concerned with the former study, on the radiated sound power (PS-SP). Especially a variation of the parameters related to the suspended ceiling are only investigated within the latter surveys. The different construction states are abbreviated by R (raw main floor construction), R/FLF (including floating floor), R/SC (including suspended ceiling) and R/FLF/SC (a combination of both).

5.1.3.1 Parametric studies for CLT floor models

The following practical restrictions are implemented for parametric studies for CLT floor models:

- The width of the individual slabs is limited to a range of:
  $1.0 \text{ m} \leq b_{\text{slab}} \leq 2.5 \text{ m}$

- The analytical first eigenfrequency of the slabs idealized as a beam $f_{\text{beam}} = \frac{\pi n^2}{2 l_x^2} \sqrt{\frac{EI_y}{\mu}}$ must lie within the boundaries of the following:
  $6.0 \text{ Hz} \leq f_{\text{beam}} \leq 15.0 \text{ Hz}$

As a result, a good approximation for practically relevant parameter combinations is simu-lated. Thus, no data is simulated for large floors with small cross sectional areas and vice versa.

PS-SP (CLT R all types)   At the time of the study, the manufacturer of the regarded CLT floors had 28 different types of cross sections in its portfolio [Metsä Wood Merk GmbH 2012], resulting in the same amount of possible modeling options. They differ in number of board layers and its individual orientation parallel or perpendicular to the main load bearing direction of the slabs. Those determine the stiffness ratio of the slab $\frac{EI_x}{EI_y}$. The influence of this parameter on the eigenfrequencies of the whole floor and its sound radiation behavior is investigated by a parametric study on the raw main floor (R). Therefore, the models are excited in location P1. The range of the individually varied parameters is given in Table 5.1.

The restrictions introduced above limited the total number of parameter combinations from 15444 to 4853. Modal superposition can be used as analysis method resulting in a total computational effort of ≈ 10 days.

Table 5.1: Varied parameters for PS-SP (CLT R all types)

Parameter	Value	Amount = factor
Length in m	$[4.0; 4.5; 5.0; 5.5; 6.0; 6.5; 7.0; 7.5; 8.0]$	$\times 9$
Floor type	$[51; 61; 71; 81; 93; 99; 85; 95; 105; 115;$ $125; 135; 147; 153; 165; 174; 186; 189; 201;$ $207; 219; 231; 240; 252; 264; 273; 285; 297]$	$\times 28$
Number of slabs	$[2; 3; 4; 5; 6; 7]$	$\times 6$
Aspect ratio	$[1.0; 1.1; 1.2; 1.3; 1.4; 1.5; 1.6; 1.7; 1.8; 1.9; 2.0]$	$\times 11$
Total number of simulations (before restrictions):		15444
Total number of simulations (final):		4853

PS-SP (CLT R/SC + R/FLF/SC Type 165) A separate parametric study is performed for the investigation of the influence of the parameters related to the suspended ceiling, since those are not considered varying for the database of the graphical user interface. In this study, eight parameters are varied, that are listed in Table 5.2. The modeling of the suspended ceiling includes acoustical fluid elements, which is why the analysis method modal superposition cannot be applied. Therefore, the parameter range has to be reduced significantly, to limit the computational effort. The simulations are based on a single CLT type, modeled as a single slab. Configurations with and without floating floor are considered. Additionally, the effect of a self-supporting ceiling, neglecting the hangers, is investigated for only one suspension grid (this parameter influences the dimensions of the grid work). The excitation was applied at location P1. Thus, 216 simulations are performed resulting in an computational effort of ≈ 24 days.

Table 5.2: Varied parameters for PS-SP (CLT R/SC + R/FLF/SC Type 165)

Parameter	Values	Amount = factor
Length in m	$[4.0; 5.0]$	$\times 2$
Aspect ratio in $-$	$[1.0; 1.5]$	$\times 2$
Floating floor	$[\text{yes}; \text{no}]$	$\times 2$
Distance floor/paneling in m	$[0.12; 0.2]$	$\times 2$
Suspension grid in m	$[0.5 \times 0.5; 1.0 \times 1.0]$	$\times 2$
Hangers	$[\text{yes}; \text{no}]$	$\times 1.5$ (only 1.0×1.0)
Boundary impedance in $-$	$[0; 0.03; 0.1]$	$\times 3$
Total number of simulations:		216

PS-GUI (CLT)   The varying parameters and their ranges for the graphical user interface-related parametric study PS-GUI are listed in Tables 5.3 to 5.5. Compared to the survey in Section 5.1.3.1, only six representative floor types are implemented. Simulations for all three locations of excitation are performed leading to a similar amount of computational effort for models with raw main floors (R). for the remaining construction states the number of parameter combinations is decreased depending on the additional effort. Thus, in case of an additional floating floor (R/FLF), the number of considered aspect ratios is decreased to two. For construction states that include a suspended ceiling, the number of simulated lengths is reduced and the whole floor is modeled as a single slab. The boundary impedance of the air cavity is set to 0.03 as described in Section 3.2.6. Applying the aforementioned restriction for the first eigenfrequencies, the total number of parameter combinations per location of excitation yields 1133 (R), 226 (R/FLF) and 32 (R/SC + R/FLF/SC).

Table 5.3: Varied parameters for the CLT floors R

Parameter	Value	Amount = factor
Length in m	$[4.0; 4.5; 5.0; 5.5; 6.0; 6.5; 7.0; 7.5; 8.0]$	$\times 9$
Floor type	$[71; 105; 147; 186; 219; 264]$	$\times 6$
Number of slabs	$[2; 3; 4; 5; 6; 7]$	$\times 6$
Aspect ratio	$[1.0; 1.1; 1.2; 1.3; 1.4; 1.5; 1.6; 1.7; 1.8; 1.9; 2.0]$	$\times 11$
Total number of simulations (before restrictions):		3580
Total number of simulations (final):		1133

Table 5.4: Varied parameter for (CLT R/FLF)

Parameter	Value	Amount = factor
Length m	$[4.0; 4.5; 5.0; 5.5; 6.0; 6.5; 7.0; 7.5; 8.0]$	$\times 9$
Floor type	$[71; 105; 147; 186; 219; 264]$	$\times 6$
Number of slabs	$[2; 3; 4; 5; 6; 7]$	$\times 6$
Aspect ratio	$[1.0; 1.5]$	$\times 2$
Total number of simulations (before restrictions):		648
Total number of simulations (final):		226

Table 5.5: Varied parameters for the CLT floors R/FLF + R/FLF/SC

Parameter	Value	Amount = factor
Length m	$[4.0; 5.0; 6.0; 7.0; 8.0]$	$\times 5$
Floor type	$[71; 105; 147; 186; 219; 264]$	$\times 6$
Number of slabs	1	$\times 1$
Aspect ratio	$[1.0; 1.5]$	$\times 2$
Total number of simulations (before restrictions):		60
Total number of simulations (final):		32

5.1.3.2 Parametric studies for lumber joist floors

In addition to the parameter's length and aspect ratio, for this survey, the specific parameters of a lumber joist ceiling manufactured by Regnauer are considered. One of them is the distance between the individual joists. It is preferred to the number of joists since the latter would require a much larger parameter range. Since the width is controlled by the aspect ratio in most cases no integral multiple can be achieved when the distance between joists is set to a fixed value. To cope with that, the parameter's value serves only as an approximation. The real distance is adapted to be the closest possible value for an integral divisor of the total width of the floor. Instead of a specific floor type the lumber joist floors are typecast by the total width of the individual joists. It is defined by the manufacturer to be either a single joist or an integer multiple of it, to fulfill statical requirements. Thus, for small spans, a single joist configuration for wider spans a double joist configuration is considered.

PS-GUI lumber joist floor Analogous to the CLT floor, the parameter ranges must be adapted to the estimated computational effort. As listed in Tables 5.6 to 5.8, for more

complex models, the lengths and aspect ratios of the constructions are decreased. In this case, this results in a total amount of parameter combinations per location of excitation of 440 (R), 132 (R/FLF) and 44 (R/SC + R/FLF/SC). The total number of simulated raw main floors and models with additional floating floor compared to the CLT simulations is decreased as well, since for LJ floor models contact elements were applied, and thus full solution analysis method required.

Table 5.6: Varied parameters for the LJ floors R

Length m	Dist. btwn joists m	width of joists in m	Amount/factor
3	$[0.3; 0.4; 0.5; 0.6]$	0.06	4
3.5	$[0.3; 0.4; 0.5; 0.6]$	0.06	4
4	$[0.3; 0.4; 0.5; 0.6]$	$[0.06; 0.12]$	8
4.5	$[0.3; 0.4; 0.5; 0.6]$	$[0.06; 0.12]$	8
5	$[0.3; 0.4; 0.5; 0.6]$	$[0.06; 0.12]$	8
5.5	$[0.3; 0.4; 0.5; 0.6]$	0.12	4
6	$[0.3; 0.4; 0.5; 0.6]$	0.12	4
Aspect ratio	$[1.0; 1.1; 1.2; 1.3; 1.4; 1.5; 1.6; 1.7; 1.8; 1.9; 2.0]$		$\times 11$
Total number of simulations:			440

Table 5.7: Varied parameters for the LJ floors R/FLF

Length m	Dist. btwn joists m	width of joists in m	Amount/factor
3	$[0.5; 0.6]$	0.06	2
3.5	$[0.4; 0.5; 0.6]$	0.06	3
4	$[0.3; 0.4; 0.5]$	0.06	4
	0.6	0.12	
4.5	$[0.3; 0.4]$	0.06	4
	$[0.5; 0.6]$	0.12	
5	0.3	0.06	4
	$[0.4; 0.5; 0.6]$	0.12	
5.5	$[0.3; 0.4; 0.5]$	0.12	3
6	$[0.3; 0.4]$	0.12	2
Aspect ratio	$[1.0; 1.1; 1.2; 1.3; 1.4; 1.5]$		$\times 6$
Total number of simulations:			132

Table 5.8: Varied parameters for the LJ floors R/SC + R/FLF/SC

Length m	Dist. btwn joists m	width of joists in m	Amount/factor
3	$[0.5; 0.6]$	0.06	2
3.5	$[0.4; 0.5; 0.6]$	0.06	3
4	$[0.3; 0.4; 0.5]$	0.06	4
	0.6	0.12	
4.5	$[0.3; 0.4]$	0.06	4
	$[0.5; 0.6]$	0.12	
5	0.3	0.06	4
	$[0.4; 0.5; 0.6]$	0.12	
5.5	$[0.3; 0.4; 0.5]$	0.12	3
6	$[0.3; 0.4]$	0.12	2
Aspect ratio	$[1.0; 1.5]$		$\times 2$
Total number of simulations:			44

5.2 Evaluation of the Results

In this section, the results of the parametric studies are evaluated. The individual varying parameters are investigated with regard to their influence on the vibro-acoustical behavior of the investigated floor systems. Dimensional analyses are performed to develop nomograms with dimensionless parameters according to the method described in Section 2.2. The application of TMD will be discussed to reduce radiated sound power. A further evaluation aims at the tabular listing of positive and negative effects of a variation of certain parameters to serve as planning aids for preliminary design of floor constructions.

5.2.1 Dimensional analysis on raw CLT floors

First, the parameters of a raw CLT floor without vibration reduction measures is evaluated. Therefore, nomograms based on dimensionless parameters are developed for the floors eigenfrequencies and the transfer function of the radiated sound power (see Section 5.3).

5.2.1.1 Eigenfrequency nomograms

The eigenfrequencies of the floor are governed by the following seven physical quantities as follows:

Length	: l	in	m
Mass per area	: μ	in	$\frac{\text{kg}}{\text{m}^2}$
Bending stiffness in x-direction	: EI_x	in	$\frac{\text{kg m}^2}{\text{s}^2}$
Bending stiffness in y-direction	: EI_y	in	$\frac{\text{kg m}^2}{\text{s}^2}$
Width	: w	in	m
Number of slabs	: n_s		
Eigenfrequencies	: f_i	in	$\frac{1}{\text{s}}$

As described in Section 2.2, $7 - 3 = 4$ dimensionless parameters can be identified to describe the system's behavior. With n_p being already dimensionless, these are:

Number of slabs	: n_s
Aspect ratio	: $\alpha = \frac{l}{w}$
Stiffness ratio	: $\beta = \frac{EI_y}{EI_x}$
Frequency ratio	: $\gamma_i = \frac{f_i}{f_{\text{beam}}}$

with f_{beam} being the first eigenfrequency of a *Euler Bernoulli* beam

$$f_{\text{beam}} = \frac{\pi}{2l^2}\sqrt{\frac{EI_x}{\mu}}.$$

Figure 5.2 shows an example of such a nomogram for parameters $n_s = 5$ and $\alpha = 1.2$. The remaining nomograms are listed in Appendix B.1. In each nomogram, the frequency ratio γ_i is plotted as a function of the stiffness ratio β. Eigenfrequencies with the corresponding index are marked in equal colors. Additionally elliptic trend lines are superimposed. Every nomogram in the appendix summarizes the results for a specific aspect ratio α, a double page of nomograms depicts all nomograms for the same number of slabs.

A detailed examination of the eigenfrequency nomograms shows the following:

- The first eigenfrequency can be approximated independent from the parameter combination by the eigenfrequency of a *Euler Bernoulli* beam.
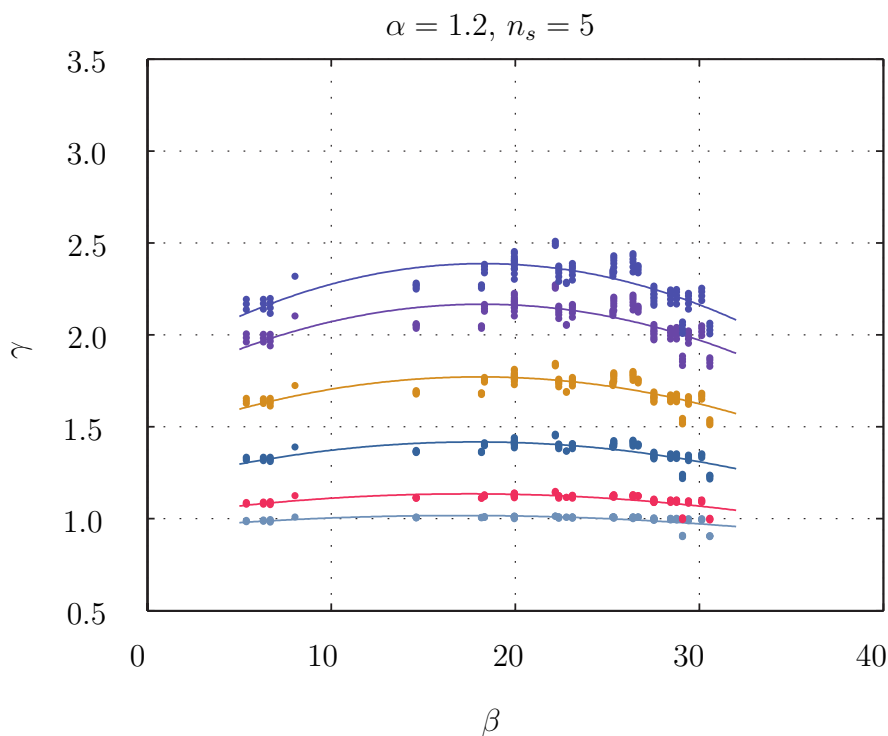
Figure 5.2: Example of an eigenfrequency nomogram

- With increasing number of coupled slabs the number of eigenfrequencies in the proximity of the first bending eigenfrequency increases.

- Depending on the stiffness ratio, eigenfrequencies with the same index show an arc-shaped behavior with higher density at the boundaries of the spectrum. The curve has a maximum at $\beta \approx 22$.

- The higher the aspect ratio of the floor, the lower is the overall scatter of the eigenfrequencies of the system. At the same time, the curve of the eigenfrequencies with same index is flattening.

5.2.1.2 Sound power nomograms

For the dimensionless representation of the sound power level the dimensionless parameters have to be complemented by a dimensionless representation of the frequency axis. It is advantageous to normalize it to the first eigenfrequency of an *Euler Bernoulli* beam since the aforementioned examination showed a good correlation to the first eigenfrequency of numerical models for each parameter combination. The sound power is represented by the transfer function with respect to the force amplitude of the excitation (see Section 5.3).
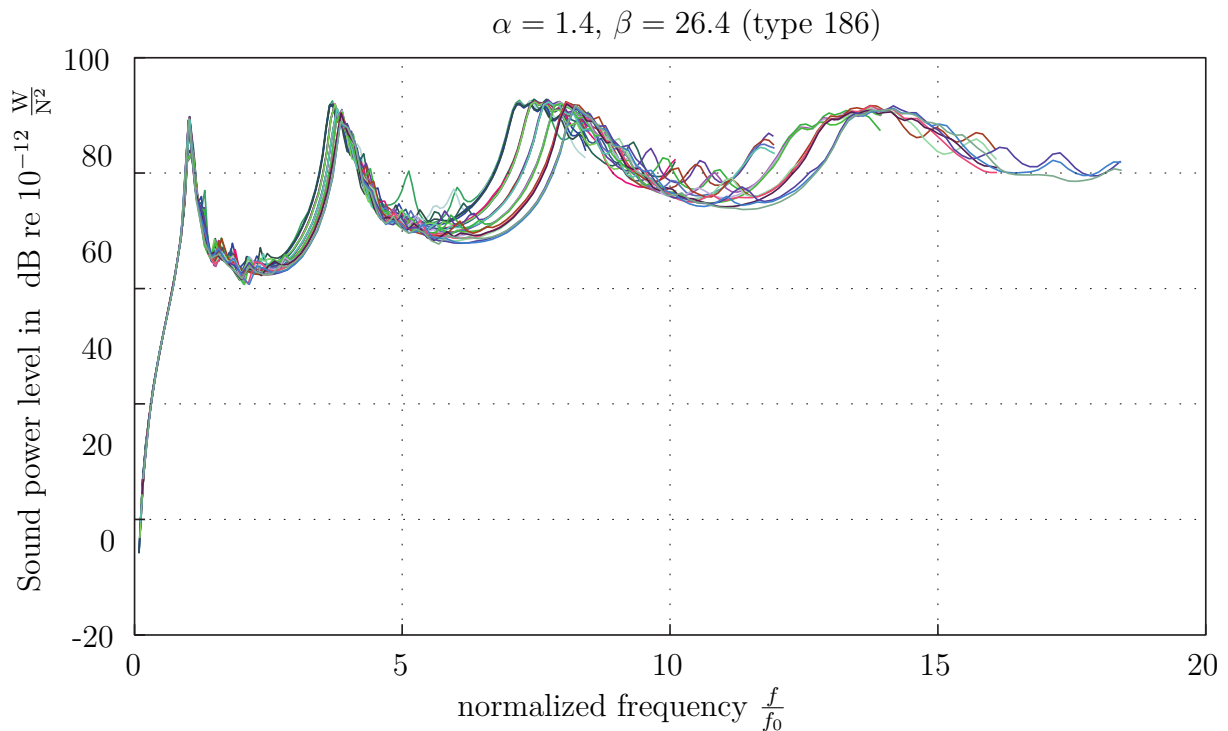
Figure 5.3: CLT R sound power nomogram: $\alpha = 1.4$; $\beta = 26.4$ (CLT type 186); Variation of n_s

In Figure 5.3, an example for a sound power nomogram is depicted. It shows the transfer function of the radiated sound power, resulting from a harmonic excitation by a single load of 1.0 N for all simulated parameter combinations with CLT type 186 and an aspect ratio of $\alpha = 1.4$. Further, nomograms with varying selected parameter configurations as well as a summary of all simulation results are shown in Appendix B.2.1.

A detailed examination of the sound power nomograms shows the following:

- The number of coupled slabs as well as the aspect ratio have low influence on the radiated sound power. The number of eigenfrequencies in the investigated frequency range increases, but the additional eigenfrequencies are not recognizable in the sound power spectrum.

- Comparing the same floor type, an increase of the length leads to a small deviation of the third bending eigenfrequency in the nomograms. The amplitude of the peaks stay the same, but the value of the normalized frequency decreases.

- A change of the floor type has a larger influence than a change of the remaining parameters. Deviations of the normalized frequencies as well as the amplitude of the peaks are recognizable already at the second bending eigenfrequency. Both values are

deceasing with increasing thickness of the floor. However, the deviations stay relatively small.

5.2.2 Application of TMDs to reduce radiated sound power

In the aforementioned evaluation of raw CLT, floors it appeared that some eigenmodes contribute mainly to the radiated sound power. This can be explained by the fact that those eigenmodes show only negligible bending perpendicular to the main load bearing direction. The corresponding wave number in y-direction is therefore equal to zero. Figure 5.4 shows one of these modes. It is the first eigenmode of a CLT model composed of four coupled slabs at $\approx$ 9 Hz. Caused by the weak coupling between the different slabs, groups of eigenmodes appear with only slightly different eigenfrequencies (compare Fig. 5.5). Those have a common wavelength in main load-bearing direction, but differ by wavelengths in perpendicular direction. While, in case of the first eigenmode of a group, the cross-section in perpendicular direction stays almost even, higher eigenmode's wavelengths decrease with increasing eigenfrequency. The modal shapes of the latter can be interpreted as a composition of torsional eigenmodes of the individual slabs. When a cross-section along the central perpendicular axis of the floor is examined, it resembles a rigid body motion rather than a bending wave. To differentiate between the two types of modes they will be referred to as "bending" and "torsional" modes in the following. As a result, if the radiated sound power is to be reduced, special attention to the bending modes has to be given. An approach to tackle this problem is the application of TMDs to minimize the amplitudes of the relevant bending modes.
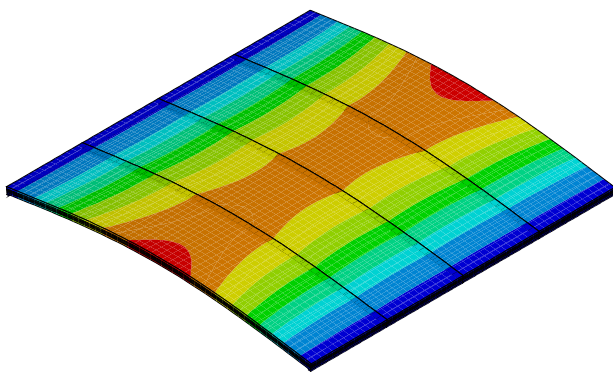
Figure 5.4: Eigenmode of a CLT floor at $\approx$ 9 Hz
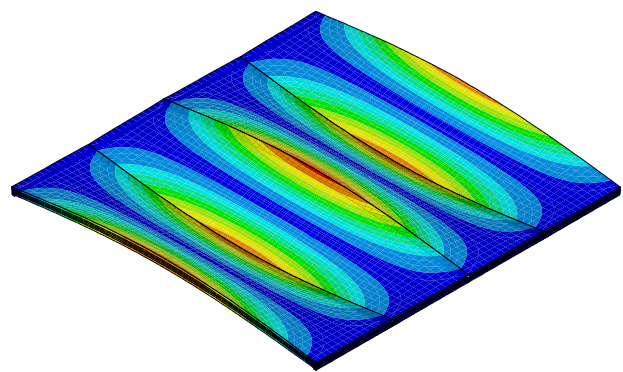
Figure 5.5: Eigenmode of a CLT floor at $\approx$ 18 Hz

5.2.2.1 Description of TMDs

A TMD consists of a mass, a spring and a dashpot. It is attached to a structure to attenuate its dynamic response. The frequency of the damper is tuned to a specific frequency. When that frequency is excited, the damper will resonate out of phase with the motion of the structure. The input energy is dissipated by the damper inertia force acting on the structure. The theory of optimizing TMDs has been widely discussed. Optimized parameters for TMDs applied to undamped SDOF systems have been derived by Den Hartog [1952] for an harmonic excitation and by Warburton and Ayorinde [1980] for white noise excitation. Optimization of MDOF systems have been investigated by Sadek et al [1997] and Warburton [1982]. They found different formulas for the optimum tuning frequencies of the damper $\omega_d = \sqrt{\frac{k_d}{m_d}}$ related to the eigenfrequency of the SDOF $\omega_\infty = \sqrt{\frac{k}{m+m_d}}$ system with rigidly attached damper mass m_d. This corresponds to a TMD with infinite damping ratio $\zeta_d = \infty$.

$$\alpha_{\text{opt}} = \frac{\omega_d}{\omega_\infty} \tag{5.1}$$

A second optimization parameter is the optimum damping ratio $\zeta_{d,\text{opt}}$. The objective of the aforementioned studies was the reduction of the main structures displacements. Since the radiated sound power is related to the structure-borne sound velocity, different optimization parameters must be regarded. Bakre and Jangid [2007] gives formulas for parameters to optimize the velocity of undamped and damped SDOF systems. The different approaches for undamped systems are summarized in Table 5.9. Input variable is the mass ratio between the structure and the damper $\mu = \frac{m_d}{m}$.

Table 5.9: Optimum parameters of TMD for undamped SDOF systems

Optimized with respect to	α_{opt}	$\zeta_{d,\text{opt}}$	Source
Displacement	$\frac{1}{1+\mu}$	$\sqrt{\frac{3\mu}{8(1+\mu)}}$	Den Hartog [1952]
Displacement	$\frac{\sqrt{1+\frac{\mu}{2}}}{1+\mu}$	$\sqrt{\frac{\mu\left(1+\frac{3}{4}\mu\right)}{4(1+\mu)\left(1+\frac{\mu}{2}\right)}}$	Warburton and Ayorinde [1980]
Velocity	$\frac{1}{\sqrt{1+\mu}}$	$\sqrt{\frac{\mu}{4}}$	Bakre and Jangid [2007]

For damped SDOF systems Bakre and Jangid [2007] derived rather complicated explicit formulas, related to the structure's damping ratio ζ_s. An optimization with respect to

velocity yields the following:

$$\alpha_{d,\text{opt}} = \frac{1}{\sqrt{1+\mu}} + \left(a_1 + a_2 + \sqrt{\mu} + a_3\mu\right)\sqrt{\mu}\zeta_s + \left(a_4 + a_5\sqrt{\mu} + a_6\mu\right)\sqrt{\mu}\zeta_s^2 \qquad (5.2)$$

$$\zeta_{d,\text{opt}} = \sqrt{\frac{\mu}{4}} + \left(a_1 + a_2 + \sqrt{\mu} + a_3\right)\sqrt{\mu}\zeta_s + \left(a_4 + a_5\sqrt{\mu} + a_6\right)\sqrt{\mu}\zeta_s^2 \qquad (5.3)$$

The coefficients a_i were obtained by minimizing the error of numerical simulations compared to the given equations. For a detailed derivation and Tables containing the optimized parameters for selected combinations refer to Bakre and Jangid [2007].

MDOF systems can be idealized as SDOF systems as long as the specific eigenfrequencies are well separated [Warburton 1982]. Rana [1996] showed that when several eigenmodes are controlled by multiple TMDs the amplitude of the oscillation at the lowest eigenfrequency is marginally increased. This effect must be considered in case of a combined sound power and vibration reduction. A method for optimizing multiple TMDs with varying parameters was derived by Joshi and Jangid [1997] showing more effectiveness than an optimized single TMD of equivalent mass. However, multiple TMD with identical dynamic characteristics are equivalent to a single TMD.

For the idealization of continuous systems such as beams or plates (with well separated eigenfrequencies) as an MDOF system, the modal mass for each eigenmode has to be calculated.

$$M_i^* = \mathbf{\Phi}_i^T \, \mathbf{M} \, \mathbf{\Phi}_i \qquad (5.4)$$

with

$\quad M_i^*$: Modal mass of eigenmode i

$\quad \mathbf{\Phi}_i$: Eigenvector i

$\quad \mathbf{M}$: Mass vector

It can be derived from a Modal Analysis, in case a numerical FE model exists (see Section 2.5). In case of the FE software ANSYS®, it is performed by normalizing the mode shapes to unity and calculating each modes total kinetic energy $E_{\text{kin,tot,i}}$. With the corresponding eigenfrequency ω_i the modal mass can be derived:

$$M_i^* = \frac{2E_{\text{kin,tot,i}}}{\omega_i^2} \qquad (5.5)$$

5.2.2.2 Equipping a single CLT slab with TMDs

The FE models of CLT floors consist of coupled slabs of identical dimensions. Therefore, a practical approach is to find TMD configurations to attenuate the velocity amplitudes of the bending waves for the individual slabs. The torsional modes of the individual slab as well as the resulting additional torsional modes of the coupled system showed low impact on the radiated sound power of the system.

A numerical model of a single slab measuring 5.5 m × 1.375 m of the five-layered CLT type Leno 105 is investigated. Material parameters and support conditions correspond to the models described in Chapter 3. The damping ratio is set to $\zeta_s = 0.03$ in this example. From a Modal Analysis, the modal parameters listed in Table 5.10 can be derived for the first three bending modes. The specific eigenfrequencies are well apart, and can, therefore, be idealized as individual SDOF systems [Warburton 1982].

Table 5.10: Modal parameters for a single CLT slab

Mode i	Eigenfrequency f_i in Hz	Modal mass M_i^* in kg	Modal shape
1	8.71	181.57	1/2 sine
2	32.71	157.07	sine
3	71.43	130.93	3/2 sine

The optimal parameters of TMDs for the attenuation of each mode individually can be derived from Bakre and Jangid [2007] for damped systems. Table 5.11 lists the resulting parameters. The mass ratios μ_i are chosen to decrease with increasing frequency to minimize the modal contamination of the eigenmodes with lower frequency [Rana 1996]. The coefficients α_{opt} and $\zeta_{d,\mathrm{opt}}$ are taken from tables in Bakre and Jangid [2007].

Table 5.11: Optimal TMD parameters for a system with 3% damping ratio; according to Bakre and Jangid [2007]

Parameters	Mode 1	Mode 2	Mode 3
Mass ratio μ_i	0.10	0.08	0.05
Damper mass $m_{d,i}$ in kg	18.16	2×6.29	3×2.18
Frequency ratio α_{opt}	0.95865	0.96705	0.97999
Damper frequency $f_{d,i}$ in Hz	8.35	31.64	70.00
Damper stiffness $k_{d,i}$ in $\frac{\mathrm{N}}{\mathrm{m}}$	$50.0 \cdot 10^3$	$2 \times 254.8 \cdot 10^3$	$3 \times 418.6 \cdot 10^3$
Damping ratio $\zeta_{d,\mathrm{opt}}$	0.1605	0.1434	0.1131
Damping constant $c_{d,i}$ in $\frac{\mathrm{Ns}}{\mathrm{m}}$	305.8	2×358.2	3×217.1
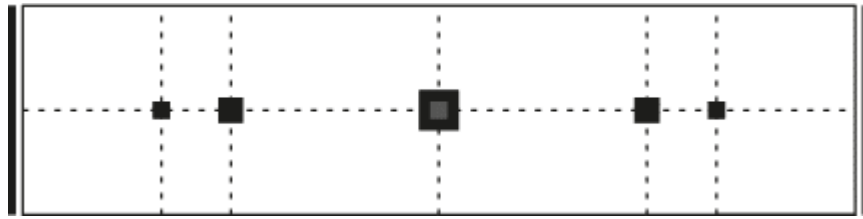
Figure 5.6: Sketch of the TMD arrangement

The TMDs are arranged for each mode in the locations of the maximum deformation depending on its modal shape. The first mode is controlled by a single TMD in the center of the slab. For the second and third modes two respectively three identical TMDs with equivalent parameters to a single one are arranged at each peak of the mode shape [Joshi and Jangid 1997]. All TMDs are mounted along the longitudinal symmetry axis of the slab, since torsional modes are not controlled. A sketch of the setup is depicted in Figure 5.6. Vertical dotted lines indicate peaks of the individual considered mode shapes.
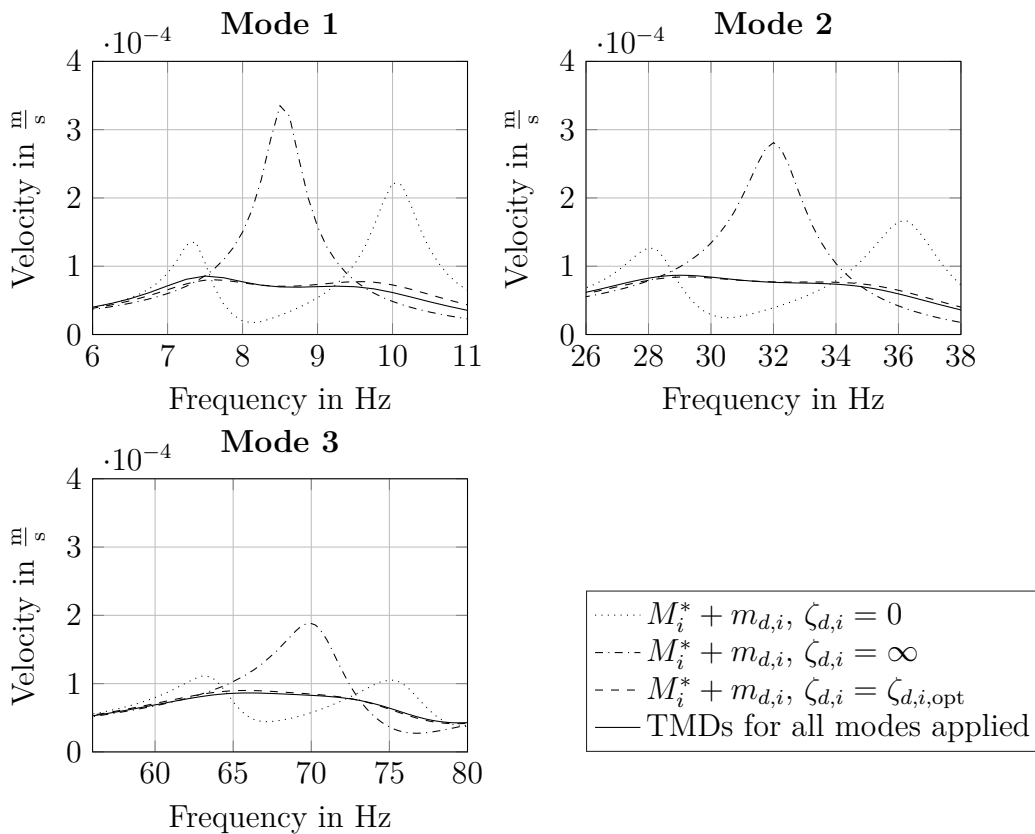
Figure 5.7: Velocity spectra at the considered eigenfrequencies with applied TMDs

The effectiveness of the TMDs is examined by a Harmonic Frequency Analysis. Therefore, the described FE model with mounted TMDs is excited by a single load of 1 N. The load is

applied at location $x = \frac{1}{6}l$ and $y = \frac{1}{2}w$. Here, every bending mode considered is excited while an excitation of torsional modes is excluded. Figure 5.7 shows details of the velocity spectra in the frequency range of the considered eigenmodes. For reasons of comparison, several configurations are investigated. In each diagram, configurations with only the TMDs for the corresponding mode are simulated and compared to the spectrum with all TMD applied. Additionally the spectra of rigidly attached tuning mass $\zeta_{d,i} = \infty$ and without a dashpot $\zeta_{d,i} = 0$ are shown. It can be observed that TMDs designed by the optimized parameters according to Bakre and Jangid [2007] result in a significant attenuation of the velocity of the main system. The two resulting peaks have nearly the same amplitudes and are located close to the intersection of the curves for $\zeta_{d,i} = 0$ and $\zeta_{d,i} = \infty$ in every case. The damping constant of the TMDs for mode 3 seems to be marginally too high, but still good results are achieved. When all TMDs are mounted the amplitudes are slightly shifted resulting in marginally higher peaks for the first mode almost equal peaks for the second and slightly lower peaks for the third. The overall performance of the slab with applied TMD is greatly improved.
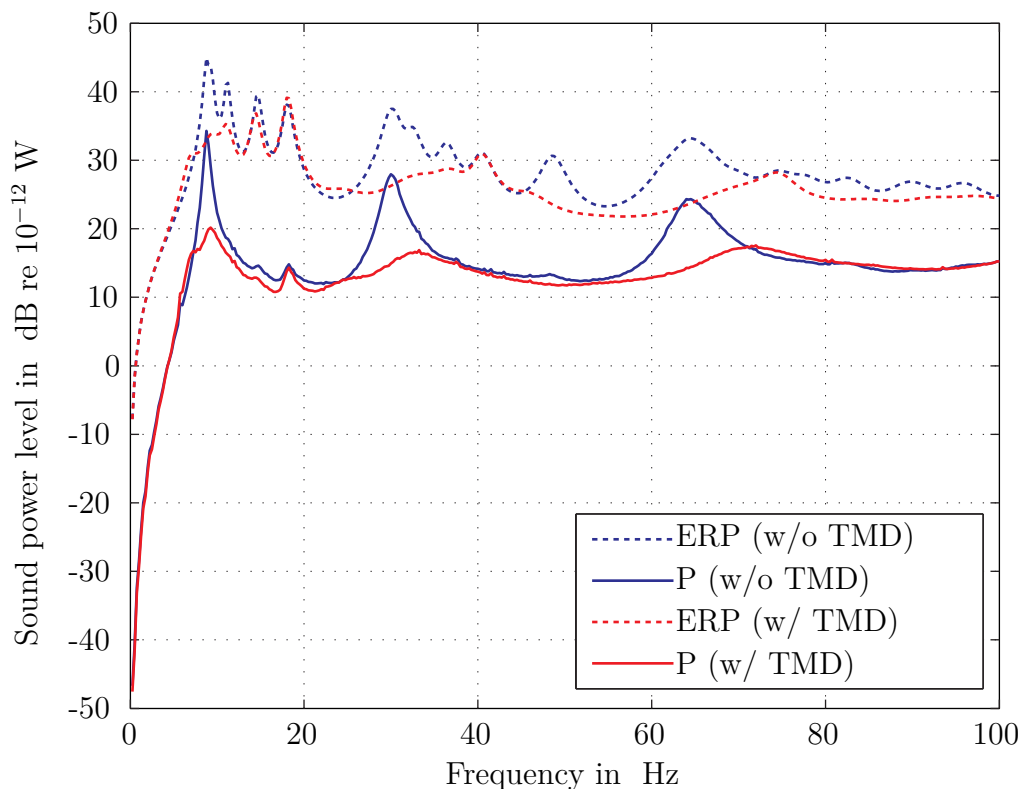
Figure 5.8: Radiated sound power of a CLT floor attenuated by TMDs

5.2.2.3 Attenuation of the sound power of a CLT floor by application of TMD

To examine the impact of the applied TMDs on the radiated sound power, an FE model of a floor consisting of four coupled CLT slabs is investigated. Every individual slab is equipped with the optimized TMDs from the previous example. A Harmonic Frequency Analysis is performed using the stochastic excitation model described in Section 3.4.2. In this way, every eigenmode of the system is excited equally and a more general view on the vibro-acoustical behavior can be achieved.

Figure 5.8 shows a comparison of spectra of the resulting radiated sound power level (P). Curves for models with and without applied TMDs are depicted. Superimposed are the corresponding spectra of the ERP when piston like vibrations are assumed. It can be observed that the sound power level can be significantly decreased in the range of the bending modes. Again, a comparison to the ERP shows that the torsional modes only marginally contribute to the radiated sound power. The applied TMDs only act on the bending modes while the torsional modes attenuation is negligible. However, those modes have larger wave numbers that lie beyond the relevant wave number range for the radiated sound power. Of course, an attenuation of the first eigenfrequency for this scientific example has low practical relevance with regard to acoustical considerations.

5.2.3 Examination of the parameters of the suspended ceiling PS-SP (CLT R/SC + R/FLF/SC, Type 165)

Caused by the large number of varying parameters in this study, only a limited parameter range is evaluated. Thus, the resulting database is too small to allow a dimensional analysis. The simulation results are therefore examined by comparing selected parameter combinations. A CLT floor model was used as main system with a floor type 165. The simulations were performed with and without additional floating floor. The parameters of the floating floor were not varied. It was chosen to be tuned to a very high resonance frequency to examine the effect on the resulting radiated sound power. As an approximation, the resonance frequency can be calculated according to DIN 4109-34:2016-07 by assuming a simplified mass-spring-mass system:

$$f_{\text{flf}} = \frac{1}{2\pi} \sqrt{s_{\text{ins}} \cdot \left(\frac{1}{\rho_{\text{scr}} \cdot d_{\text{scr}}} + \frac{1}{\rho_{\text{spr}} \cdot d_{\text{CLT}}} \right)} = 107.7 \text{ Hz} \tag{5.6}$$

with

$$
\begin{array}{lll}
f_{\text{flf}} & : & \text{Resonance frequency} \\
s_{\text{ins,l}} = 20 \cdot 10^6 \ \tfrac{\text{N}}{\text{m}^3} & : & \text{Dynamic stiffness of the insulation} \\
\rho_{\text{scr,l}} = 2000 \ \tfrac{\text{kg}}{\text{m}^3} & : & \text{Density of the screed} \\
d_{\text{scr}} = 0.05 \ \text{m} & : & \text{Thickness of the screed} \\
\rho_{\text{spr,m}} = 470 \ \tfrac{\text{kg}}{\text{m}^3} & : & \text{Density of spruce} \\
d_{\text{CLT}} = 0.165 \ \text{m} & : & \text{Thickness of the CLT floor}
\end{array}
\tag{5.7}
$$

5.2.3.1 Suspension height

The influence of different distances between the main floor and the paneling of the suspended ceiling is shown in the diagrams in Appendix B.2.2. Diagrams of radiated sound power level for floor with and without floating floor are depicted with varying length and aspect ratios for a suspension grid of $a_x = 0.1$ m. Additionally, the influence of the impedance at the boundaries of the air cavity is shown. An example of such a diagram is given in Figure 5.9. It shows the resulting sound power levels for a CLT floor without floating floor with dimensions 5.0×5.0 m.
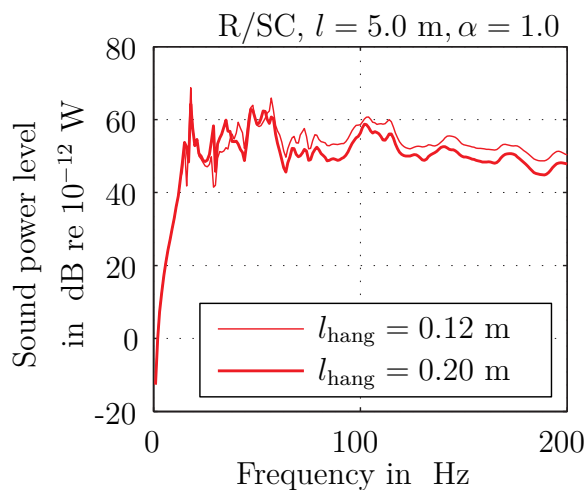
Figure 5.9: Radiated sound power for varying suspension heights with regards to the length of the hanger l_{hang}
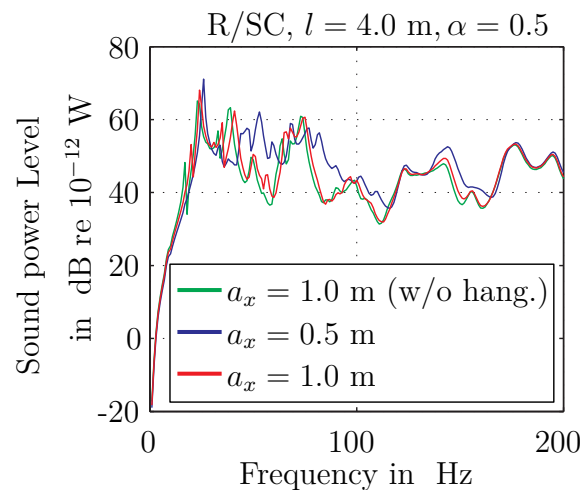
Figure 5.10: Radiated sound power for varying suspension grids a_x, with and without hangers

It can be observed that in the investigated frequency range $0 - 200$ Hz the sound power level is generally decreasing with increasing suspension height h. In the shown example,

the difference between the two curves for $h = 0.20$ m and $h = 0.12$ m is about 3 dB. The curves differ above a frequency of ≈ 50 Hz while below this frequency no major deviation is observable.

5.2.3.2 Suspension grid work with and without hangers

An evaluation of the variation of the suspension grid can be performed by comparing the diagrams in Appendix B.2.3. Analogue to the aforementioned evaluation of the suspension heights diagrams with different lengths and aspect ratios as well as impedance values are shown with and without floating floor. Additionally, the varying suspension heights are considered. An example is shown in Figure 5.10. Again, the radiated sound power is depicted, this time for a CLT floor with dimensions 4.0 m × 2.0 m without floating floor.

In contrast to the aforementioned evaluation, the size of the suspension grid has only a minor influence on the radiated sound power. Most parameter combinations show a slightly higher sound power level for smaller grid sizes between 50 and 100 Hz, with increasing frequency the curves converge. It is remarkable that configurations with a self-supported ceiling (without hangers) show no major deviation from a suspended ceiling.
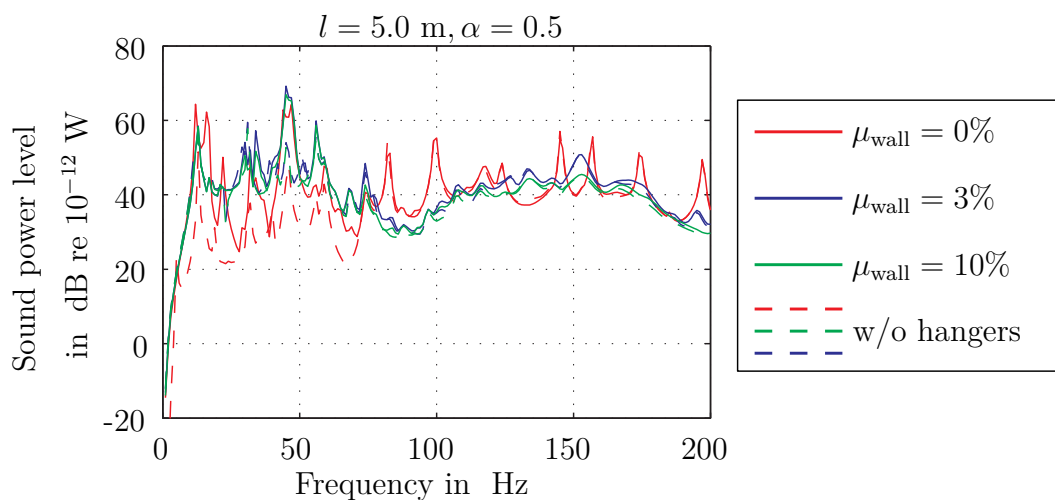
Figure 5.11: Radiated sound power level for varying absorption coefficients μ_{wall}, with and without hangers

5.2.3.3 Boundary impedance of the air cavity

The upper and lower boundary of the air inside the cavity is defined by the main floor and the paneling of the suspended ceiling. The remaining boundaries are practically formed by the walls of the room underneath the floor. In case of the floor testing facility in Rosenheim, those walls are made of reinforced concrete. Since the walls are not modeled in the FE model, the reverberant behavior of the walls is substituted by a boundary impedance. It is normalized to a absorption factor μ_{wall} which ranges from zero to unity representing reverberant and fully absorbing boundaries. The diagrams in Appendix B.2.4 show the radiated sound power level of different parameter combination for absorption factors 0.03, 0.10 compared to reverberant conditions. An example is given in Figure 5.11. A CLT floor with floating floor measuring 5.0 m × 2.5 m with a suspension grid of $a_x = 1.0$ m and a suspension height of $h = 0.12$ m is shown. Additionally, the resulting sound power level for a self supported ceiling is superimposed.

In the reverberant configuration $\mu_{\mathrm{wall}} = 0$ clearly the resonances of the air volume are visible above the frequency of ≈ 50 Hz. It can be observed that the resonance peaks flatten out with increasing absorption at the boundaries. An increase of the absorption from 3% to 10% only marginally deviates the curve of the radiated sound power. The reverberant configuration shows a curve with prominent peaks. As mentioned in Section 5.2.3.2, the difference between suspended and self-supported ceiling are negligible above a frequency of 50 Hz. This can be explained by the governing influence of the resonances inside the air cavity. This result has to be handled with care, since no absorbing material was implemented into the cavity neither in the simulations nor during the measurements, while this is usually the case in practice.

5.2.3.4 Dimensions and aspect ratio

The influence of a variation of the length and aspect ratio of different floors are shown in diagrams in Appendix B.2.5. The results are summarized for varying absorption factors and subdivided into the different simulated lengths and construction states. The resulting sound power level curves are plotted in two ways. In one diagram, a representation of each individual curve is given and for a better visualization, the mean sound power level of simulations with the same aspect ratio as well as the corresponding envelope range is depicted in a second diagram. An example of the mean sound power level representation is given in Figure 5.12. It shows the results for a CLT floor with floating floor with a length of 4.0 m and an absorption factor of $\mu_{\mathrm{wall}} = 0.10$ for different aspect ratios.

Up to a frequency of ≈ 50 Hz the three curves show little deviation. Beyond this frequency, the sound power level of an aspect ratio of $\alpha = 1.0$ is up to 10 dB higher than for an aspect ratio of $\alpha = 0.5$. The curves for $\alpha = 0.5$ and $\alpha = 1.5$ converge between 100 Hz and 150 Hz. For some parameter configurations the sound power levels of $\alpha = 1.0$ and $\alpha = 1.5$ converge above 150 Hz. Avoiding quadratic dimensions of a floor seems advantageous.
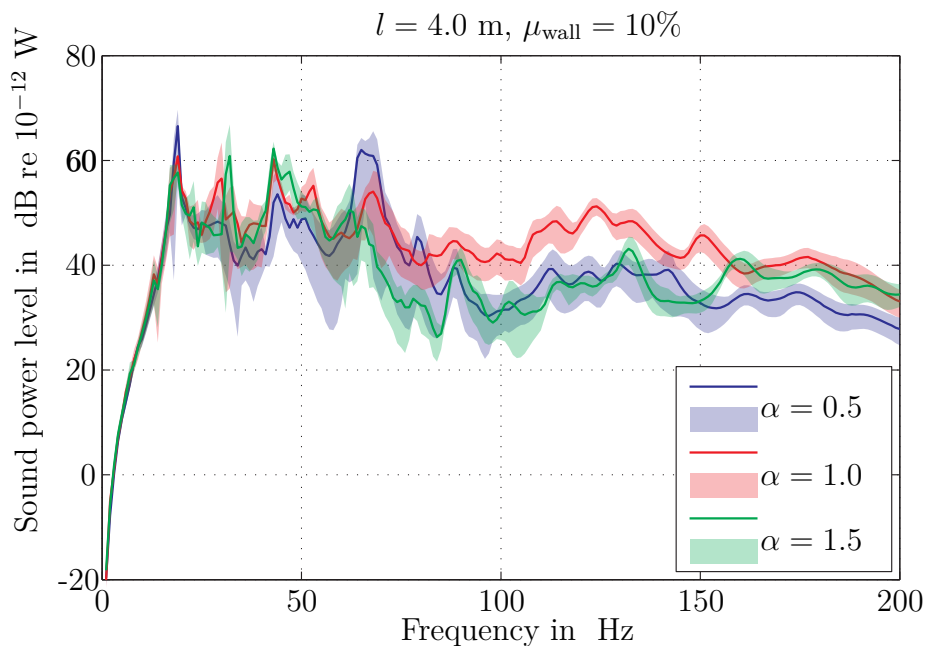
Figure 5.12: Mean value of the radiated sound power for simulations with varying aspect ratios α

A comparison of the mean radiated sound power levels for CLT floor models with length of 4.0 m and 5.0 m is shown for various parameter combinations in diagrams in Appendix B.2.6. It can be observed that when a suspended ceiling or a floating floor is applied the sound power levels show little deviation even if the first eigenfrequencies differ. This indicates that in those construction states the vibro-acoustic behavior above a frequency of ≈ 30 Hz is governed by the influence of the floating floor and the suspended ceiling rather than the main floors characteristics.

5.2.4 Evaluation of the LJ floor and its construction states (PS-GUI LJ floor)

For the examination of the influence of the parameters of the lumber joist floors no specific parametric study is performed. Those parameters are evaluated by an investigation of the data base collected for the graphical user interface (PS-GUI LJ). This parametric study

is performed with different levels of discretization, depending on the construction state. The radiated sound power levels for parameter configurations that were simulated for all construction states are compared in Appendix B.2.7. For a better visualization the results are given preliminary for each construction state separately and in subsequent diagrams summarized for all construction states. Different construction states are visualized by colors, beam widths by varying line thicknesses and distances between the beams by different line styles. For each simulated length and aspect ratio individual diagrams are drawn. An example of such a diagram is given in Figure 5.13. It shows a summary of the resulting radiated sound power levels for simulations with length $l = 450$ cm and an aspect ratio of $\alpha = 1.0$.
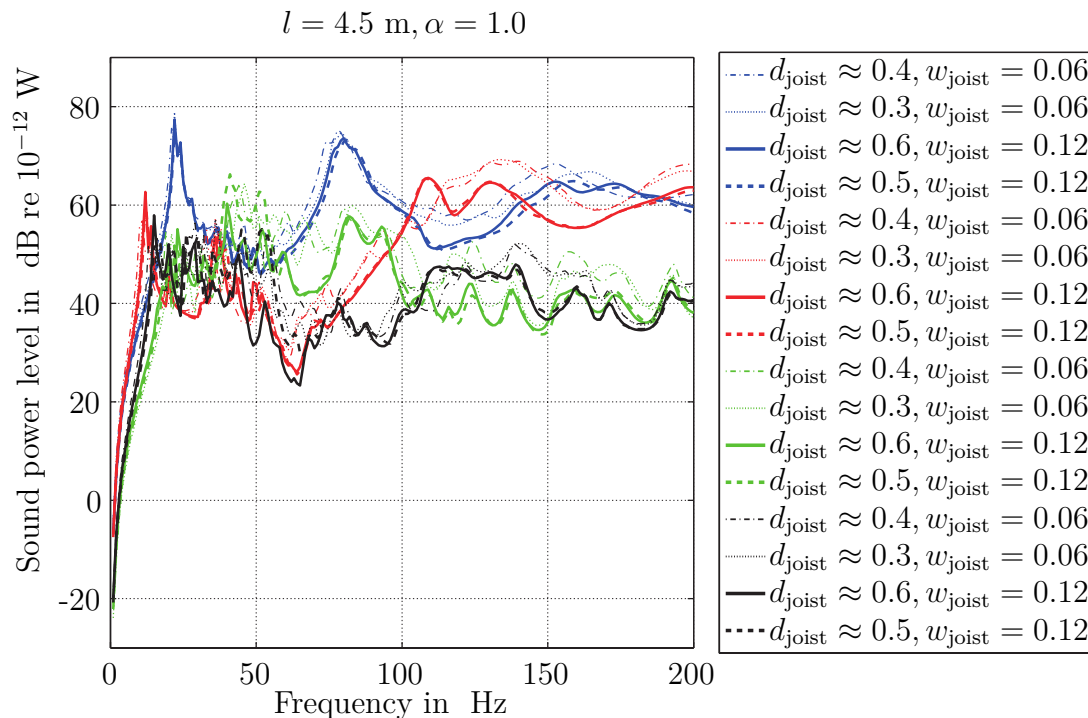
Figure 5.13: Comparison of different construction states (R=blue; R/FLF=red; R/SC=green, R/FLFS=black), distance between beams ay in cm and beam width bb in cm

5.2.4.1 Distance between the beams

From a comparison of the results, it can be stated, that the distance between the beams in general has a minor influence on the radiated sound power. For some parameter combinations, including a suspended ceiling deviations in the frequency range below 100 Hz are observable. Thus, smaller distances tend to lead to higher radiated sound power level. This can be explained by the fact that the suspension grid is linked to the distance between

the beams, and therefore a smaller distance lead to smaller grid sizes and more radiation analogue to Section 5.2.3.2.

5.2.4.2 Joist width

A variation of the joist width showed little influence on the resulting sound power level. An increase of the width tend to result in marginally lower sound power levels above a frequency of 50 Hz.

5.2.4.3 Construction states

A comparison of the different construction states shows several major differences in the curves of the sound power level. Within the results of the raw floors pronounced peaks at the eigenfrequencies for longitudinal bending modes are observable. The curves of the remaining construction states show a more diffuse behavior. The amplitudes in the range of the first eigenfrequencies are decreased significantly compared to the raw floor. The three curves show little deviation up to a frequency of $\approx$ 50 Hz, construction states with floating floor keep a slightly lower level. Above this frequency the curves separate. Construction states with suspended ceiling result in lower sound power than the raw ceiling, whereas when also a floating floor is added the curves are decreased even more. At 100 Hz the construction state with only floating floor gives sound power levels partly larger than the raw ceiling. This is caused by the resonance of the floating floor. It turns out the implementation of only a single static type of floating floor leads to poor results for some parameter configurations as far as practical applications are concerned. This effect is weakened by the complementary implementation of a suspended ceiling. A reduction of $\approx$ 20 dB is observable.

5.2.5 Summary of the influences of the different parameters

In conclusion, the results of the examination from Section 5.2 are summarized in Table 5.12. The degree of influence of the individual parameters on the resulting radiated sound power is indicated by the following symbols: small increase "$-$"; no effect "o"; small and significant decrease "$+$" and "$++$"; only with applied suspended ceiling (SC). For construction states including a floating floor the result depends on whether its resonance frequency lies within "$-$" or outside "$++$" the specified frequency range.

Table 5.12: Influence of the change of the parameter on the resulting radiated sound power

Parameter	Statement	Frequency range in Hz		
		$0-50$	$50-100$	$100-200$
CLT floor: type	the bigger the profile	o	+	+
CLT floor: number of slabs	the more	o	o	o
LJ floor: beam width	the wider	o	+	+
LJ floor: beam distance	the greater	+(SC)	+(SC)	o
Suspension height	the greater	o	+	+
Suspension grid size	the greater	+	+	o
Ceiling	suspended compared to self supported	o	o	o
Absorption coefficient of the cavity's walls	the greater	o	+	+
Aspect ratio	if quadratic	o	−	−
Floating floor	with compared to without	+	+ + /−	+ + /−
Suspended ceiling	with compared to without	+	+	++

5.3 Transfer Functions and Force Spectra

The numerical simulations concerning the radiated sound power of the floor constructions are carried out by Harmonic Frequency Analyses (see Section 3.5.2). As described in Sections 3.4.1, the amplitude of the harmonic excitation for every evaluated frequency step is $F(f) = 1.0$ N. Thus, the structure-borne sound velocity, the evaluation model for the sound power spectrum in Section 3.7.1 is based on, can be replaced by the mobility

$$V(f) = \frac{v(f)}{F(f)} \tag{5.8}$$

with respect to the force spectrum $F(f)$. Since the radiated sound power (2.128) is dependent on the term $|v|^2$ and the equation is linear, a transfer function can be derived by separating the force spectrum

$$H(f) = \frac{P(f)}{F^2(f)}. \tag{5.9}$$

The radiated sound power due to a random excitation can thus be approximated by multiplying the transfer function $H(f)$ by the specific force spectra of the excitation.

$$\tilde{P}(f) = H(f) \cdot |\mathcal{F}\{F(t)\}|^2 \tag{5.10}$$

The results, however, are limited to the locations of the single loads that are applied to the numerical model. A common application in building acoustics is the excitation by a standard tapping machine or by a walking pedestrian.

5.3.1 Standard tapping machine

A detailed load model for an excitation by a standard tapping machine within an FE analysis is derived by Rabold [2010]. He compares state of the art load models of varying precision and develops highly precise models for time and frequency domain investigations. It is shown that the excitation mechanism depends on the momentum of the hammers I, but is also affected by the contact stiffness of the target surface K_c, which effects the contact time T_c, and on the admittance and the global movement of the floor. However, a force spectrum, which holds for every transfer function it has to be multiplied with, cannot be derived from such a detailed model. A simplified approximation has to be chosen, which is introduced by Cremer et al [2005] and will be presented in the following.
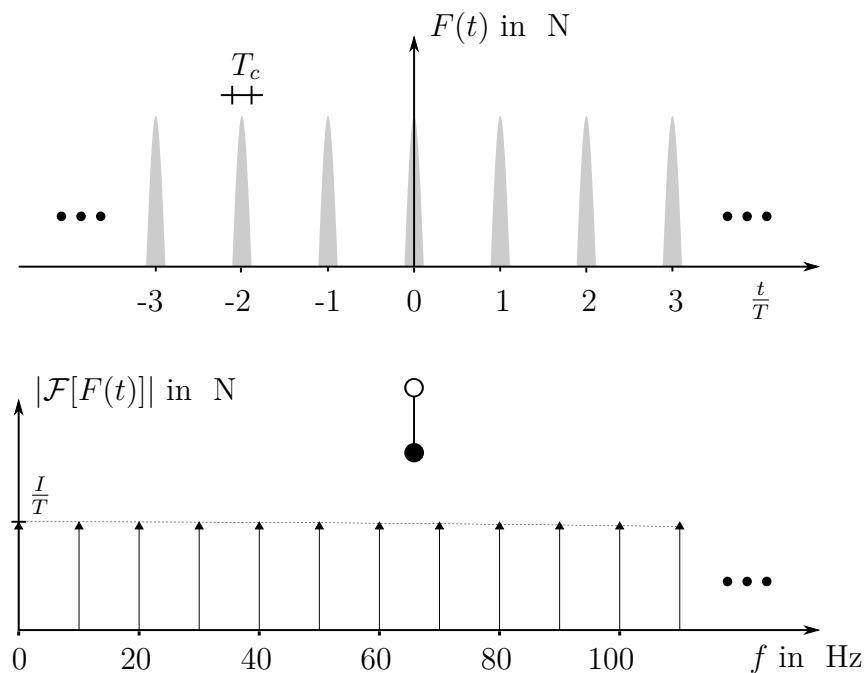
Figure 5.14: Time and frequency domain of a taping machine load function [Cremer et al 2005]

The excitation mechanism of a tapping machine is a standardized procedure. The device consists of five steel cylinders each with a mass of $M_0 = 0.5$ kg and a radius of the tip of $r = 0.015$ m. They are arranged on a straight line with an even distribution of $d = 0.10$ m. Each cylinder hits the floor with a frequency of $f_1 = 2.0$ Hz falling down from a height of $h = 0.04$ m. As an idealization the location of the contact can be assumed coincidental, which leads to a combined excitation frequency of $f_s = 10.0$ Hz. In each period, the cylinders perform a free fall, leading to an impact speed of

$$v_0 = \sqrt{2gh} = 0.886 \; \tfrac{\text{m}}{\text{s}}. \tag{5.11}$$

with the gravity $g = 9.81 \; \tfrac{\text{m}}{\text{s}^2}$. The time history of the excitation force thus consists of a number of peaks that are $T = \frac{1}{f_s} = 0.1$ s apart. The time history can be expressed by the *Fourier* series

$$F(t) = \Re \left\{ \sum_{-\infty}^{\infty} F_n e^{in\omega_s t} \right\} = \sum_{-\infty}^{\infty} F_n \cos(n\omega_s t) = 2 \sum_{n=0}^{\infty} F_n \cos(n\omega_s t) + F_0 \tag{5.12}$$

with Fourier coefficients F_n and circular frequency $\omega_s = 2\pi f_s$. When moving the origin $t = 0$ precisely to the maximum of one peak and assuming a symmetric time history, it can be reduced to its cosine components. The *Fourier* coefficients F_n are determined as follows:

$$F_n = \frac{1}{T} \int_{-\infty}^{\infty} F(t) \cos n\omega_s t dt \tag{5.13}$$

It can be assumed, that $\cos(n\omega_s t) \approx 1$, when the contact period of the hammer with the floor is very short compared to the time period between two impacts. Thus the *Fourier* coefficients yield

$$F_n \approx \frac{1}{T} \int_0^T F(t) dt = \frac{I}{T} \tag{5.14}$$

with the momentum of the steel cylinder I. Thus, the amplitude of the excitation force F_n is constant over the frequency. This approximation is valid up to a frequency of $f \approx \frac{1}{T_c}$, with the contact time T_c [Cremer et al 2005]. The impulse of the steel cylinder ranges depends on the kind of the contact

$$M_0 v_0 \leq I \leq 2 M_0 v_0 \tag{5.15}$$

with the ideal plastic contact as the lower and the ideal elastic contact as the upper limit.

According to Cremer et al [2005] it can be approximated by

$$I \approx \sqrt{2} M_0 v_0 = 0.626 \ \tfrac{\text{kgm}}{\text{s}}. \tag{5.16}$$

When applying this approximation to lightweight wooden floor constructions, some errors are induced, since this model is well suited only for floors with low admittances and hard surfaces. Since the frequency range of the transfer functions within the following examinations is limited to the 100 Hz third octave band, the restriction to hard surfaces can be excluded. Figure 5.14 shows the time history $F(t)$ and the approximated frequency spectrum $|\mathcal{F}[F(t)]|$ in N according to the assumptions made above. To give an impression on the error induced by this approximation the frequency spectrum of a single impulse causing a half-sine shaped contact force with a contact time of $T_c = 0.001$ s, scaled by 10, is superimposed (dotted line). For the observed frequency range it is very small and can be neglected.

5.3.2 Walking pedestrian

Different to the tapping machine, the time history of a pedestrian load is obviously not standardized. Several approaches for a parametric description were presented in recent time. Most of them focus on the description of induced vibrations, which usually range up to the third harmonic of the footfall frequency (e.g. Butz [2006]). A different approach for the use within acoustical examinations was given by Schanda et al [2013], which included the hit of the heel. This impulse-like excitation was found to play a major role for acoustical considerations [Schanda et al 2013].

In the scope of this thesis, the latter approach is applied. As mentioned before, the transfer functions were simulated only for limited driving point locations. Thus an actual walking of the pedestrian cannot be considered. The time history of the induced force is developed by a superposition of single footsteps with a repetition period of $\frac{1}{f_{step}}$. In Figure 5.15 the superposed signal is shown (continuous line) superimposed by the time history of an individual footstep (dashed lines and gray). The hit of the heel can be identified as the sharp peak at the start of the signal. For the following examinations a signal $F(t)$ of a representative pedestrian of mass 75.0 kg with a footfall frequency of $f_{step} = 1.6$ s is chosen. As shown in Figure 5.15 the *Fourier* transformed $|\mathcal{F}[F(t)]|$ consists of discrete impulses with a repetition interval of f_{step}. The abscissa is in logarithmic scale. As expected, the spectrum is slowly decaying with significant amplitudes in the considered frequency range, caused by the hit of the heel.
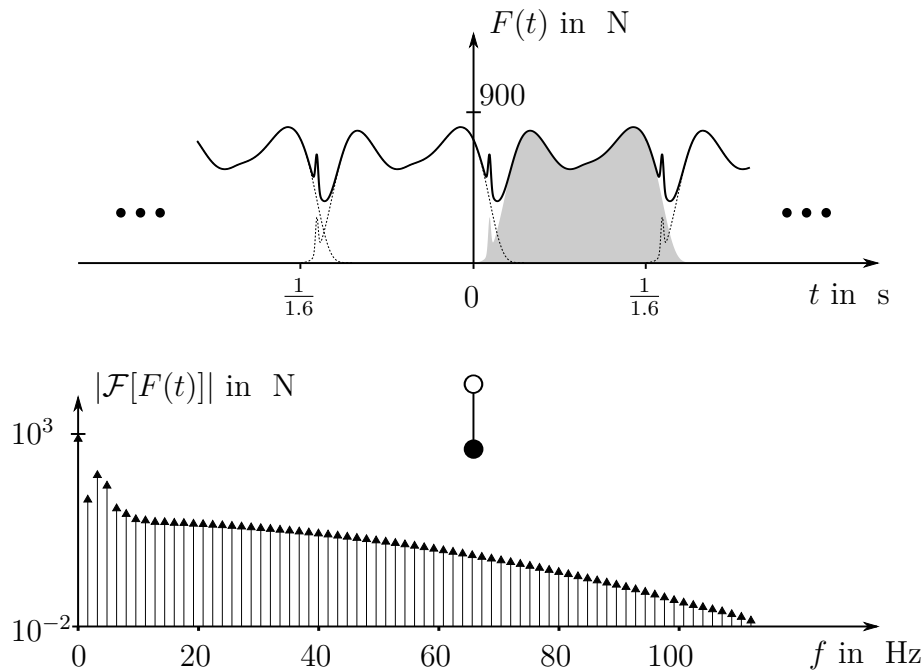
Figure 5.15: Time and frequency domain of a pedestrian load function [Schanda et al 2013]

5.4 Coefficients for the Evaluation at Low Frequencies

Floor constructions in residential buildings have to meet sound insulation requirements. Concerning the impact sound insulation, the requirements for the German market are formulated in DIN 4109-1:2016-07. In practice, floor constructions are rated concerning the weighted normalized impact sound pressure level $L_{n,w}$ (laboratory measurements) according to DIN EN ISO 717-2:2013-06. This single value is derived from octave or third-octave impact sound pressure levels L_i, that are measured with an excitation by a standard tapping machine [DIN EN ISO 10140-3:2015-11]. In case of third octave measurements, the frequency bands from 100 to 3150 Hz must be taken into account. The impact sound pressure levels are further processed, concerning the measured reverberation time, and thus yielding for the normalized impact sound pressure levels

$$L_n = L_i + 10 \log \frac{A}{A_0}. \tag{5.17}$$

The equivalent sound absorption area A is derived from the reverberation time $T = 0.16\frac{V}{A}$ with the volume of the receiving room V. The equivalent sound absorption area is $A_0 = 10$ m^2. Hence, variations for different room situations will not influence the results. By shifting a standard reference curve, according to DIN EN ISO 717-2:2013-06, towards the

measured curve of L_n, the single value $L_{n,w}$ can be determined as the value of the reference curve at 500 Hz. A spectrum adaption term C_I may be used to take into account the different source spectra of a tapping machine and a pedestrian. Its frequency range can optionally be adapted to an increased frequency range from 50 to 2500 Hz, and thus is assigned $C_{I,50_2 500}$.
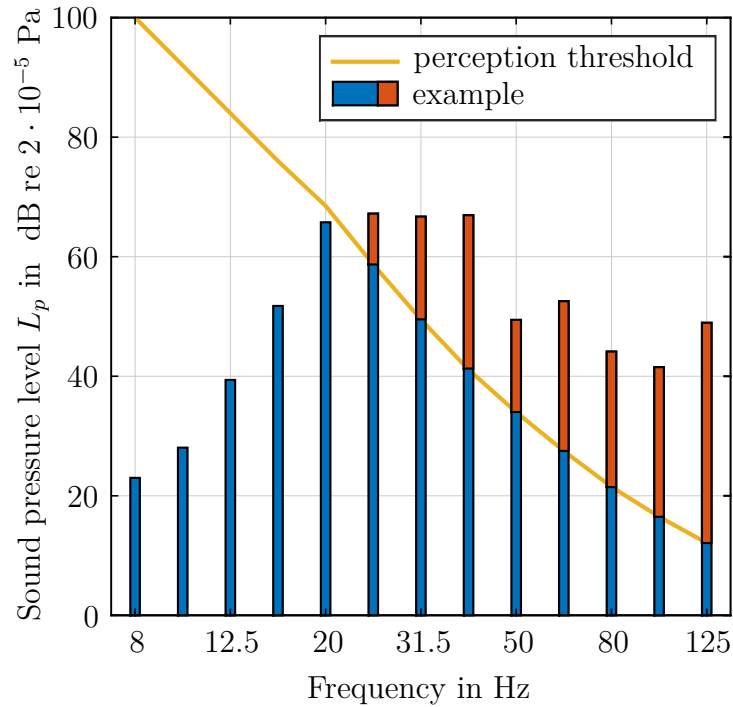
Figure 5.16: Example of a simulated sound pressure level of a LJ floor with FLF and SC (blue); superimposed: the perception threshold (orange) and the values above the threshold (red)

A direct calculation of the impact sound level $L_{n,w}$ from the simulated data is not possible, due to the insufficient simulated frequency range defined for the parameter studies, which leads to an upper limit octave band of 100 Hz resp. 125 Hz. Thus, a coefficient must be developed, derived from the simulated data, that correlates with the single value $L_{n,w}$. Therefore, in a first step, the radiated sound power is evaluated for an excitation with a standard tapping machine by multiplying the transfer functions of the simulated sound power spectra by the force spectrum of the tapping machine (see Section 5.3.1) according to Equation 5.10. The resulting narrow-band spectra are subsequently transformed into third octave bands. The sound power level can then be transferred into a sound pressure level under simplified assumption of a diffuse sound field by

$$L_{p,diff,i} = L_{W,i} - 10 \log_{10} \left(\frac{A_{ref}}{A_{eq}} \right) \tag{5.18}$$

with $A_{ref} = 4.0$ m^2 and the equivalent sound absorption area $A_{eq} = 10$ m^2. The latter is

chosen in accordance to DIN EN ISO 717-2:2013-06 ($A_0 = 10\ \mathrm{m}^2$) to enhance a comparability of the results. Of course, this does not hold properly for small rooms. The results are further processed by applying the perception threshold according to DIN 45680:2013-09 Entwurf to consider the psycho-acoustical perception. Figure 5.16 shows an example of a third octave sound pressure level with superimposed perceptual threshold (orange).

The sum level of the values above this threshold serves as the desired coefficient. An investigation of the simulated results [Fünfer 2016] showed, that the sum level from 50 to 100 Hz ($L_{sum,50-100}$) gives a sufficient approximation of the total frequency range, since the third octave bands below 50 Hz have only a minor impact on the result. In addition, this frequency range is covered by the usual measurement frequency range of impact sound insulation.

(a) $L_{sum,50-100}$ for tapping machine load   **(b)** $L_{sum,25-100}$ for pedestrian load
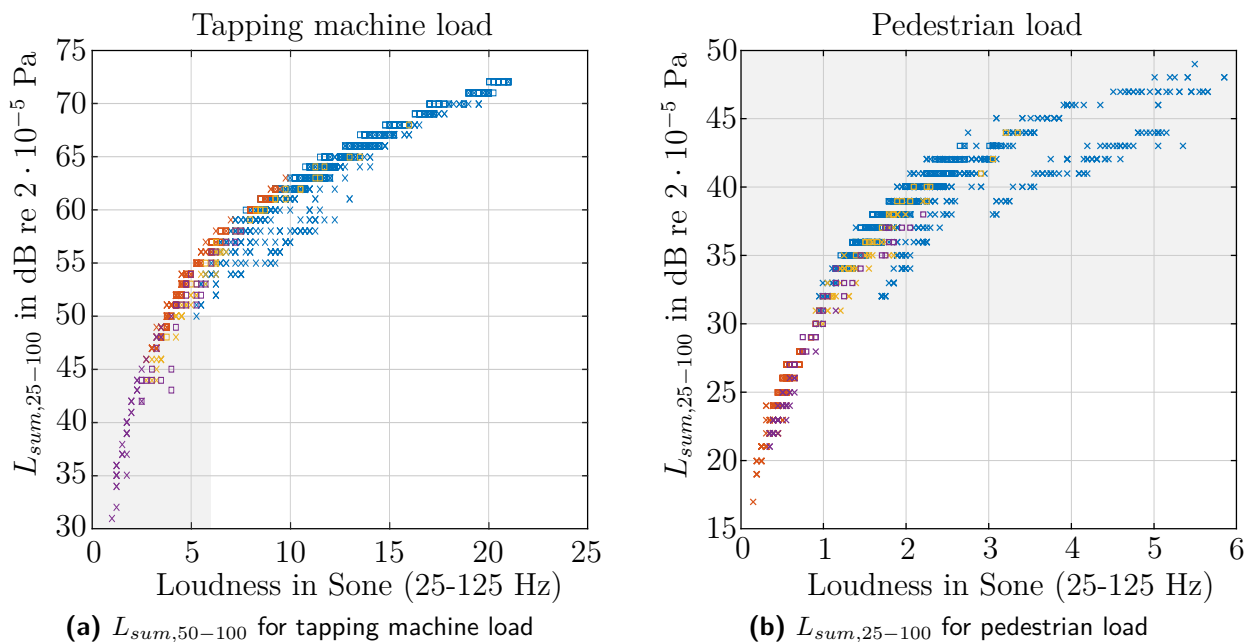
Figure 5.17: Correlation of the coefficients compared to the loudness by *E. Zwicker* for LJ (X) and CLT (□) floors with construction states: R (blue), R/FLF (red), R/SC (yellow), and R/FLF/SC (purple)

As a validation, the developed coefficient is compared to the loudness, computed out of the same set of data, according to the method proposed by *E. Zwicker* [DIN 45631:1991-03]. A good correlation can be achieved, as shown in Figure 5.17a.

A similar evaluation can be performed for an excitation by a force spectrum of a walking pedestrian. In this case, the lower frequency bands do have a major impact. Thus, the coefficient for a pedestrian excitation is formed by the sum level of the third octave bands from 25 to 100 Hz. Figure 5.17b shows again the correlation to the loudness. The force spectrum, described in Section 5.3.2, of a pedestrian of 75 kg with a footstep frequency of

1.6 Hz is applied. Again, a good correlation can be observed. Especially the floors with an additional screed show lower amplitudes. The diagrams in Figure 5.17, for a better visualization, cover different parameter ranges. To avoid a miss-interpretation, overlapping parameter ranges are marked in gray.
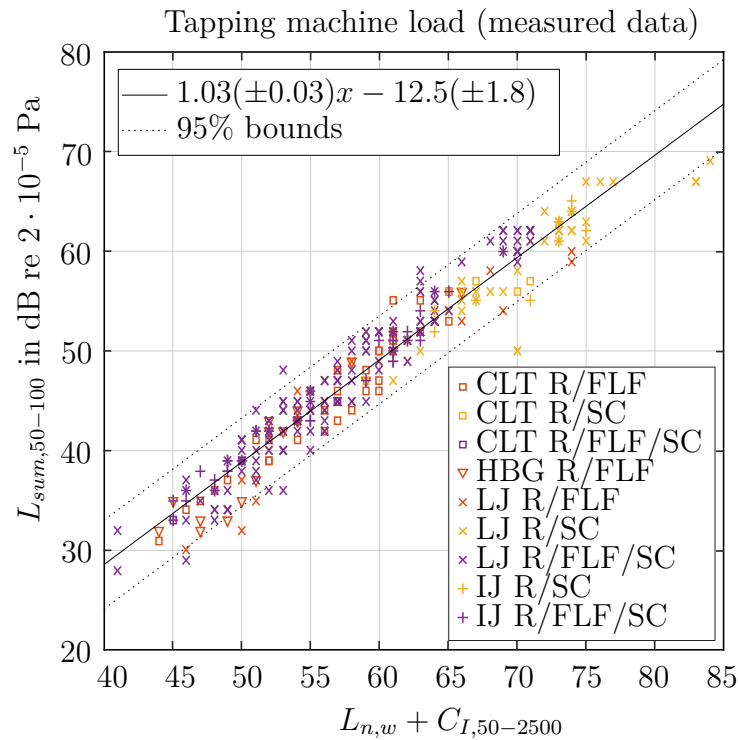
Figure 5.18: Correlation between the coefficient $L_{sum,50-100}$ and the impact sound level with spectrum adaption term $L_{n,w} + C_{I,50-2500}$ for measurement data of different wooden floor constructions (IJ: I-joist floor); superimposed: a linear trend line with 95% confidence bounds

The coefficients derived from the simulated data cannot directly be compared to the impact sound level, as mentioned before. Instead a comparison based on measurement data is performed as shown in Figure 5.18. It shows the database for a variety of wooden floor constructions, archived by the IFT Rosenheim, out of which the construction catalog for DIN 4109-33:2016-07 was derived. Here, the coefficient $L_{sum,50-100}$ is compared to the standard footfall noise level $L_{n,w}$, complemented by the spectrum adaption term $C_{I,50-2500}$. A good linear correlation is observable, the coefficient of determination is $R^2 = 0.94$. The values differ only by a fixed value of 12.5 dB with a standard deviation of ± 1.8 dB. Thus, the estimated $L_{n,w} + C_{I,50-2500}$ can easily be extrapolated from the coefficient $L_{sum,50-100}$. For a maximum footfall noise level of 53 dB, as proposed by Rabold [2011] for a sufficient comfort level, a floor construction meets the requirements for $L_{sum,50-100} \leq 43$ dB. The derived coefficients are implemented into the graphical user interface described in Section 5.5.

5.5 Graphical User Interface (GUI)

A pursuing research at the University for Applied Science Rosenheim scopes on the enhancing of the GUI already developed within the research project "Vibood" [Kohrmann et al 2014]. It processes the data from the parametric survey presented in Section 5.1.3.1, that are implemented as transfer functions according to Section 5.3. Its development status is pending, hence, the actual development state will be presented [Kohrmann et al 2016]. Since the program is designed in German language, the following description will provide hints on the translation.
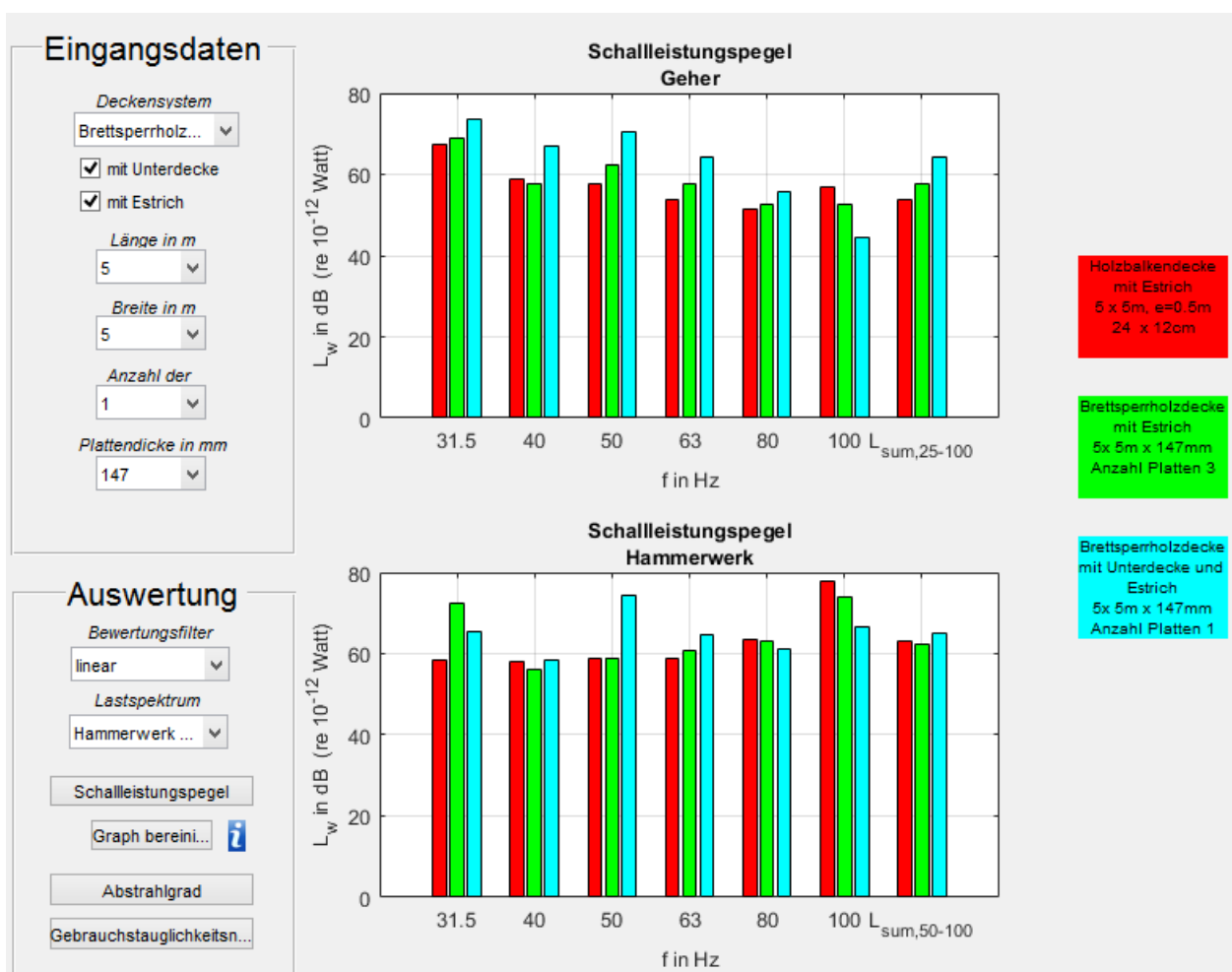
Figure 5.19: Screen-shot of the Graphical User Interface

The GUI combines multiple evaluation possibilities. An example is shown in Figure 5.19. The floor constructions of interest (Deckensystem) as well as its dimensions (Länge, Breite, etc.) can be chosen in the input section (Eingangsdaten). Further, an excitation type (Lastspektren) can be chosen for an acoustical evaluation as well as a specific weighting

function (Bewertungsfilter). Thus, the stored transfer functions are multiplied by the load spectra of a walking pedestrian or a standard tapping machine to derive the resulting radiated sound power. Up to three different floor constructions can be displayed (different color) and compared for both types of excitation. The acoustical evaluation can be done in three different ways with varying degree of detail. The standard configuration shows the third octave spectra of the sound power level from 31.5 to 100 Hz. For more detailed considerations the small band results accompanied by the individual radiation efficiency (Abstrahlgrad) can be opened in a Pop-Up window. A fast comparison of different constructions can be done by the implemented coefficients derived in Section 5.4. As mentioned before, a classification according to the predicted weighted normalized impact sound pressure level can be done.

As an additional functionality, the statutory proof of the serviceability linked to vibrations (Gebrauchstauglichkeitsnachweis) can be provided for the chosen floor. This can be done according to DIN EN 1995-1-1:2010-12 or optional by the modified method developed by *P. Hamm* and *A. Richter* [Winter et al 2010][Hamm et al 2010]. An advantage compared to already existing tools consists of the possibility to compare the calculated to the simulated results. Thus possible oversizing caused by the simplified calculation approach can be identified and avoided.

The GUI will be available online at `http://www.fh-rosenheim.de/lasm.html`.

6 Conclusion

6.1 Summary

In the present thesis, a numerical approach on the prediction of the vibro-acoustic characteristics of timber floor constructions in the frequency range below 125 Hz is proposed. The research aims on the necessity to develop design tools to support the practical engineer prior to construction. Up to now, there exist only simplified design models for the prediction of the vibro-acoustical behavior of floor constructions including noise and vibration abatement. They were essentially developed for traditional heavy weight constructions, which might be misleading in case of timber floors due to the differences in the impedances of the system's components. Thus, numerical models are developed to predict the vibro-acoustic characteristics in a highly realistic way.

It is shown, that an application of the FEM to develop numerical models of floor constructions is a suitable approach. Structural models for three representative floor constructions (CLT floor, LJ floor, and HBG floor) are developed, including FLF and SC. The models are designed entirely parametric to enable parametric studies. Further, they are optimized for an automated process, which also includes idealizations to limit the computational effort. Those idealizations comprise the support conditions and the coupling between individual main floor components. It is shown, that the damping coefficients, as well as the material properties, whether idealized or not, can be calibrated with regard to measured modal parameters.

In case of CLT, the idealizations imply, that the material parameters cannot be taken from literature. It is shown, that in this case, a Model Updating procedure with respect to matching eigenmodes can provide idealized material properties. Another idealization models the originally two-layered, multi-bodied paneling of the SC as a single homogeneous plate. It is shown, that idealized stiffness properties can be achieved by an investigation in the wavenumber domain, comparing the resulting wave number spectra of measured and simulated results. Other constructions, as wooden joists, OSBs, and resilient hangers can be calibrated straight forward with regard to the fundamental eigenfrequency derived by EMAs.

Different load models are applied to the structural models and the dynamic responses are simulated within Harmonic Frequency and Transient Analyses. It is shown, that a walking pedestrian can be simulated by a simplified load model. The dynamic response can further be evaluated to characterize the achievable comfort levels of floor constructions with regards to current standardizations. The frequency spectra of the stucture-borne sound velocities of the floors caused by single and ROTR excitation is derived in the spatial domain. It is shown, that the resulting radiated sound power levels can be predicted using ITMs out of the structure-borne sound velocity pattern in the wavenumber domain. An acoustical evaluation model is presented using zero-padding in the spatial domain in combination with an averaged wavenumber depended kernel function. The procedure proved equivalent effectiveness and accuracy in the prediction of the radiation efficiency compared to spatial domain methods. It is validated by intensity measurements. The valid frequency range for this method, in case of airborne excitation or transmission paths including an air-filled cavity, is evaluated by measurements with varying sampling intervals. It is shown, that in this case the radiation is mainly caused by forced vibrations, thus aliasing effects with respect to resonant vibrations can be neglected up to a specific frequency described by a proposed criterion.

Within a case study, different approaches for the modeling of the air inside the cavity are compared. It is shown, that the sound transmission through a floor construction including suspended ceiling is to a large extend carried by the cavity modes. In particular, every axial, tangential and oblique mode has to be modeled. Models, which only include axial modes in vertical direction lead to erroneous results.

Parametric studies are performed to investigate the floor's vibro-acoustic characteristics with regard to a change of the geometrical parameters. It is shown, that a Dimensional Analyses can describe the fundamental frequencies of CLT floor constructions, as well as the radiated sound power. Further, eigenmodes are identified, which have a major contribution to the resulting sound radiation, while the influence of others is negligible. A consequent approach is the attenuation of these modal vibrations. It is shown, that an application of optimized TMDs can significantly reduce the radiated sound power of raw CLT floors. Further parametric studies investigate the parameters related to the suspended ceiling and varying construction states. The influence of the alternating parameters are analyses and compared within a table.

The results of the parametric studies are processed in the form of transfer functions and stored into a database. This database is accessible by a GUI. The data can be evaluated for a pedestrian load and a tapping machine load by multiplying the specific spectra to the transfer functions of the sound power level. A coefficient is derived to predict the weighted

normalized impact sound pressure level out of the simulated results. By establishing a database of pre-simulated data, the advantages of highly realistic models are provided to the practical engineer without the disadvantages related to the computation costs, both, with respect to computation time, as well as the cost for the required FE software licenses.

6.2 Outlook

The developed models only cover a small sample of timber floor constructions provided by selected manufacturers. Even though the models are designed entirely parametric, only a few parameters are investigated in detail. Another limitation is induced by various idealizations, which are made to reduce the overall computational effort. Thus, the presented findings can only be considered as a pilot study. Further work is recommended, that can in parts built-up on the models developed, by complementing them, or developing additional models for alternate floor constructions.

In particular, the floating floor model is not varied within the presented studies. The same holds for the resilient suspension hangers considered. The model's material parameters are calibrated, but remained fixed. No statistical considerations are applied. Thus, succeeding studies on the existing models can comply:

- A variation of the floating floor model's parameters

- Implementation of alternate spring and damping coefficients for resilient hangers

- A probabilistic study on the statistical scatter of the material properties

The structural models presented are developed for one-way, single-span configurations only. Two idealization are considered to have a major impact. The receiving room is not part of the model and the cavity between main floor and suspended ceiling is modeled without sound absorbing fillings. Also, the floating floor model only consists of a screed on top of an impact sound insulation layer. For future investigation, the models need to be supplemented by the following:

- Alternate support conditions, including two-way and multi-span configurations

- Implementation of sound absorbing fillings for the suspended ceiling model

- Adding a model for the receiving room

- Supplementation of the floating floor model by a filling finish

Up to now, the database for the intended GUI consists only of a few floor constructions. However, further research can develop additional structural model, that can easily be implemented into the described automated process of the parametric studies. Thus, the database can be complement to increase the benefit for the practical engineer, when designing acoustically optimized timber floor constructions.

Appendix

List of Figures (Appendix)

A Description of the Implemented Finite Elements

A.1 COMBIN14

This element is depicted in Figure A.1 and described as follows:
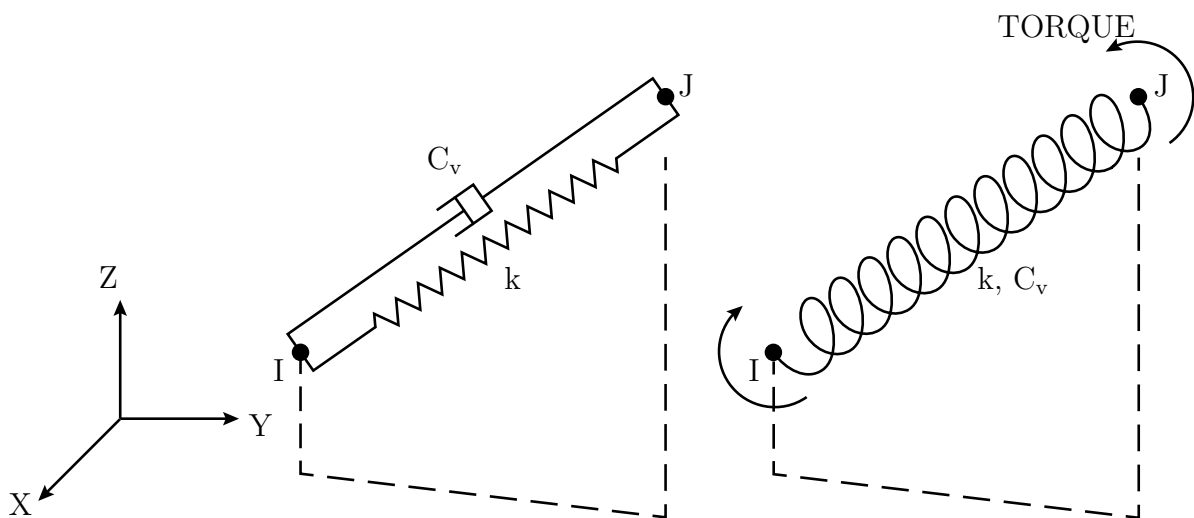
Figure A.1: COMBIN14-element [ANSYS, Inc. 2013]

COMBIN14 has longitudinal or torsional capability in 1-D, 2-D, or 3-D applications. The longitudinal spring-damper option is a uniaxial tension-compression element with up to three degrees of freedom at each node: translations in the nodal x, y, and z directions. No bending or torsion is considered. The torsional spring-damper option is a purely rotational element with three degrees of freedom at each node: rotations about the nodal x, y, and z axes. No bending or axial loads are considered.

The spring-damper element has no mass. Masses can be added by using the appropriate mass element (see MASS21). The spring or the damping capability may be removed from the element.[...]

The element is defined by two nodes, a spring constant (k) and damping coefficients $(c_v)_1$ and $(c_v)_2$. The damping capability is not used for static or undamped modal analyses. The longitudinal spring constant should have units of Force / Length, the damping coefficient units are Force * Time / Length. The torsional spring constant and damping coefficient have units of Force * Length / Radian and Force * Length * Time / Radian, respectively. For a 2-D axisymmetric analysis, these values should be on a full 360° basis. [ANSYS, Inc. 2013]

A.2 MASS21

This element is depicted in Figure A.2 and described as follows:
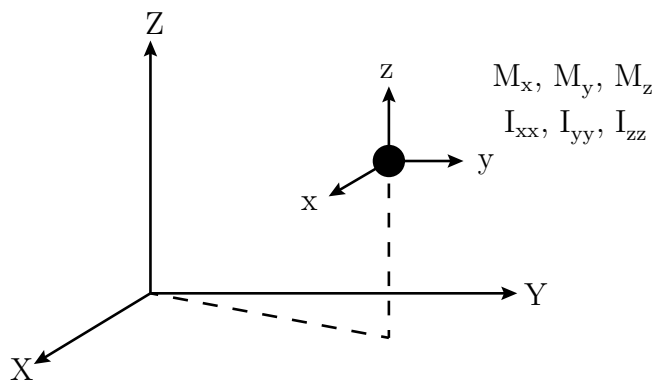
Figure A.2: MASS21-Element [ANSYS, Inc. 2013]

MASS21 is a point element having up to six degrees of freedom: translations in the nodal x, y, and z directions and rotations about the nodal x, y, and z axes. A different mass and rotary inertia may be assigned to each coordinate direction. [...]

The mass element is defined by a single node, concentrated mass components (Force*Time²/Length) in the element coordinate directions, and rotary inertias (Force*Length*Time²) about the element coordinate axes. The element coordinate system may be initially parallel to the global Cartesian coordinate system or to the nodal coordinate system [...]. The element coordinate system rotates with the nodal coordinate rotations during a large deflection analysis. Options are available to exclude the rotary inertia effects and

to reduce the element to a 2-D capability [...]. If the element requires only one mass input, it is assumed to act in all appropriate coordinate directions [ANSYS, Inc. 2013]

A.3 FLUID30

This element is depicted in Figure A.3 and described as follows:
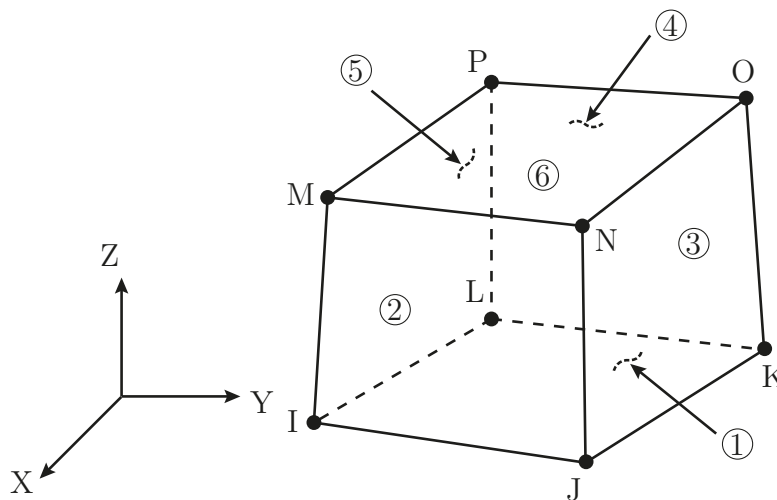
Figure A.3: FLUID30-element [ANSYS, Inc. 2013]

Use FLUID30 [...] to model the fluid medium and the interface in fluid/structure interaction problems. Typical applications include sound wave propagation and submerged structure dynamics. The governing equation for acoustics, namely the 3-D wave equation, has been discretized taking into account the coupling of acoustic pressure and structural motion at the interface. The element node has four degrees of freedom per node: translations in the nodal x, y and z directions, and pressure. The translations are applicable only at nodes on the interface. Acceleration effects like those in sloshing problems may be included.

The elements have the capability to include damping of sound-absorbing material at the interface as well as damping within the fluid. The elements can be used with or without other 3-D structural elements to perform symmetric, unsymmetric or damped modal [...], full harmonic [...], and full transient method analyses [...]

The elements are defined by eight nodes [...], a reference pressure, and the isotropic material properties. The reference pressure [...] is used to calculate the element sound pressure level

(defaults to 20x10^{-6} N/m^2). [...] The dissipative effect due to fluid viscosity can be included [...]. [ANSYS, Inc. 2013]

A.4 TARGE170

This element is depicted in Figure A.4 and described as follows:
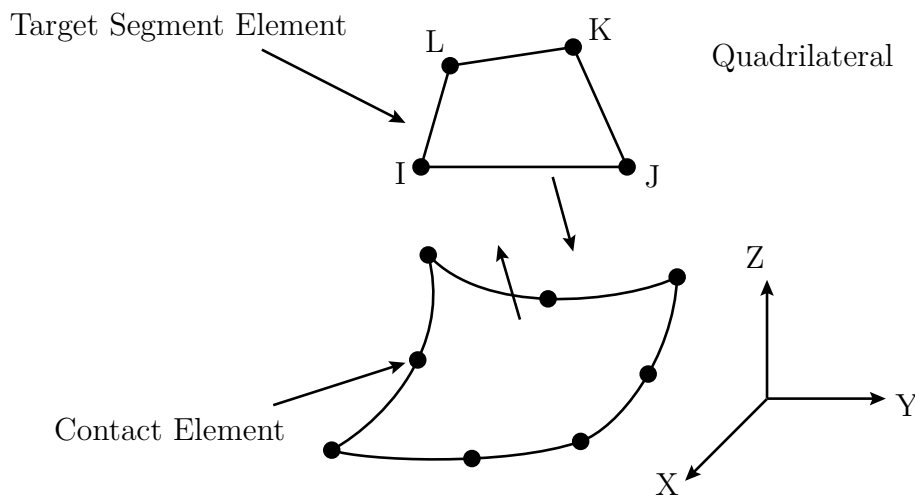
Figure A.4: TARGE170-element [ANSYS, Inc. 2013]

TARGE170 is used to represent various 3-D 'target' surfaces for the associated contact elements ([...] CONTA174 [...]). The contact elements themselves overlay the solid, shell, or line elements describing the boundary of a deformable body and are potentially in contact with the target surface, defined by TARGE170. This target surface is discretized by a set of target segment elements (TARGE170) and is paired with its associated contact surface [...]. You can impose any translational or rotational displacement, temperature, voltage, and magnetic potential on the target segment element. You can also impose forces and moments on target elements. [ANSYS, Inc. 2013]

A.5 CONTA174

This element is depicted in Figure A.5 and described as follows:
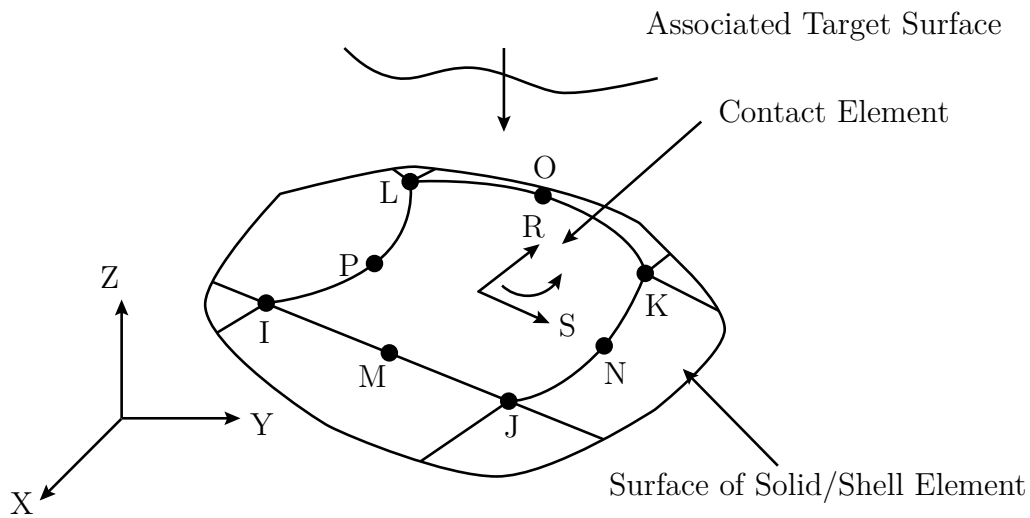
Figure A.5: CONTA174-element [ANSYS, Inc. 2013]

CONTA174 is used to represent contact and sliding between 3-D 'target' surfaces (TARGE170) and a deformable surface, defined by this element. The element is applicable to 3-D structural and coupled field contact analyses.

The element is located on the surfaces of 3-D solid or shell elements with midside nodes ([...] SOLID186 [...]).

The element has the same geometric characteristics as the solid or shell element face with which it is connected [...]. Contact occurs when the element surface penetrates one of the target segment elements (TARGE170) on a specified target surface. [ANSYS, Inc. 2013]

A.6 SHELL181

This element is depicted in Figure A.6 and described as follows:

SHELL181 is suitable for analyzing thin to moderately-thick shell structures. It is a four-node element with six degrees of freedom at each node: translations in the x, y, and z directions, and rotations about the x, y, and z-axes. [...]

SHELL181 is well-suited for linear, large rotation, and/or large strain nonlinear applications. [...] In the element domain, both full and reduced integration schemes are supported. [...] [ANSYS, Inc. 2013]
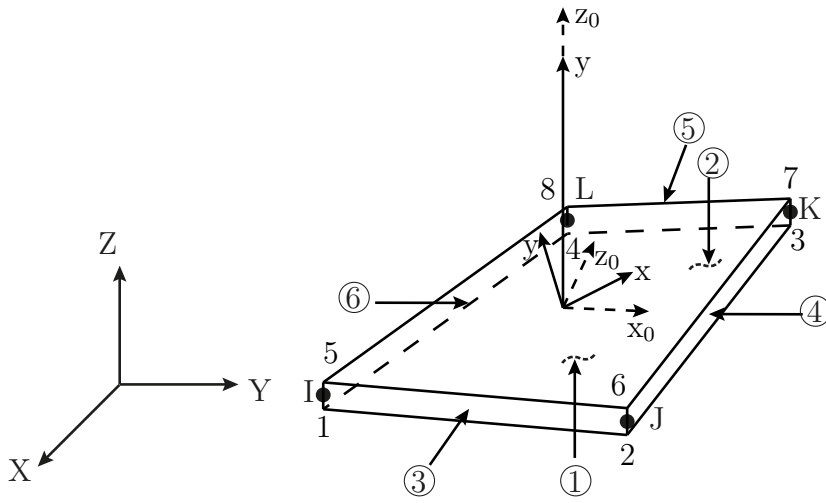
Figure A.6: SHELL181-element [ANSYS, Inc. 2013]

A.7 SOLID185

This element is depicted in Figure A.7 and described as follows:
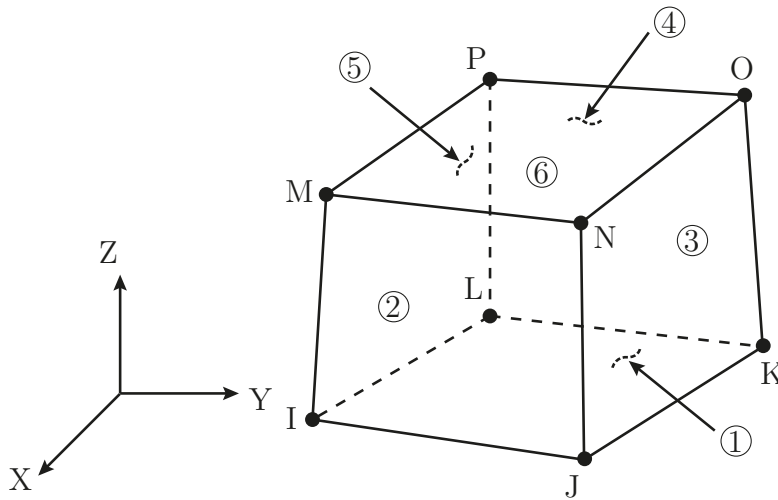
Figure A.7: SOLID185-element [ANSYS, Inc. 2013]

SOLID185 is used for 3-D modeling of solid structures. It is defined by eight nodes having three degrees of freedom at each node: translations in the nodal x, y, and z directions. The element has plasticity, hyperelasticity, stress stiffening, creep, large deflection, and large strain capabilities. It also has mixed formulation capability for simulating deformations of

nearly incompressible elastoplastic materials, and fully incompressible hyperelastic materials. [ANSYS, Inc. 2013]

Trilinear form functions are used for the displacements [Müller and Groth 2007]. Such elements are without countermeasures prone to a variety of stiffening effects (e.g. locking effects). To minimize these effects several options are available in Ansys® for the SOLID185-element. Shear locking is prevented by using the "Simplified Enhanced Strain Formulation". Other than the "Enhanced Strain Formulation" for this method only the internal DOFs are implemented [ANSYS, Inc. 2013].

A.8 SOLID186

This element is a higher-order version of SOLID185. It is depicted in Figure A.7 and described as follows:

SOLID186 is a higher order 3-D 20-node solid element that exhibits quadratic displacement behavior. The element is defined by 20 nodes having three degrees of freedom per node: translations in the nodal x, y, and z directions. [ANSYS, Inc. 2013]
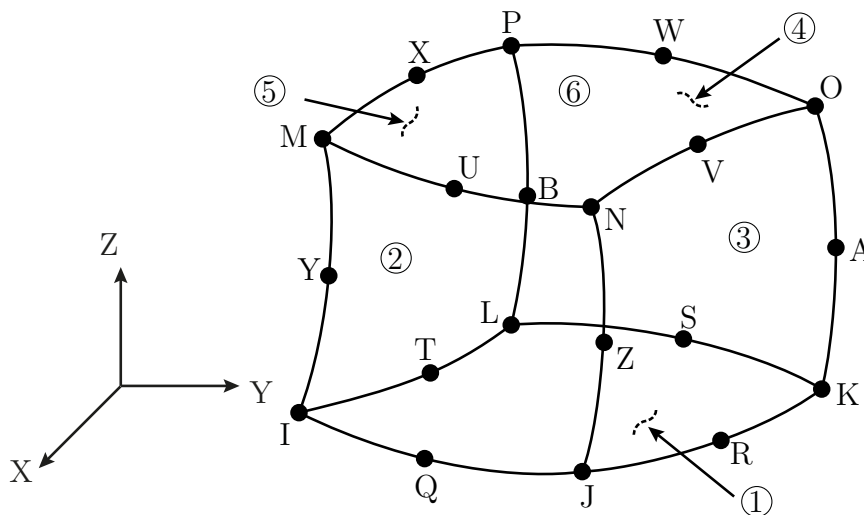
Figure A.8: SOLID186-element [ANSYS, Inc. 2013]

A.9 BEAM188

This element is depicted in Figure A.8 and described as follows:

BEAM188 is suitable for analyzing slender to moderately stubby/thick beam structures. The element is based on Timoshenko beam theory which includes shear-deformation effects. [...]

The element is a linear, quadratic, or cubic two-node beam element in 3-D. BEAM188 has six [...] degrees of freedom at each node. These include translations in the x, y, and z directions and rotations about the x, y, and z directions. [...] This element is well-suited for linear, large rotation, and/or large strain nonlinear applications.[ANSYS, Inc. 2013]
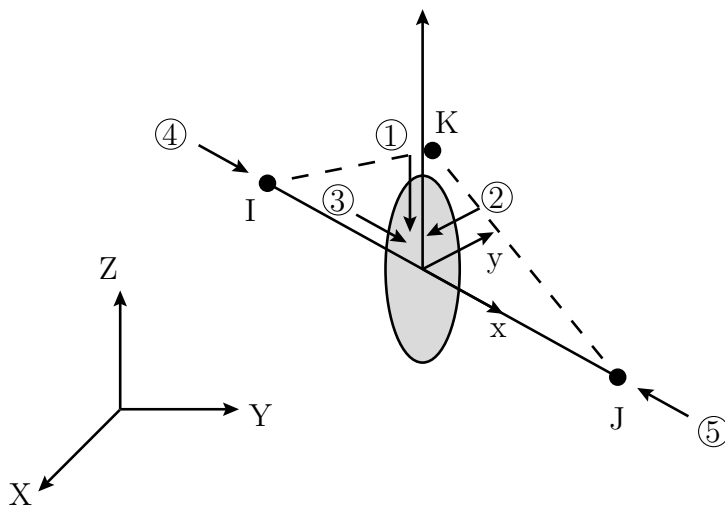
Figure A.9: BEAM188-element [ANSYS, Inc. 2013]

B Simulation Results

B.1 Eigenfrequency Nomograms
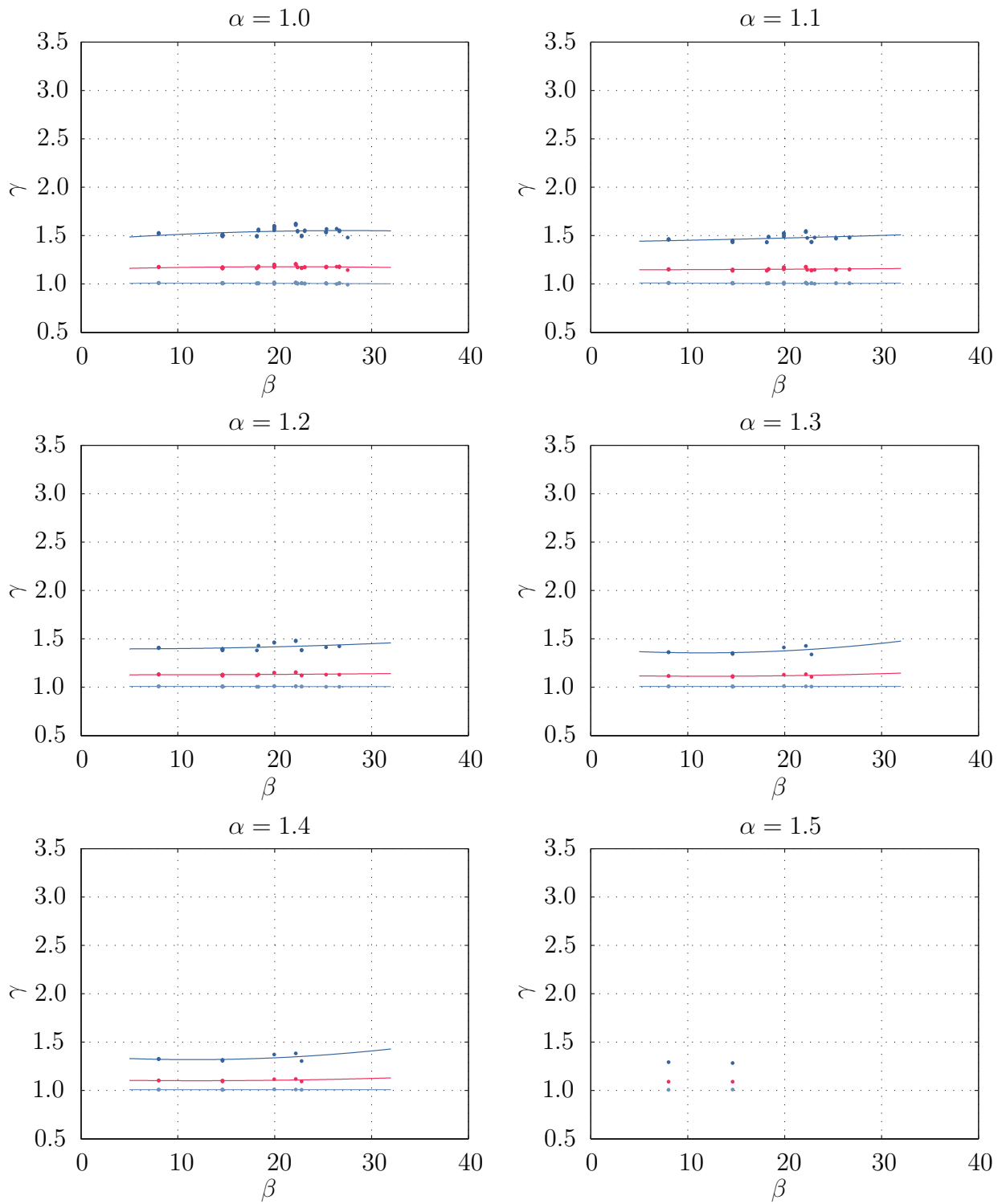
Figure B.1: CLT-R Eigenfrequency nomograms: $n_s = 2$, $1.0 \leq \alpha \leq 1.6$
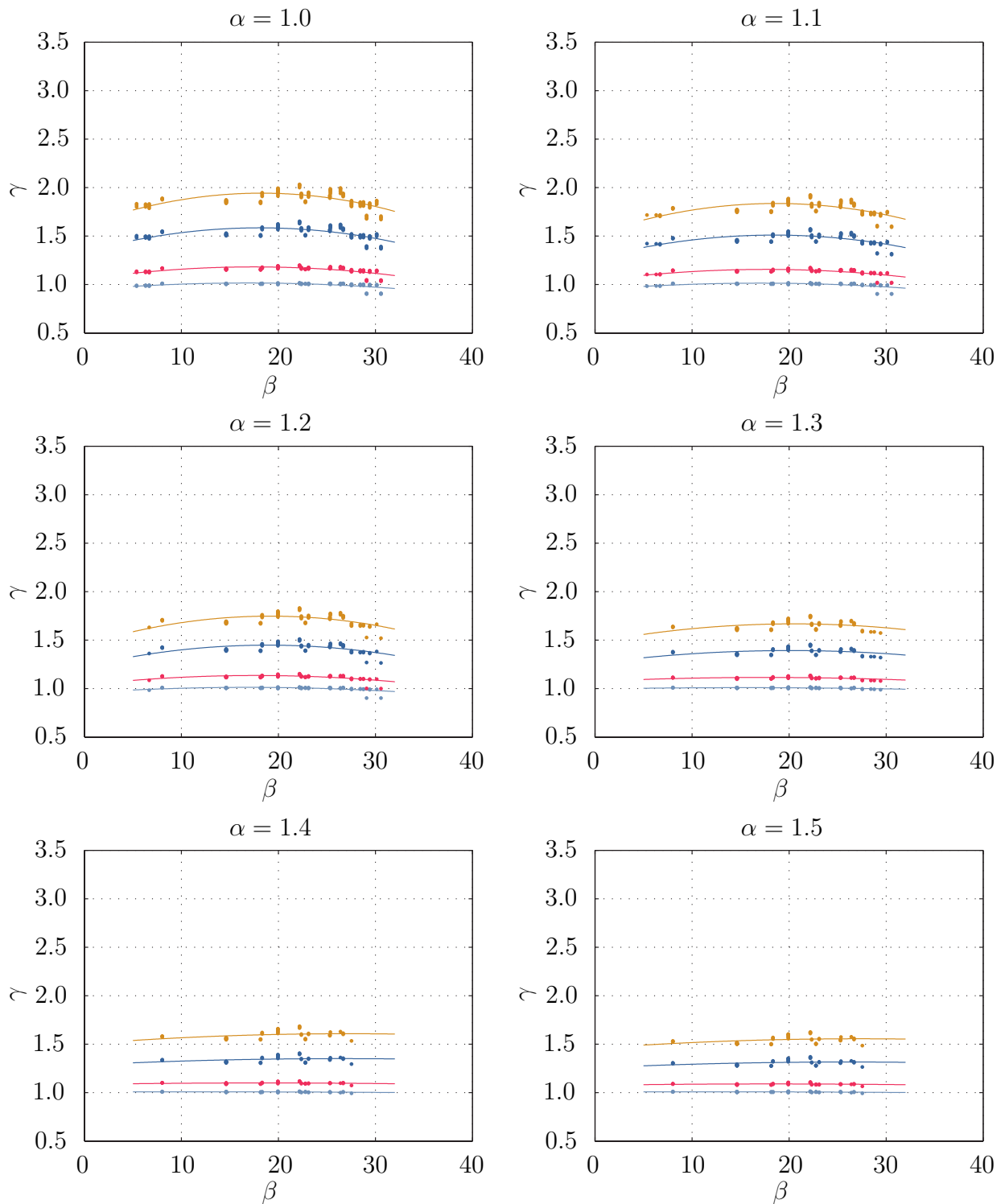
Figure B.2: CLT-R Eigenfrequency nomograms: $n_s = 3$, $1.0 \leq \alpha \leq 1.6$
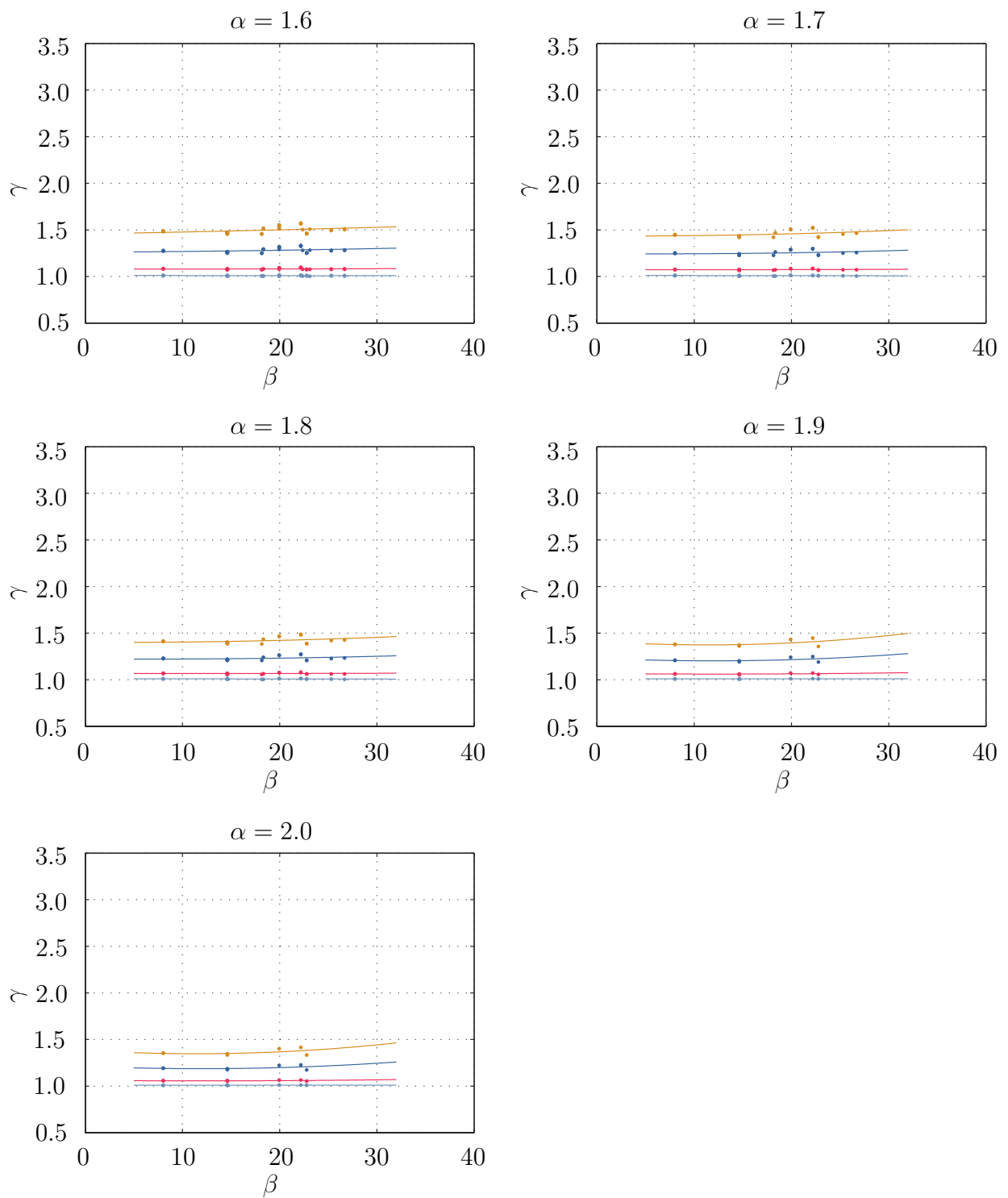
Figure B.3: CLT-R Eigenfrequency nomograms: $n_s = 3$, $1.7 \leq \alpha \leq 2.0$
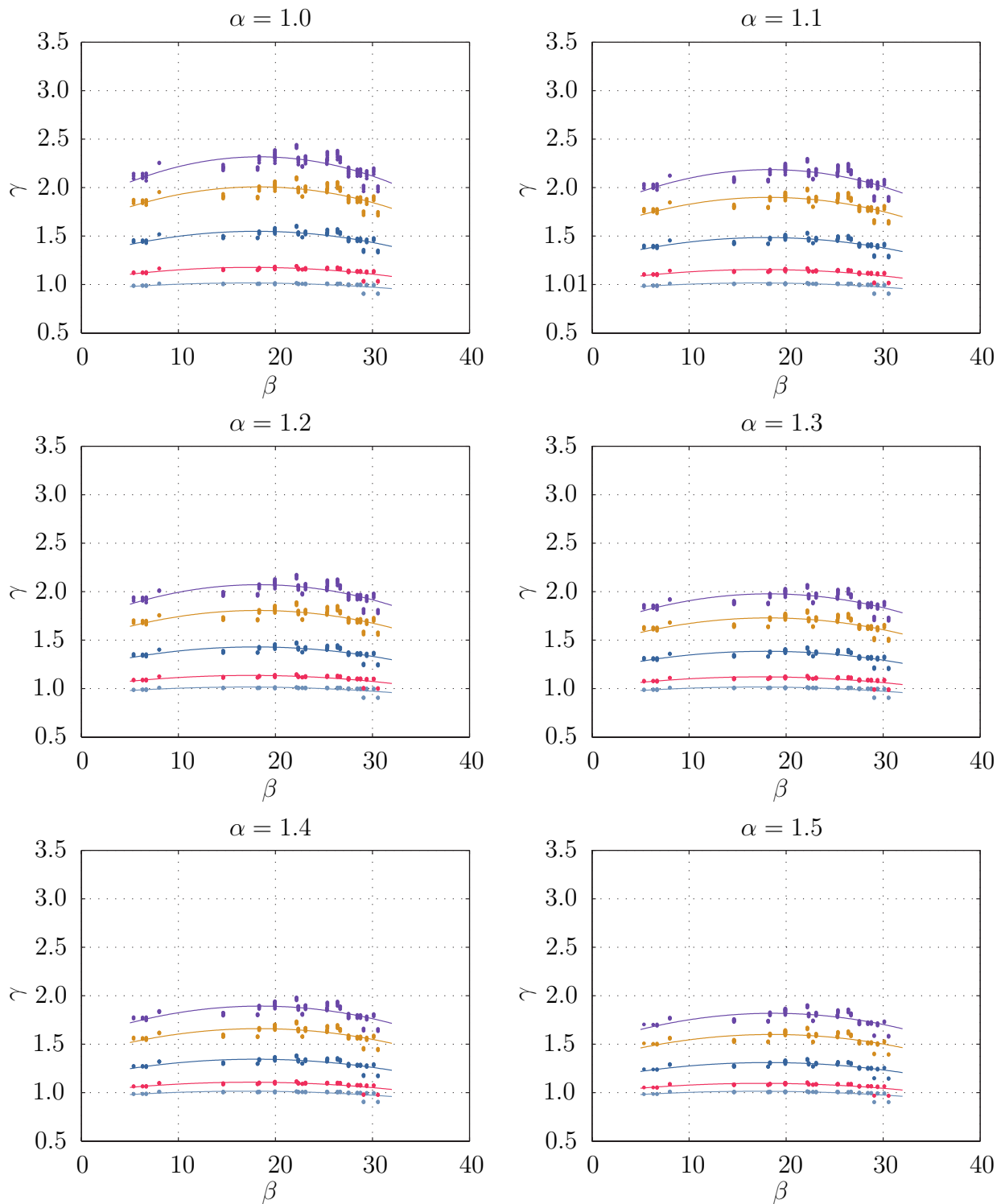
Figure B.4: CLT-R Eigenfrequency nomograms: $n_s = 4$, $1.0 \leq \alpha \leq 1.6$
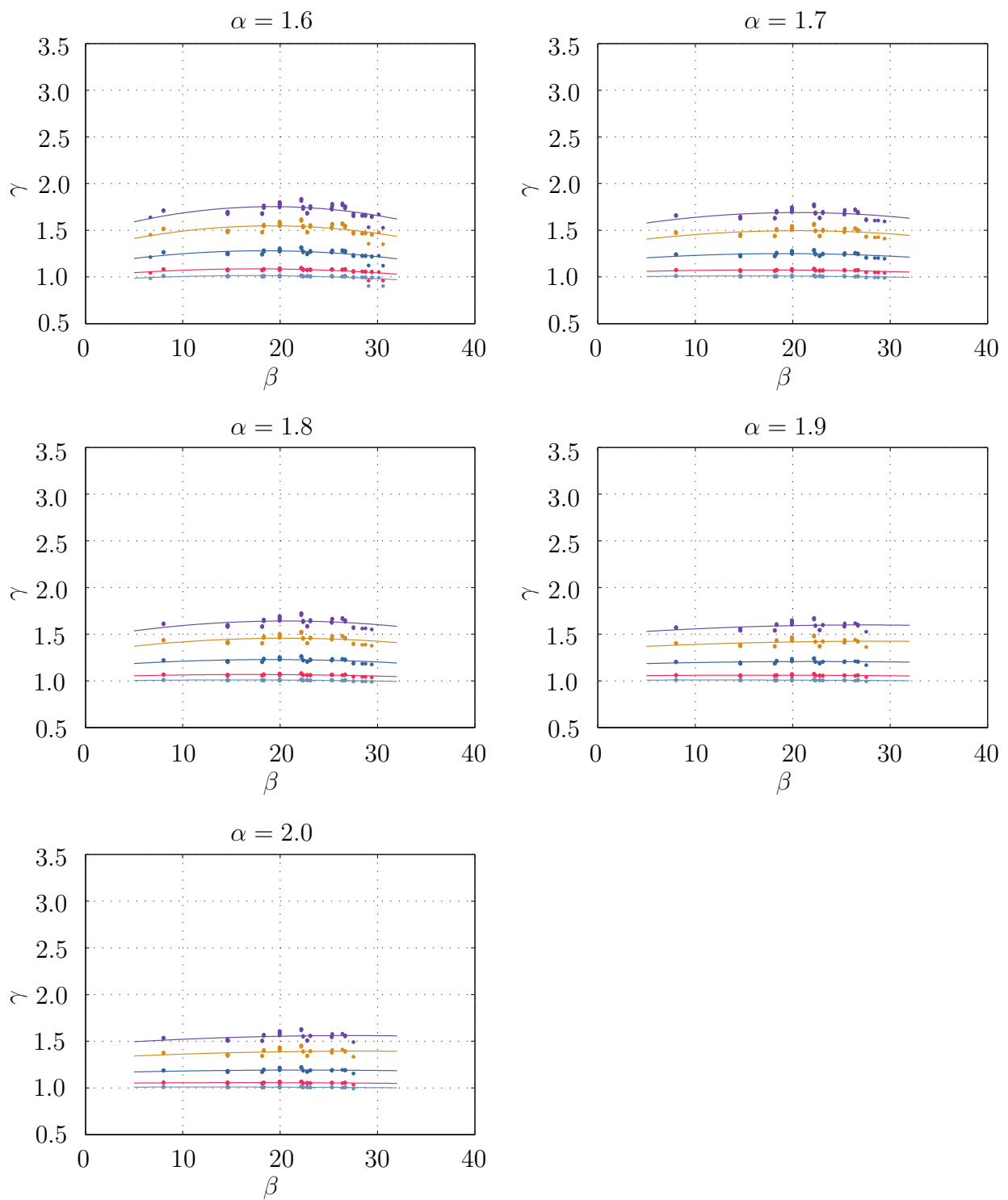
Figure B.5: CLT-R Eigenfrequency nomograms: $n_s = 4$, $1.7 \leq \alpha \leq 2.0$
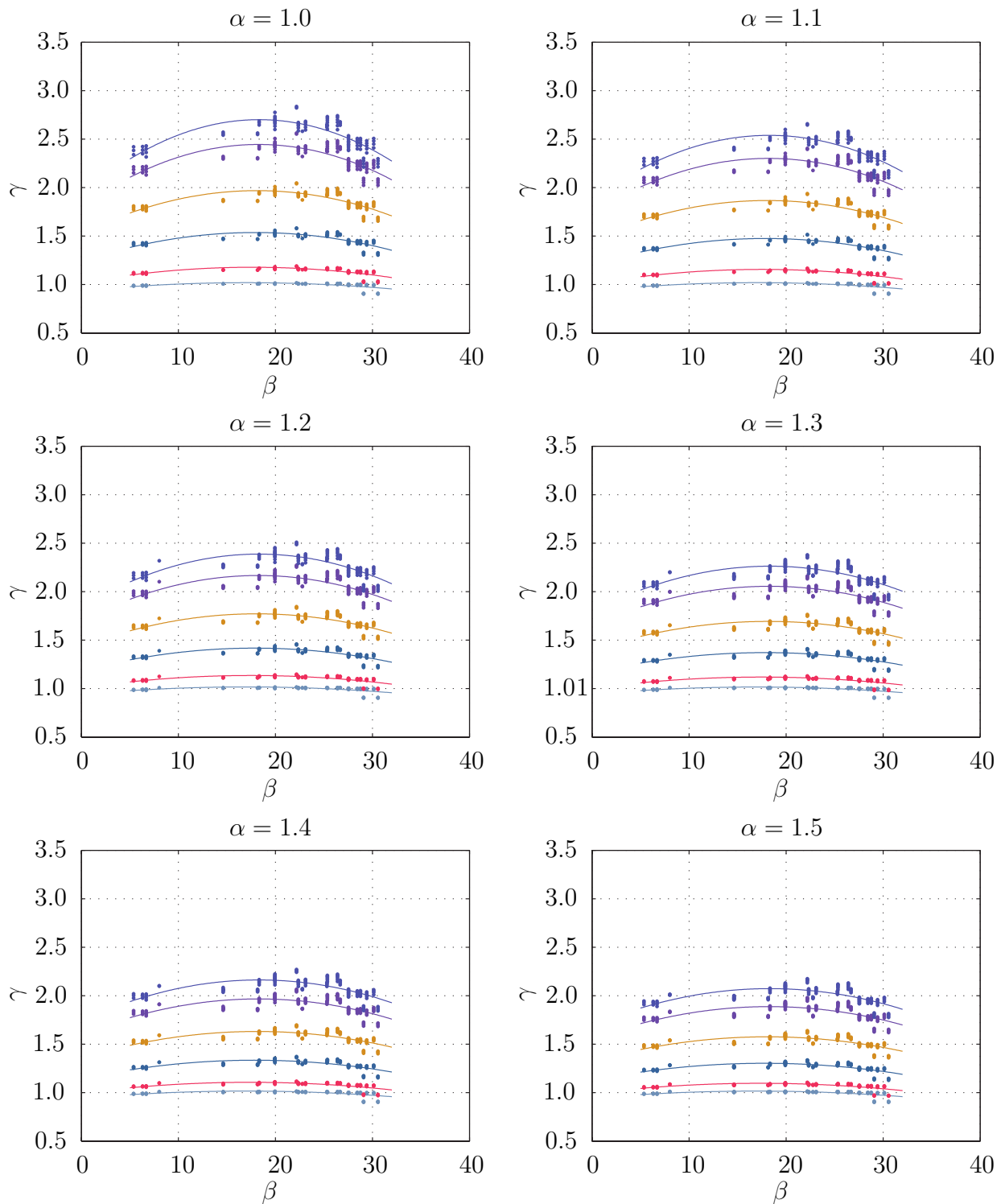
Figure B.6: CLT-R Eigenfrequency nomograms: $n_s = 5$, $1.0 \leq \alpha \leq 1.6$
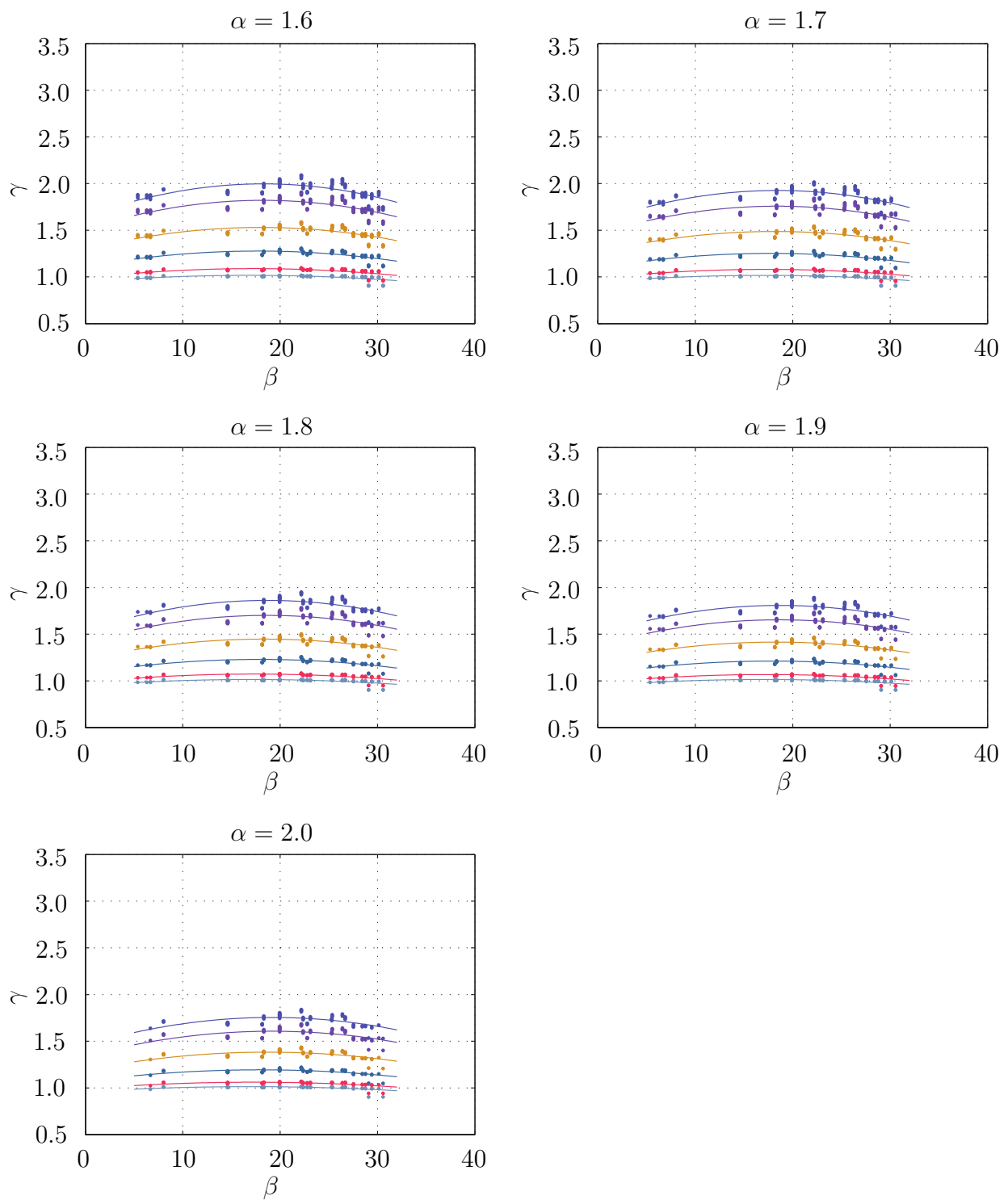
Figure B.7: CLT-R Eigenfrequency nomograms: $n_s = 5$, $1.7 \leq \alpha \leq 2.0$
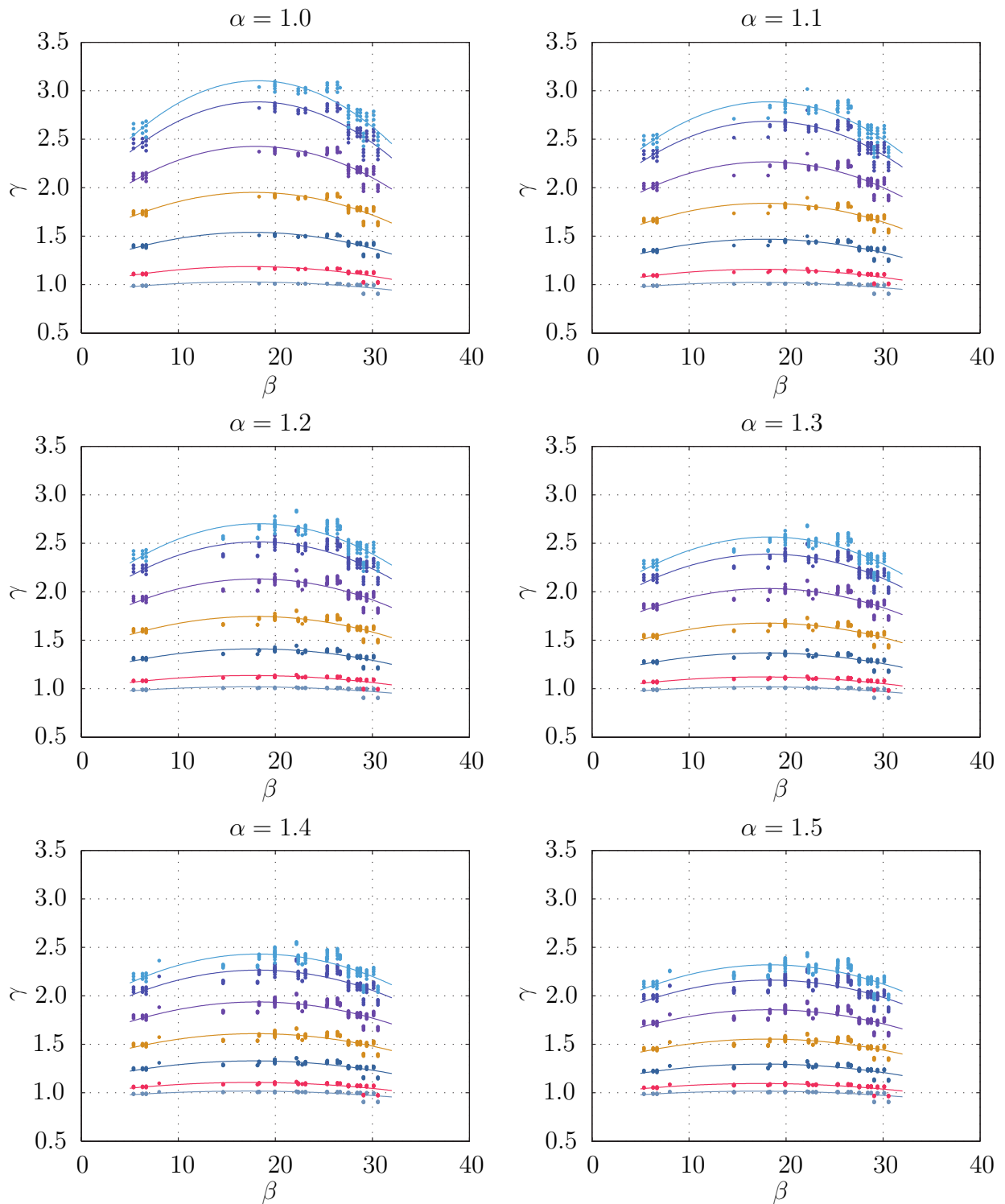
Figure B.8: CLT-R Eigenfrequency nomograms: $n_s = 6$, $1.0 \leq \alpha \leq 1.6$
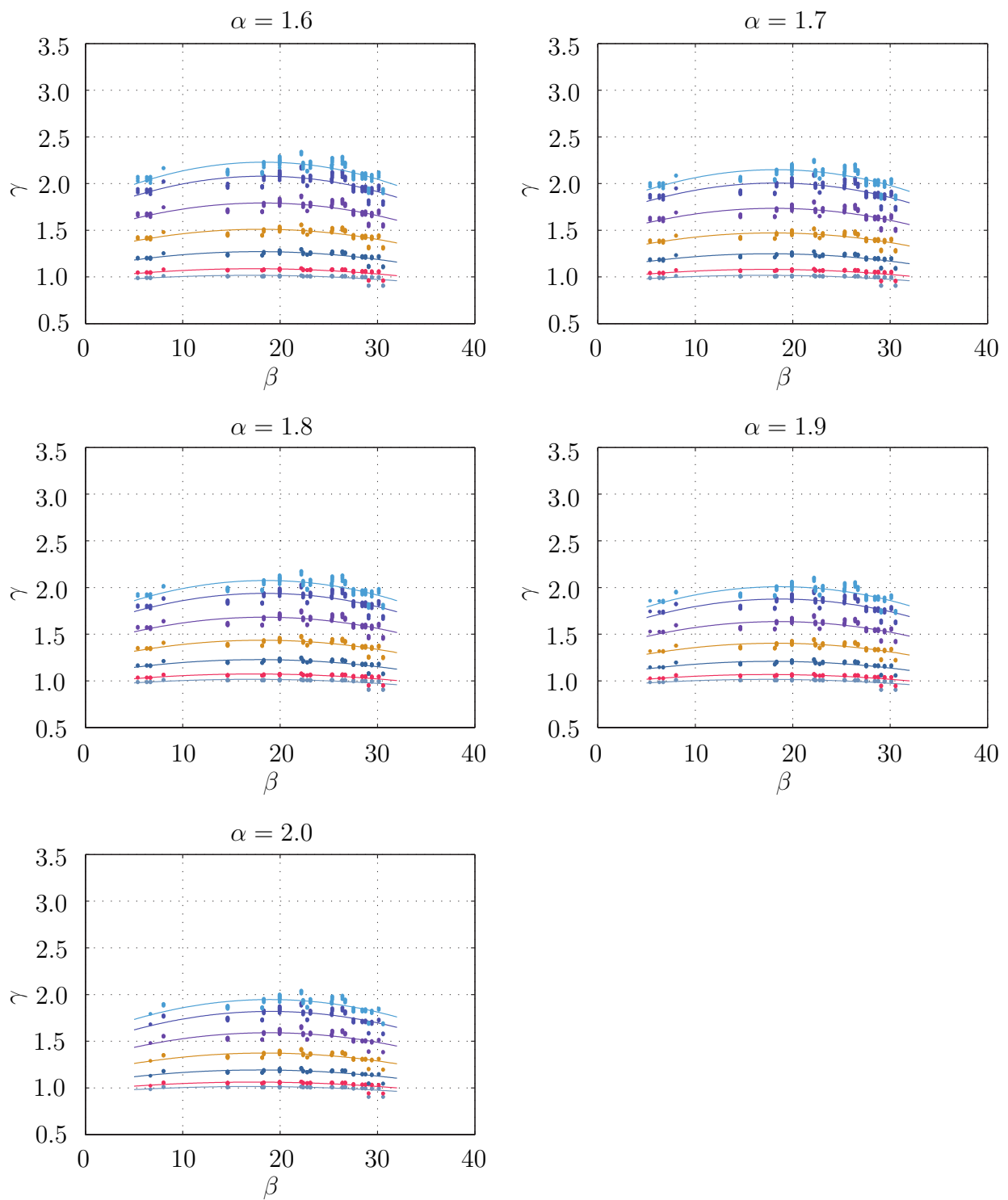
Figure B.9: CLT-R Eigenfrequency nomograms: $n_s = 6$, $1.7 \leq \alpha \leq 2.0$
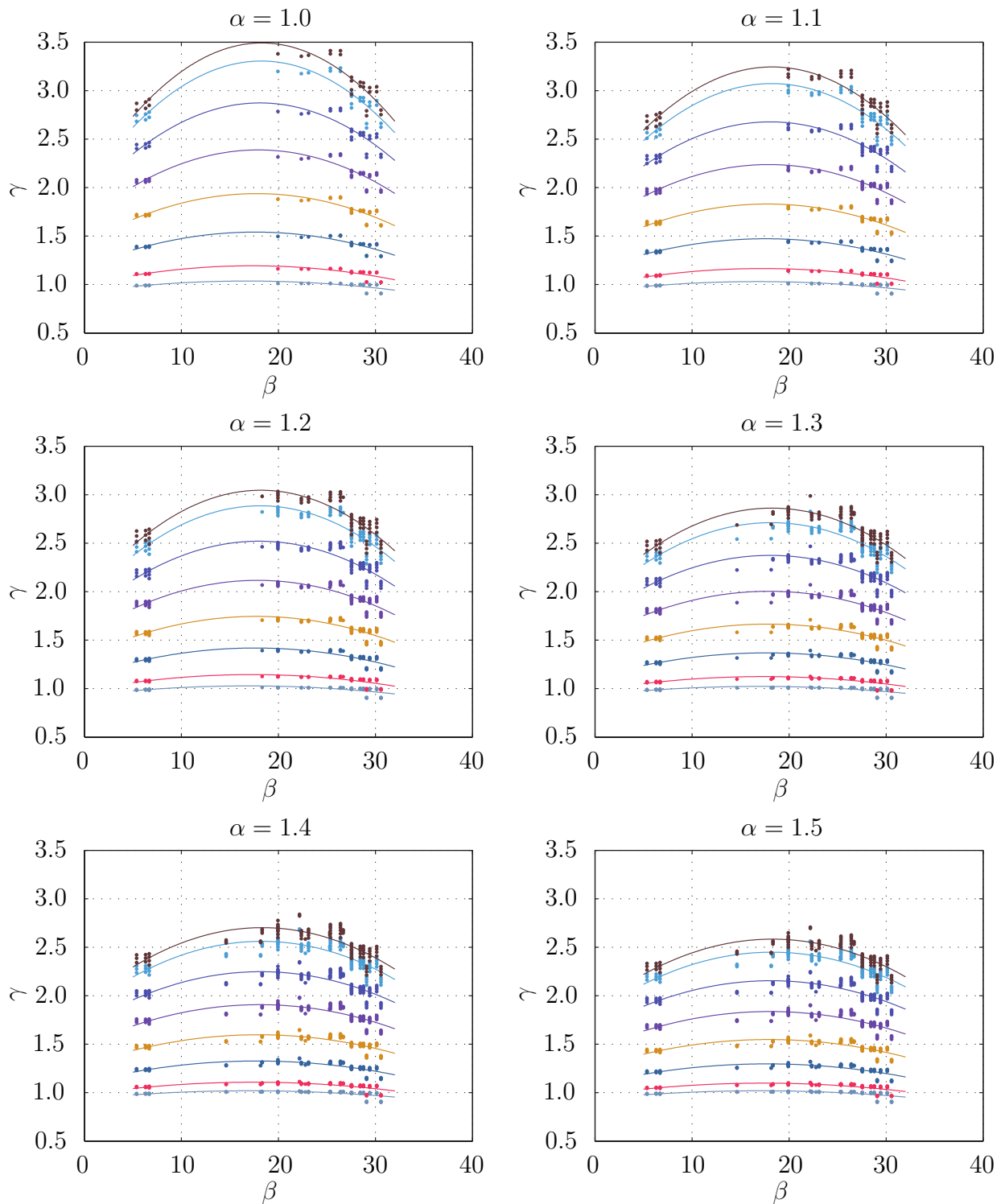
Figure B.10: CLT-R Eigenfrequency nomograms: $n_s = 7$, $1.0 \leq \alpha \leq 1.6$
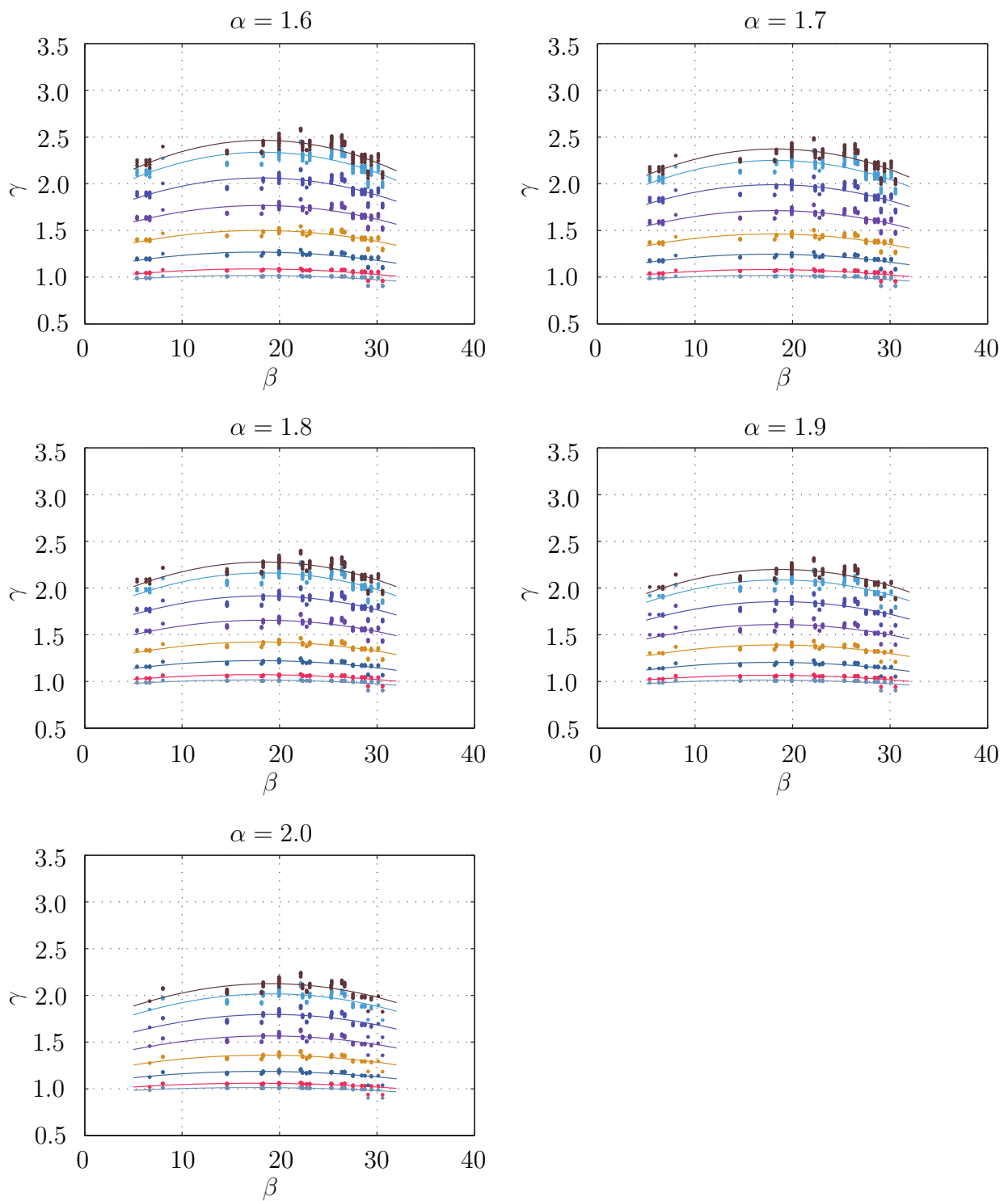
Figure B.11: CLT-R Eigenfrequency nomograms: $n_s = 7$, $1.7 \leq \alpha \leq 2.0$

B.2 Radiated Sound Power

B.2.1 Nomograms
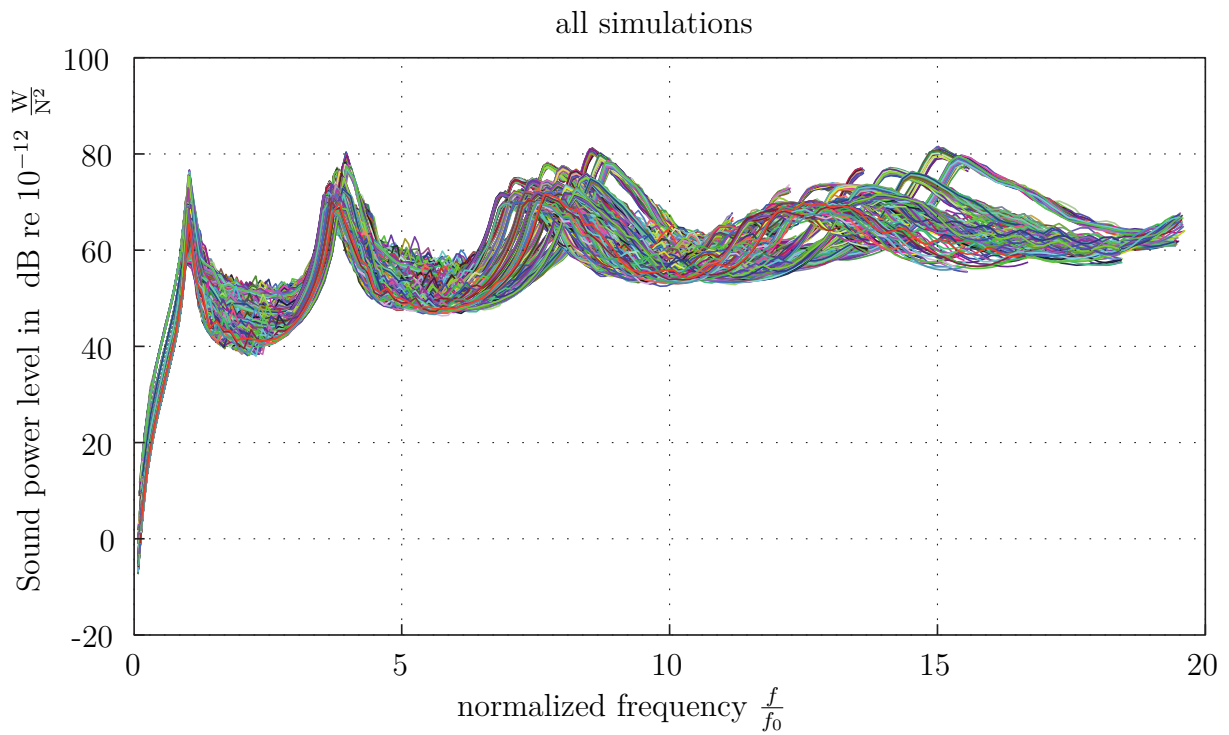
Figure B.12: CLT-R Sound power nomogram: all simulations
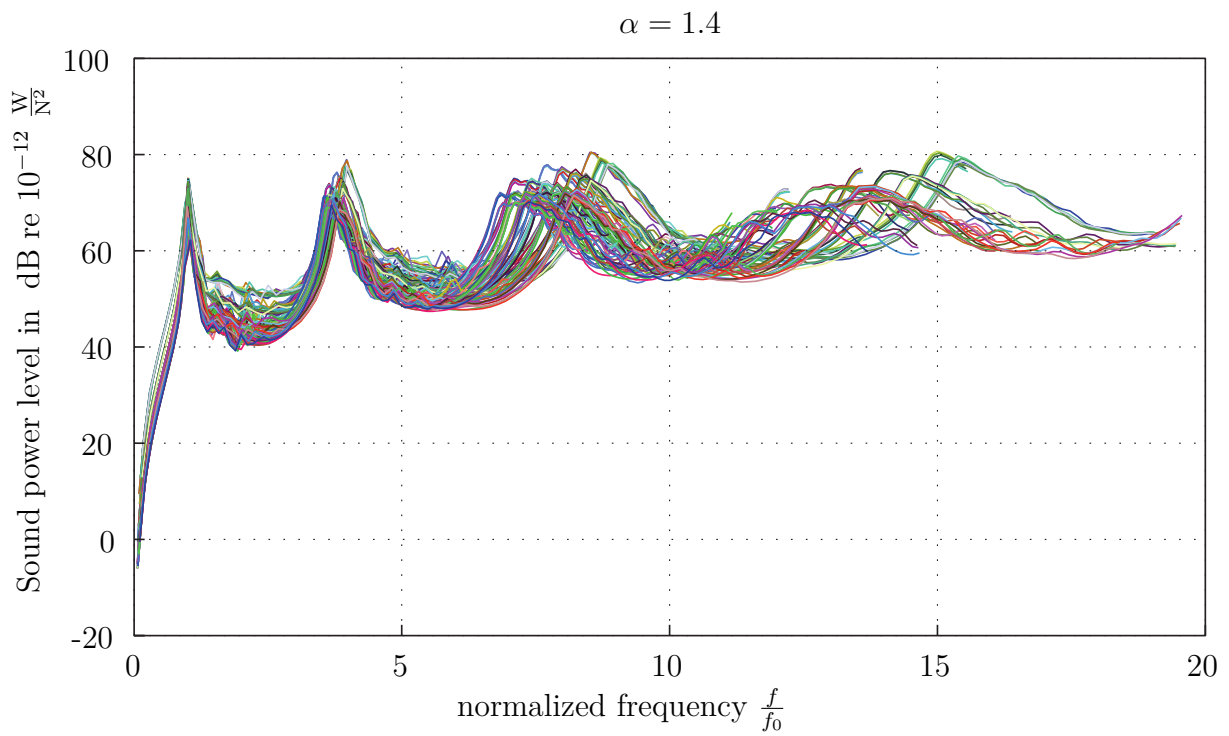
Figure B.13: CLT-R Sound power nomogram: $\alpha = 1.4$
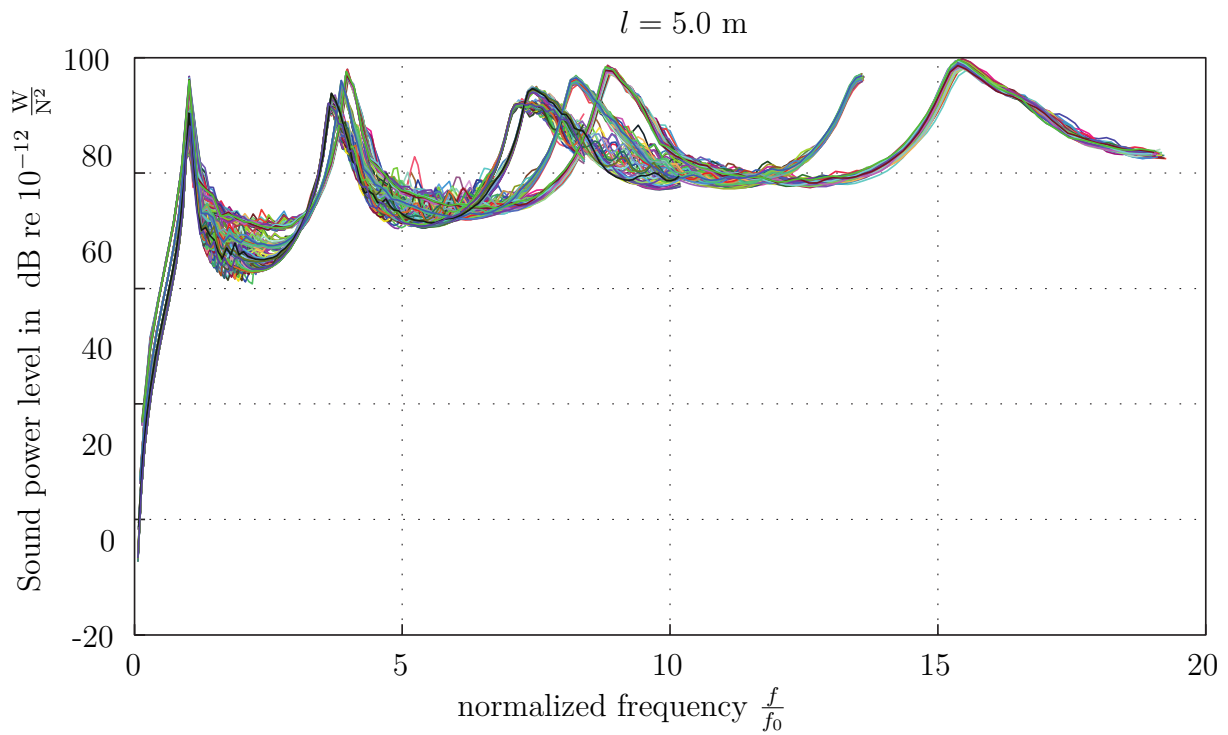
$l = 5.0$ m

Figure B.14: CLT-R Sound power nomogram: $l = 5.0$ m

$\beta = 26.4$ (type 186)
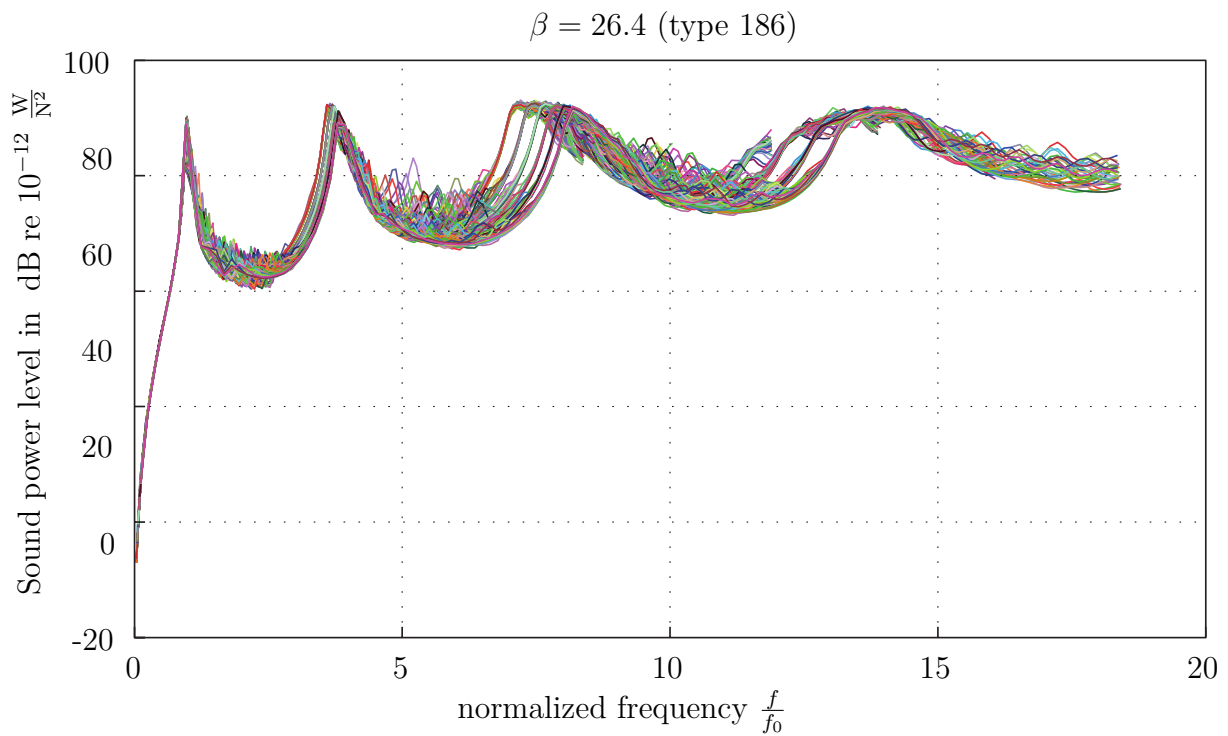
Figure B.15: CLT-R Sound power nomogram: $\beta = 26.4$ (Floor type 186)
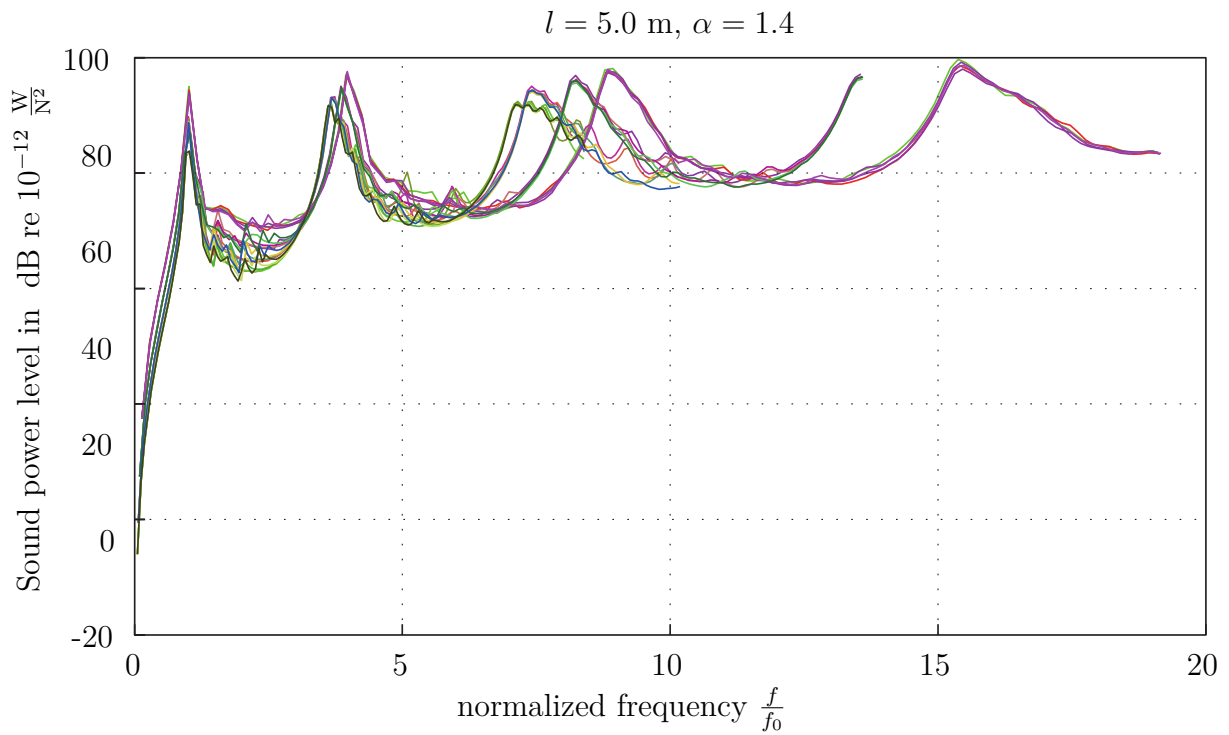
Figure B.16: CLT-R Sound power nomogram: $l = 5.0$ m; $\alpha = 1.4$
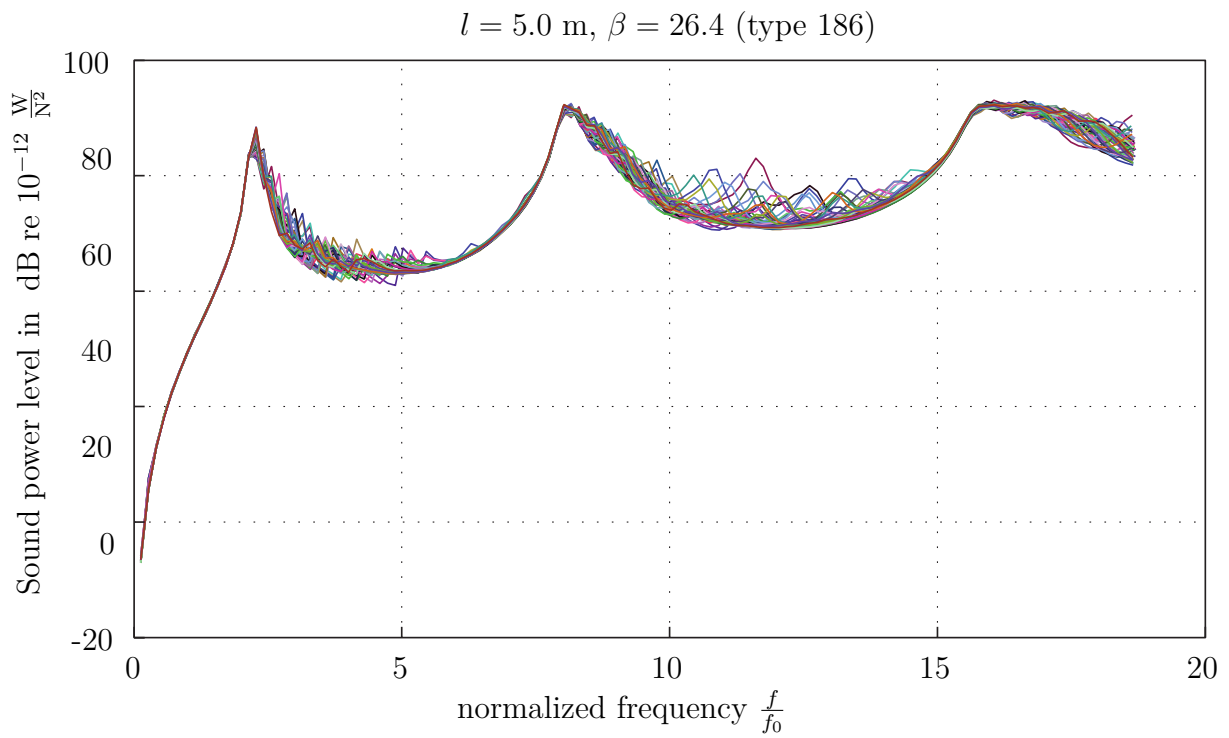
Figure B.17: CLT-R Sound power nomogram: $l = 5.0$ m; $\beta = 26.4$ (Floor type 186)
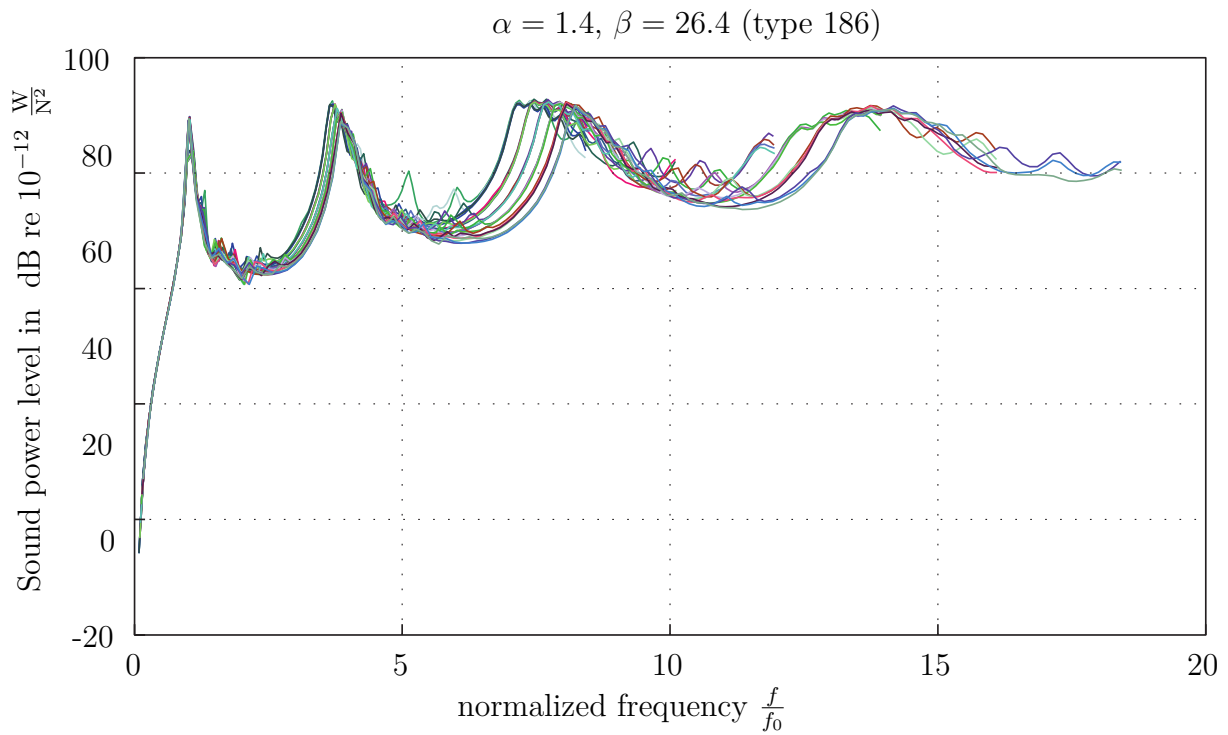
Figure B.18: CLT-R Sound power nomogram: $\alpha = 1.4$; $\beta = 26.4$ (Floor type 186)
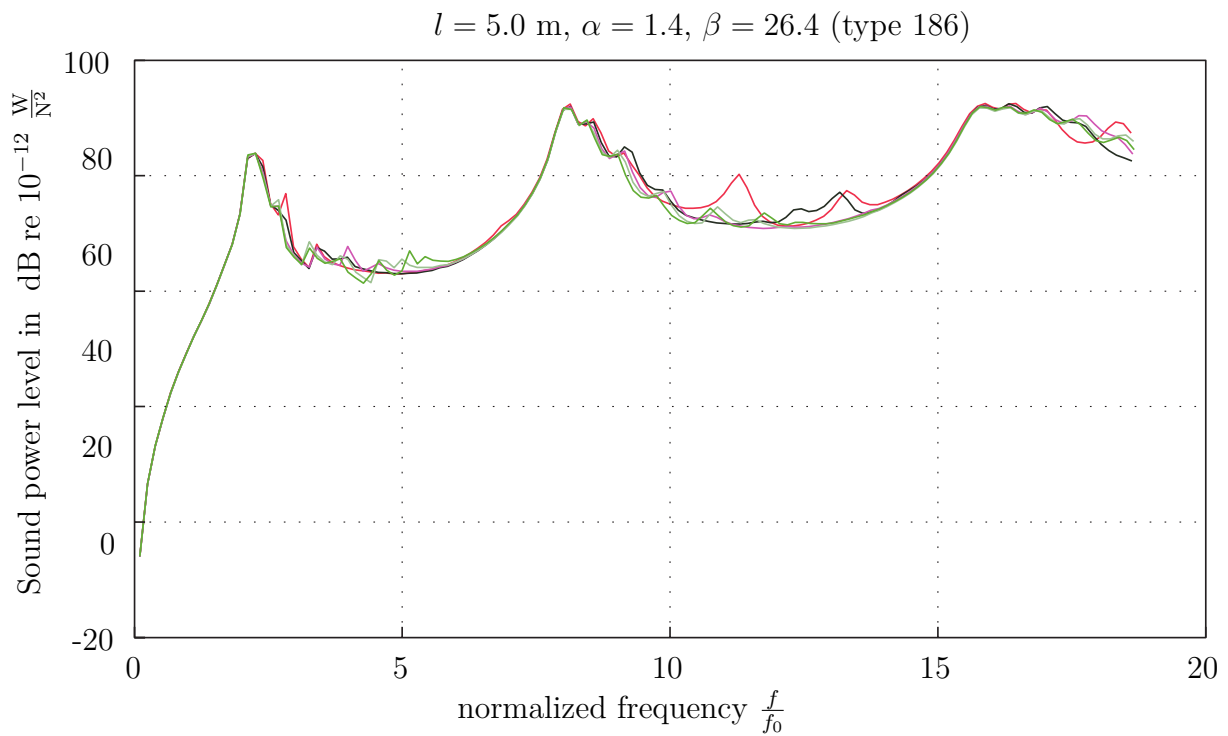
Figure B.19: CLT-R Sound power nomogram:: $l = 5.0$ m; $\alpha = 1.4$; $\beta = 26.4$ (Floor type 186)

B.2.2 Effect of different lengths of the suspension hangers
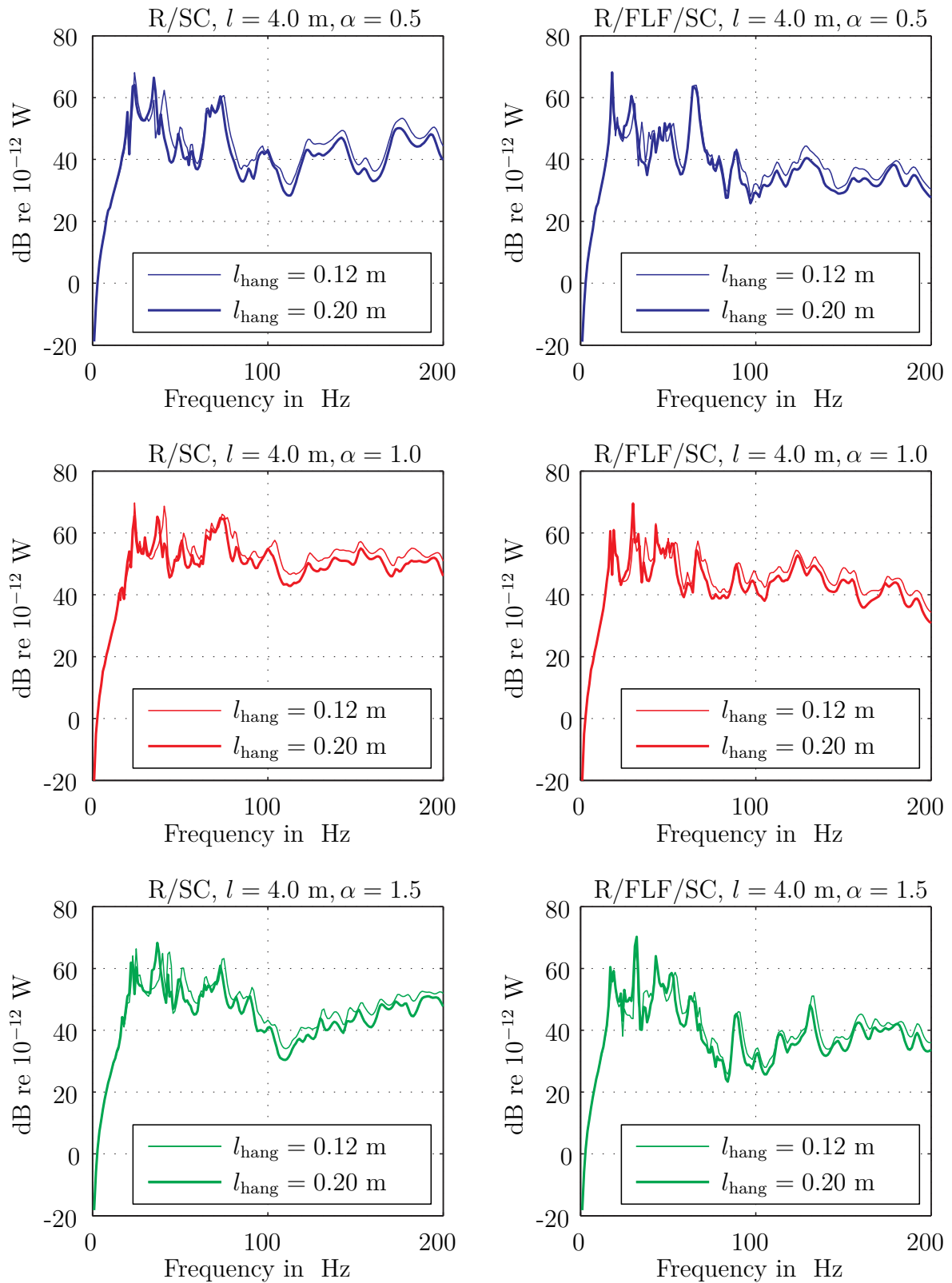
Figure B.20: Sound power level, CLT, Effect of different lengths of the suspension hangers: $l = 4.0$ m, $a_x = 1.0$ m , $\mu_{\mathrm{wall}} = 3\%$
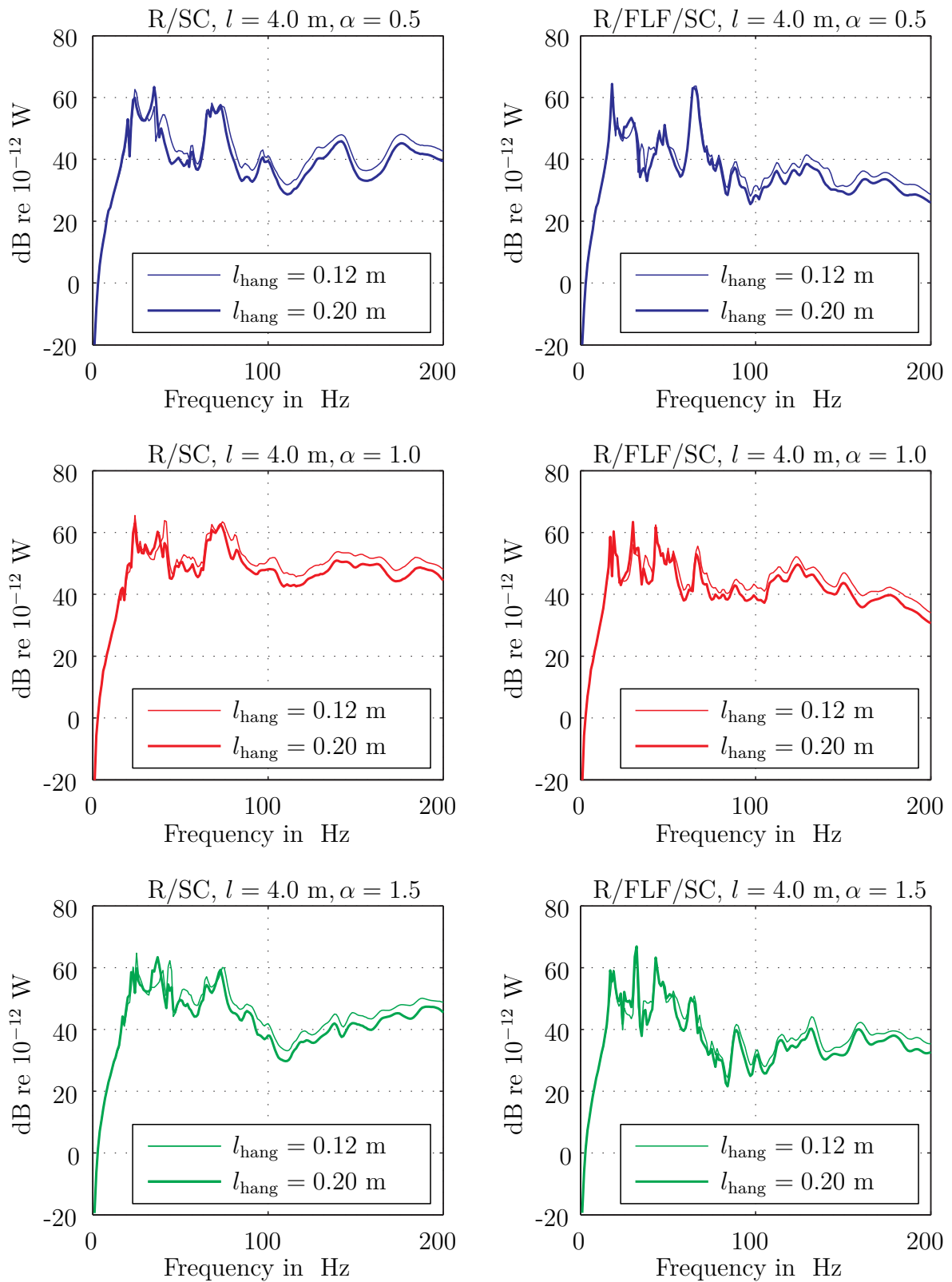
Figure B.21: Sound power level, CLT, Effect of different lengths of the suspension hangers: $l = 4.0$ m, $a_x = 1.0$ m , $\mu_{\text{wall}} = 10\%$
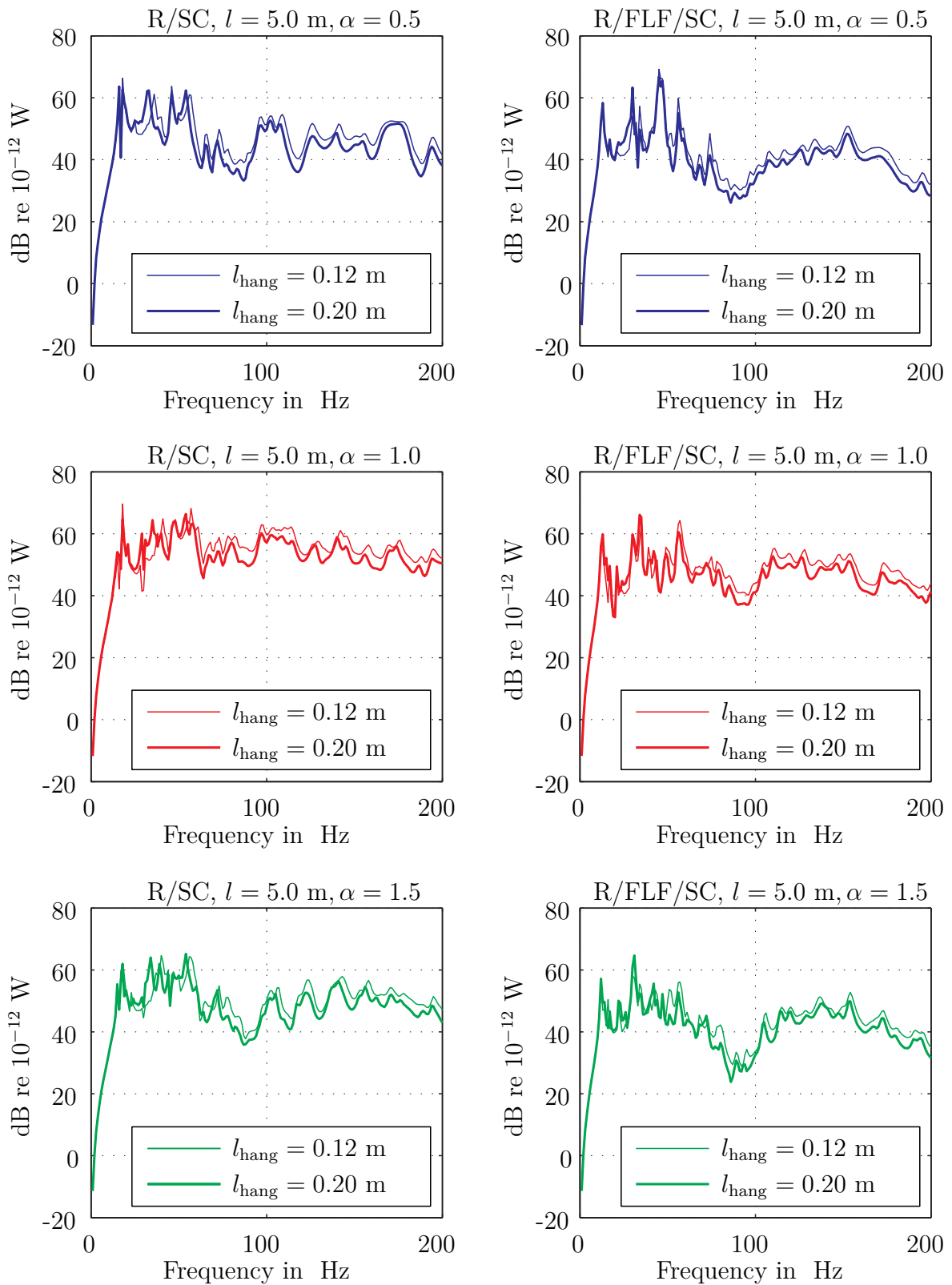
Figure B.22: Sound power level, CLT, Effect of different lengths of the suspension hangers: $l = 5.0$ m, $a_x = 1.0$ m , $\mu_{\text{wall}} = 3\%$
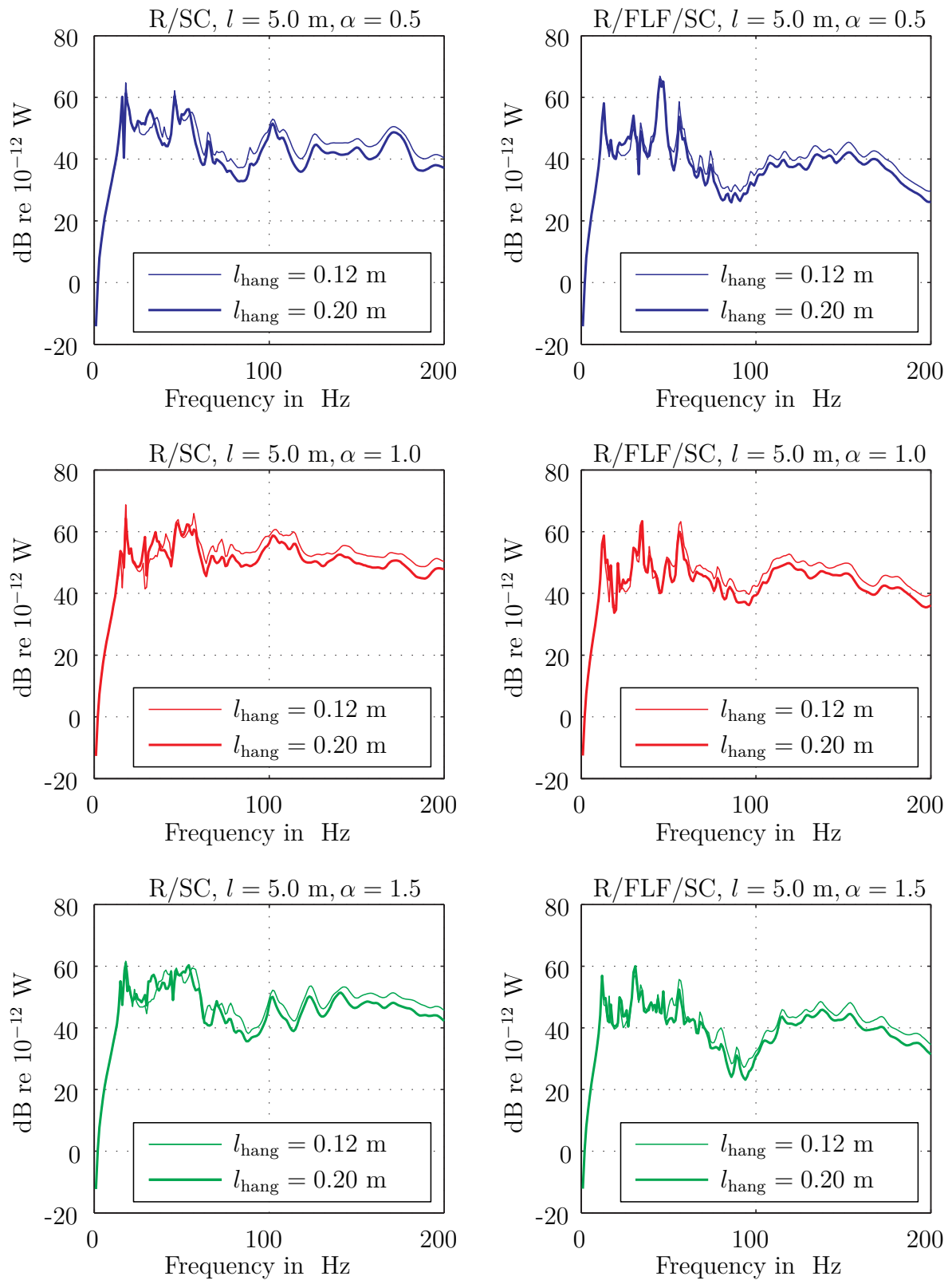
Figure B.23: Sound power level, CLT, Effect of different lengths of the suspension hangers: $l = 5.0$ m, $a_x = 1.0$ m , $\mu_{\text{wall}} = 10\%$

B.2.3 Variation of the suspension grid (with and without suspension hangers)
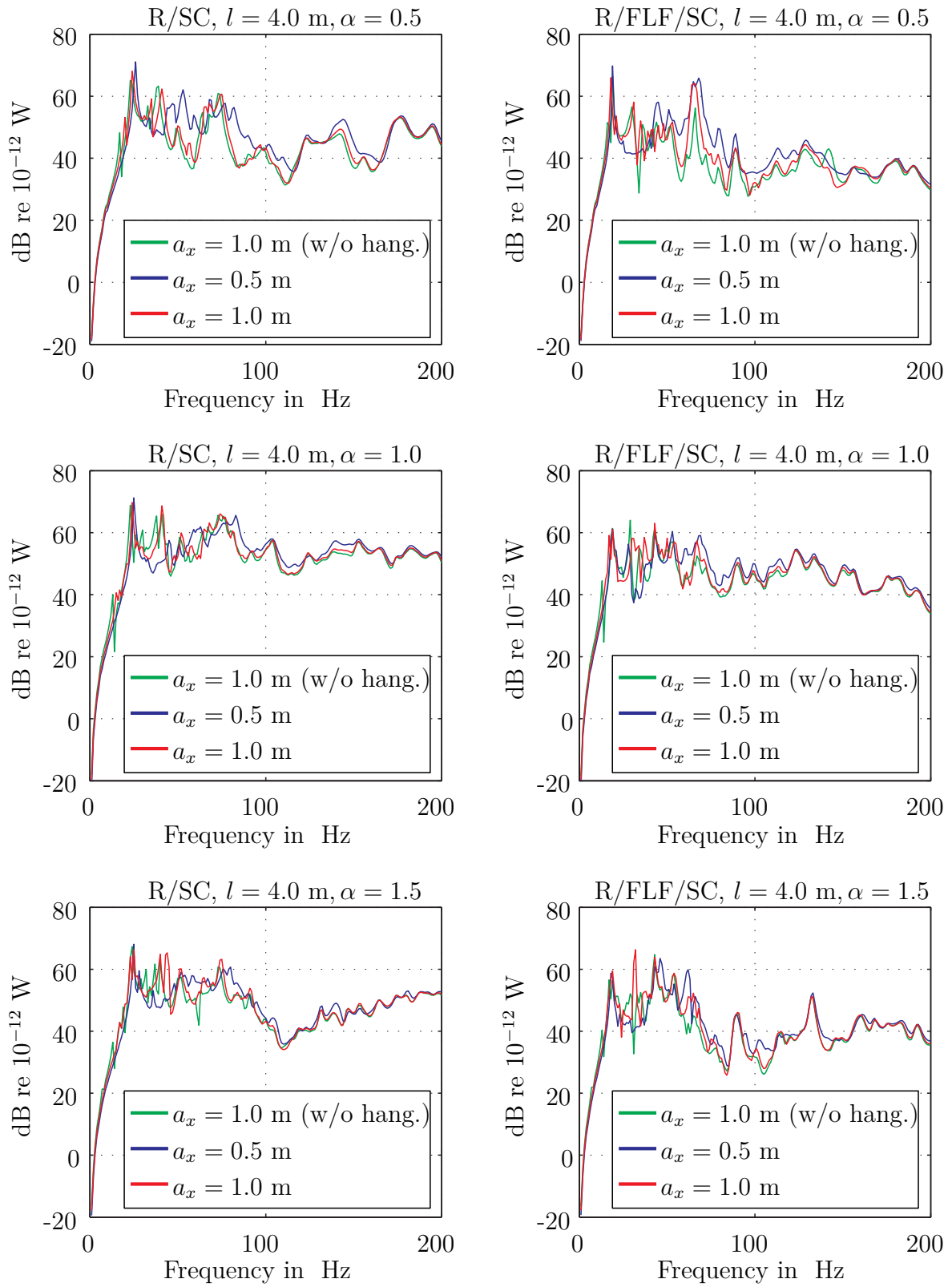
Figure B.24: Sound power level, CLT, Variation of the suspension grid: $l = 4.0$ m , $l_\text{hang} = 0.12$ m , $\mu_\text{wall} = 3\%$
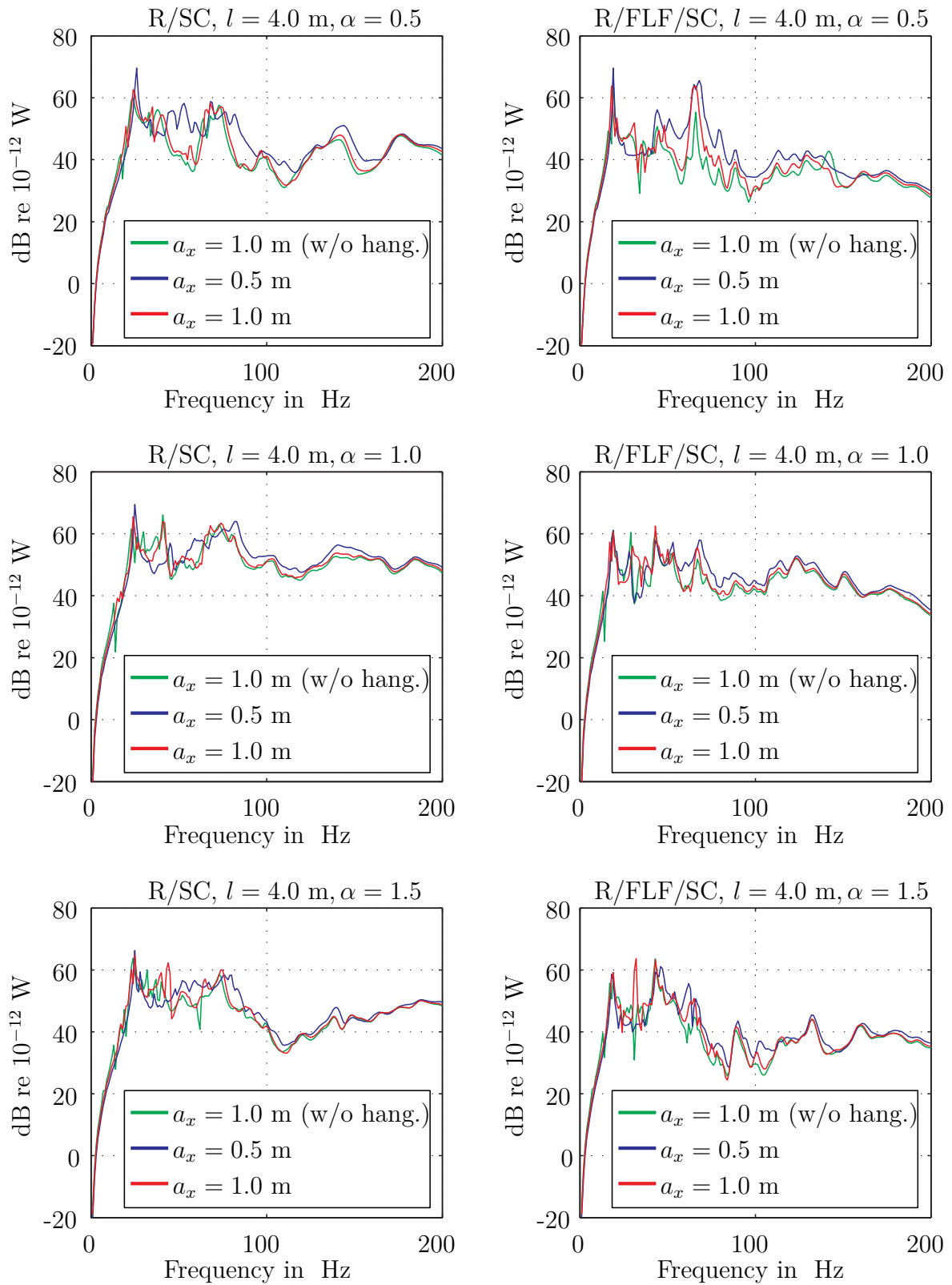
Figure B.25: Sound power level, CLT, Variation of the suspension grid: $l = 4.0$ m, $l_{\mathrm{hang}} = 0.12$ m , $\mu_{\mathrm{wall}} = 10\%$
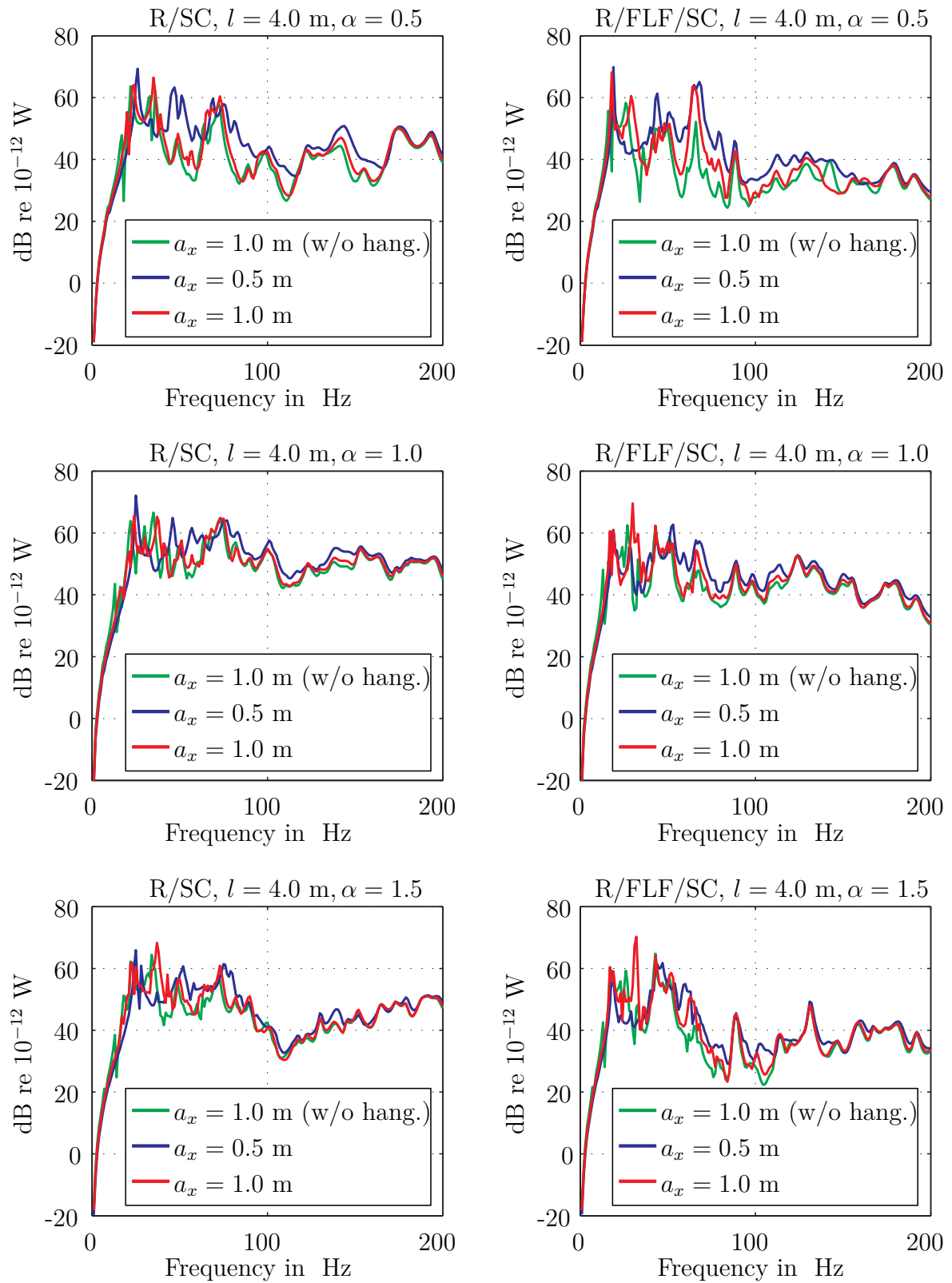
Figure B.26: Sound power level, CLT, Variation of the suspension grid: $l = 4.0$ m, $l_{\text{hang}} = 0.20$ m , $\mu_{\text{wall}} = 3\%$
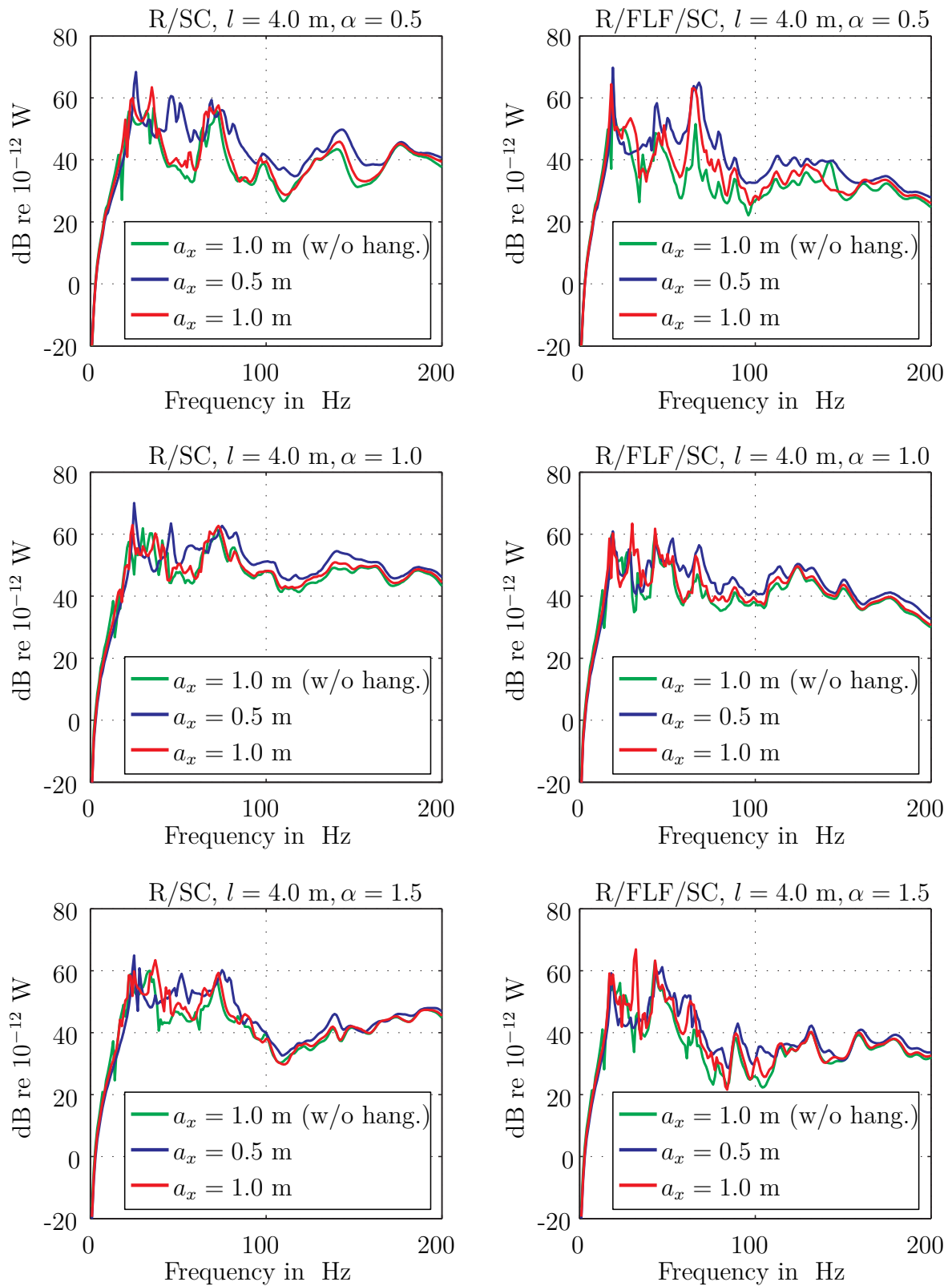
Figure B.27: Sound power level, CLT, Variation of the suspension grid: $l = 4.0$ m, $l_{\mathrm{hang}} = 0.20$ m , $\mu_{\mathrm{wall}} = 10\%$
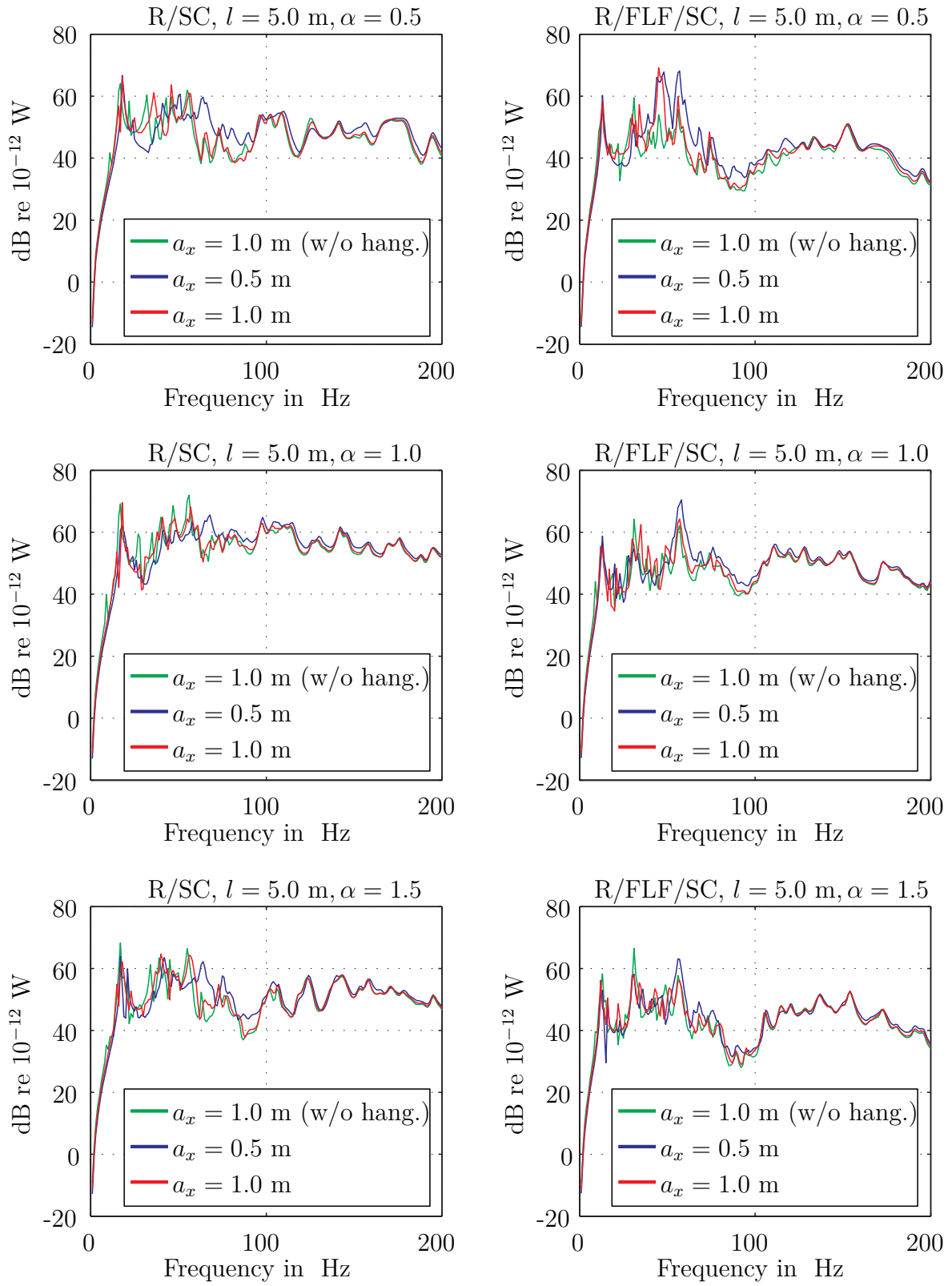
Figure B.28: Sound power level, CLT, Variation of the suspension grid: $l = 5.0$ m, $l_{\mathrm{hang}} = 0.12$ m , $\mu_{\mathrm{wall}} = 3\%$
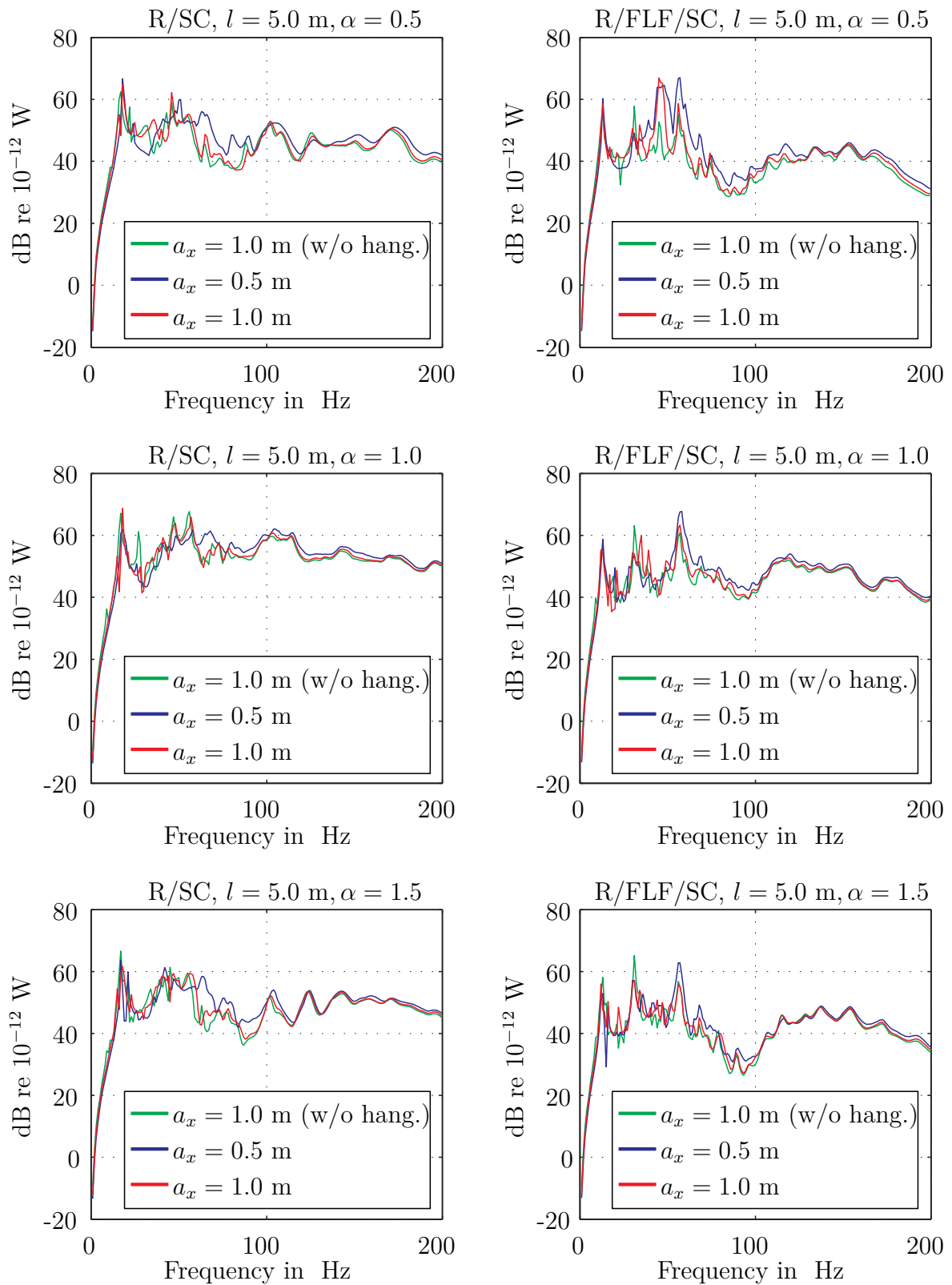
Figure B.29: Sound power level, CLT, Variation of the suspension grid: $l = 5.0$ m, $l_{\text{hang}} = 0.12$ m , $\mu_{\text{wall}} = 10\%$
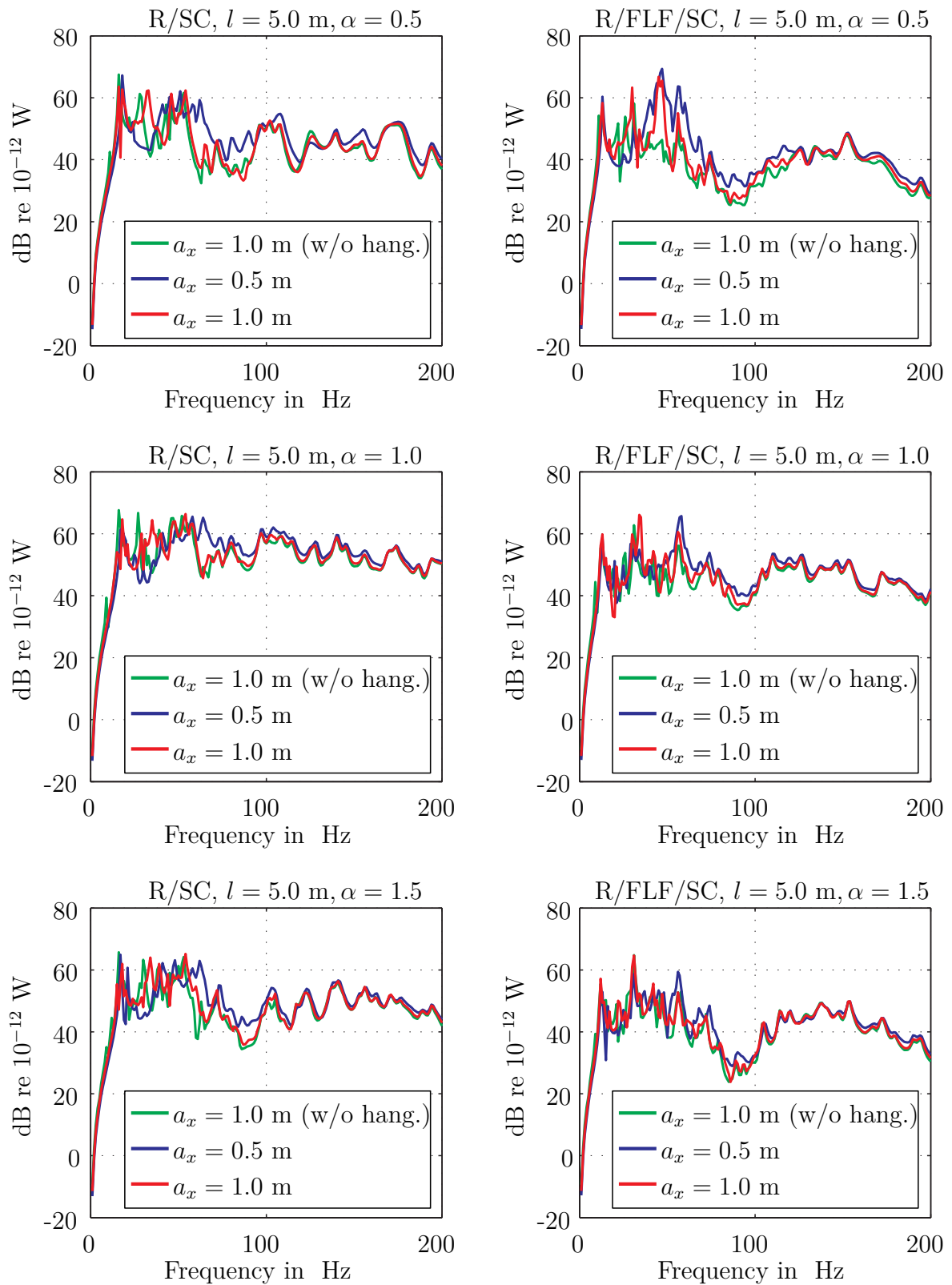
Figure B.30: Sound power level, CLT, Variation of the suspension grid: $l = 5.0$ m, $l_{\text{hang}} = 0.20$ m , $\mu_{\text{wall}} = 3\%$
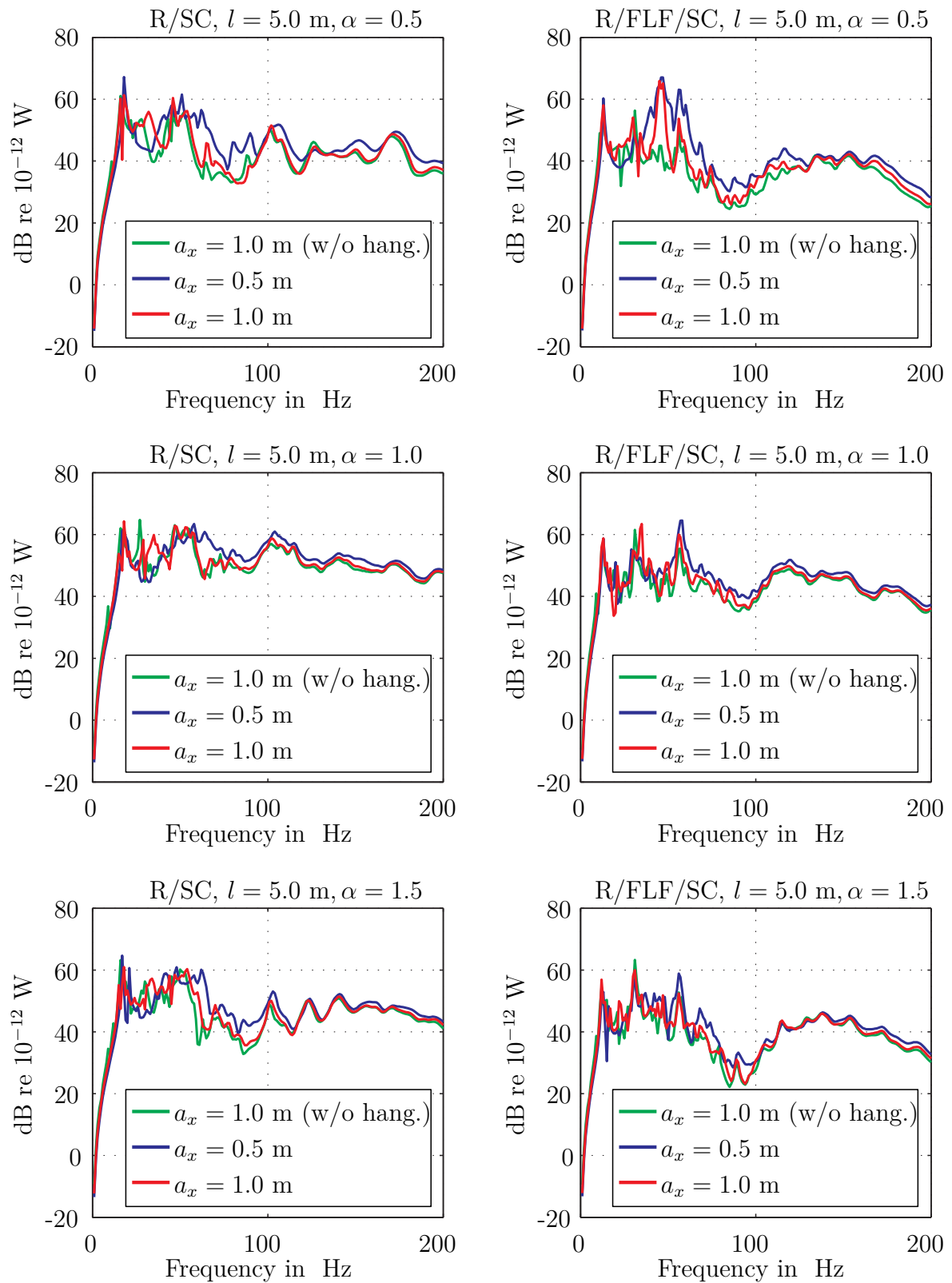
Figure B.31: Sound power level, CLT, Variation of the suspension grid: $l = 5.0$ m, $l_\text{hang} = 0.20$ m, $\mu_\text{wall} = 10\%$

B.2.4 Investigation of the absorption factor at the boundaries
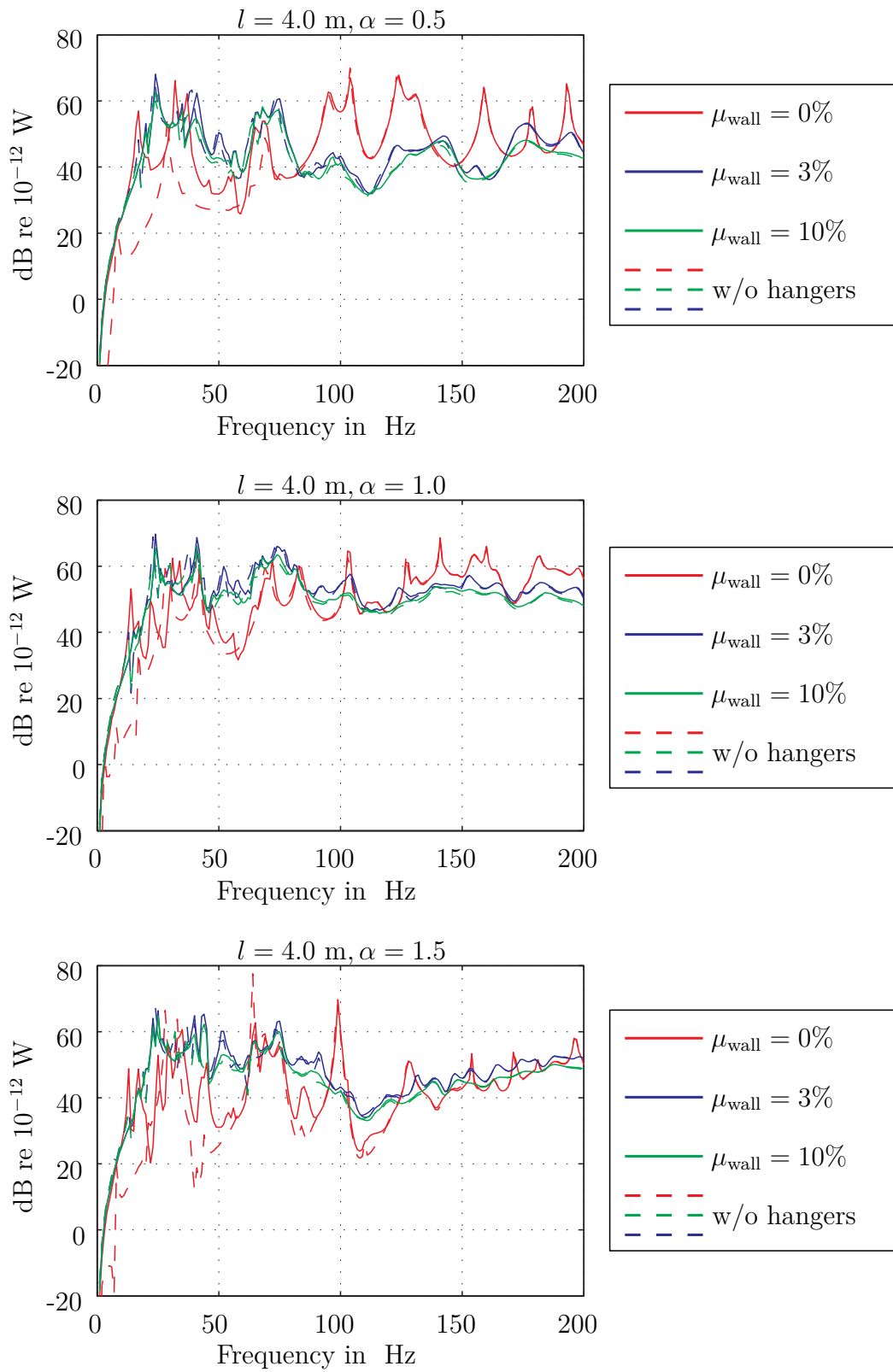
Figure B.32: Sound power level, CLT-R/SC, Comparison of different absorption factors, length $l = 4.0$ m, $a_x = 0.1$ m, $l_{\mathrm{hang}} = 12$ cm
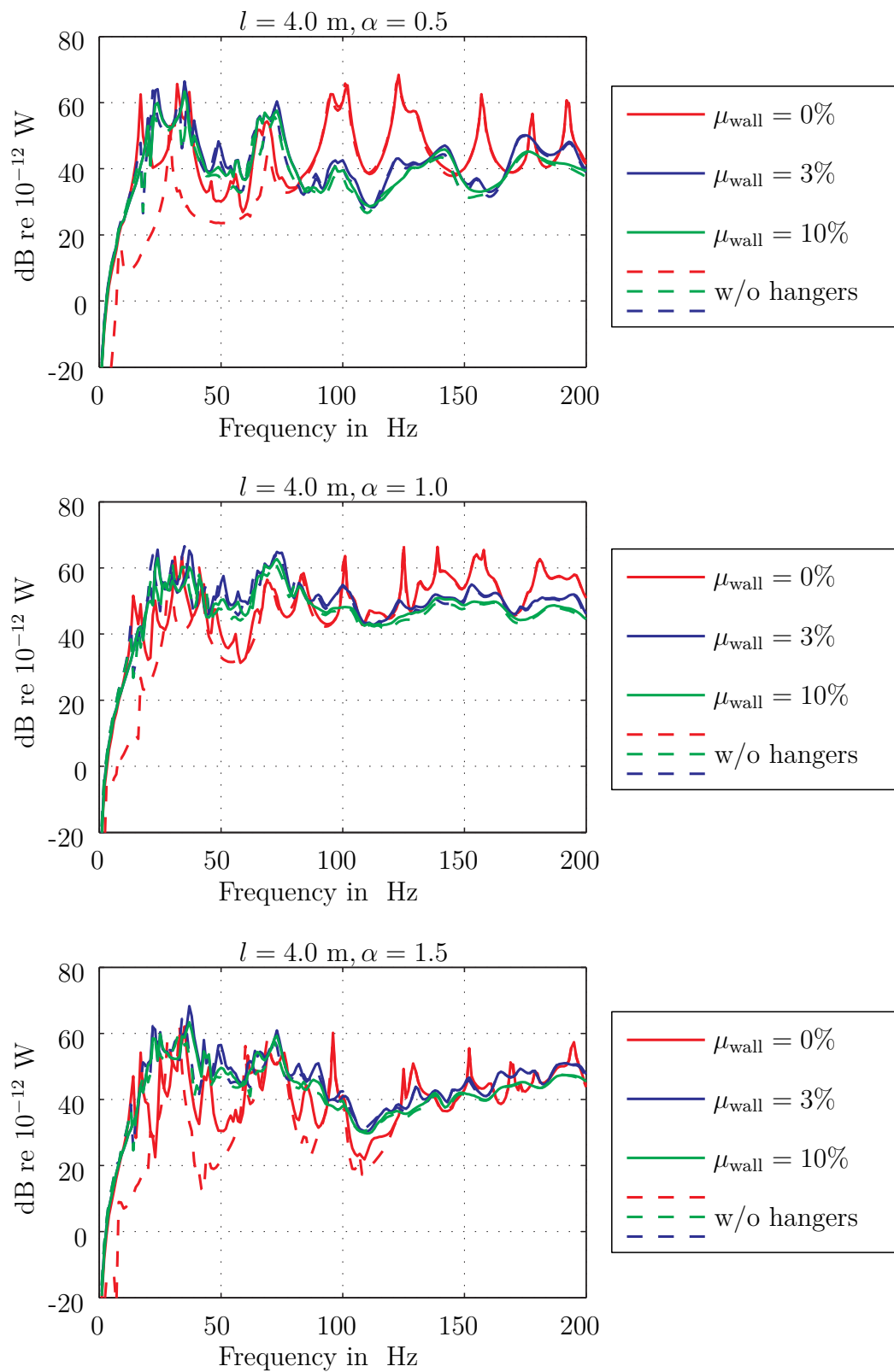
Figure B.33: Sound power level, CLT-R/SC, Comparison of different absorption factors: $l = 4.0$ m, $a_x = 1.0$ m, $l_{\text{hang}} = 0.20$ m
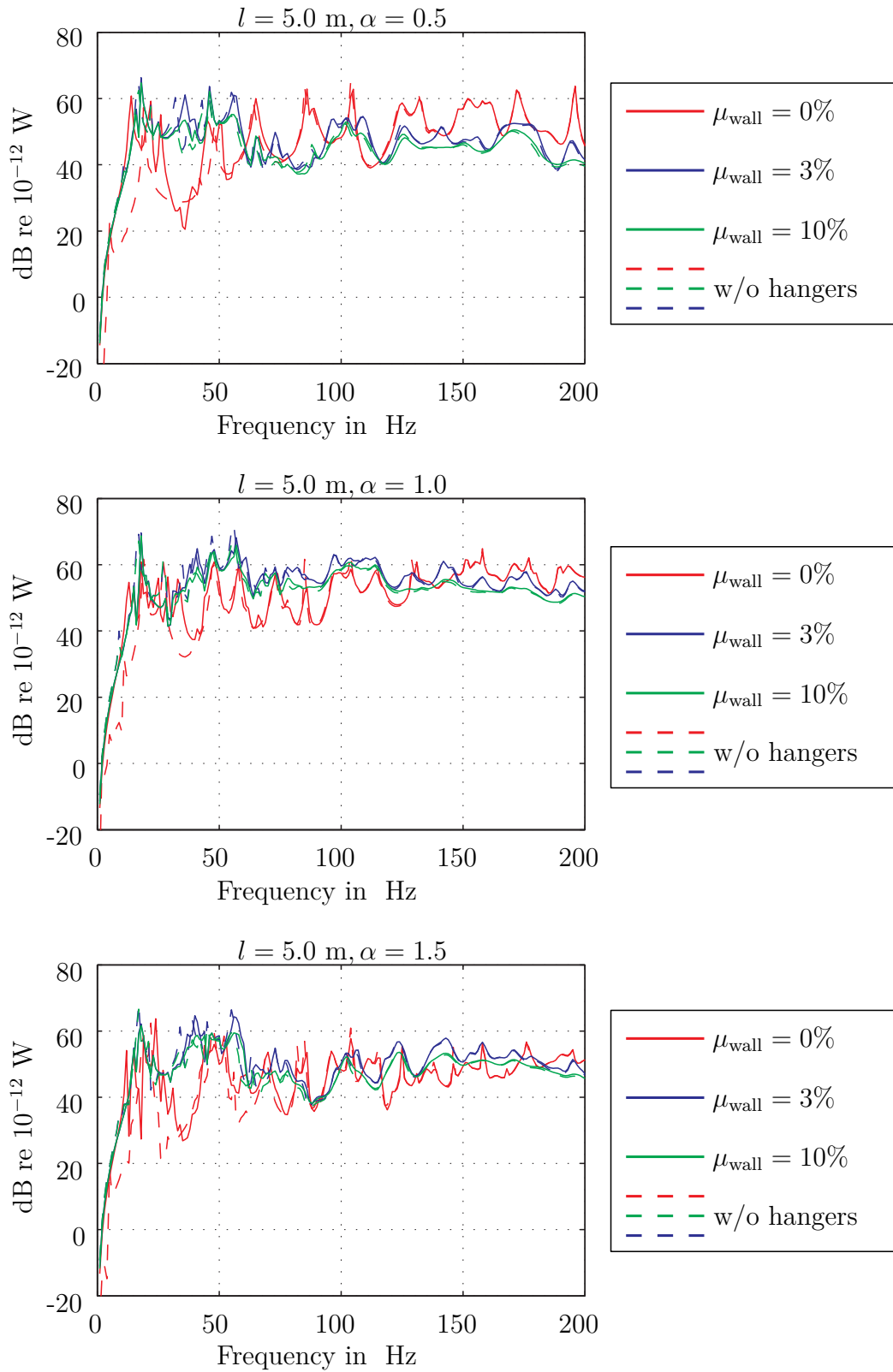
Figure B.34: Sound power level, CLT-R/SC, Comparison of different absorption factors: $l = 5.0$ m, $a_x = 1.0$ m, $l_{\text{hang}} = 0.12$ m
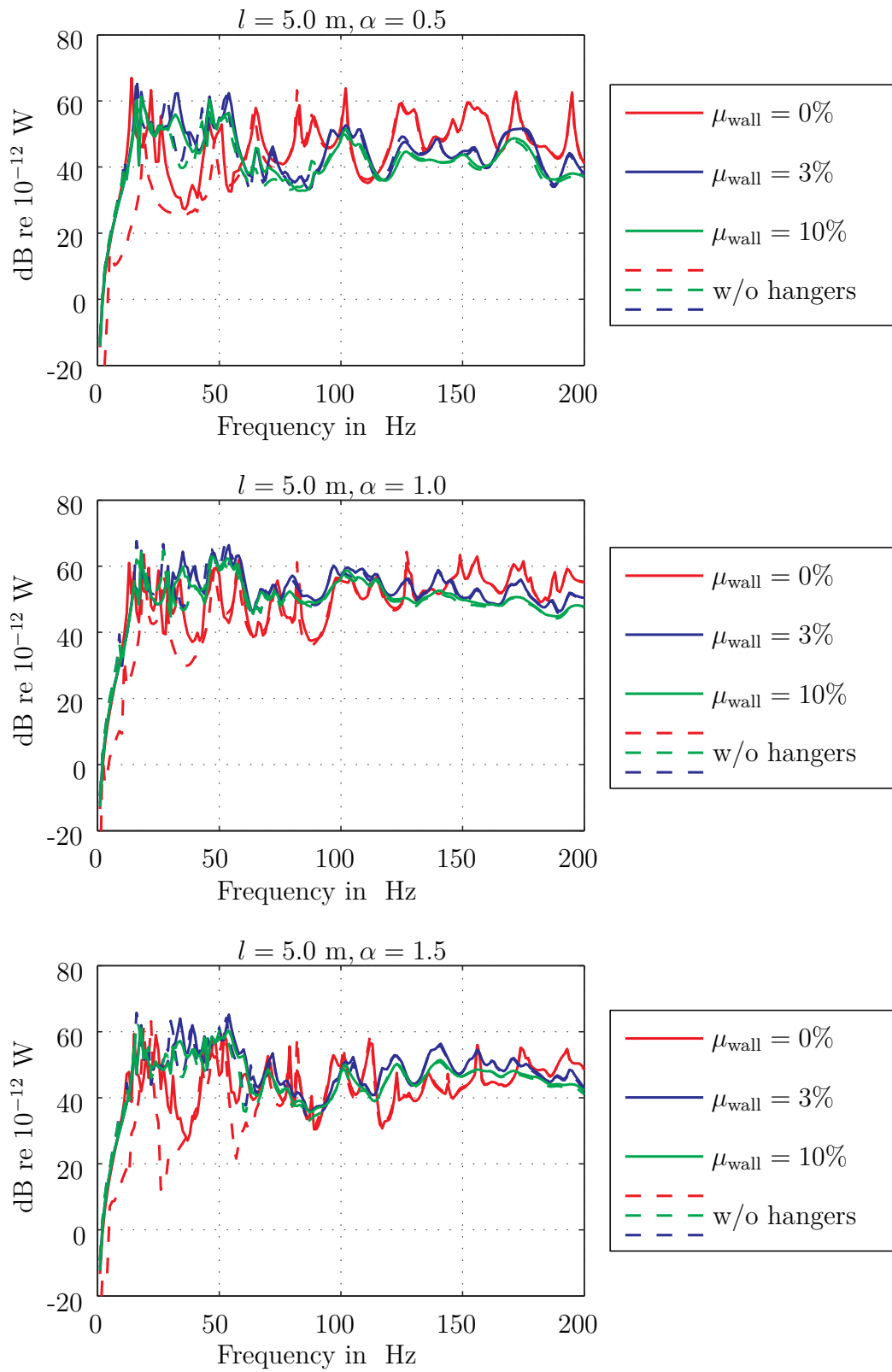
Figure B.35: Sound power level, CLT-R/SC, Comparison of different absorption factors:$l = 5.0$ m, $a_x = 1.0$ m,$l_{\mathrm{hang}} = 0.20$ m
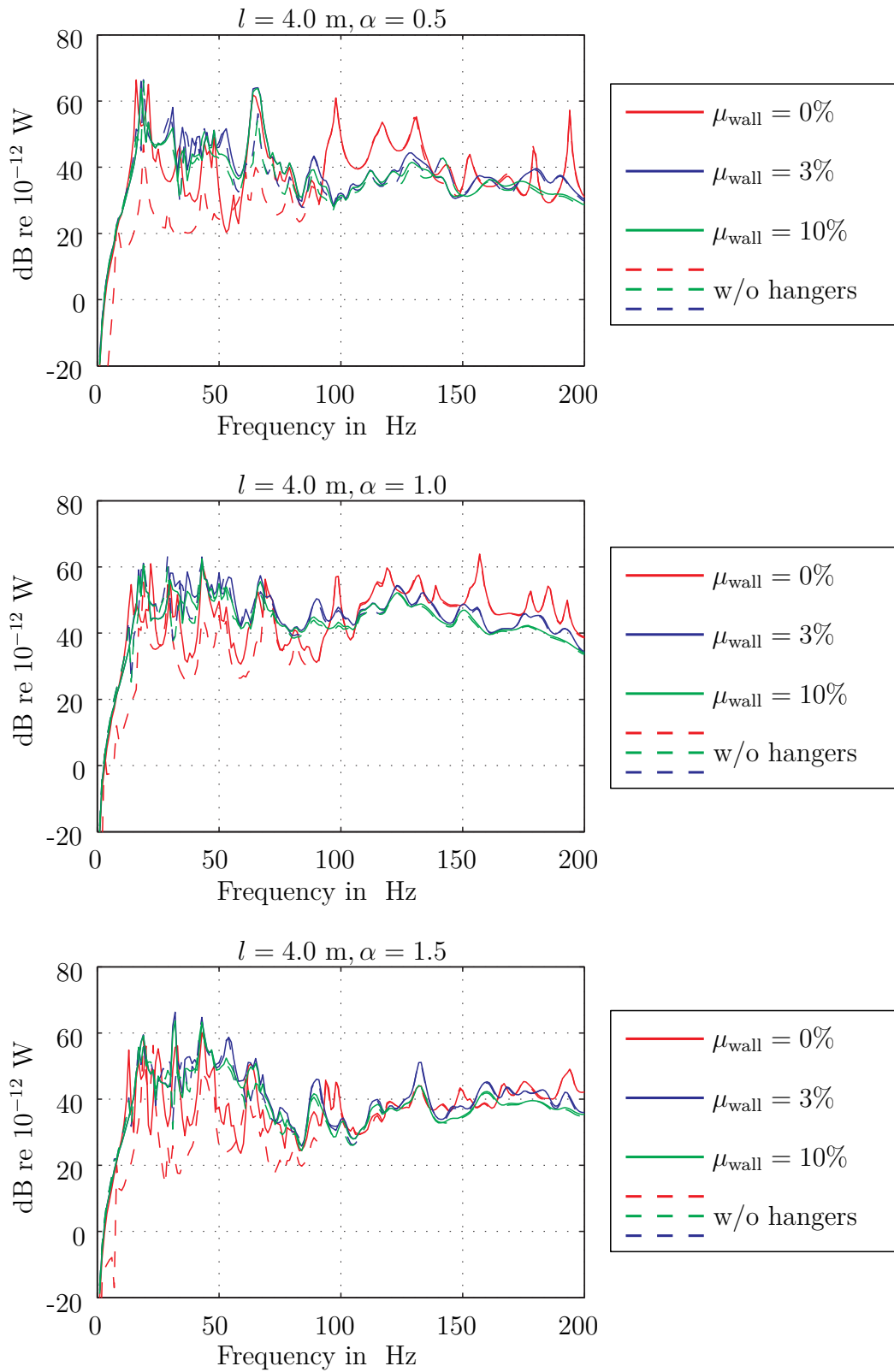
Figure B.36: Sound power level, CLT-R/FLF/SC, Comparison of different absorption factors: $l = 4.0$ m, $a_y = 1.0$ m, $l_{\text{hang}} = 0.12$ m
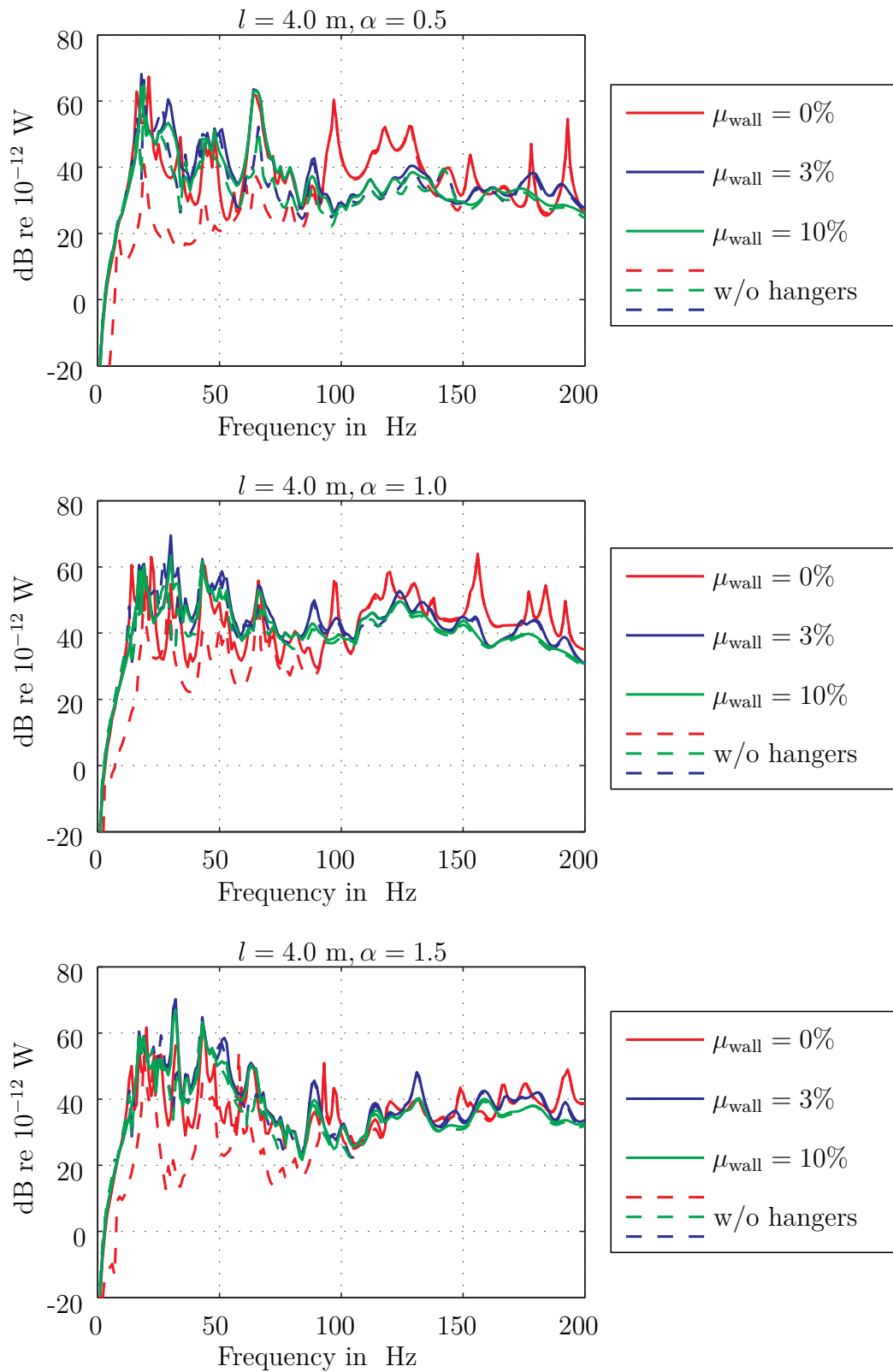
Figure B.37: Sound power level, CLT-R/FLF/SC, Comparison of different absorption factors:$l = 4.0$ m, $a_x = 1.0$ m,$l_{\text{hang}} = 0.20$ m
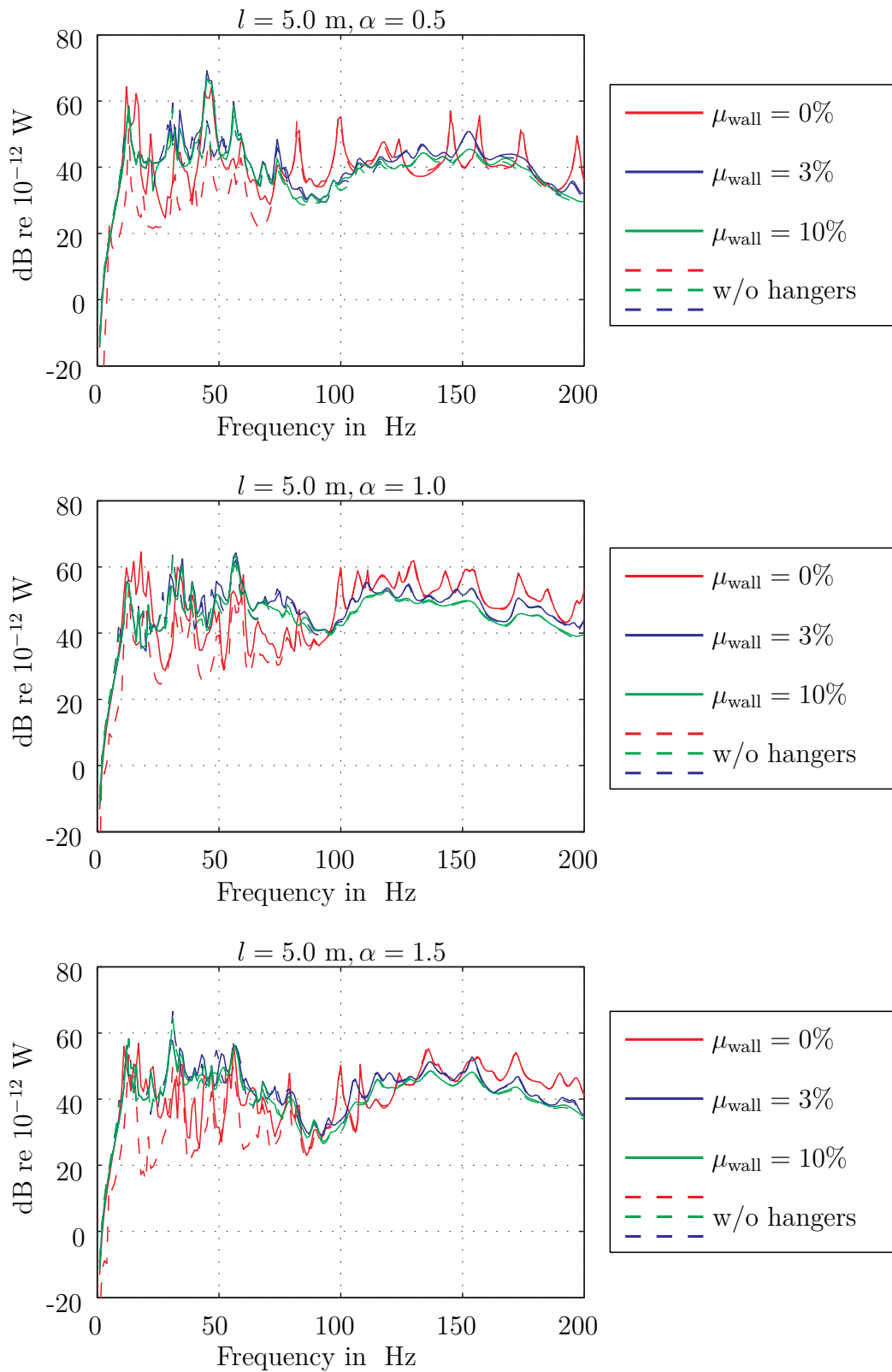
Figure B.38: Sound power level, CLT-R/FLF/SC, Comparison of different absorption factors: $l = 5.0$ m, $a_x = 1.0$ m, $l_{\text{hang}} = 0.12$ m
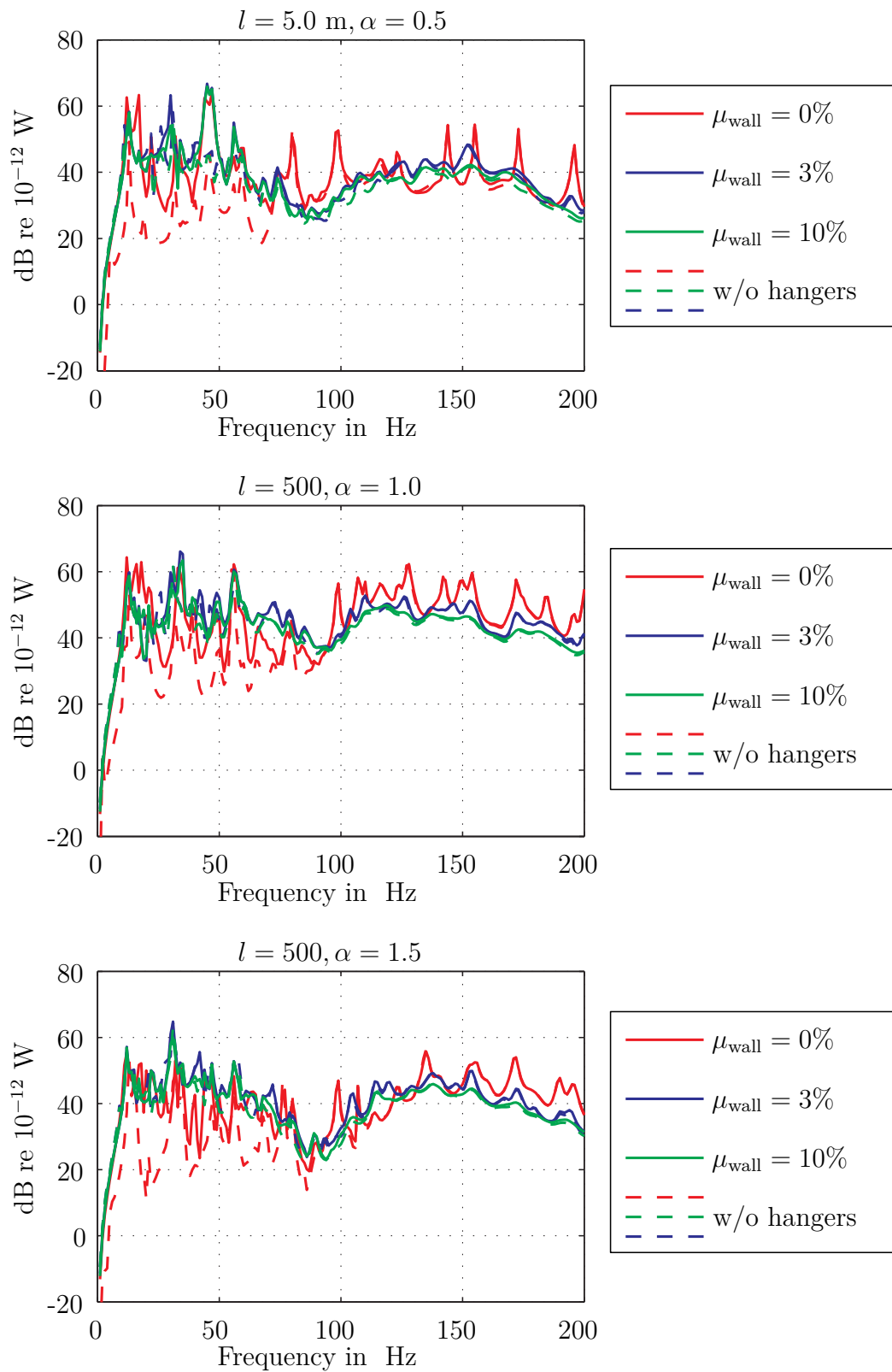
Figure B.39: Sound power level, CLT-R/FLF/SC, Comparison of different absorption factors:$l = 5.0$ m, $a_x = 1.0$ m,$l_{\text{hang}} = 0.20$ m

B.2.5 Comparison of the aspect ratios of the floors (single measurements and mean values)
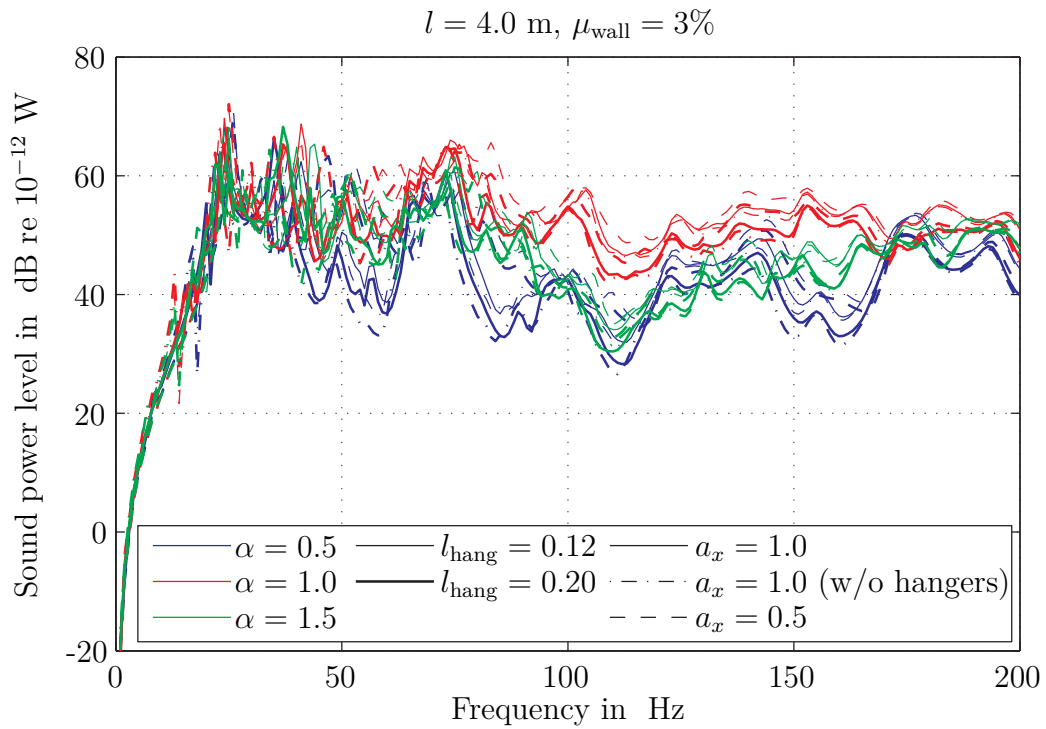
Figure B.40: CLT-R/SC, Comparison of the aspect ratios of the floors: $l = 4.0$ m, $\mu :$ wall $= 3\%$; l_{hang} and a_x in   m
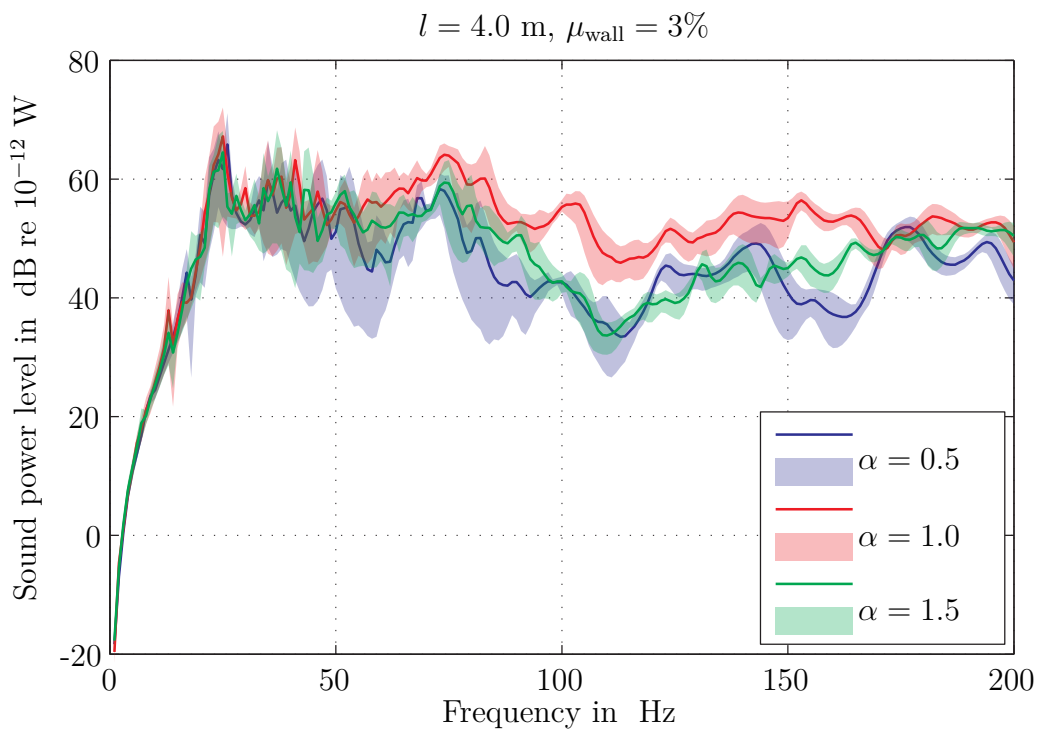
Figure B.41: CLT-R/SC, Comparison of the aspect ratios of the floors: $l = 4.0$ m, $\mu_{\mathrm{wall}} = 3\%$; mean value and envelope
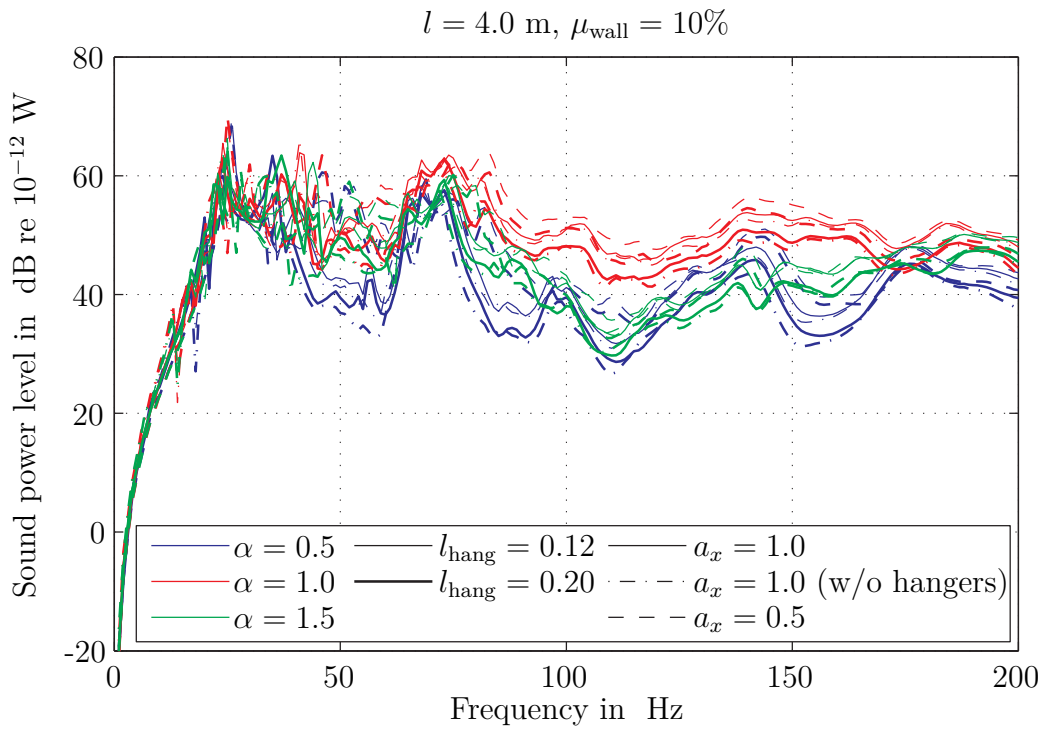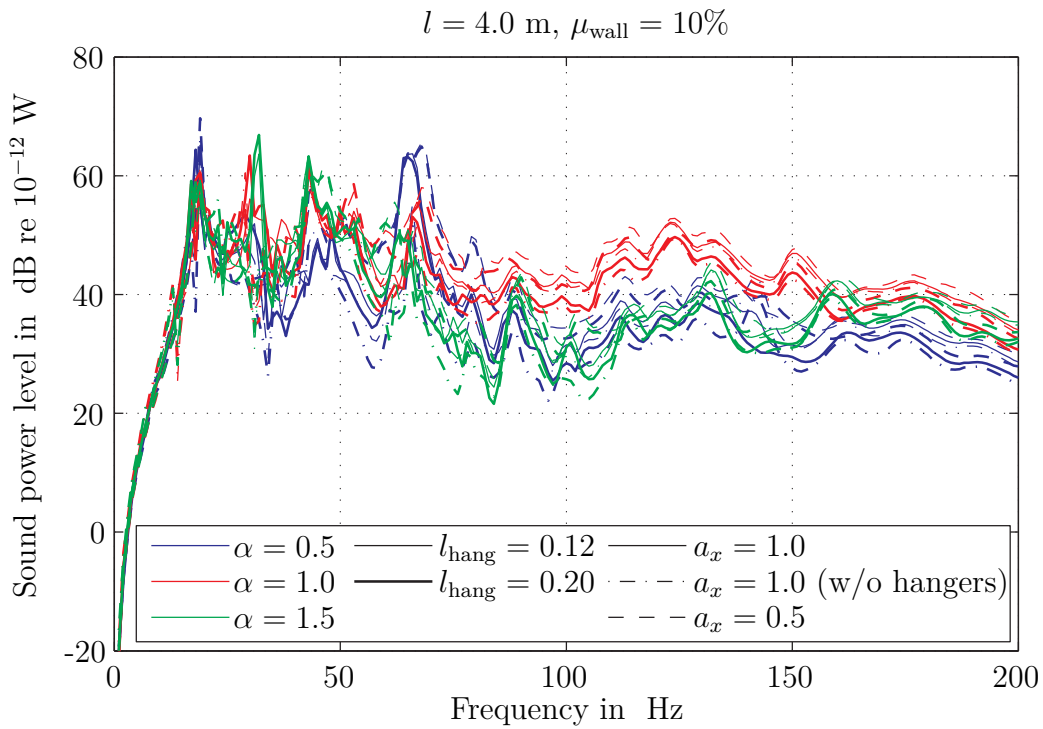
Figure B.42: CLT-R/SC, Comparison of the aspect ratios of the floors: $l = 4.0$ m, $\mu_{\text{wall}} = 10\%$; l_{hang} and a_x in m
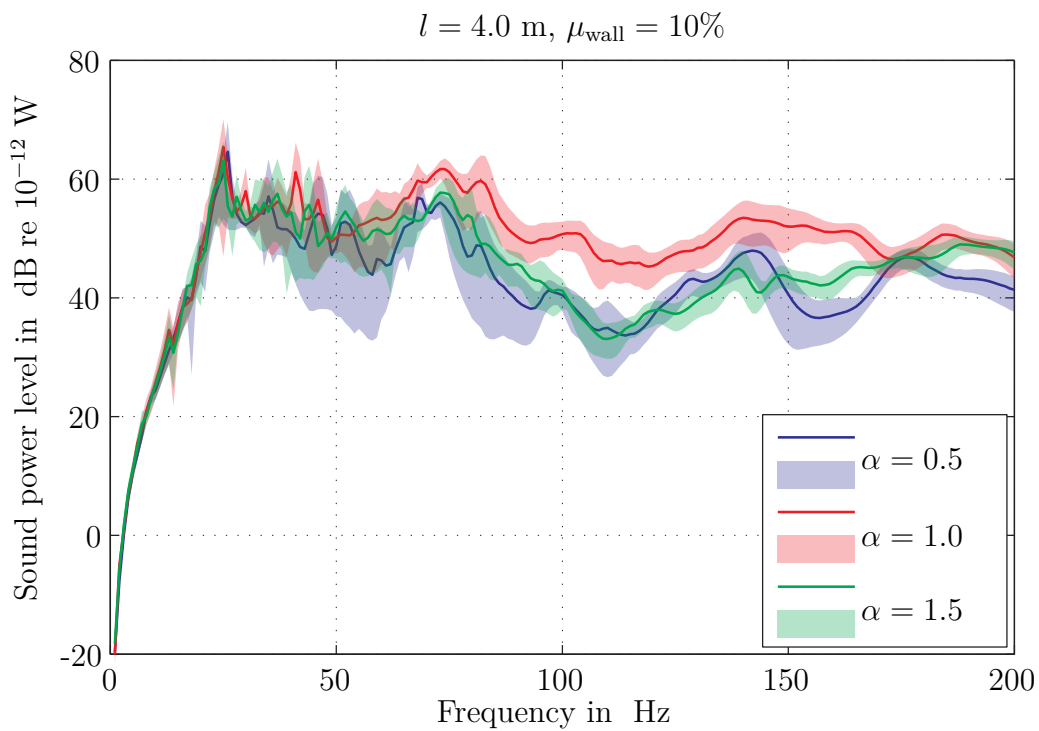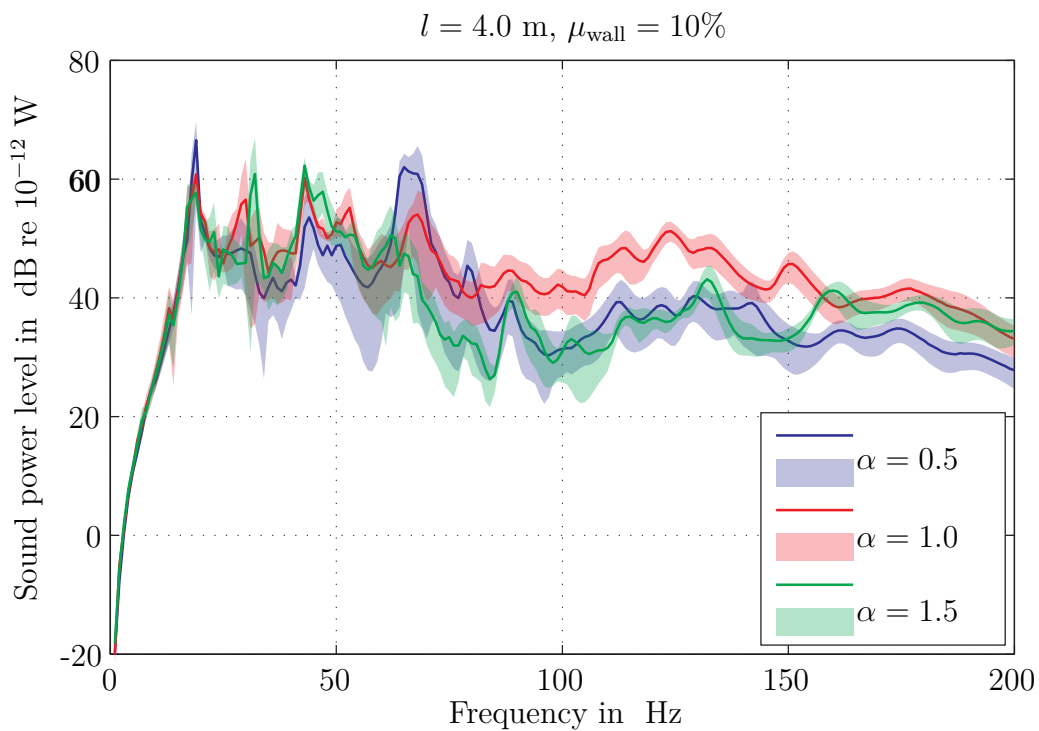

Figure B.43: CLT-R/SC, Comparison of the aspect ratios of the floors: $l = 4.0$ m, $\mu_{\text{wall}} = 10\%$; mean value and envelope
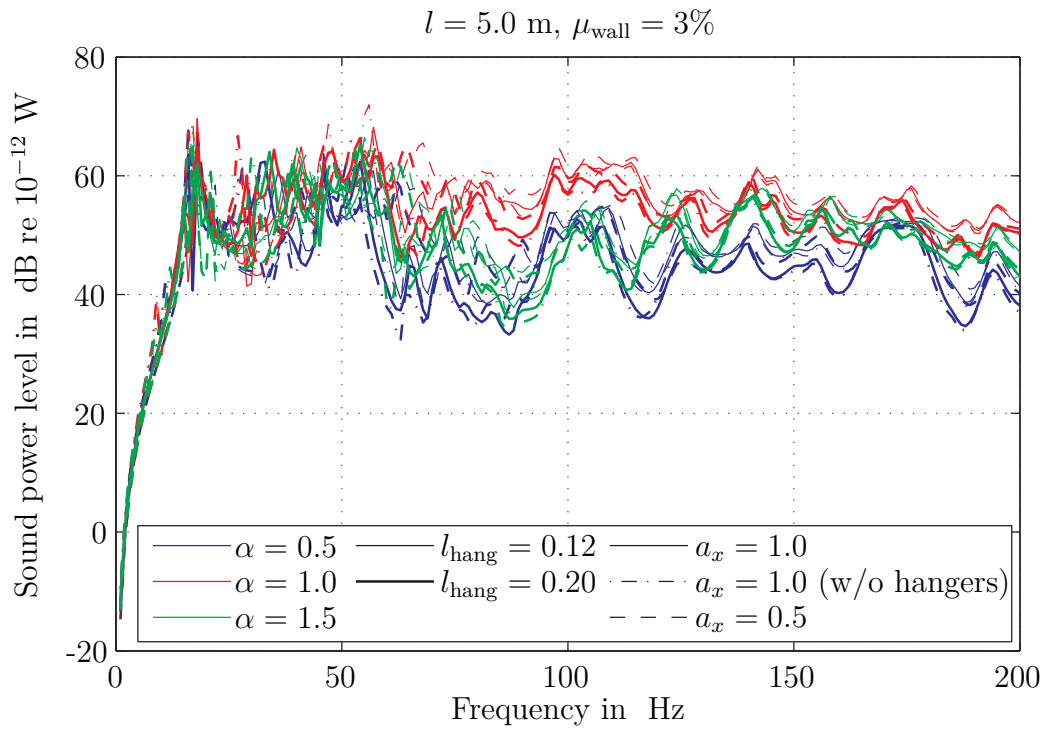
Figure B.44: CLT-R/SC, Comparison of the aspect ratios of the floors: $l = 5.0$ m, $\mu_{\text{wall}} = 3\%$; l_{hang} and a_x in m
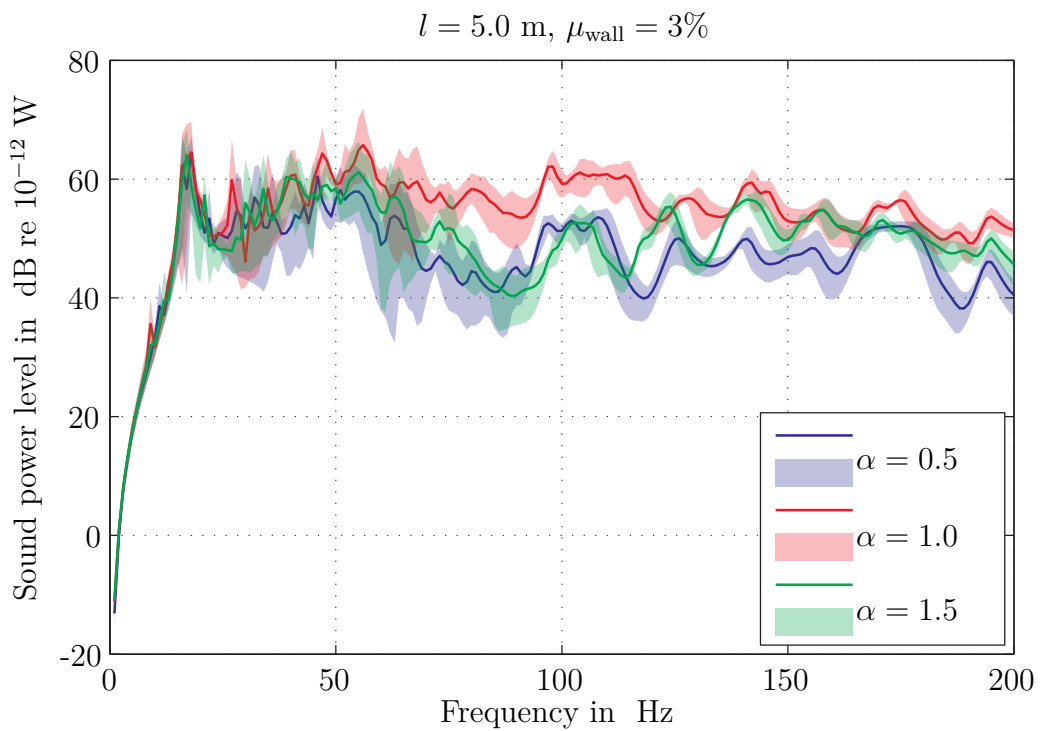
Figure B.45: CLT-R/SC, Comparison of the aspect ratios of the floors: $l = 5.0$ m, $\mu_{\text{wall}} = 3\%$; mean value and envelope
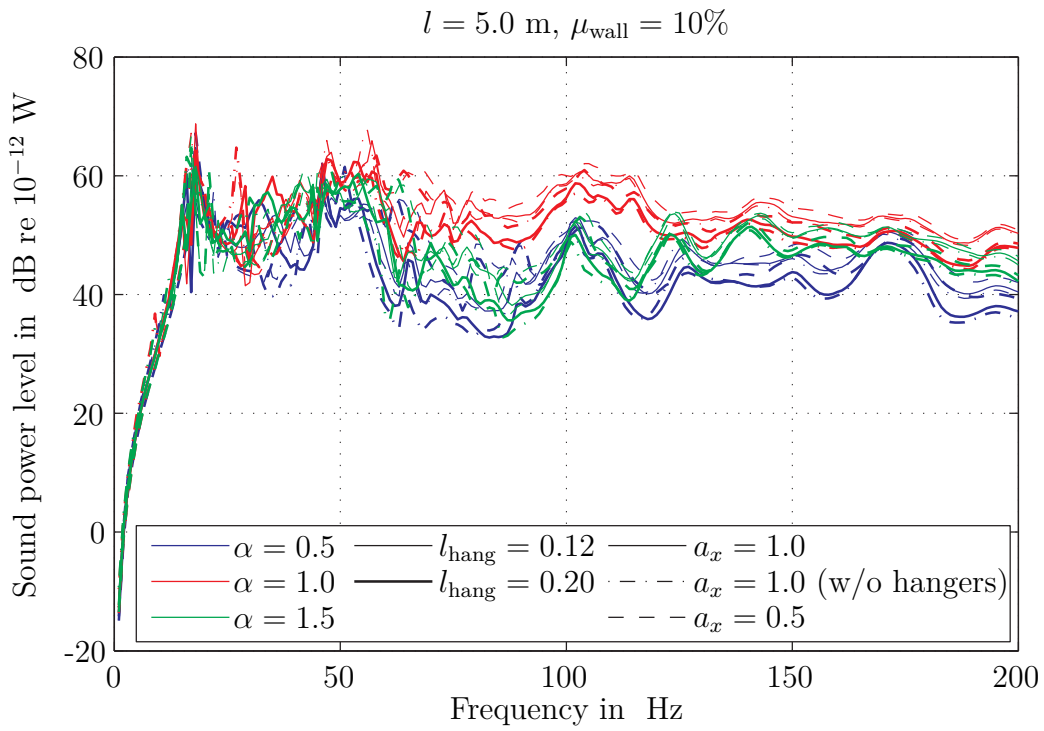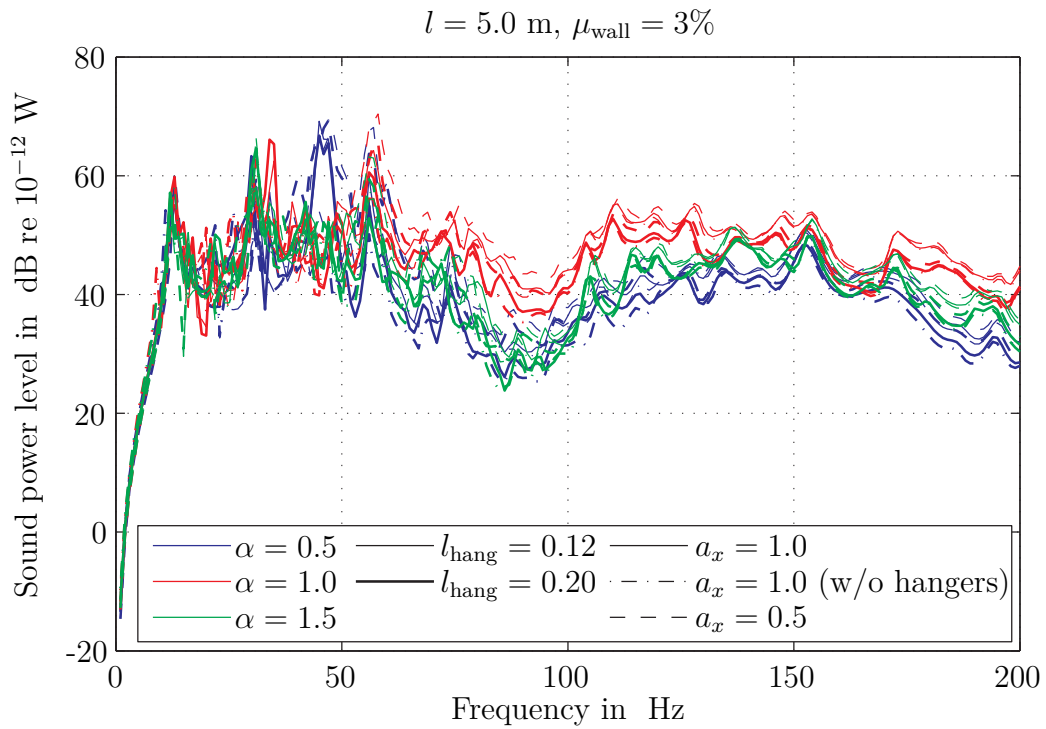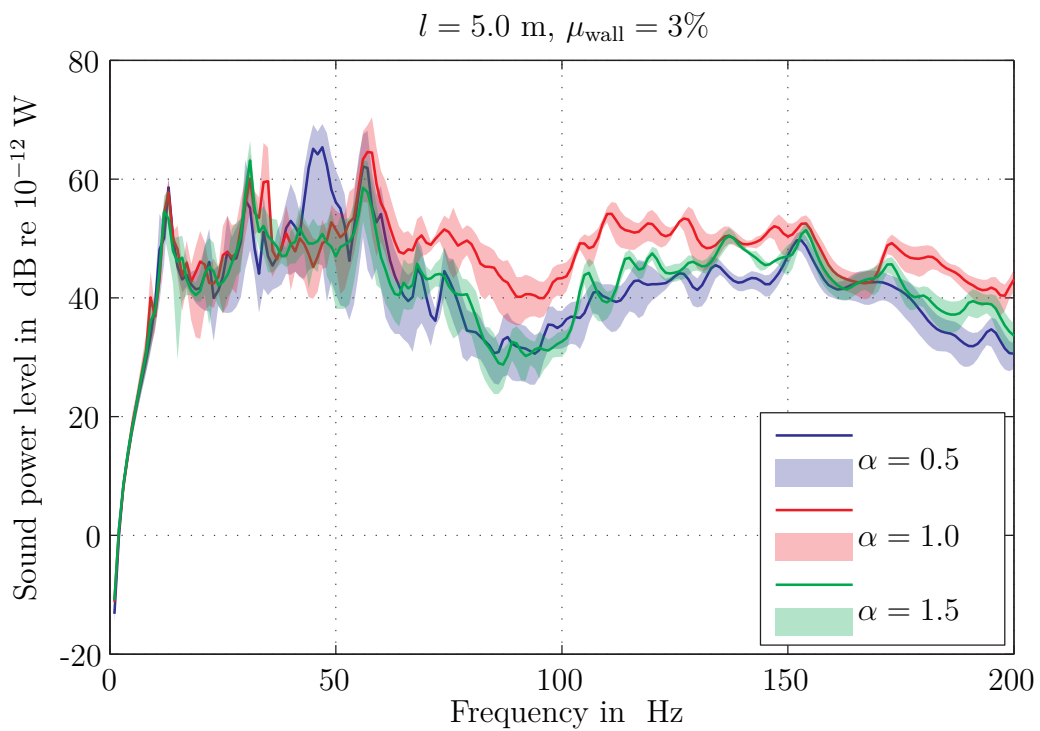
$l = 5.0$ m, $\mu_{\text{wall}} = 10\%$

Figure B.46: CLT-R/SC, Comparison of the aspect ratios of the floors: $l = 5.0$ m, $\mu_{\text{wall}} = 10\%$; l_{hang} and a_x in m
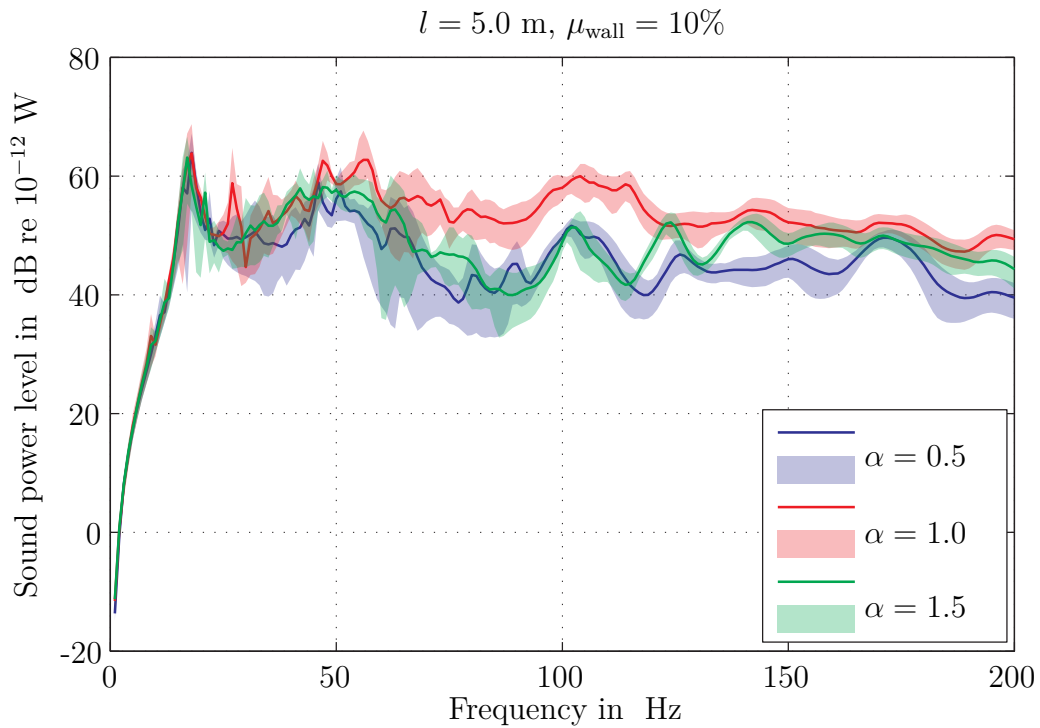
$l = 5.0$ m, $\mu_{\text{wall}} = 10\%$

Figure B.47: CLT-R/SC, Comparison of the aspect ratios of the floors: $l = 5.0$ m, $\mu_{\text{wall}} = 10\%$; mean value and envelope
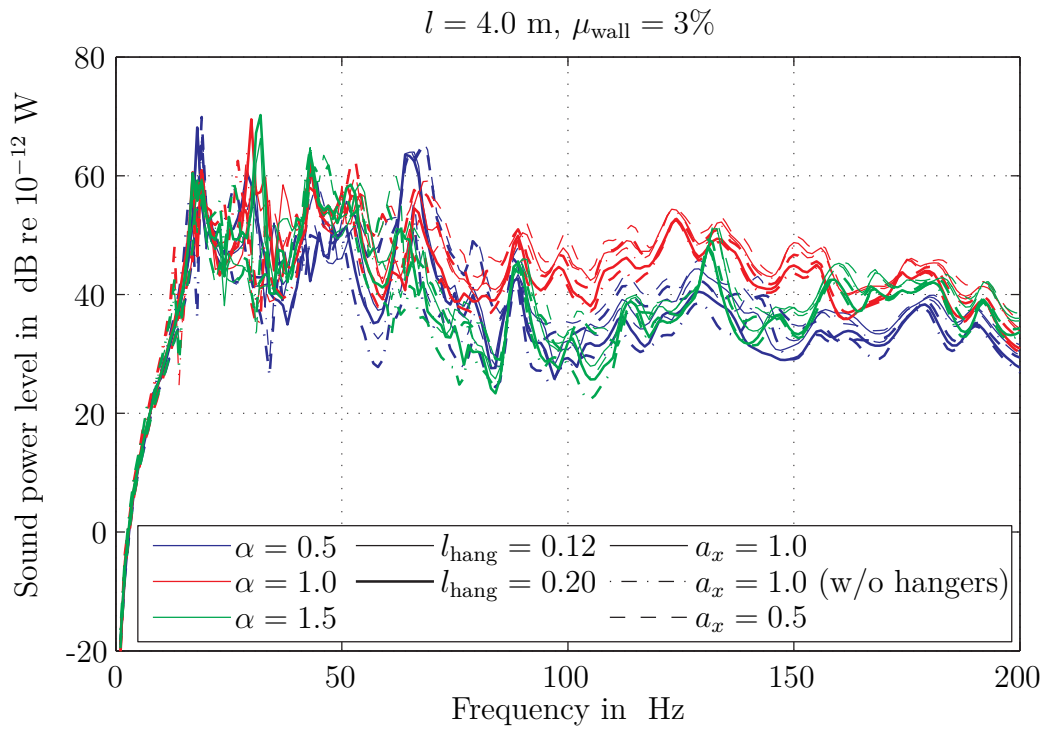
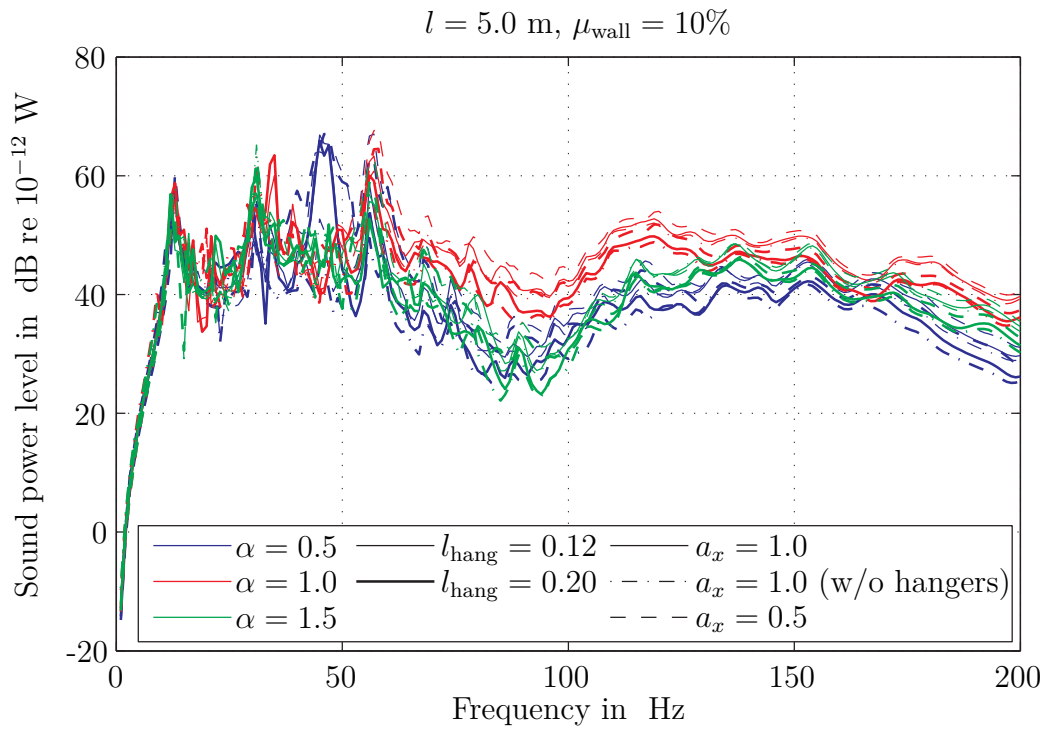**Figure B.48:** CLT-R/FLF/SC, Comparison of the aspect ratios of the floors: $l = 4.0$ m, $\mu_{\mathrm{wall}} = 3\%$; l_{hang} and a_x in m
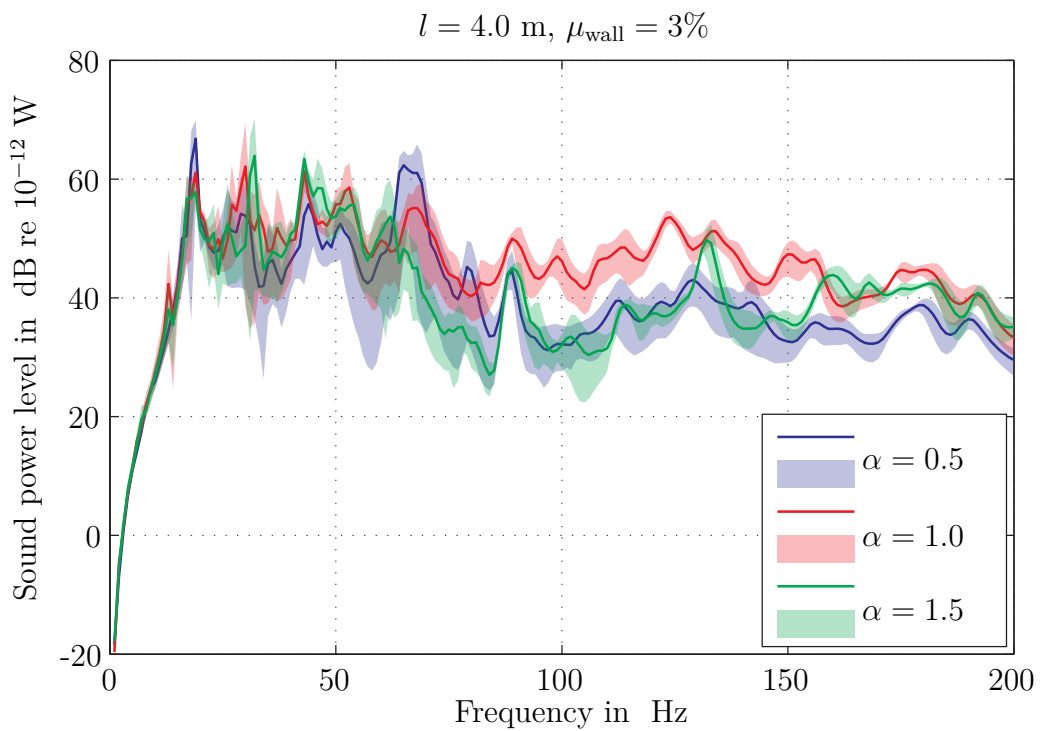
Figure B.49: CLT-R/FF/SC, Comparison of the aspect ratios of the floors: $l = 4.0$ m, $\mu_{\mathrm{wall}} = 3\%$; mean value and envelope

$$l = 4.0 \text{ m}, \mu_{\text{wall}} = 10\%$$

Figure B.50: CLT-R/FLF/SC, Comparison of the aspect ratios of the floors: $l = 4.0$ m, $\mu_{\text{wall}} = 10\%$; l_{hang} and a_x in m
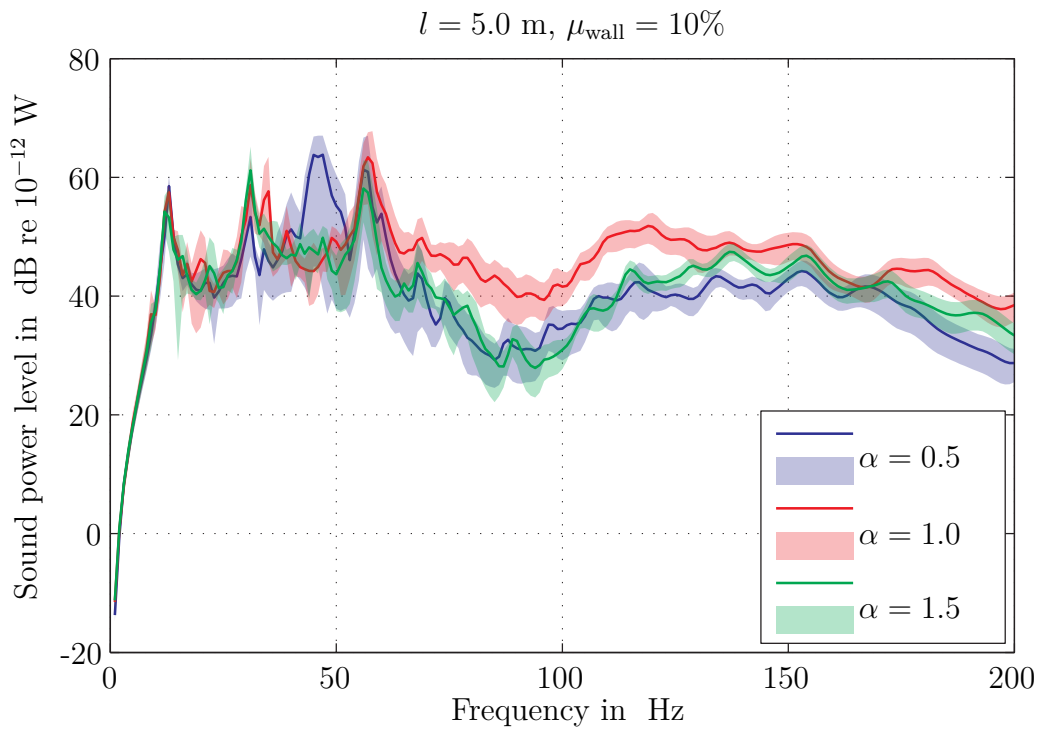
$$l = 4.0 \text{ m}, \mu_{\text{wall}} = 10\%$$

Figure B.51: CLT-R/FLF/SC, Comparison of the aspect ratios of the floors: $l = 4.0$ m, $\mu_{\text{wall}} = 10\%$; mean value and envelope

Figure B.52: CLT-R/FLF/SC, Comparison of the aspect ratios of the floors: $l = 5.0$ m, $\mu_{\text{wall}} = 3\%$; l_{hang} and a_x in m

Figure B.53: CLT-R/FLF/SC, Comparison of the aspect ratios of the floors: $l = 5.0$ m, $\mu_{\text{wall}} = 3\%$; mean value and envelope

$$l = 5.0 \text{ m}, \ \mu_{\text{wall}} = 10\%$$

Figure B.54: CLT-R/FLF/SC, Comparison of the aspect ratios of the floors: $l = 5.0$ m, $\mu_{\text{wall}} = 10\%$; l_{hang} and a_x in m

$$l = 5.0 \text{ m}, \ \mu_{\text{wall}} = 10\%$$

Figure B.55: CLT-R/FLF/SC, Comparison of the aspect ratios of the floors: $l = 5.0$ m, $\mu_{\text{wall}} = 10\%$; mean value and envelope

B.2.6 Comparing different floor lengths (mean values)
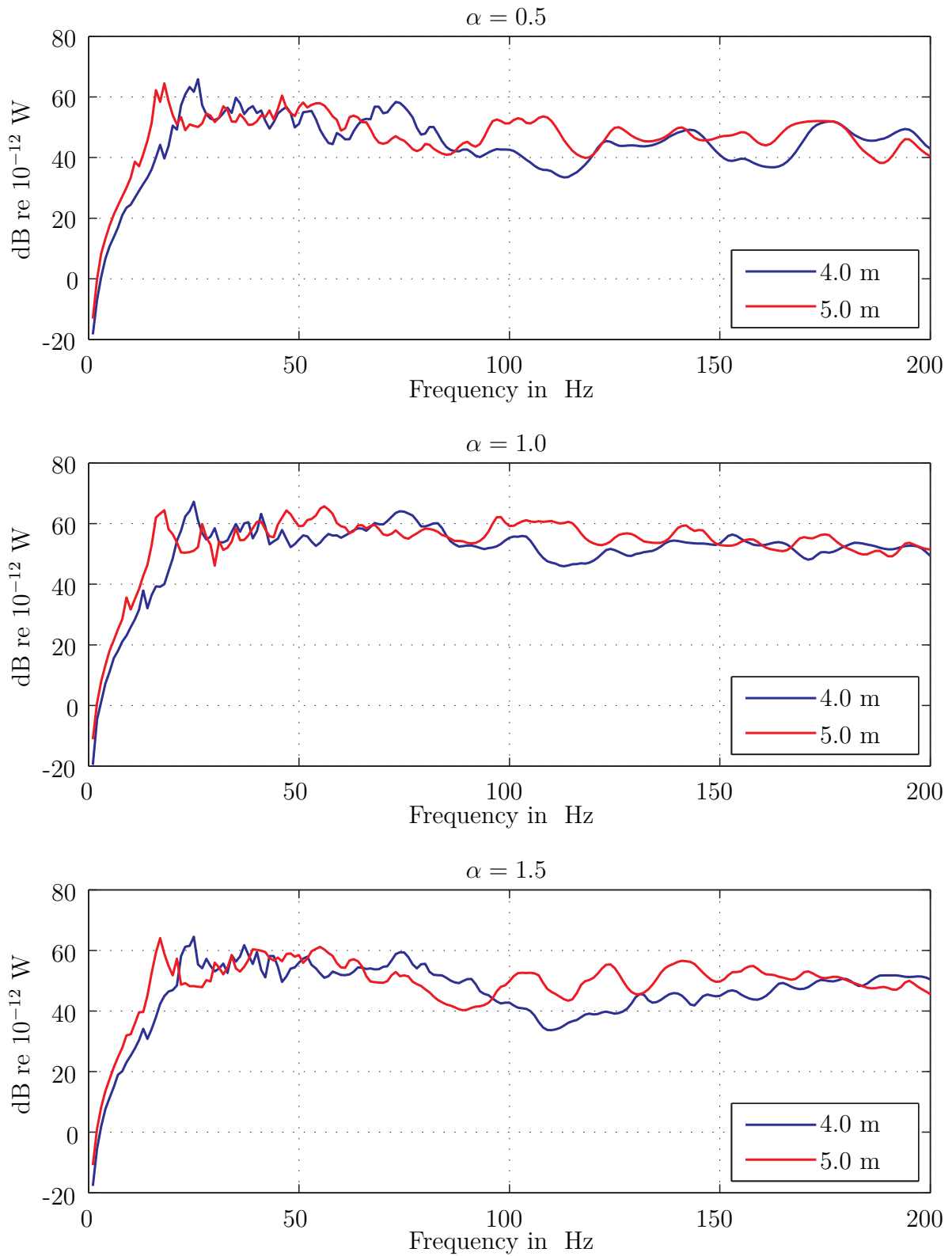
Figure B.56: Sound power level, CLT-R/SC, Comparing different lengths: $\mu_{\mathrm{wall}} = 3\%$, mean values
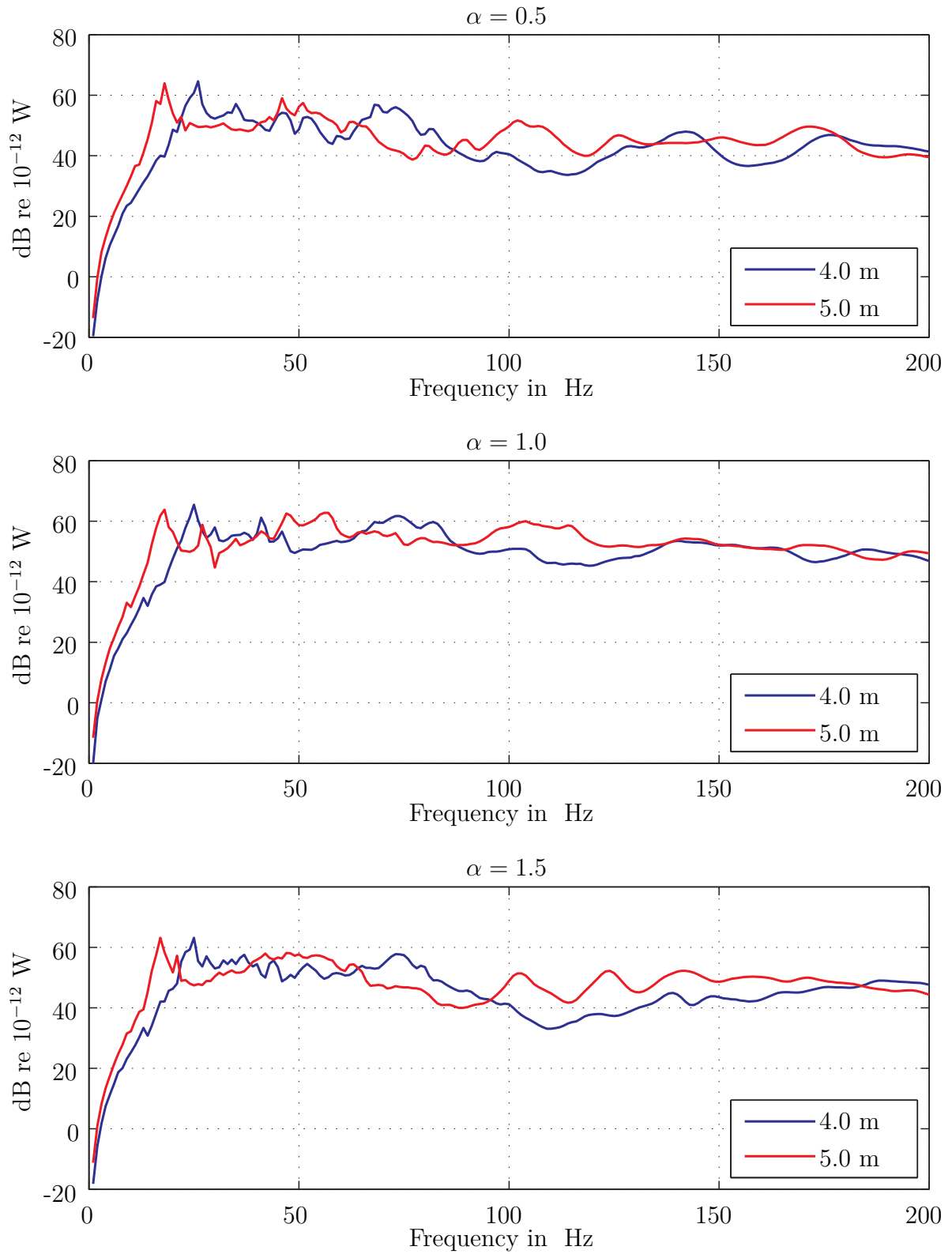
Figure B.57: Sound power level, CLT-R/SC, Comparing different lengths: $\mu_{\text{wall}} = 10\%$, mean values
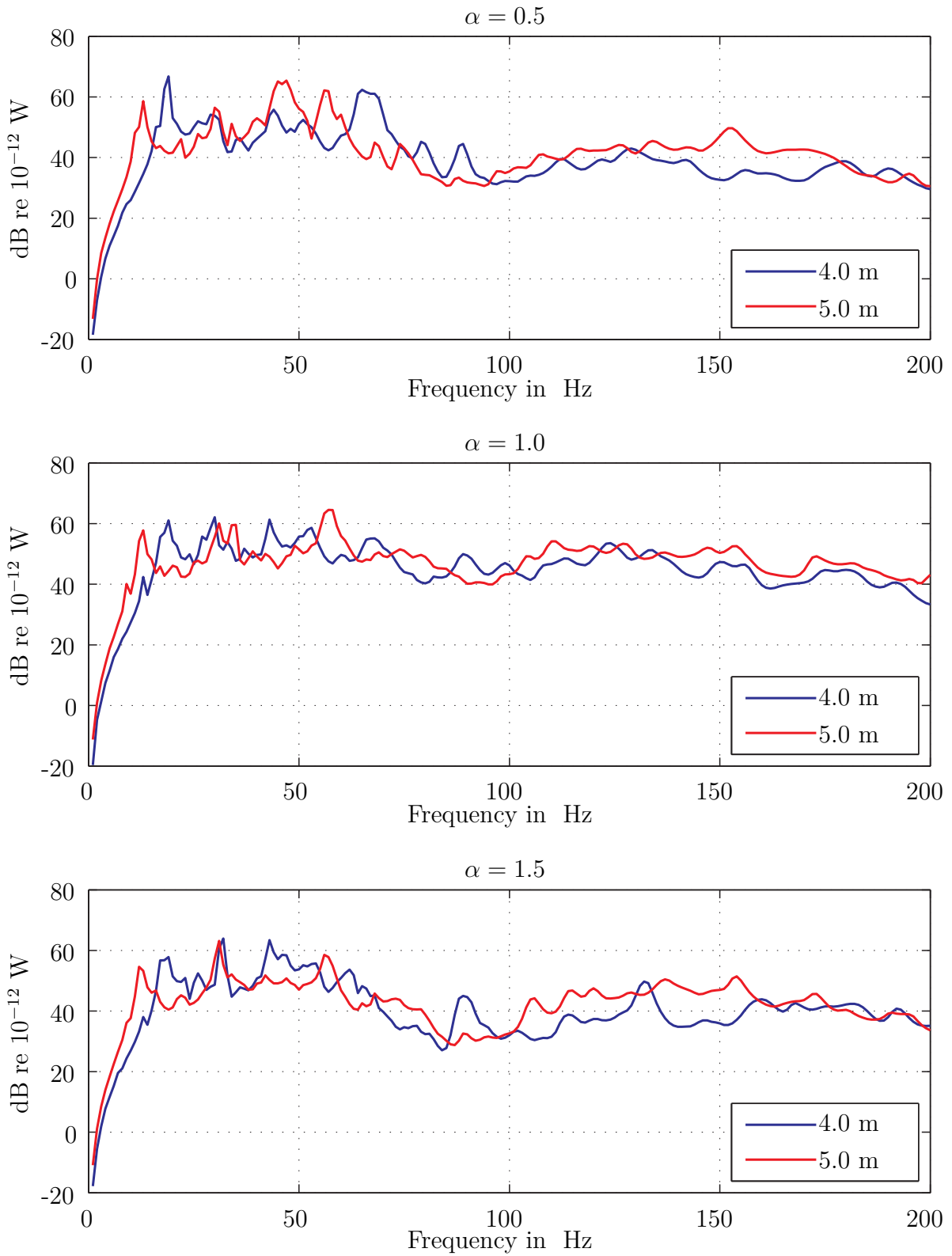
Figure B.58: Sound power level, CLT-R/FLF/SC, Comparing different lengths: $\mu_{\text{wall}} = 3\%$, mean values
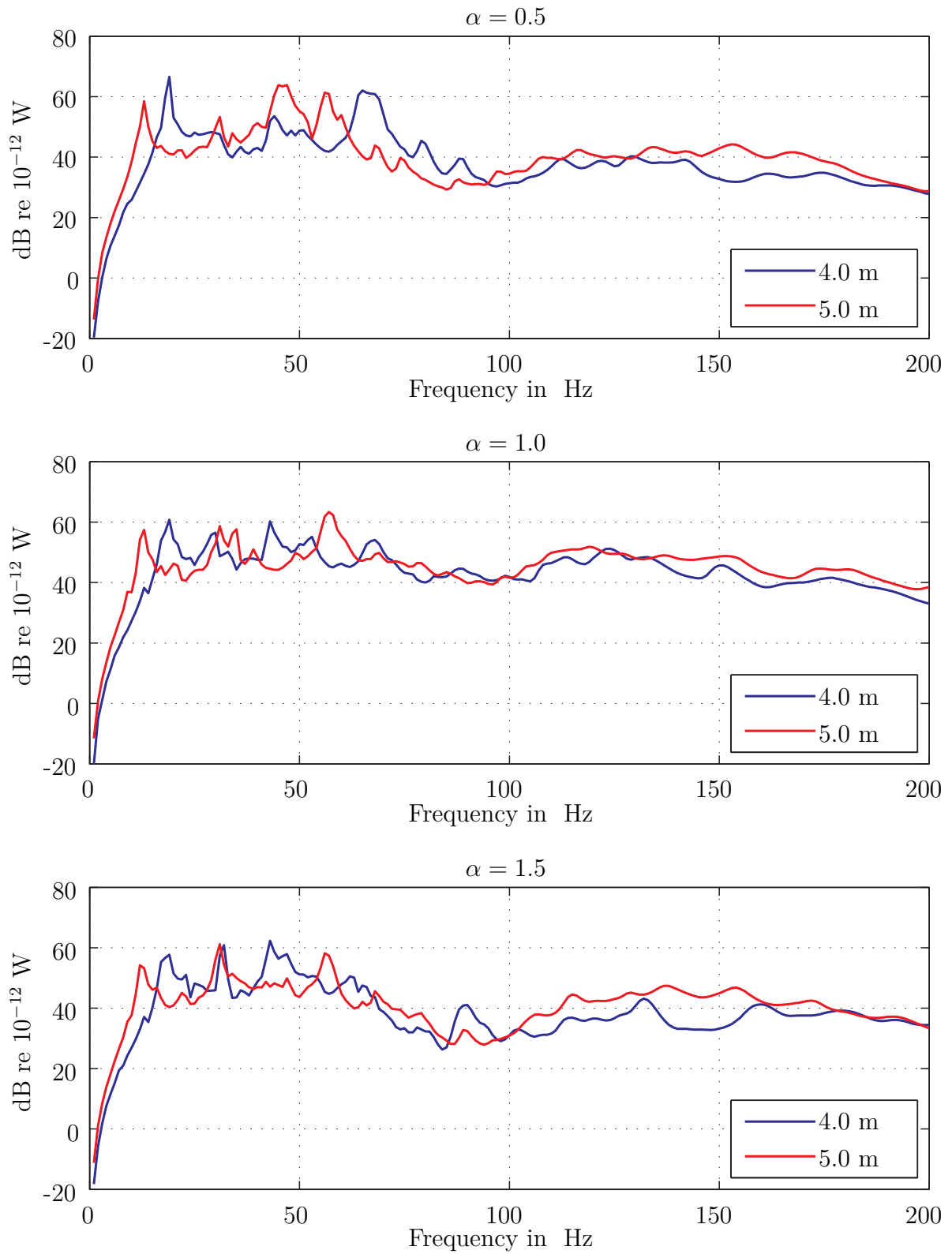
Figure B.59: Sound power level, CLT-R/FLF/SC, Comparing different lengths: $\mu_{\text{wall}} = 10\%$, mean values

B.2.7 Effects of a variation of the distance between the joists and the width of the joists of an LJ floor for varying construction states
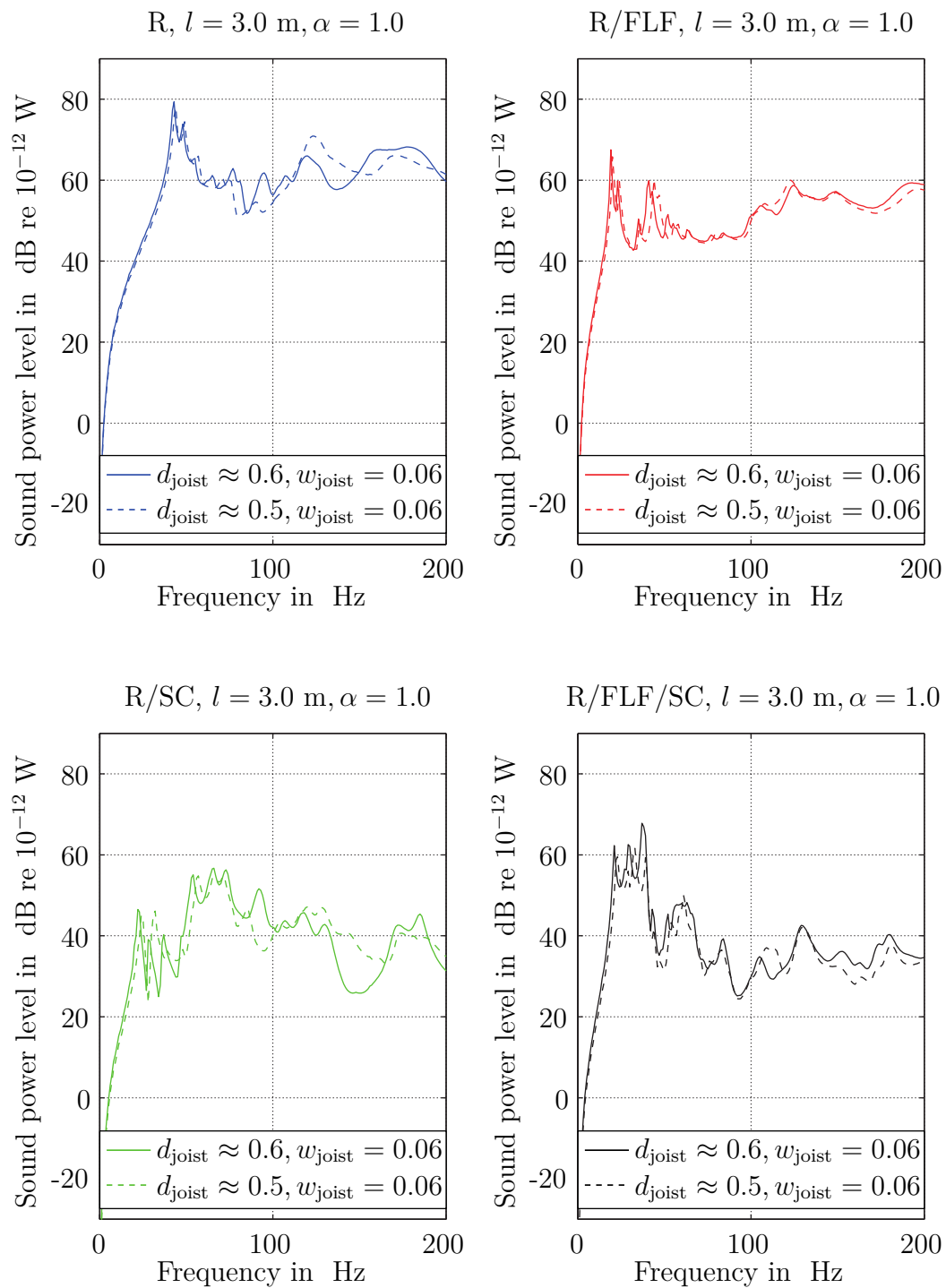
Figure B.60: LJ, Variation of the distance between the joists d_{joist} and the width of the joists w_{joist} in m: $l = 3.0$ m, $\alpha = 1.0$
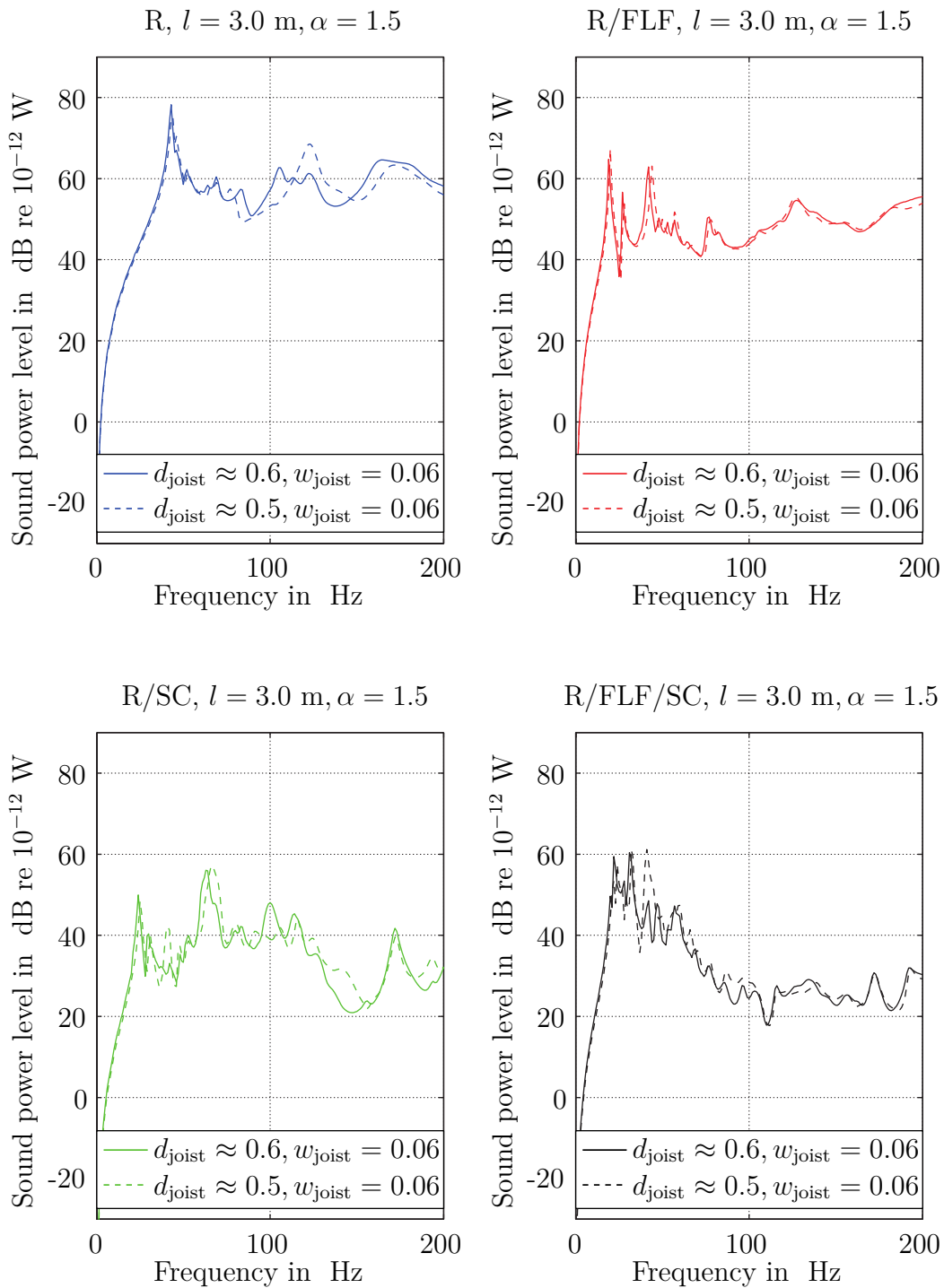
Figure B.61: LJ, Variation of the distance between the joists d_{joist} and the width of the joists w_{joist} in m: $l = 3.0$ m, $\alpha = 1.5$
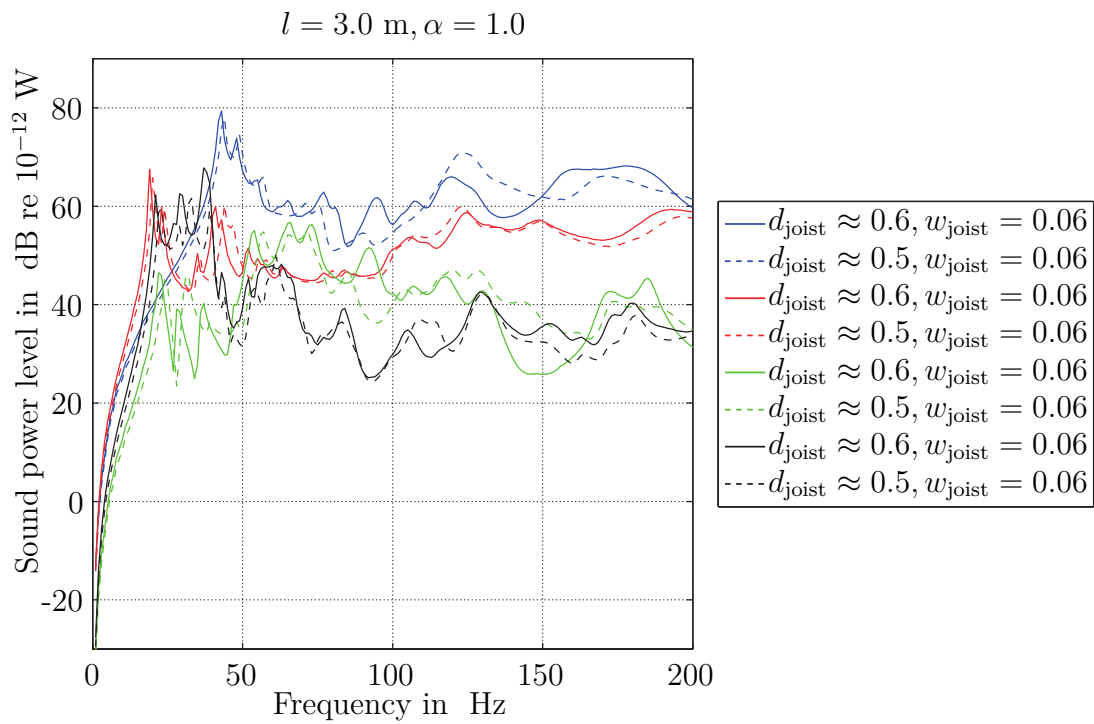
Figure B.62: LJ, Variation of the distance between the joists d_{joist} and the width of the joists w_{joist} in m: $l = 3.0$ m, $\alpha = 1.0$; R(blue), R/FLF(red), R/SC(green), R/FLF/SC(black)
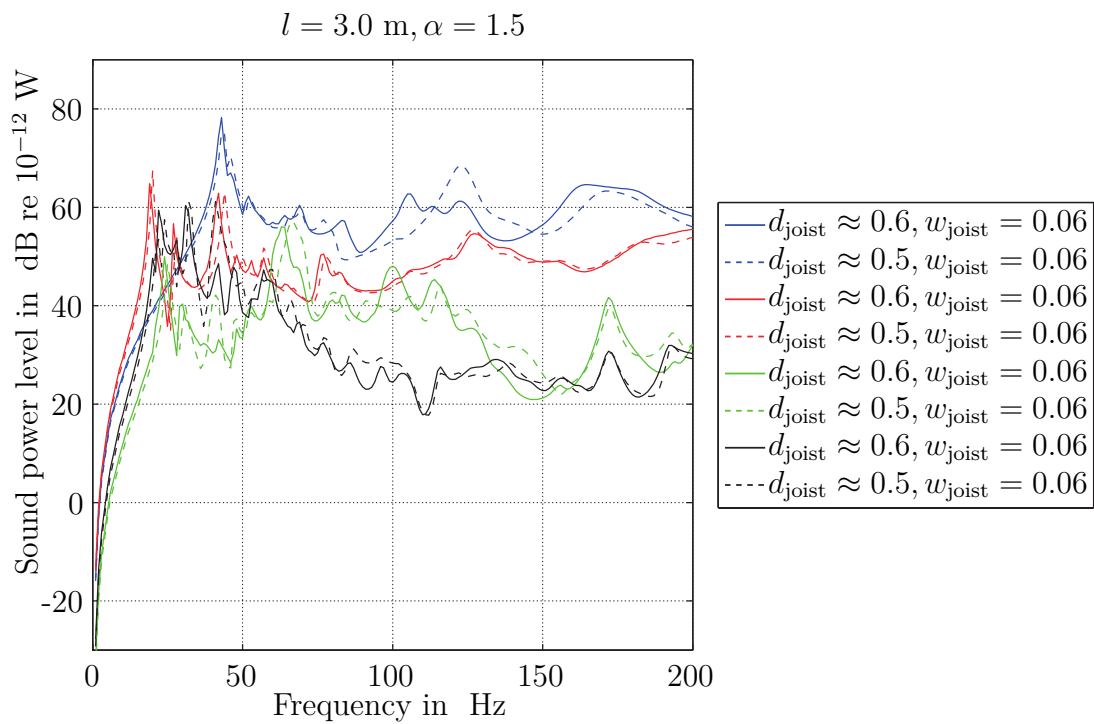

Figure B.63: LJ, Variation of the distance between the joists d_{joist} and the width of the joists w_{joist} in m: $l = 3.0$ m, $\alpha = 1.5$; R(blue), R/FLF(red), R/SC(green), R/FLF/SC(black)
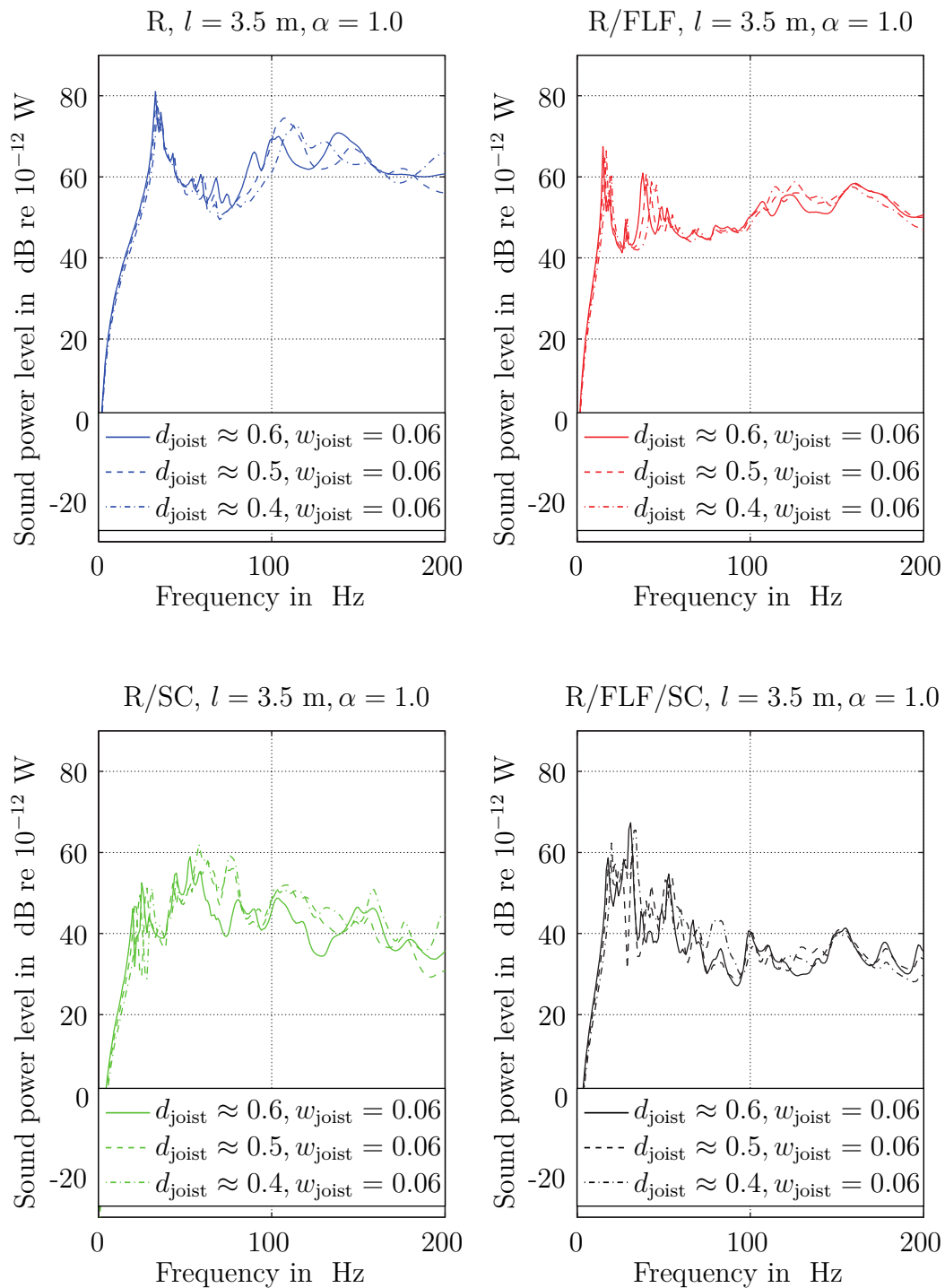
Figure B.64: LJ, Variation of the distance between the joists d_{joist} and the width of the joists w_{joist} in m: $l = 3.5$ m , $\alpha = 1.0$

Figure B.65: LJ, Variation of the distance between the joists d_{joist} and the width of the joists w_{joist} in m: $l = 3.5$ m , $\alpha = 1.5$
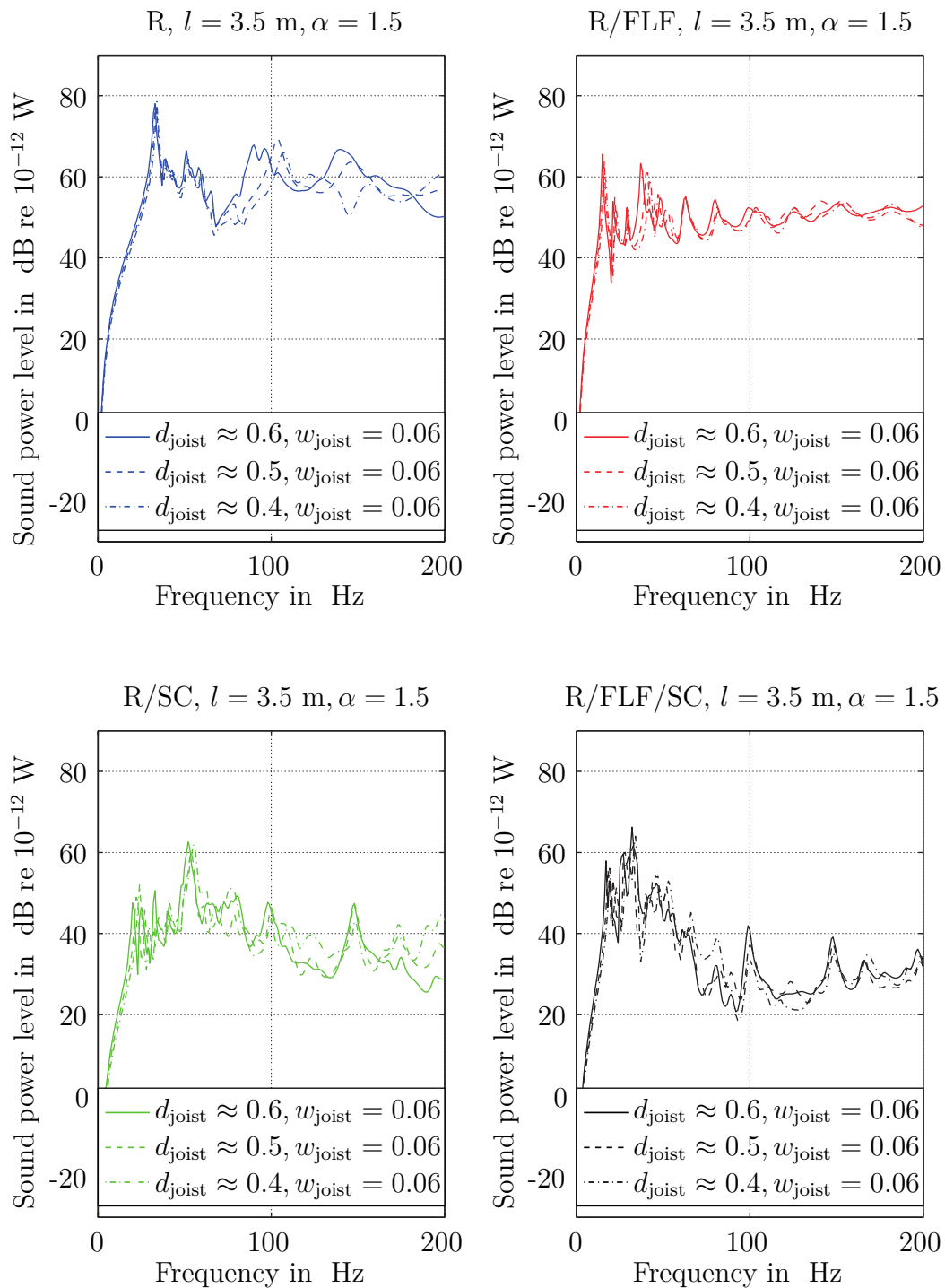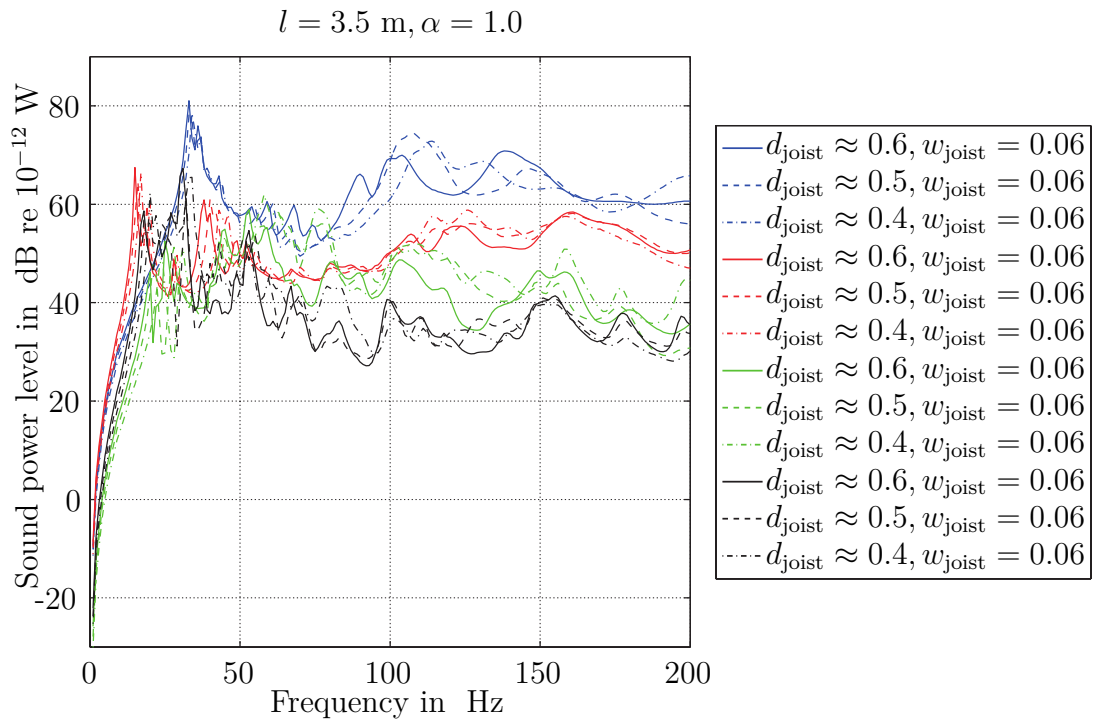
Figure B.66: LJ, Variation of the distance between the joists d_{joist} and the width of the joists w_{joist} in m: $l = 3.5$ m , $\alpha = 1.0$; R(blue), R/FLF(red), R/SC(green), R/FLF/SC(black)

Figure B.67: LJ, Variation of the distance between the joists d_{joist} and the width of the joists w_{joist} in m: $l = 3.5$ m , $\alpha = 1.5$; R(blue), R/FLF(red), R/SC(green), R/FLF/SC(black)

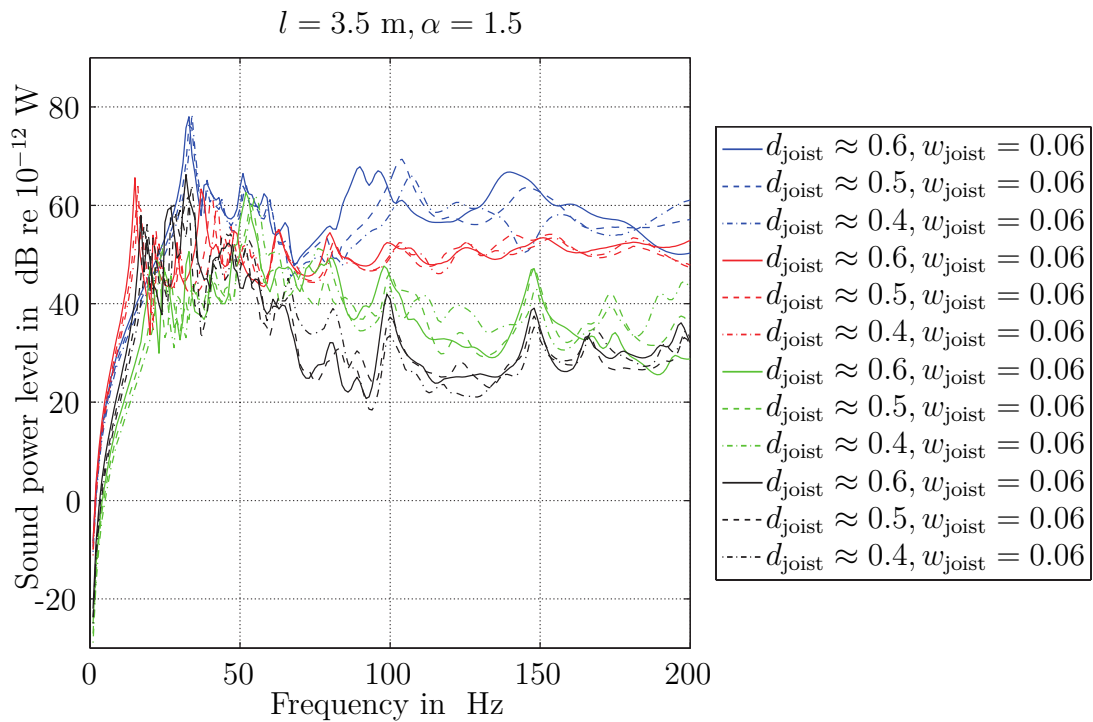**Figure B.68:** LJ, Variation of the distance between the joists d_{joist} and the width of the joists w_{joist} in m: $l = 4.0$ m, $\alpha = 1.0$

R, $l = 4.0$ m, $\alpha = 1.5$

R/FLF, $l = 4.0$ m, $\alpha = 1.5$

R/SC, $l = 4.0$ m, $\alpha = 1.5$

R/FLF/SC, $l = 4.0$ m, $\alpha = 1.5$

Figure B.69: LJ, Variation of the distance between the joists d_{joist} and the width of the joists w_{joist} in m: $l = 4.0$ m, $\alpha = 1.5$

Figure B.70: LJ, Variation of the distance between the joists d_{joist} and the width of the joists w_{joist} in m: $l = 4.0$ m, $\alpha = 1.0$; R(blue), R/FLF(red), R/SC(green), R/FLF/SC(black)
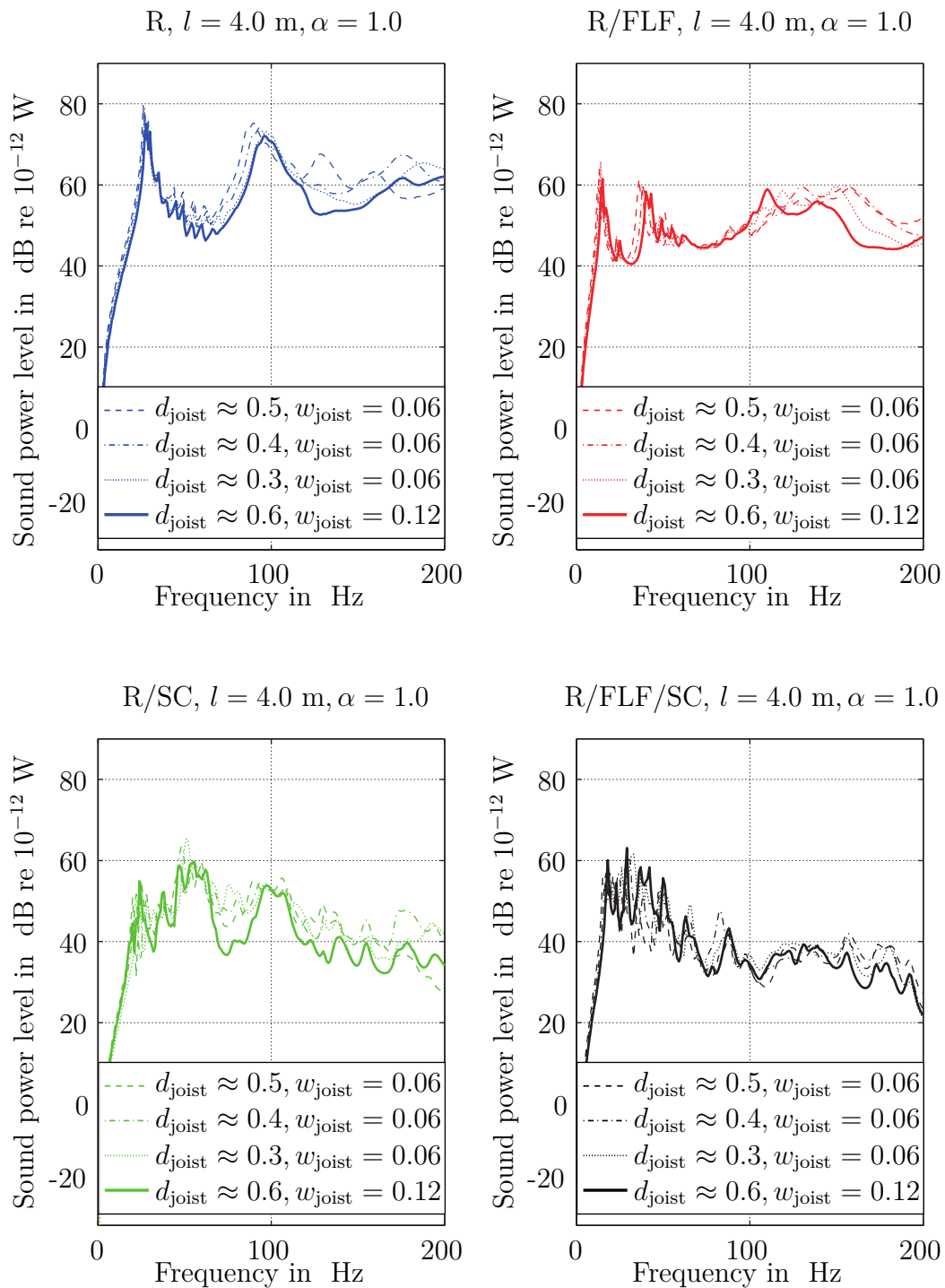

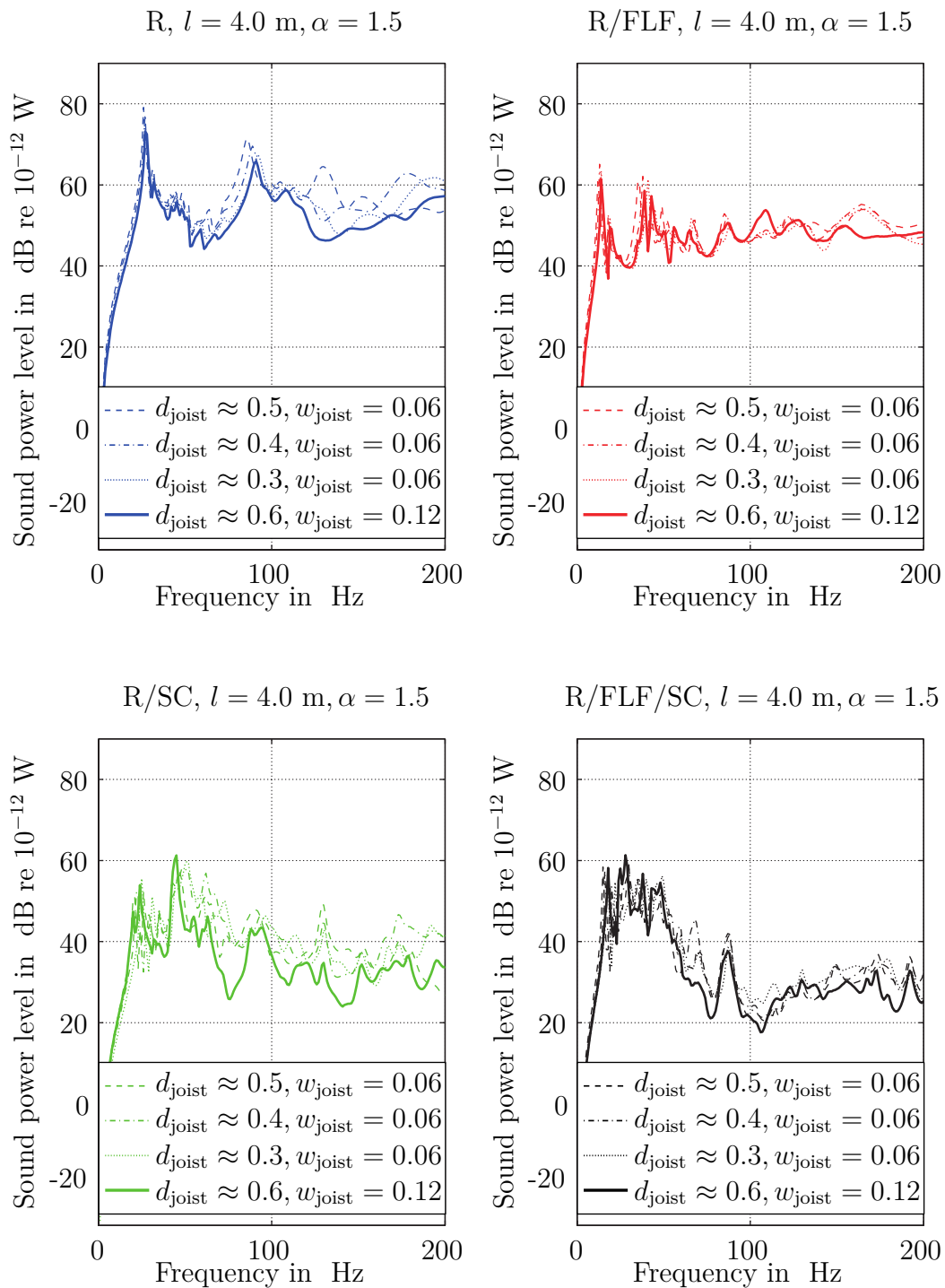**Figure B.71:** LJ, Variation of the distance between the joists d_{joist} and the width of the joists w_{joist} in m: $l = 4.0$ m, $\alpha = 1.5$; R(blue), R/FLF(red), R/SC(green), R/FLF/SC(black)

R, $l = 4.5$ m, $\alpha = 1.0$

R/FLF, $l = 4.5$ m, $\alpha = 1.0$

R/SC, $l = 4.5$ m, $\alpha = 1.0$

R/FLF/SC, $l = 4.5$ m, $\alpha = 1.0$

Figure B.72: LJ, Variation of the distance between the joists d_{joist} and the width of the joists w_{joist} in m: $l = 4.5$ m, $\alpha = 1.0$

Figure B.73: LJ, Variation of the distance between the joists d_{joist} and the width of the joists w_{joist} in m: $l = 4.5$ m, $\alpha = 1.5$
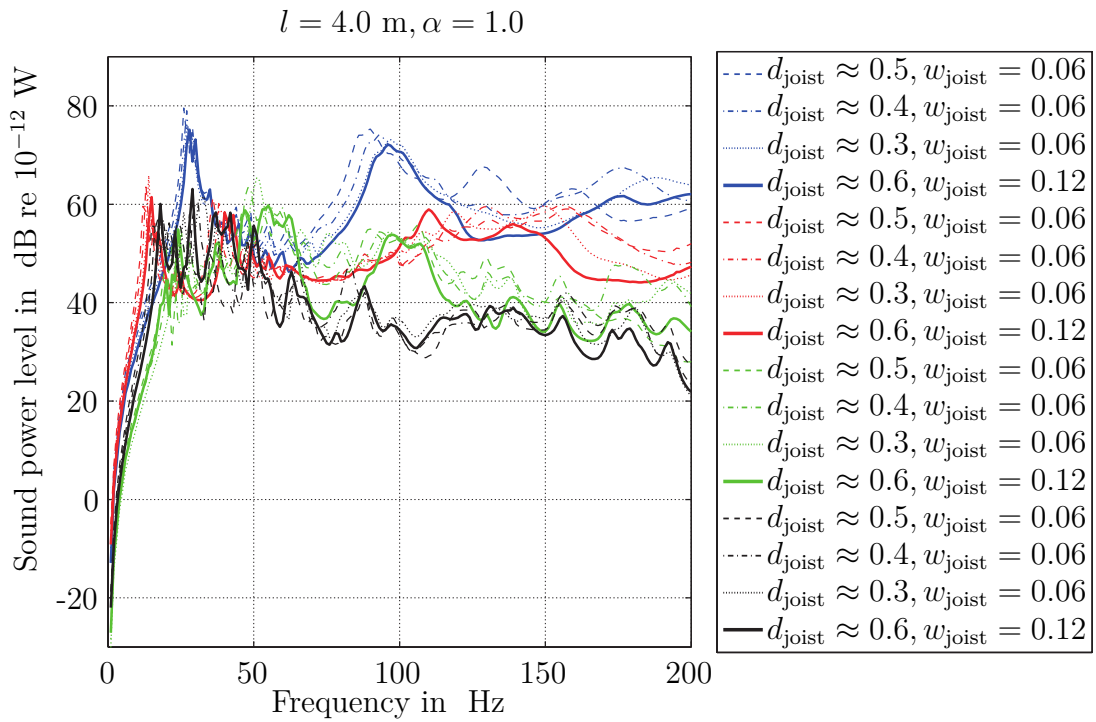
$$l = 4.5 \text{ m}, \alpha = 1.0$$

Figure B.74: LJ, Variation of the distance between the joists d_{joist} and the width of the joists w_{joist} in m: $l = 4.5$ m, $\alpha = 1.0$; R(blue), R/FLF(red), R/SC(green), R/FLF/SC(black)
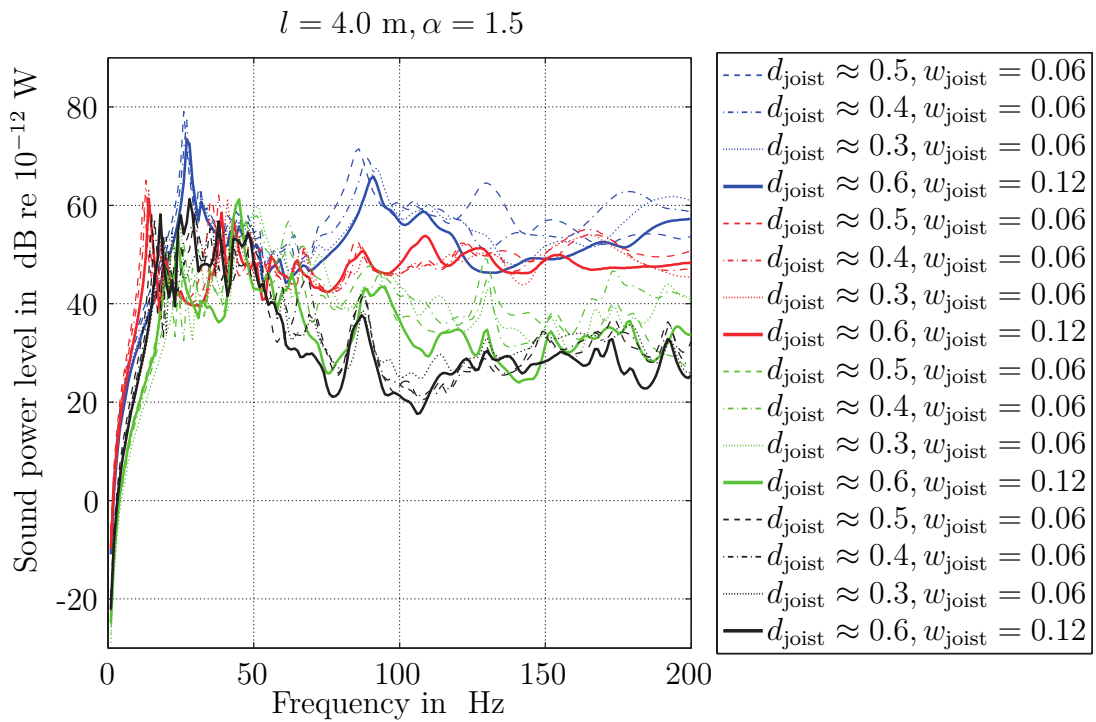
$$l = 4.5 \text{ m}, \alpha = 1.5$$

Figure B.75: LJ, Variation of the distance between the joists d_{joist} and the width of the joists w_{joist} in m: $l = 4.5$ m, $\alpha = 1.5$; R(blue), R/FLF(red), R/SC(green), R/FLF/SC(black)
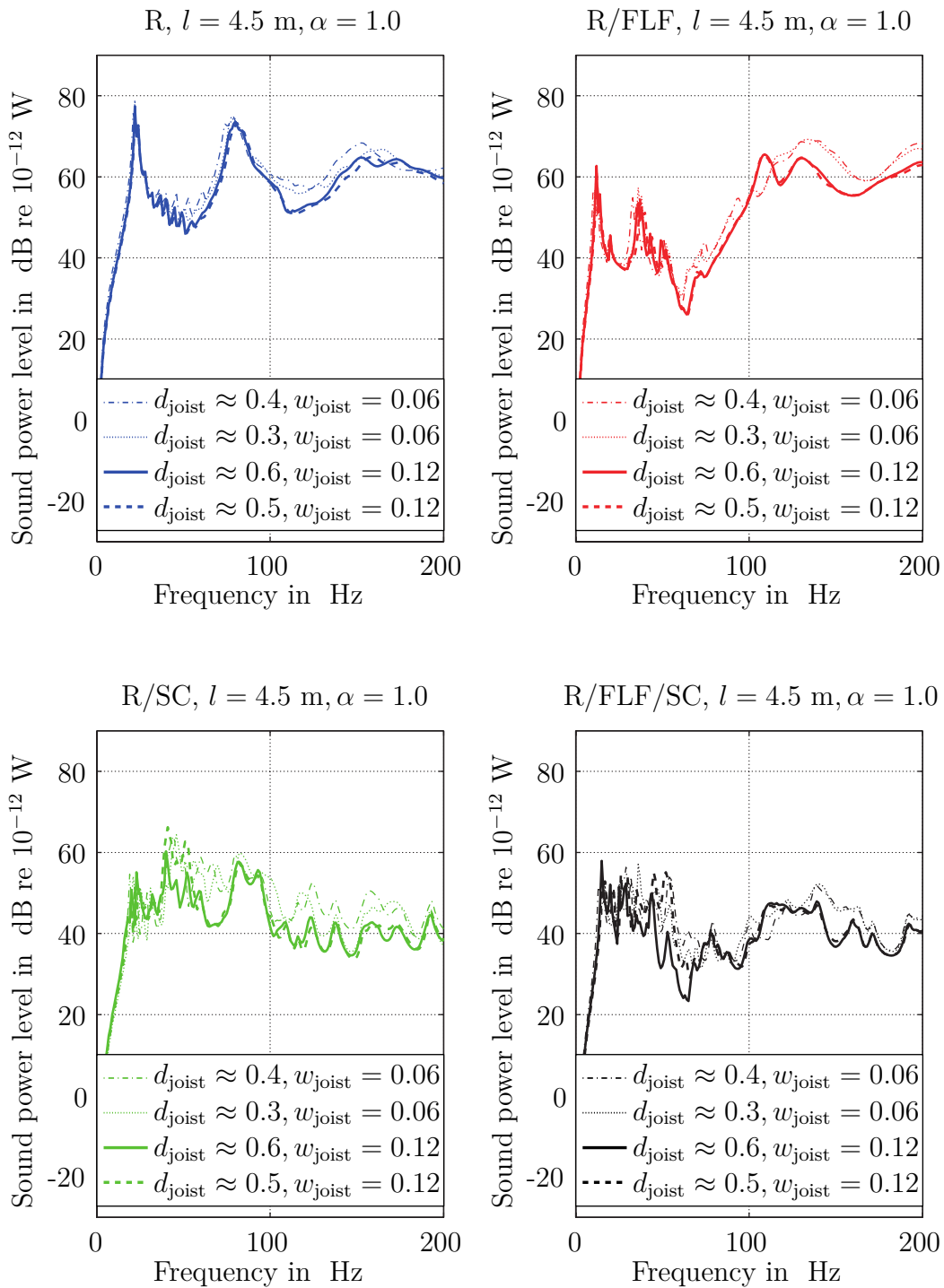
Figure B.76: LJ, Variation of the distance between the joists d_{joist} and the width of the joists w_{joist} in m: $l = 5.0$ m, $\alpha = 1.0$
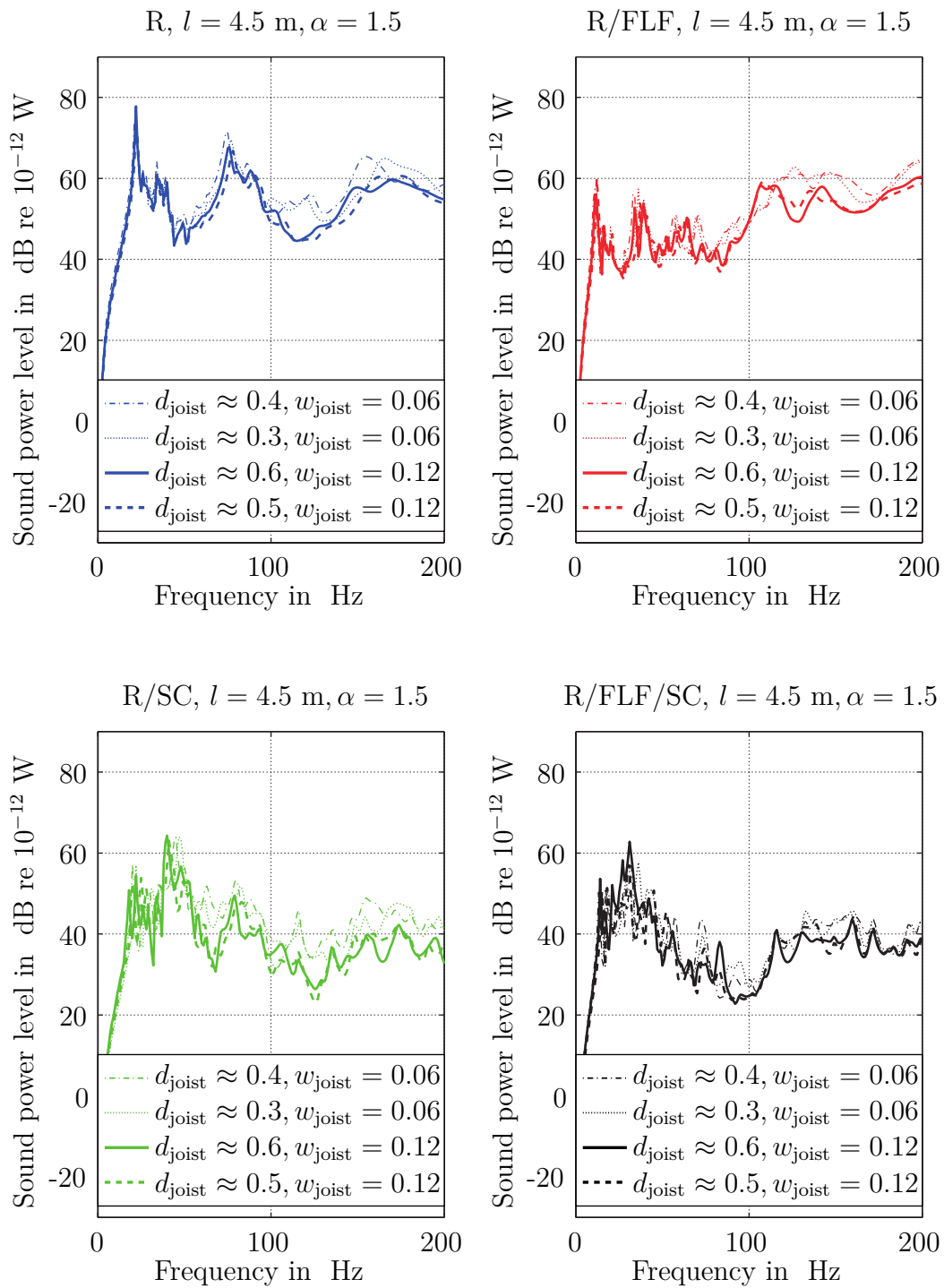
Figure B.77: LJ, Variation of the distance between the joists d_{joist} and the width of the joists w_{joist} in m: $l = 5.0$ m, $\alpha = 1.5$

$$l = 5.0 \text{ m}, \alpha = 1.0$$

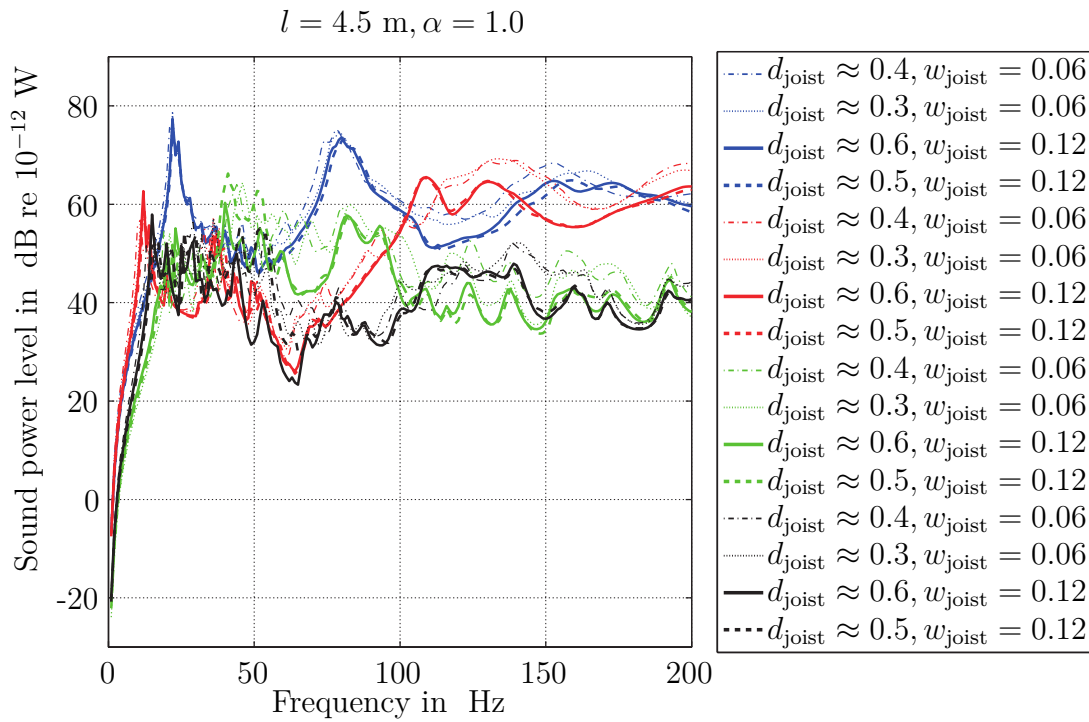**Figure B.78:** LJ, Variation of the distance between the joists d_{joist} and the width of the joists w_{joist} in m: $l = 5.0$ m, $\alpha = 1.0$; R(blue), R/FLF(red), R/SC(green), R/FLF/SC(black)

$$l = 5.0 \text{ m}, \alpha = 1.5$$

Figure B.79: LJ, Variation of the distance between the joists d_{joist} and the width of the joists w_{joist} in m: $l = 5.0$ m, $\alpha = 1.5$; R(blue), R/FLF(red), R/SC(green), R/FLF/SC(black)
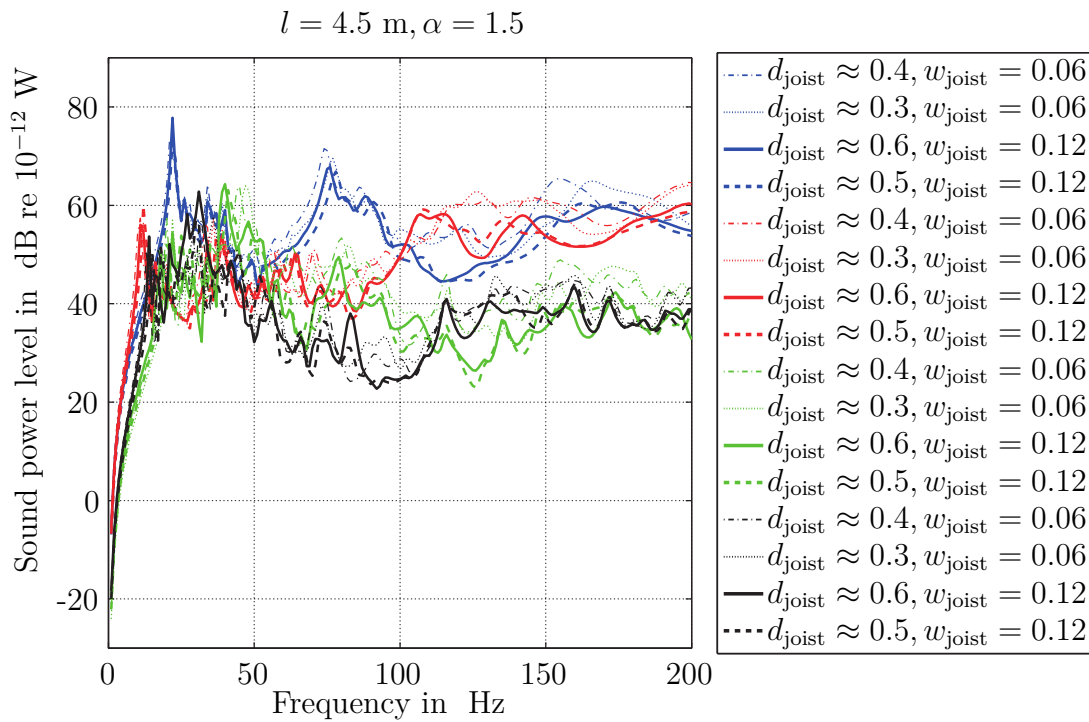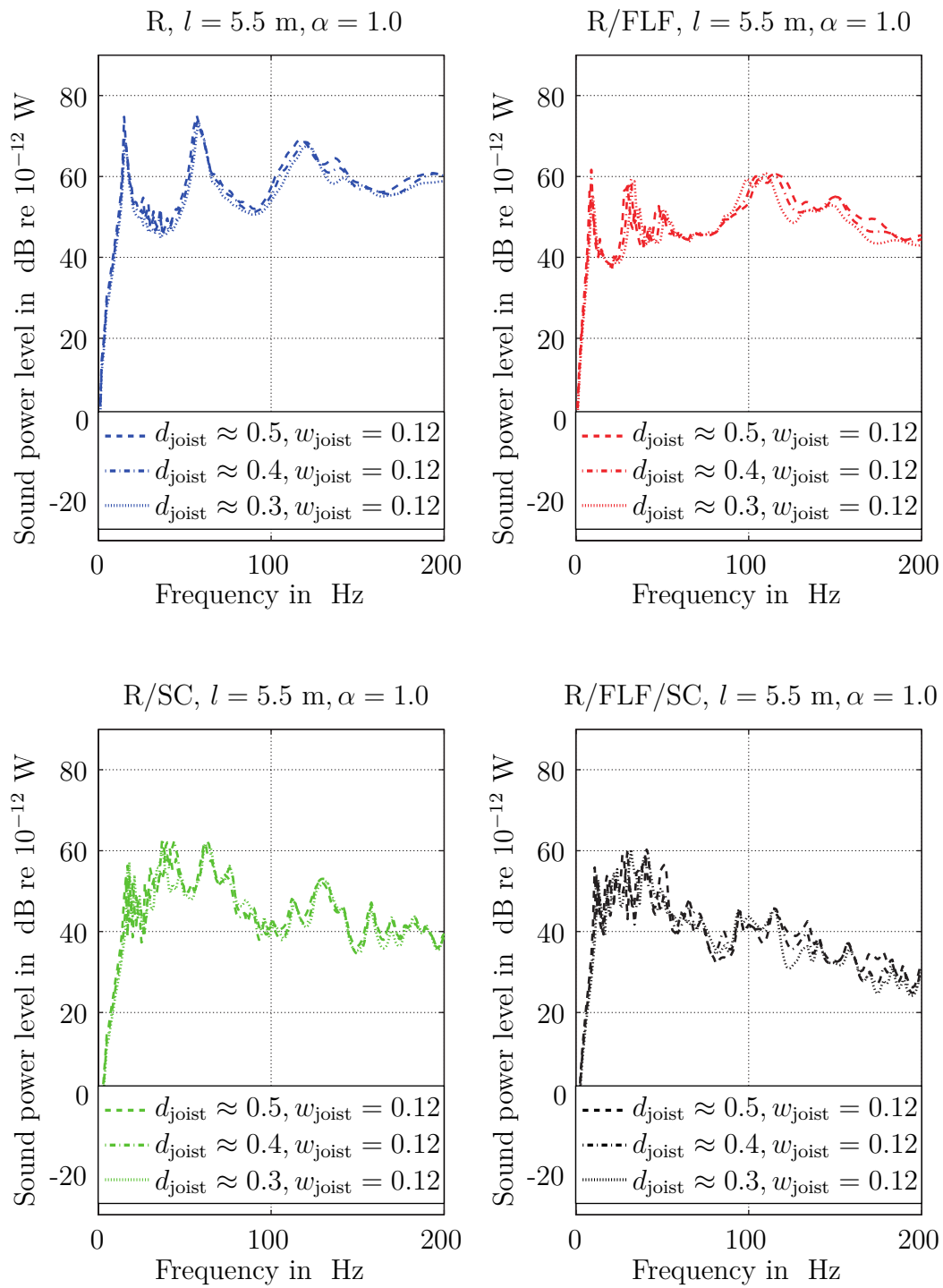
Figure B.80: LJ, Variation of the distance between the joists d_{joist} and the width of the joists w_{joist} in m: $l = 5.5$ m, $\alpha = 1.0$
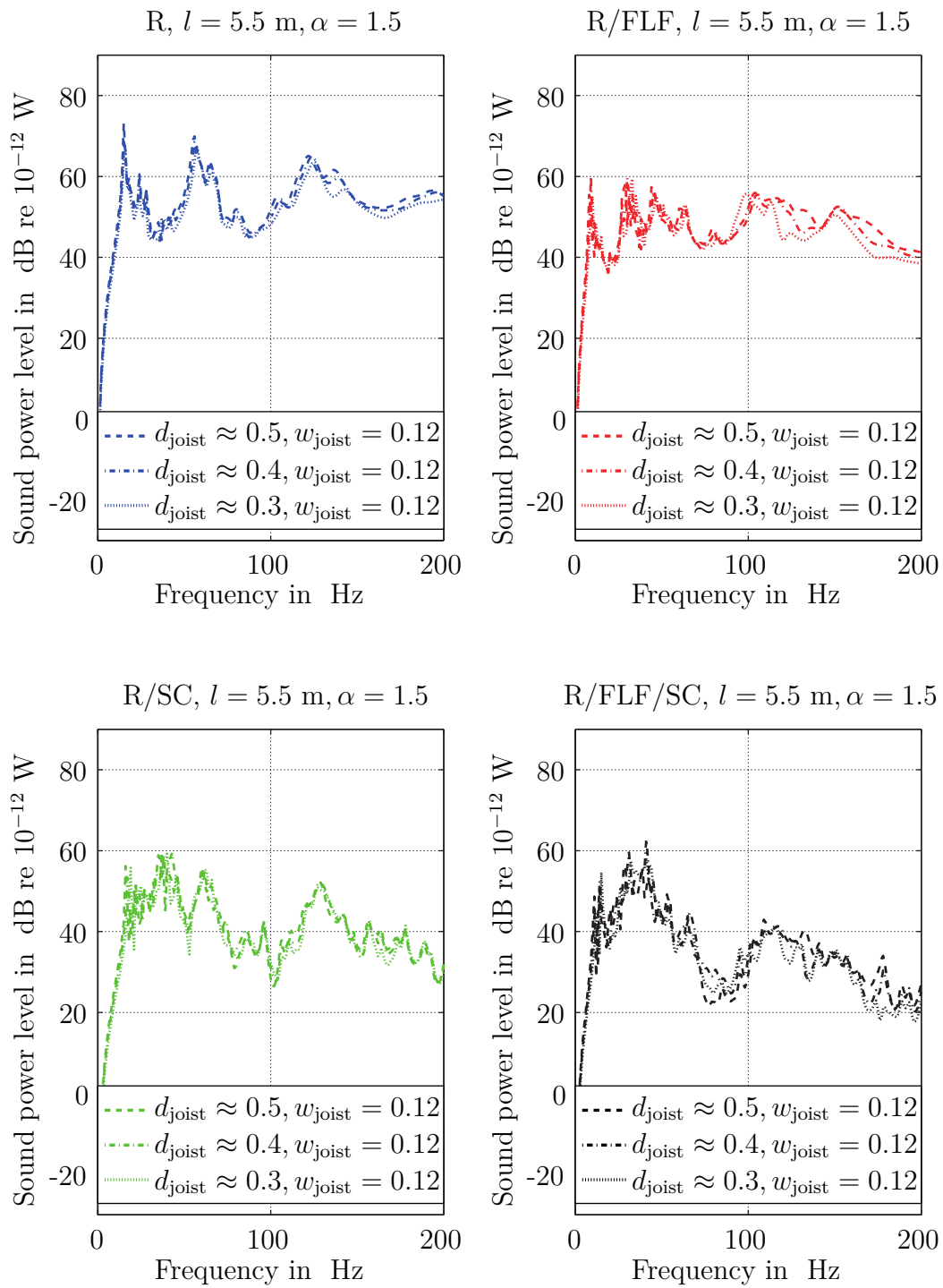
Figure B.81: LJ, Variation of the distance between the joists d_{joist} and the width of the joists w_{joist} in m: $l = 5.5$ m, $\alpha = 1.5$
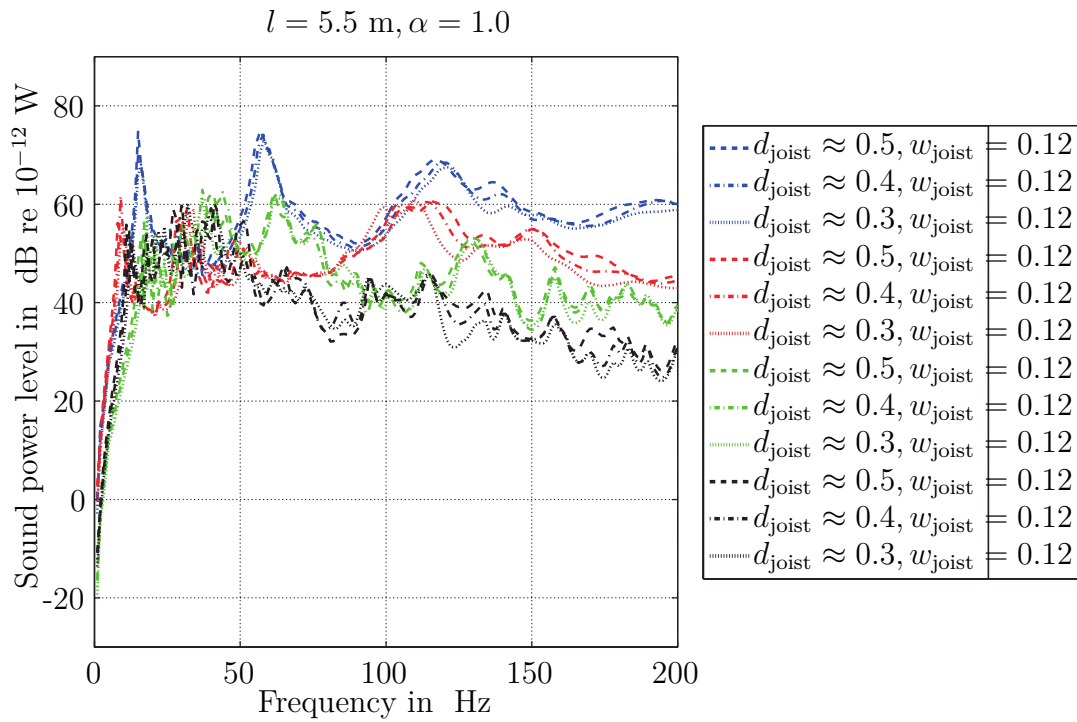
$$l = 5.5 \text{ m}, \alpha = 1.0$$

Figure B.82: LJ, Variation of the distance between the joists d_{joist} and the width of the joists w_{joist} in m: $l = 5.5$ m, $\alpha = 1.0$; R(blue), R/FLF(red), R/SC(green), R/FLF/SC(black)
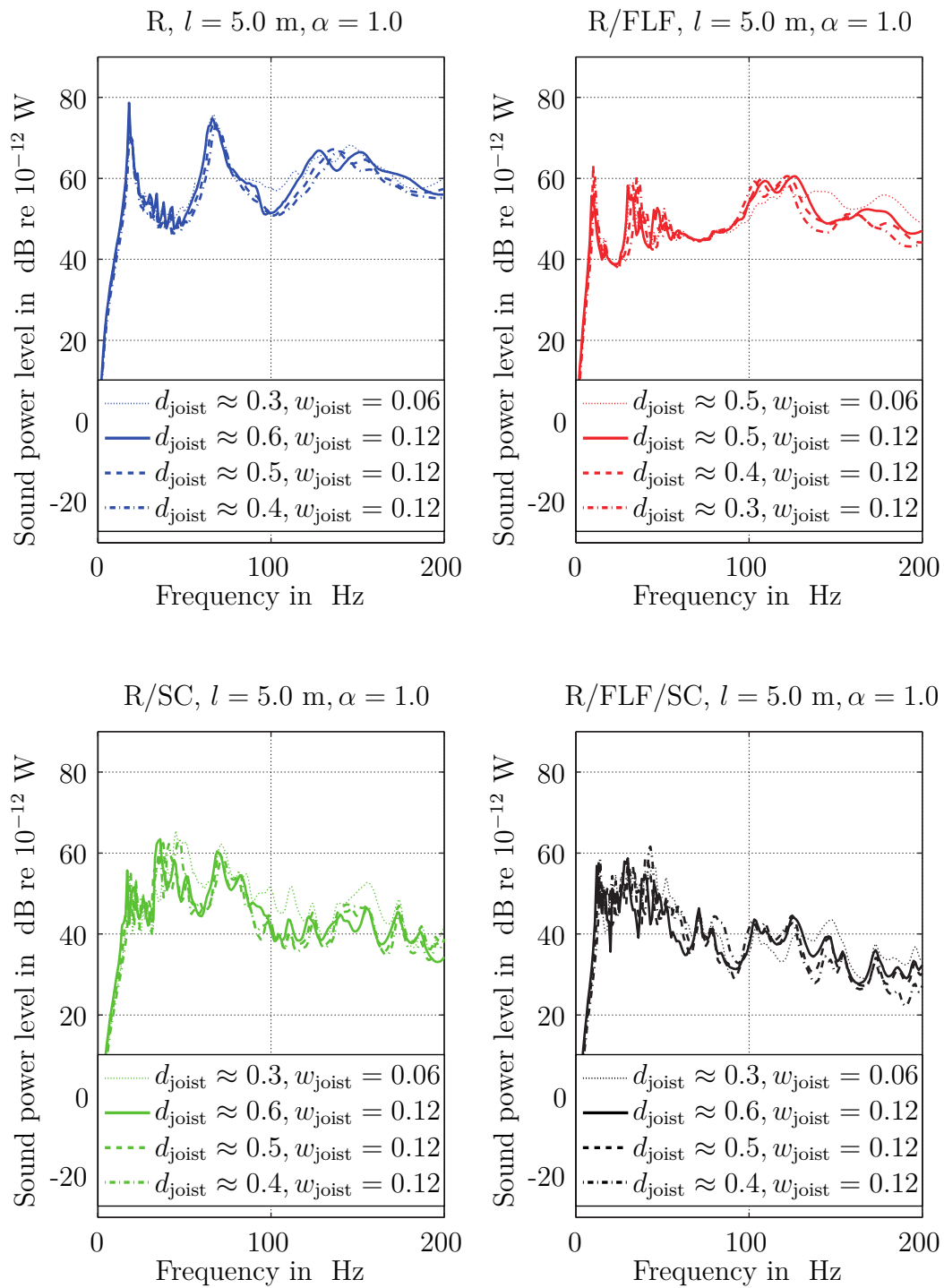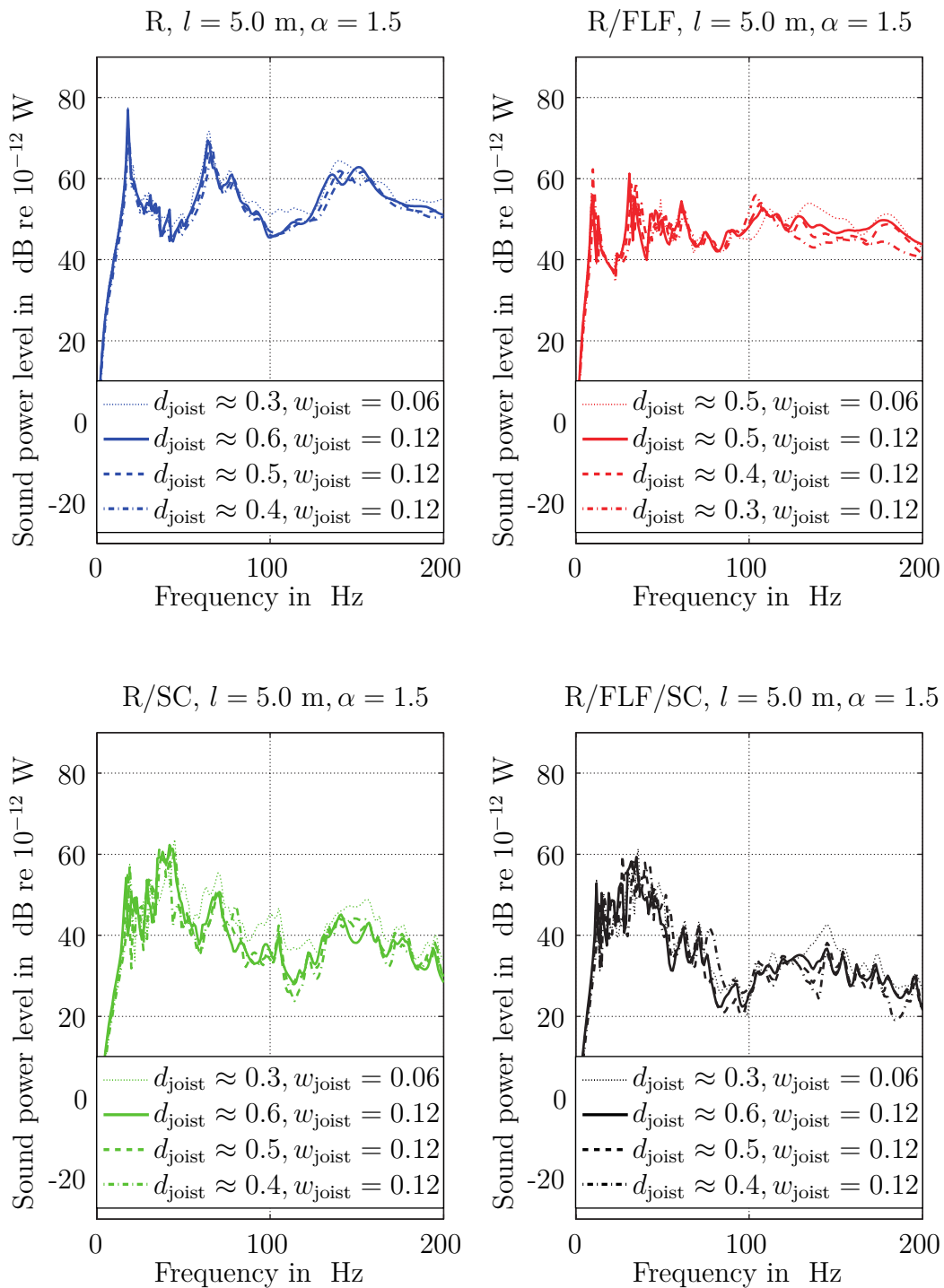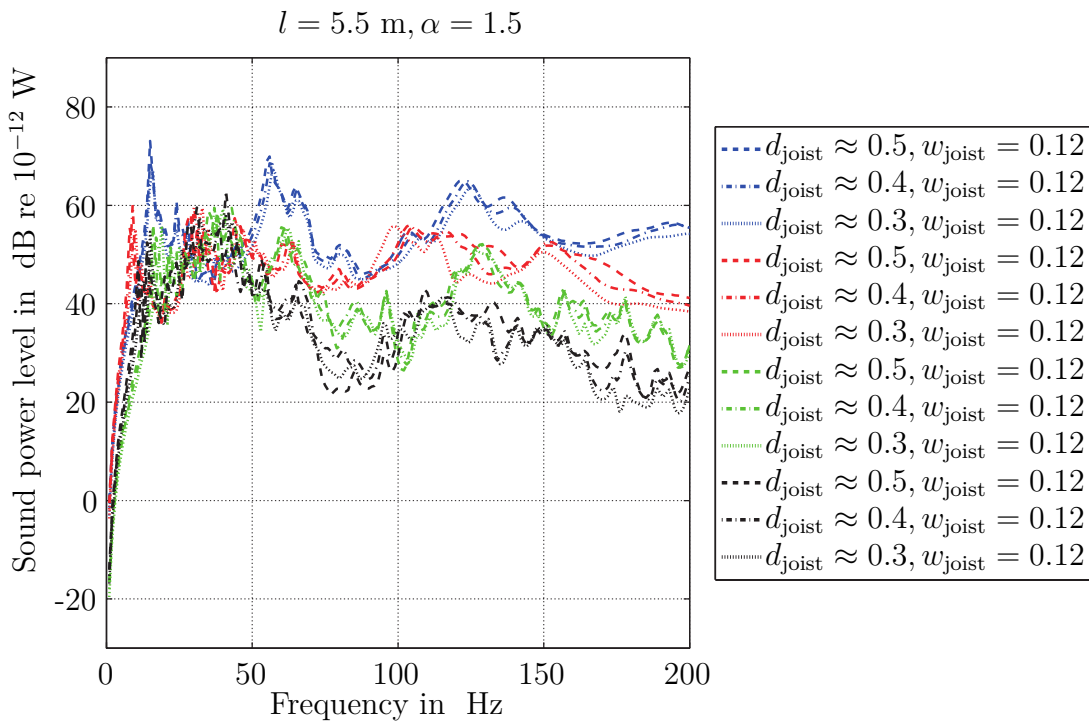
$$l = 5.5 \text{ m}, \alpha = 1.5$$

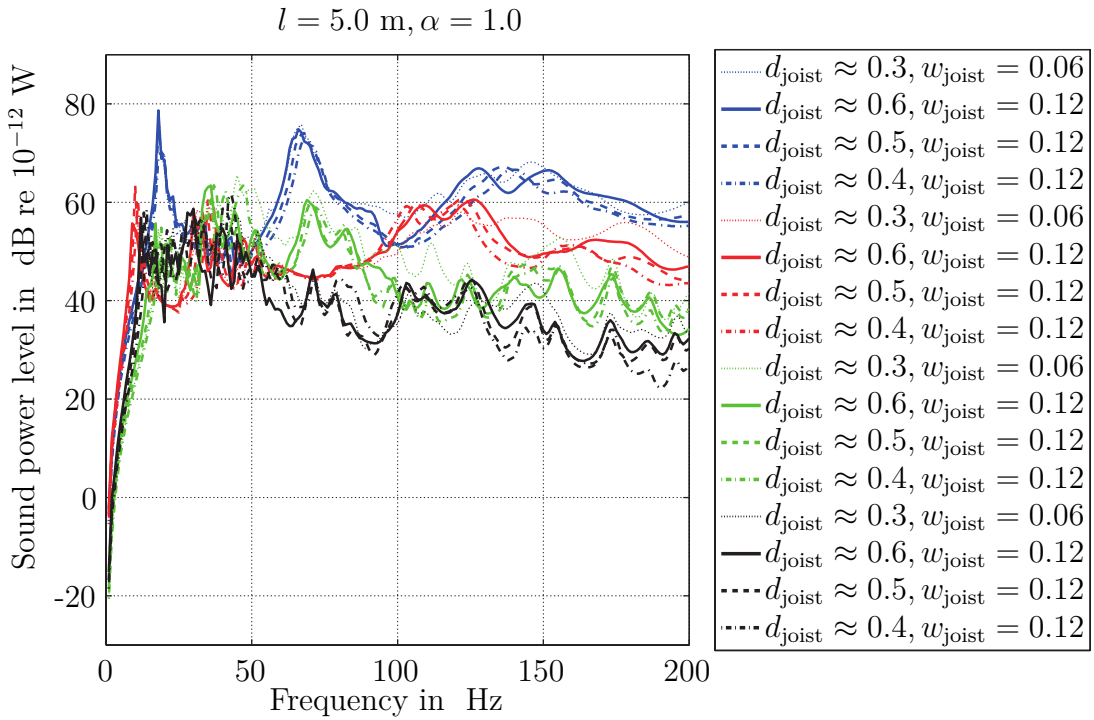**Figure B.83:** LJ, Variation of the distance between the joists d_{joist} and the width of the joists w_{joist} in m: $l = 5.5$ m, $\alpha = 1.5$; R(blue), R/FLF(red), R/SC(green), R/FLF/SC(black)
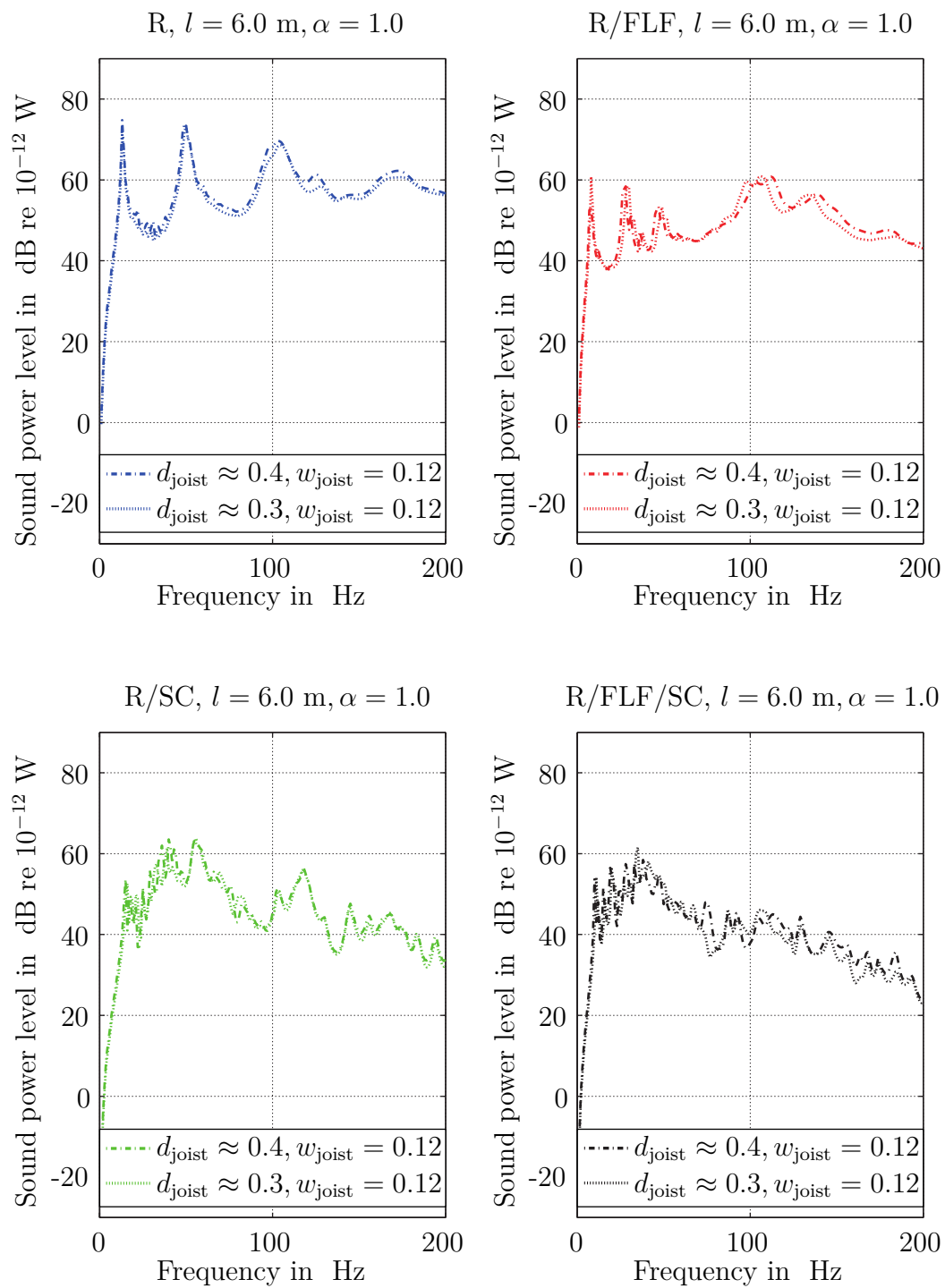
Figure B.84: LJ, Variation of the distance between the joists d_{joist} and the width of the joists w_{joist} in m: $l = 6.0$ m, $\alpha = 1.0$
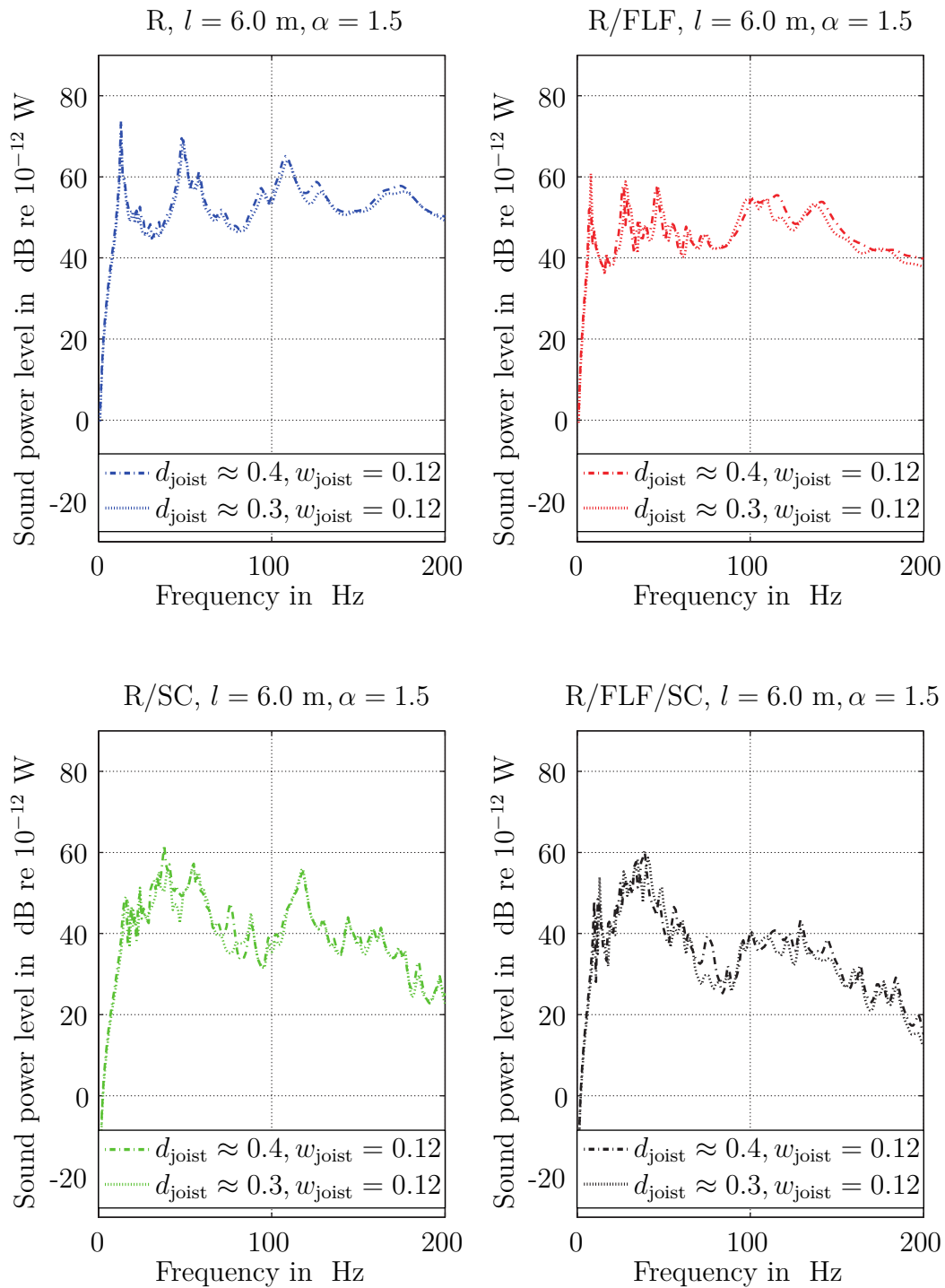
Figure B.85: LJ, Variation of the distance between the joists d_{joist} and the width of the joists w_{joist} in m: $l = 6.0$ m, $\alpha = 1.5$

$l = 6.0$ m, $\alpha = 1.0$

Figure B.86: LJ, Variation of the distance between the joists d_{joist} and the width of the joists w_{joist} in m: $l = 6.0$ m, $\alpha = 1.0$; R(blue), R/FLF(red), R/SC(green), R/FLF/SC(black)
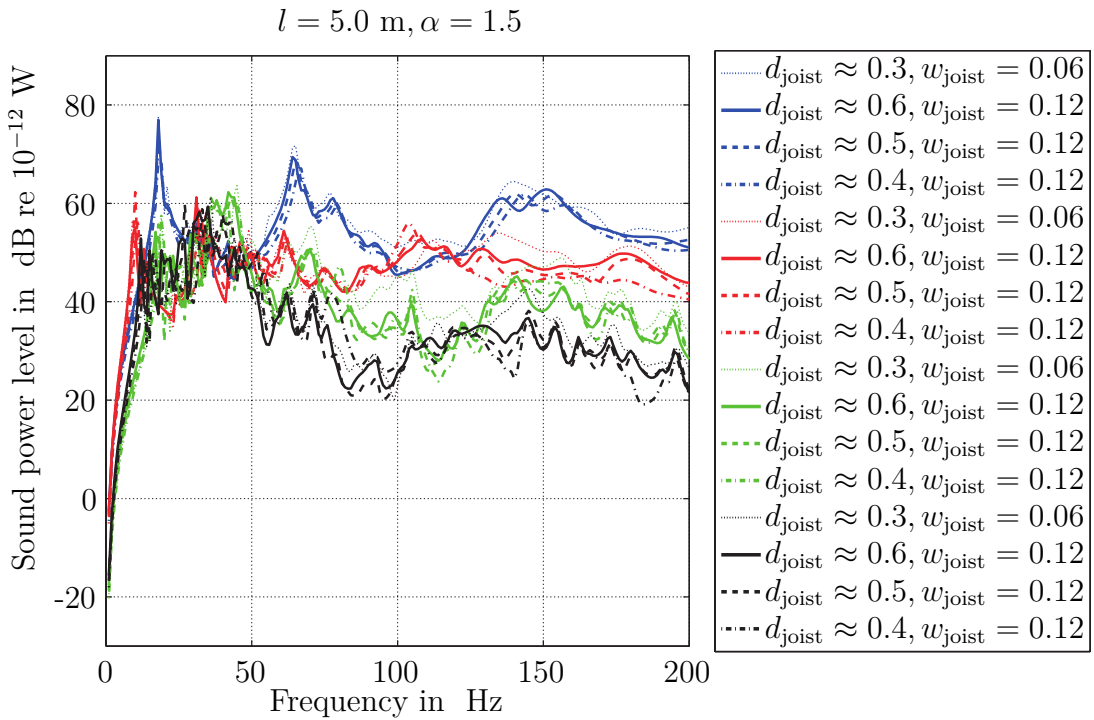
$l = 6.0$ m, $\alpha = 1.5$

Figure B.87: LJ, Variation of the distance between the joists d_{joist} and the width of the joists w_{joist} in m: $l = 6.0$ m, $\alpha = 1.5$; R(blue), R/FLF(red), R/SC(green), R/FLF/SC(black)

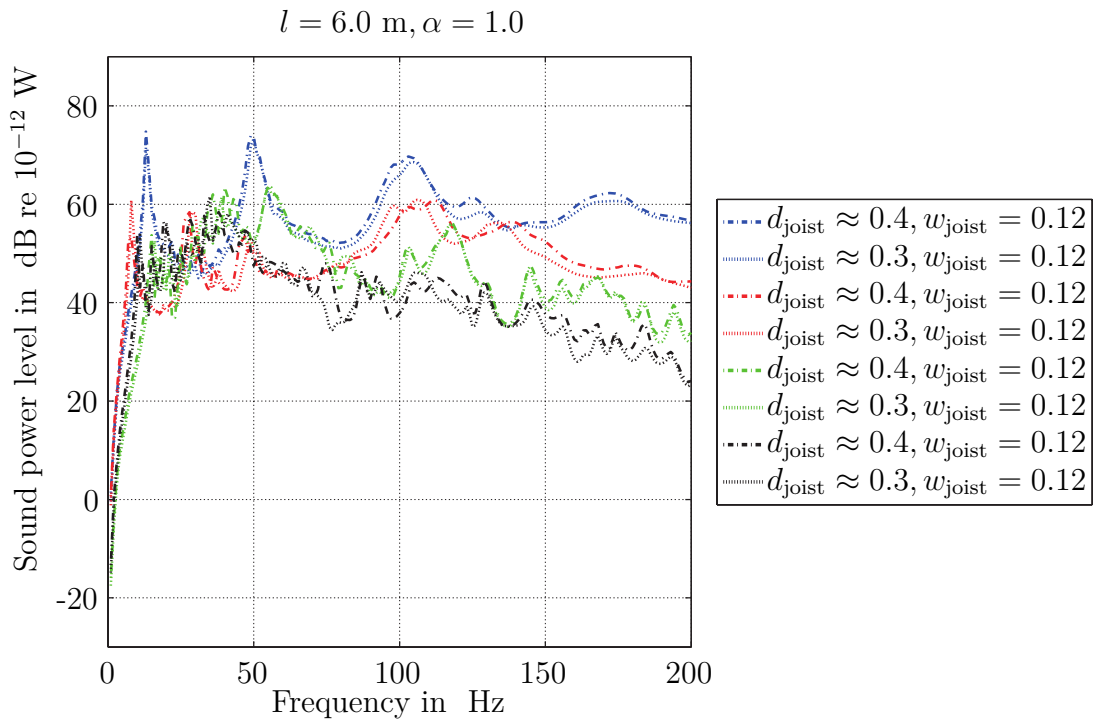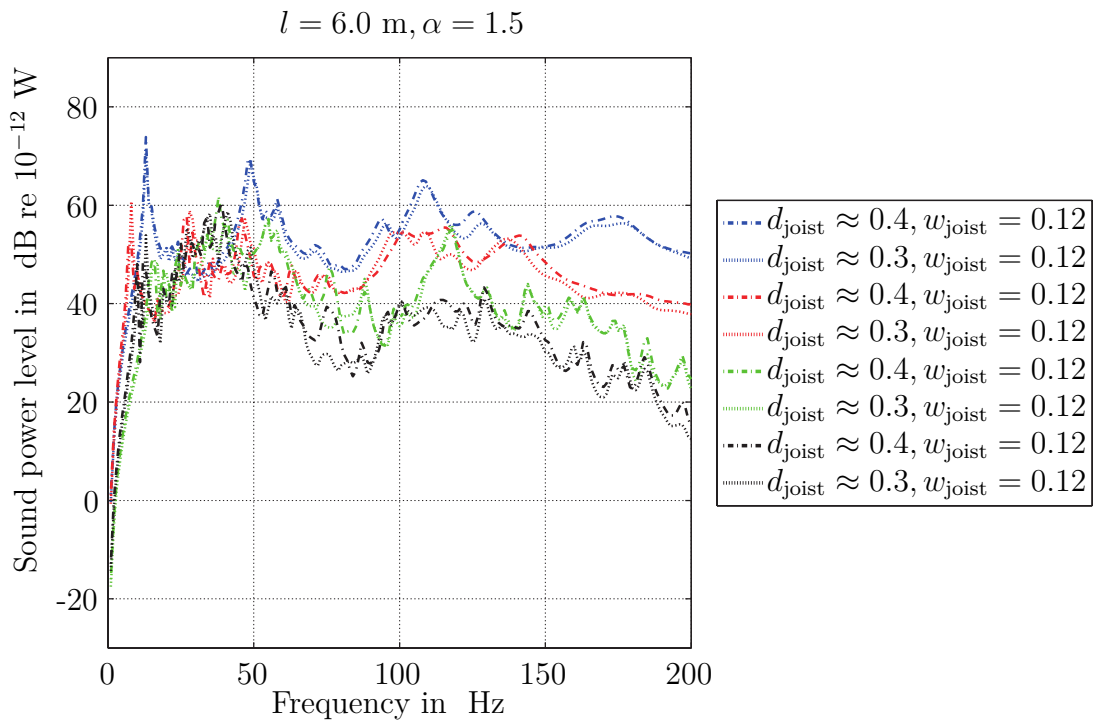# Bibliography

[Aicher and Dill-Langer 2000] AICHER, S. ; DILL-LANGER, G.: Basic consideration to rolling shear madulus in wooden boards. In: *Otto-Graf-Journal* 11 (2000), p. 157–166

[Allemang 2003] ALLEMANG, R. J.: The Modal Assurance Criterion - Twenty Years of Use and Abuse. In: *Sound and Vibration* (2003), August, p. 14 – 21

[Allert 2014] ALLERT, B.: *Simulation von Bremsenquietschen: Ein Beitrag zur Prognosegüte*, Technische Universität München, Ph.D. thesis, 2014

[Andersen et al 2012] ANDERSEN, L. V. ; KIRGKEGAARD, P. H. ; DICKOW, N. ; PERSSON, K.: Influence of wall surface and air modelling in finite-element analysis of sound transmission between rooms in lightweight buildings. In: *Internoise*, 2012

[Angerer 2011] ANGERER, Ludwig: *Berechnung des akustischen Abstrahlverhaltens von Verbunddeckensystemen mit abgehängter Decke*, Technische Universität München, Master's thesis, 2011

[ANSYS, Inc. 2013] ANSYS, INC.: ANSYS Mechanical APDL Element Reference. 2013. – Documentation

[Bakre and Jangid 2007] BAKRE, S. V. ; JANGID, R. S.: Optimum parameters of tuned mass damper for damped main system. In: *Structural control and health monitoring* 14 (2007), p. 448–470

[Bangert 2000] BANGERT, F.: *Schallleistungsberechnung und Schallquellenlokalisierung anhand von Schallintensitätsmessungen*, Fachhochschule Düsseldorf, Diplomarbeit, 2000

[Bathe 2002] BATHE, K. J.: *Finite-Elemente-Methoden.* Springer Verlag, 2002

[Beerends et al 2003] BEERENDS, R. J. ; TER MORSCHE, H. G. ; GERG, J. C. Van der ; VRIE, E. M. Van der: *Fourier and Laplace Transforms.* Cambridge University Press, 2003

[Blaß and Flaig 2012] BLASS, H. J. ; FLAIG, M.: *Karlsruher Berichte zum Ingenieurholzbau.* Volume 24: *Stabförmige Bauteile aus Brettsperrholz.* Karsruhe : KIT Scientific Publishing, 2012

[Bogensperger et al 2010] BOGENSPERGER, T. ; FITZ, M. ; HAMM, P. ; SCHICKHOFER, G.: Untersuchung des Schwingungsverhaltens von Deckensystemen aus Brettsperrholz (BSP). In: *Bauingenieur* 85 (2010), Nr. 1, p. 45–52

[Borch 2013]   BORCH, F.: Analysis of Eigen Frequencies and Mode Shapes for Wooden Structured Floors - Vibration technical investigation / Technische Universität München. 2013. – Research report

[Brüel & Kjaer 1993]   BRÜEL & KJAER: *Schallintensität*. Brüel & Kjaer, 1993

[Bridgman 1922]   BRIDGMAN, P. W.: *Dimensional Analysis*. Yale University Press, 1922

[Brigham 1974]   BRIGHAM, E. O.: *The fast fourier Transform*. Springer-Hall, Inc., 1974

[Brunskog and Hammer 2002]   BRUNSKOG, J. ; HAMMER, P.: Measurement of the acoustic properties of resilient, statically tensile loaded devices in lightweight structures. In: *Building Acoustics* 9 (2002), Nr. 2, p. 99–137

[Buckingham 1914]   BUCKINGHAM, E.: On physically similar systems; illustrations of the use of dimensional equation. In: *Physical Review* 4 (1914), Nr. 4, p. 345–376

[Butz 2006]   BUTZ, E.C.: *Beitrag zur Berechnung fußgängerinduzierter Brückenschwingungen*, Rheinisch-Westfälische Technische Hochschule Aachen, Ph.D. thesis, 2006

[Chaves 2013]   CHAVES, E. W. V.: *Notes on Continuum Mechanics*. Springer Verlag, 2013

[Churchill and Hopkins 2013a]   CHURCHILL, C. ; HOPKINS, C.: Development of SEA models of composite heavyweight-lightweight floors by incorporating measured stiffness data for suspended ceiling hangers. In: *Internoise*, 2013

[Churchill and Hopkins 2013b]   CHURCHILL, C. ; HOPKINS, C.: Prediction of dynamic properties of a cross lamlamina timber plate from an investigation of the eigenmodes using a scanning laser vibrometer. In: *AIA-DAGA*, 2013

[Churchill et al 2011]   CHURCHILL, C. ; HOPKINS, C. ; KRAJCI, L.: Modelling airborne sound transmission across a hybrid heavyweight-lightweight floor using Statistical Energy Analysis. In: *Forum Acusticum*, 2011

[Cremer et al 2005]   CREMER, L. ; HECKL, M. ; PETERSSON, B.A.T.: *Structure Borne Sound*. 3. Springer Verlag, 2005

[Den Hartog 1952]   DEN HARTOG, J.P.: *Mechanische Schwingungen*. Springer Verlag, 1952

[DIN 12369-1:2001-04]   DIN 12369-1:2001-04: *Holzwerkstoffe - Charakteristische Werte für die Berechnung und Bemessung von Holzbauwerken - Teil 1: OSB, Spanplatten und Faserplatten*. Beuth Verlag GmbH

[DIN 4109-1:2016-07]   DIN 4109-1:2016-07: *Schallschutz im Hochbau - Teil 1: Mindestanforderungen*. Beuth Verlag GmbH

[DIN 4109-33:2016-07]   DIN 4109-33:2016-07: *Schallschutz im Hochbau - Teil 33: Daten für die rechnerischen Nachweise des Schallschutzes (Bauteilkatalog) - Holz-, Leicht- und Trockenbau*. Beuth Verlag GmbH

[DIN 4109-34:2016-07]   DIN 4109-34:2016-07: *Schallschutz im Hochbau - Teil 34: Daten für die rechnerischen Nachweise des Schallschutzes (Bauteilkatalog) - Vorsatzkonstruktionen vor massiven Bauteilen.* Beuth Verlag GmbH

[DIN 4150-2:1999-06]   DIN 4150-2:1999-06: *Erschütterungen im Bauwesen - Teil 2: Einwirkung von Menschen in Gebäuden.* Beuth Verlag GmbH

[DIN 45631:1991-03]   DIN 45631:1991-03: *Berechnung des Lautstärkepegels und der Lautheit aus dem Geräuschspektrum - Verfahren nach E. Zwicker.* Beuth Verlag GmbH

[DIN 45669-1:2010-09]   DIN 45669-1:2010-09: *Messsung von Schwingungsimmissionen - Teil 1:Schwingungsmesser - Anforderungen und Prüfungen.* Beuth Verlag GmbH

[DIN 45680:2013-09 Entwurf]   DIN 45680:2013-09 ENTWURF: *Messung und Beurteilung tieffrequenter Geräuschimmissionen.* Beuth Verlag GmbH

[DIN EN 1995-1-1:2010-12]   DIN EN 1995-1-1:2010-12: *Eurocode 5: Bemessung und Konstruktion von Holzbauten; Teil 1-1: Allgemeines - Allgemeine Regeln und Regeln für den Hochbau.* Beuth Verlag GmbH

[DIN EN ISO 10140-3:2015-11]   DIN EN ISO 10140-3:2015-11: *Akustik - Messung der Schalldämmung von Bauteilen im Prüfstand - Teil 3: Messung der Trittschalldämmung.* Beuth Verlag GmbH

[DIN EN ISO 717-2:2013-06]   DIN EN ISO 717-2:2013-06: *Akustik – Bewertung der Schalldämmung in Gebäuden und von Bauteilen – Teil 2: Trittschalldämmung.* Beuth Verlag GmbH

[DIN EN ISO 9614-1:2009-11]   DIN EN ISO 9614-1:2009-11: *Bestimmung der Schalleistungspegel von Geräuschquellen aus Schallintensitätsmessungen Teil 1: Messung an diskreten Punkten.* Beuth Verlag GmbH

[Feichter 2013]   FEICHTER, I.: *Spannungs- und Traglastberechnungen an ausgewählten Problemen der Holz-Massivbauweise in Brettsperrholz*, TU Graz, Master's thesis, 2013

[Floden 2014]   FLODEN, O.: *Vibrations in lightweight structures - efficiency and reduction of numerical models*, Lund University, Sweden, Ph.D. thesis, 2014

[Fünfer 2016]   FÜNFER, C.: *Bewertung der abgestrahlten Schallleistung im Frequenzbereich unter 125 Hz von leichten Deckenonstruktionen bei Normhammerwerks- und Geheranregung*, Hochschule Rosenheim, Bachelor's thesis, 2016

[Friswell and Mottershead 1995]   FRISWELL, M. ; MOTTERSHEAD, J.E.: *Finite element model updating in structural dynamics.* Springer Verlag, 1995

[Getzner 2016]   GETZNER: *Overview Sylomer.* Internet. 2016. – URL https://www.getzner.com/de/downloads

[Glunz 2016]   GLUNZ: *AGEPAN OSB 4 / PUR, Produktdatenblatt.* Internet. 2016. – URL http://www.glunz.de/produkt_konstruktiv/gruppe/276/daten

[Gülzow 2008]   GÜLZOW, A.:   *Zerstörungsfreie Bestimmung der Biegesteifigkeiten von Brettsperrholzplatten*, Eidgenössiche Technische Hochsule Zürich, Ph.D. thesis, 2008

[Greim 2012]   GREIM, A.: *Identifikation der Materialparameter einer Brettsperrholzdecke durch Kalibrierung eines numerischen Modells mit gemessenen Eigenfrequenzen*, Technische Universität München, Master's thesis, 2012

[Grimsel 1999]   GRIMSEL, M.: *Mechanisches Verhalten von Holz*, Technische Universität Dresden, Ph.D. thesis, 1999

[Hamm et al 2010]   HAMM, P. ; RICHTER, A. ; WINTER, S.: Floor vibrations - new results. In: *WTCE 2010*, 2010

[Hanke 2012]   HANKE, T.:   *Auslegung und Konstruktion von Schwingungstilgern für Holzdeckenkonstruktionen*, Hochschule Rosenheim, Diplomarbeit, 2012

[Hashimoto 2001]   HASHIMOTO, N.:   Measurement of sound radiation efficiency by the discrete calculation method. In: *applied acoustics* 62 (2001), p. 429–446

[Hopkins 2007]   HOPKINS, C.: *Sound insulation.* Elsevier Ltd., 2007

[Jacobsen et al 1998]   JACOBSEN, F. ; CUTANDA, H. ; JUHL, P. M.:   A numerical and experimental investigation of the performance of sound intensity probes at high frequencies. In: *J. Acoust. soc. Am.* 103 (1998), February, Nr. 2, p. 953–961

[Joshi and Jangid 1997]   JOSHI, A. S. ; JANGID, R. S.:   Optimum parameters of multiple tuned mass dampers for base-excited damped systems. In: *Journal of Sound and Vibration* 202 (1997), Nr. 5, p. 657–667

[Knauf 2013]   KNAUF: *Knauf Wallboard GKB.* Internet. August 2013. – URL `http://www.knauf.de/wmv/?id=3338`

[Knauf 2014]   KNAUF: *Knauf Fließestrich FE 50 Largo floor screed.* Internet. May 2014. – URL `http://www.knauf.de/wmv/?id=1663`

[Kohrmann et al 2016]   KOHRMANN, M. ; EHAM, H. ; FÜNFER, C. ; VÖLTL, R. ; BUCHSCHMID, M. ; U., Schanda ; G., Müller: Planungshilfen zur schalltechnischen Bewertung von Deckensystemen aus Holz bei tiefen Frequenzen. In: *DAGA 2016*, 2016

[Kohrmann et al 2014]   KOHRMANN, M. ; R., Völtl ; G., Müller ; U., Schanda ; M., Buchschmid: Abschlussbericht zum AiF Forschungsvorhaben „VibWood"; Planungshilfen zur schall- und schwingungstechnischen Beschreibung von Holzdecken und zur Bewertung und Dimensionierung von angepassten Schwingungsschutzsystemen / Technische Universität München/ Hochschule Rosenheim. 2014. – Research report

[Kretschmann 2010]   KRETSCHMANN, D.: *Mechanical properties of wood: Wood handbook: wood as an engineering material: chapter 5.* Centennial ed. Madison, WI : U.S. Dept. of Agriculture, Forest Service, Forest Products Laboratory, 2010

[Lafont et al 2013]   LAFONT, T. ; TOTARO, N. ; LE BOT, A.: Review of statistical energy analysis hypotheses in vibroacoustics. In: *Proc. R.Soc. A*, 2013

[Lerch et al 2009]   LERCH, R. ; SESSLER, G. ; WOLF, D.: *Tecakustik Akustik.* Springer Verlag, 2009

[Lieblang 2000]   LIEBLANG, P.: *Beitrag zur Beschreibung des elastischen Materialverhaltens von Holz mit Methoden der Mikromechanik*, Rheinisch-Westfählische Technische Hochschule Aachen, Ph.D. thesis, 2000

[Ljunggren 2006]   LJUNGGREN, F.: *Floor Vibration - Dynamic Properties and Subjective Perception*, Luea University of Technology, Sweden, Ph.D. thesis, 2006

[Lyon and DeJong 1995]   LYON, R. H. ; DEJONG, R. G.: *Theory and Application of Statistical Energy Analysis.* Second Edition. Butterworth-Heinemann, 1995

[Mahn and Hopkins 2013]   MAHN, J. ; HOPKINS, C.: Competitive wooden floor systems - multi-objective optimization based on acoustics improvement. In: *AIA-DAGA*, 2013

[Mandal and Asif 2007]   MANDAL, M. ; ASIF, A.: *Continuous and Discrete Time Signals and Systems.* Cambridge University Press, 2007

[Mascia and Lahr 2006]   MASCIA, N. T. ; LAHR, F. A. R.: Remarks on orthotropic elastic models applied to wood. In: *Materials Research* 9 (2006), Nr. 3, p. 301–310

[Maynard et al 1985]   MAYNARD, J. D. ; WILLIAMS, E. G. ; LEE, Y.: Nearfield acoustic holography: I. Theory of generalized holography and the development of NAH. In: *Acoustical Sciety of America* 78 (1985), Nr. 4, p. 1395–1413

[Maznikova 2012]   MAZNIKOVA, Gergana: *Baupraktische Untersuchung der Tragkonstruktion abgehängter Deckensysteme - Numerisches Modell und messtechnische Untersuchung*, Technische Universität München, Bachelor's thesis, 2012

[Meistring 2005]   MEISTRING, Philip: *FEM-Simulation des Schwingungsverhaltens eines Holzstegträgers zum Abgleich elastomechanischer Größen*, Hochschule Rosenheim, Master's thesis, 2005

[Metsä Wood Merk GmbH 2012]   METSÄ WOOD MERK GMBH: *Leno® Broschüre.* August 2012. – URL http://www.metsawood.de/bauundkonstruktion/downloads/Documents/Leno_Broschuere_DE_082012.pdf

[Müller 2002]   MÜLLER, G.: Structure-borne sound – phenomena and prediction. In: *Fifth European Conference on Structural Dynamics*, 2002, p. 111–122

[Müller 2010a]   MÜLLER, G.: Continuum Mechanics and Tensor Analysis / Lehrstuhl für Baumechanik - Technische Universität München. 2010. – Lecture notes

[Müller 2010b]   MÜLLER, G.: Selected Topics of Technical Acoustics / Lehrstuhl für Baumechanik, Technische Universität München. 2010. – Lecture notes

[Müller 2011] MÜLLER, G.: Baudynamik / Lehrstuhl für Baumechanik - Technische Universität München. 2011. – Lecture notes

[Müller and Buchschmid 2011] MÜLLER, G. ; BUCHSCHMID, M.: *Untersuchungen zum Schwingungsverhalten leichter Verbunddeckensysteme.* Aachen : Shaker Verlag, 2011

[Müller and Groth 2007] MÜLLER, G. ; GROTH, C.: *FEM für Praktiker.* Volume 1: *Grundlagen.* 8., neu bearb. Aufl. Renningen : expert-Verl., 2007

[Mottershead and Friswell 1993] MOTTERSHEAD, J. E. ; FRISWELL, M. I.: Model updating in structural dynamics: a survey. In: *Journal of Sound and Vibration* 167 (1993), Nr. 2, p. 347–375

[Negeira 2013] NEGEIRA, J.: *Vibration in lightweight buildings - Perception and prediction*, Lund University, Ph.D. thesis, 2013

[Neuhaus 2009] NEUHAUS, H.: *Ingenieurholzbau: Grundlagen - Bemessung - Nachweise - Beispiele.* Vieweg + Teubner Verlag, 2009

[Nilsson and Liu 2013] NILSSON, A. ; LIU, B. ; PRESS, Science (Editor.): *Vibro-Acoustics.* Volume 2. Second. Berlin Heidelberg : Springer Verlag, 2013

[Petersen 1996] PETERSEN, C.: *Dynamik der Baukonstruktionen.* Vieweg Verlag, 1996

[Pierce 2007] PIERCE, A. ; ROSSING, T. D. (Editor.): *Springer handbook of acoustics.* Springer Verlag, 2007

[Rabold 2010] RABOLD, A.: *Anwendung der Finite Element Methode auf die Trittschallberechnung*, Technische Universität München, Ph.D. thesis, 2010

[Rabold 2011] RABOLD, A.: Trittschalldämmung richtig bewerten. In: *1. Internationale Schall- und Akustiktage*, 2011

[Rana 1996] RANA, R.: Response control of structures by tuned mass dampers and their generalizations. In: *Eleventh world conference on eathquake engineering*, 1996

[Ranz 2007] RANZ, T.: Ein feuchte- und temperaturabhängiger anisotroper Werkstoff: Holz. In: *Beiträge zur Materialtheorie* 2 (2007)

[Reuter 2011] REUTER, Claus: *Numerische Modellierung und messtechnische Verifkation einer stochastischen Anregung durch Fußgänger*, Technische Universität München, Master's thesis, 2011

[Reuter 1971] REUTER, R. C.: Concise Property Transformation Relations for an Anisotropic Lamina. In: *J. composite materials* 5 (1971), p. 270–272. – April

[Runtemund 2006] RUNTEMUND, K.: *Beitrag zur Prognose der Erschütterungsausbreitung infolge bewegter Lasten in Tunnels unter Verwendung dimensionsloser Kennzahlen*, Technische Universität München, Diplomarbeit, 2006

[Sadek et al 1997]   SADEK, F. ; MOHRAZ, B. ; TAYLOR, A. W. ; CHUNG, R. M.:   A method of estimating tehe parameters of tuned mass dampers for seismic applications. In: *Earthquake Engineering & Structural Dynamics* 26 (1997), p. 617–635

[Schanda et al 2013]   SCHANDA, U. ; TRÖBS, H. ; VÖLTL, R. ; BECKER, P.: Semi-empirical model of the impact force of a walking person in the time domain and generated impact sound spectra. In: *Internoise*, 2013

[Sonon 2001]   SONON, A. A.: The Physical Basics of Dimensional Analysis / Massachusetts Institude of Technologie. 2001. – Research report

[Sremcevic Witzig 2012]   SREMCEVIC WITZIG, J.:   *Model reduction methodes in room acoustical simulation at aow frequencies*, Technische Universität München, Ph.D. thesis, 2012

[Stelzmann et al 2008]   STELZMANN, U. ; GROTH, C. ; MÜLLER, G.: *FEM für Praktiker.* Volume 2: *Strukturdynamik.* 5., neu bearb. Aufl. Renningen : expert-Verl., 2008

[Tröbs 2013]   TRÖBS, H.M.: *Schallintensitätsmessung an einer abgehängten Unterdecke und Reduzierung ihrer Schallabstrahlung*, Hochschule Rosenheim, Bachelor's thesis, 2013

[VDI 2038 Blatt 2: 2013-01]   VDI 2038 BLATT 2: 2013-01: *Gebrauchstauglichkeit von Bauwerken bei dynamischenEinwirkungen. Untersuchungsmethoden und Beurteilungsverfahren der Baudynamik. Schwingungen und Erschütterungen - Prognose, Messung, Beurteilung und Minderung.* Verein Deutscher Ingenieure

[Warburton 1982]   WARBURTON, G. B.: Optimum absorber parameters for various combinations of response and excitation parameters. In: *Earthquake Engineering & Structural Dynamics* 10 (1982), Nr. 3, p. 381–401

[Warburton and Ayorinde 1980]   WARBURTON, G. B. ; AYORINDE, E. O.: Optimum absorber parameters for simple systems. In: *Earthquake Engineering & Structural Dynamics* 8 (1980), Nr. 3. – ISSN 1096-9845

[Weckendorf et al 2015]   WECKENDORF, J. ; TORATTI, T. ; SMITH, I. ; TANNERT, T.: Vibration serviceability performance of timber floors. In: *Eur. J. Wood Prod.* (2015)

[Weimar and Jochem 2013]   WEIMAR, H. (Editor.) ; JOCHEM, D. (Editor.): *Holzverwendung im Bauwesen - Eine Marktstudie im Rahmen der „Charta für Holz".* Johann Heinrich von Thünen-Institut, 2013 (Thünen Report 9)

[Wiechert 2005]   WIECHERT, L.: *1:1 Modell einer Verbunddeckenkonstruktion Erstellung zweier Finite-Elemente-Modelle in APDL (ANSYS Parametric Design Language) und Gegenüberstellung der Ergebnisse der Modalanalysen Grundlagen der Statistischen Energieanalyse*, Technische Universität München, Master's thesis, 2005

[Williams and Maynard 1982]   WILLIAMS, G. ; MAYNARD, D.: Numerical evaluation of the Rayleigh Integral for planar radiators using FFT. In: *J. Acoust. soc. Am.* 72 (1982), December, Nr. 6, p. 2020–2030

[Winter 2012]   WINTER, C.: *Messtechnische Untersuchung leichter Deckentragwerke im Wellenzahlbereich und Prognose der abgestrahlten Schallleistung*, Technische Universität München - Lehrstuhl für Baumechanik, Master's thesis, 2012

[Winter et al 2014]   WINTER, C. ; M., Buchschmid ; MECKING, S. ; WEINEISEN, C. ; G., Müller ; U., Schanda: Modelling the sound transmission across junctions of building components by energy influence coefficients. In: *Proceedings of the 9th International Conference on Structural Dynamics*, 2014, p. 3265–3271

[Winter et al 2010]   WINTER, S. ; HAMM, P. ; RICHTER, A.: Schwingungstechnische Optimierung von Holz- und Holz-Beton-Verbunddecken: Entwicklung von Bemessungs- und Konstruktionsregeln auf der Grundlage eines kalibrierten FEM-Modells und unter Berücksichtigung des Dissipations-Potentials unterschiedlicher Deckenaufbauten / TU München. 2010. – Research report

[Zierep 1982]   ZIEREP, J.: *Ähnlichkeitsgesetze und Modellregeln der Strömungslehre*. Karlsruhe : Verlag G. Braun, 1982